

FLEXURAL BEHAVIOUR OF RECTANGULAR FRP TUBES FULLY OR PARTIALLY FILLED WITH REINFORCED CONCRETE

Comportement en flexion de tubes en PRF rectangulaires entièrement ou
partiellement remplis de béton armé

Thèse de doctorat
Spécialité: génie civil

Ahmed Mohamed Abouzied SOLIMAN

A dissertation submitted in partial fulfillment
of the requirements for the degree of
Doctor of Philosophy
(Civil Engineering)

Jury: Prof. / Radhouane MASMOUDI, PE., PhD (directeur de recherche)
Prof. / Omar CHAALLAL, PE., PhD
Prof. / Ehab EL-SALAKAWY, PE., PhD
Chief, Structures Division, MTQ / Gérard DESGAGNÉ, PE., M.Sc.
Prof. / Richard GAGNÉ, PE., PhD

ABSTRACT

Recently, fiber-reinforced polymer (FRP) composite materials have been used in the field of civil engineering constructions especially in corrosive environments. They can be used as internal reinforcement for beams, slabs, and pavements, or as external reinforcement for rehabilitation and strengthening different structures. One of their innovative applications is the concrete-filled FRP tubes (CFFTs) which are becoming an alternative for different structural members such as piles, columns, bridge girders, and bridge piers due to their high performance and durability. In such integrated systems, the FRP tubes act as stay-in-place forms, protective jackets for the embedded concrete and steel, and as external reinforcement in the primary and secondary direction of the structural member.

Extensive research was developed on CFFTs as columns, but comparatively limited research was carried out on CFFTs as beams especially those with rectangular sections. The circular sections exhibit magnificent confinement efficiency in case of columns. However, the rectangular sections have higher moment of inertia and flexural stiffness to resist the applied loads and deformations in case of beams. Moreover, the construction and architectural requirements prefer the rectangular section of beams, rather than the circular beams, due to its stability during installation and its workability during connecting to other structural members like slabs and columns. Also, CFFTs that are completely filled with concrete are not optimal for applications governed by pure bending, because the excess weight of the cracked concrete below the neutral axis may increase the transportation and installation cost.

This dissertation presents experimental and theoretical investigations on the flexural behaviour of rectangular CFFT beams with steel rebar. These hybrid FRP-concrete-steel tubular rectangular beams contain outer rectangular filament-wound glass-FRP (GFRP) tubes to increase the sectional moment of inertia, to provide flexural and shear reinforcement, and to protect the inner structural elements (concrete and steel) against corrosion. The outer tubes were fully-or-partially filled with concrete and were reinforced with steel rebar at the tension side only. Inner hollow circular or square filament-wound GFRP tubes, shifted toward the tension zone, were provided inside the CFFT beam to eliminate the excess weight of the

cracked concrete at the tension side, to confine actively the concrete at the compression side and to act as reinforcement at the tension side. The surfaces of tubes adjacent to concrete were roughened by sand coating to fulfill the full composite action of such hybrid section. Several test variables were chosen to investigate the effect of the outer and inner tubes thickness, fibers laminates, and shape on the flexural behaviour of such hybrid CFFT beams. To fulfil the objectives of the study, twenty-four full-scale beam specimens, 3200 mm long and $305 \times 406 \text{ mm}^2$ cross section, were tested under a four-point bending load. These specimens include eight fully-CFFT beams with wide range of tube thickness of 3.4 mm to 14.2 mm, fourteen partially-CFFT beams with different outer and inner tubes configurations, and two conventional steel-reinforced concrete (RC) beams as control specimens.

The results indicate outstanding performance of the rectangular fully and partially-CFFT beams in terms of strength-to-weight ratio and ductility compared to the RC beams. The fully-CFFT beams with small tube thickness failed in tension by axial rupture of fibers at the tension side. While, the fully-CFFT beams with big tube thickness failed in compression by outward buckling of the outer tube compression flange with warning signs. The results indicate also that the flexural strength of the fully-CFFT beams was ascending nonlinearly with increasing the tubes thickness until a certain optimum limit. This limit was evaluated to define under-and-over-reinforced CFFT sections, and consequently to define the tension and compression failure of fully-CFFT beams, respectively. The inner hollow tubes act positively in reinforcing the partially-CFFT beams and confining the concrete core at the compression side. The strength-to-weight ratio of the partially-CFFT beams attained higher values than that of the corresponding fully-CFFT beams. Generally, the partially-CFFT beams failed gradually in compression due to outward buckling of the outer tube compression flange with signs of confining the concrete core at the compression side. The inner circular voids pronounced better performance than the square inner voids, however they have the same cross sectional area and fiber laminates.

Theoretical section analysis based on strain compatibility/equilibrium has been developed to predict the moment-curvature response of the fully-CFFT section addressing the confinement and tension stiffening of concrete. The analytical results match well the experimental results in terms of moment, deflection, strains, and neutral axis responses. In addition, analytical

investigation was conducted to examine the validity of the North American design codes provisions for predicting the deflection response of fully and partially-CFFT beams. Based on these investigations, a new power and assumptions were proposed to Branson's equation to predict well the effective moment of inertia of the CFFT section. These assumptions consider the effect of the GFRP tube strength, thickness and configuration, in addition to the steel reinforcement ratio. The proposed equations predict well the deflection in the pre-yielding and post-yielding stages of the hybrid FRP-concrete-steel CFFT rectangular beams.

Keywords: Fiber-Reinforced Polymer, Filament Winding, Concrete-Filled FRP Tube, Beams, Flexural behaviour, Deflection.

RÉSUMÉ

Les matériaux composites en polymère renforcé de fibres (PRF) ont récemment été utilisés dans le domaine des constructions de génie civil, en particulier dans les environnements corrosifs. Elles peuvent être utilisées comme une armature interne pour des poutres, dalles et les trottoirs, ou comme une armature externe pour la réhabilitation et le renforcement de différentes structures. L'une de leurs applications novatrices est les tubes de polymères renforcés de fibres remplis de béton (TPFRB¹) qui sont en train de devenir une alternative pour divers éléments structuraux tels que les pieux, les colonnes, les poutres et les piliers de ponts en raison de leur haute performance et durabilité. Dans de tels systèmes intégrés, les tubes PRF agissent comme un coffrage permanent, une chemise protectrice pour le béton et l'acier encastrés, et comme une armature externe dans les directions longitudinale et transversale de l'élément structural.

La recherche a été concentrée sur les TPRFB comme des colonnes, mais très peu de recherche a été effectuée les TPRFB comme des poutres particulièrement celles à section rectangulaire. La section circulaire présente une efficacité de confinement efficace en cas de colonnes. Toutefois, la section rectangulaire a un moment d'inertie plus élevé et une rigidité flexionnelle plus efficace pour résister les charges appliquées et les déformations dans le cas des poutres. Par ailleurs, les travaux de construction et les exigences architecturales préfèrent la section rectangulaire des poutres, plutôt que les poutres circulaires, en raison de sa stabilité pendant l'installation et sa maniabilité lors de la connexion à d'autres membres structuraux comme les dalles et les colonnes. En outre, les poutres TPRFB qui sont complètement remplis de béton ne sont pas optimales pour les applications contrôlées par la flexion pure, puisque le béton fissuré en dessous de l'axe neutre ne contribue pas à la résistance et augmente le poids propre et les coûts de transport et d'installation.

Cette thèse présente des études théoriques et expérimentales sur le comportement en flexion de poutres rectangulaires (TPRFB) en béton armé. Ces poutres rectangulaires tubulaires hybrides en PRF-béton-acier sont composées de tubes rectangulaires externes fabriquées par

¹ TPRFB est l'acronyme du terme en anglais CFFT : Concrete-Filled FRP-Tubes

enroulement filamentaire. Ces tubes fournissent un renforcement de flexion et de cisaillement; et protègent le béton armé contre la corrosion. Les poutres peuvent être soit entièrement ou partiellement remplies de béton. Des tubes intérieurs (de section circulaires ou carrés) en polymères renforcés de fibres de verre (PRFV) sont positionnés dans la zone tendue de la poutre afin de réduire le poids et d'éliminer le béton fissuré en traction. Pour augmenter l'action composite de la section hybride, les surfaces des tubes adjacents au béton ont été rendues rugueuses par enrobage de sable. Plusieurs variables ont été choisis pour étudier l'effet de l'épaisseur des tubes extérieurs et intérieurs, les laminés de fibres, et la forme sur le comportement en flexion de ces poutres hybrides (TPRFB). Pour atteindre les objectifs de l'étude, vingt-quatre échantillons de poutre pleine grandeur, ayant une longueur de 3200 mm et une section transversale de $305 \times 406 \text{ mm}^2$, ont été testés sous une flexion à quatre points. Ces échantillons comprennent huit poutres de TPRFB entièrement remplies avec une large gamme d'épaisseur du tube externe de 3.4 mm à 14.2 mm, quatorze poutres de TPRFB partiellement remplies avec différentes configurations de tubes extérieurs et intérieurs, et deux poutres en béton armé conventionnel, comme échantillons de référence.

Les résultats indiquent une performance exceptionnelle des poutres rectangulaires de TPRFB entièrement et partiellement remplies en termes du rapport de la résistance sur la masse et de la ductilité par rapport aux poutres en béton armé conventionnel. Les poutres de TPRFB entièrement remplies avec un tube de petite épaisseur ont rompu de façon moins ductile en tension par rupture axiale des fibres. Les poutres de TPRFB entièrement remplies et ayant une grande épaisseur ont rompu de façon ductile en compression par flambage local vers l'extérieur des parois en compression du tube externe. Les résultats indiquent également que la résistance à la flexion des poutres de TPRFB entièrement remplies augmente d'une façon non linéaire avec l'augmentation de l'épaisseur des tubes jusqu'à une certaine limite optimale. Cette limite a été évaluée pour définir les sections TPRFB sous-armées et surarmées et, par conséquent, pour définir la rupture en tension et en compression des poutres de TPRFB entièrement remplies, respectivement. Les tubes creux intérieurs agissent positivement dans le renforcement des poutres de TPRFB partiellement remplies et en confinant le noyau de béton du côté en compression. En général, les poutres de TPRFB partiellement remplies ont rompu en compression par flambage local vers l'extérieur des parois en compression du tube

externe. Les vides circulaires intérieurs ont montré une meilleure performance que les vides carrés intérieurs, bien qu'ils aient la même superficie de la section transversale et le même taux de PRF.

Une analyse théorique basée sur la compatibilité des déformations d'une section en flexion a été développée pour prédire la réponse moment-courbure de la poutre TPRFB en tenant compte des pourcentages de confinement externe et interne. Les résultats analytiques et les résultats expérimentaux s'accordent en termes de moment, flèche, déformations, et positions de l'axe neutre. En outre, une étude analytique a été menée afin d'examiner la validité des codes de conception nord-américains pour prédire la réponse en flexion des poutres TPRFB. En se basant sur les résultats de ces études, de nouvelles équations ont été proposées pour mieux prédire le moment effectif d'inertie de la section et une nouvelle procédure de conception pour prédire les capacités ultimes. Ces équations considèrent l'effet de la résistance des tubes en PRFV externe et interne que le taux d'armature en acier. En outre, ils prédisent bien la flèche dans les phases avant et après la limite élastique des poutres rectangulaires hybrides à haute performance.

Mots-clés : Polymère renforcé de fibres (PRF), enroulement filamentaire, Tubes de PRF remplis de béton, poutres, comportement en flexion, flèche.

PRESENTATION OF THE CANDIDATE

EDUCATION

- B.Sc. in civil engineering, Faculty of Engineering, Helwan University, Cairo, Egypt, 2004. The undergraduate grade was Distinction with honor rank (91.44%) and the 1st of my colleagues (1/300).
- M.Sc. degree in RC structures. M.Sc. thesis titled "Behaviour of flat slab-corner column connection", Civil Engineering department, Faculty of Engineering, Helwan University, Cairo, Egypt, 2009.
- Now, Ph.D. candidate in the field of RC structures, Civil Engineering department, Faculty of Engineering, Sherbrooke University, Sherbrooke, Quebec, Canada.

The candidate has participated in the following publications during his doctorate study at Sherbrooke University:

US PATENT 61/897,429

R. Masmoudi and A. Abouzied, (2013). "Composite structural member, method for manufacturing same, and connecting assemblies for composite structural members", International Application Number: PCT/CA2014/051045", US Patent 61/897,429.

JOURNAL PUBLICATIONS:

- 1) A. Abouzied and R. Masmoudi, (2015). "Structural performance of new fully and partially concrete-filled rectangular FRP-tube beams", *Elsevier Journal of Construction and Building Materials*, Vol.101: 652–660.
- 2) A. Boumarafi, A. Abouzied, R. Masmoudi, (2015). "Harsh environments effects on the axial behaviour of circular concrete-filled fibre reinforced-polymer (FRP) tubes", *Elsevier Journal of Composites: Part B*, Vol.83: 81-87.
- 3) A. Abouzied and R. Masmoudi, (2016). "New high-performance rectangular FRP-tube beams partially filled with concrete", *ACI-Special Publication*, SP-15.

- 4) A. Abouzied and R. Masmoudi, (2016). “Flexural behaviour of rectangular FRP-tubes filled with reinforced concrete: experimental and theoretical studies”, *Elsevier Journal of Engineering Structures*, ENGSTRUCT-S-16-00088, (In review).
- 5) A. Abouzied and R. Masmoudi, (2016). “Effective moment of inertia of rectangular FRP-tube beams fully or partially filled with reinforced concrete”, *Journal of Structural Engineering ASCE*, (Submitted).
- 6) A. A. Ahmed, M. Hassan, H. Mohamed, A. Abouzied, and R. Masmoudi, (2016). “Axial behavior of circular CFFT long columns internally reinforced with steel, carbon and glass longitudinal bars”, *Elsevier Journal of Engineering Structures*, ENGSTRUCT-D-15-01381, (In review).

CONFERENCE PUBLICATIONS:

- 1) A. Abouzied, M. Ammar, R. Masmoudi, (2011). “Nanoparticles effect on the physical and mechanical properties of FRP filament-winded composites”, *Proceedings of 26th ASC Annual Technical Conference (the Second Joint US-Canada Conference on Composites)*, Montreal, Canada, September 2011, pp 1131-1140.
- 2) A. Abouzied, R. Masmoudi, R. Gagne, A. Tagnit-Hamou, (2012). “Effect of nanoparticles added to vinyl ester resin on the compressive behaviour of square concrete-filled GFRP tubes”, *Proceedings of 6th International Conference on Advanced Composite Materials in Bridges and Structures ACMPS-VI*, Kingston, Canada, May 2012, pp 496-503.
- 3) A. Abouzied, M. Ammar, R. Masmoudi, (2012). “Nanoparticles effect on FRP filament-winded composites performance”, *Proceedings of CICE 6th International Conference on FRP Composites in Civil Engineering (CICE)*, Rome, Italy, June 2012.
- 4) A. Abouzied and R. Masmoudi, (2012). “Square columns confined by GFRP tube or steel ties”, *Proceedings of FRPRCS 11th International Symposium on fiber reinforced Polymer for reinforced Concrete structures*, Portugal, December 2012.
- 5) A. Abouzied and R. Masmoudi, (2013). “Performance of square concrete-filled FRP tubes versus steel reinforced concrete columns”, *Proceedings of 2nd conference on Smart Monitoring, Assessment and Rehabilitation of Civil Structures SMAR 2013*, Istanbul, Turkey, September 2013.

- 6) A. Abouzied and R. Masmoudi, (2014). “Flexural behaviour of new partially concrete-filled filament-wound rectangular FRP tube beams”, *Proceedings of 4th International Structural Specialty Conference CSCE*, Halifax, NS, May 2014, CST-171-(1-10).
- 7) A. Abouzied and R. Masmoudi, (2015). “New design of rectangular partially concrete-filled filament-wound FRP tube beam”, *Proceedings of 3rd conference on Smart Monitoring, Assessment and Rehabilitation of Civil Structures SMAR 2015*, Antalya, Turkey, September 2015.
- 8) R. Masmoudi, A. Abouzied, H. Mohamed, (2015) “New hybrid concrete filled FRP stay-in-place forms as high-performance structural members”. *Proceedings of 13th Arab Structural Engineering Conference ASEC*, University of Blida, Blida, Algeria, December 2015.
- 9) A. Abouzied and R. Masmoudi, (2016). “Deflection of Rectangular Concrete-Filled FRP Tube Beams”, *Proceedings of 7th International Conference on Advanced Composite Materials in Bridges and Structures ACMPS-VII*, Vancouver, British Columbia, Canada, August 2016 (Submitted).
- 10) A. Abouzied and R. Masmoudi, (2016). “Flexural behaviour of rectangular FRP-tubes filled with reinforced concrete: experimental and analytical investigations”, *Proceedings of 5th International Structural Specialty Conference CSCE*, London, ON, Canada, June 2016, (Submitted).

ACKNOWLEDGEMENT

Thanks to Almighty ALLAH for the gracious kindness in all the endeavors, I have taken up in my life.

I would like to express my sincere greatest appreciation and thanks to my supervisor Professor Radhouane Masmoudi for offering me the opportunity to work on such a challenging subject. I am so proud to work with him. All of the guidance, insight, helpful advice, and constant encouragement provided throughout the course of the dissertation are greatly appreciated. I owe him an unbelievable amount of gratitude for his prominent role in helping me to achieve one of the greatest accomplishments in my life.

Sincere words of thanks must also go to the technical staff at the Structures Laboratory, Department of Civil Engineering at Sherbrooke University, especially, Mr. Éric Beaudoin, for his assistance during the fabrication, construction and testing of the specimens.

In addition, the author is thankful to Natural Science and Engineering Research Council of Canada (NSERC) and the Fonds québécois de la recherche sur la nature et les technologies (FQRNT) for their partially sponsored financial support. The authors also acknowledge the contribution of the Canadian Foundation for Innovation (CFI) for the infrastructure used to conduct testing.

My deep appreciation and thanks are expressed to my father, my mother, my brothers for their support, endless love and encouragement.

Finally, I owe my deepest love and appreciation to my dear wife for her steadfast support and continuous encouragement. She was always there to give me the push for this challenge and to face all life obstacles. I cannot present this work without expressing my love to my son Omar who wish to be engineer like me, and my daughter Aliaa who enlightened my life with her smile.

TABLE OF CONTENTS

| | |
|--|--------------|
| ABSTRACT | i |
| RÉSUMÉ | v |
| PRESENTATION OF THE CANDIDATE | ix |
| ACKNOWLEDGEMENT | xiii |
| TABLE OF CONTENTS | xv |
| LIST OF TABLES | xxi |
| LIST OF FIGURES | xxiii |
| | |
| CHAPTER 1: INTRODUCTION | 1 |
| 1.1 GENERAL | 1 |
| 1.2 RESEARCH OBJECTIVES | 4 |
| 1.3 METHODOLOGY..... | 5 |
| 1.4 THESIS OUTLINES..... | 6 |
| | |
| CHAPTER 2: LITERATURE REVIEW | 9 |
| 2.1 INTRODUCTION..... | 9 |
| 2.2 FRP COMPOSITE MATERIALS | 10 |
| 2.2.1 Fibers..... | 10 |
| 2.2.1.1 Glass Fibers | 11 |
| 2.2.1.2 Carbon Fibers | 11 |
| 2.2.1.3 Aramid Fibers..... | 12 |
| 2.2.2 Polymer Resins | 12 |
| 2.2.2.1 Polyester Resin | 13 |
| 2.2.2.2 Epoxy Resin..... | 13 |
| 2.2.2.3 Vinyl Ester Resin..... | 13 |
| 2.2.3 Fillers | 14 |
| 2.3 FRP COMPOSITE MANUFACTURING PROCESSES | 14 |
| 2.3.1 Pultrusion Process..... | 15 |
| 2.3.2 Resin Transfer Molding (RTM) Process..... | 15 |

| | | |
|--|---|-----------|
| 2.3.3 | Vacuum Assisted Resin Transfer Molding (VARTM) Process..... | 16 |
| 2.3.4 | Compression Molding Process | 16 |
| 2.3.5 | Filament Winding Process | 16 |
| 2.4 | CONCRETE-FILLED FRP TUBES UNDER FLEXURE | 18 |
| 2.4.1 | General Review..... | 18 |
| 2.4.2 | Effect of Inner Concrete Core..... | 19 |
| 2.4.3 | Effect of Concrete Strength | 19 |
| 2.4.4 | Effect of Tube Thickness | 20 |
| 2.4.5 | Effect of Tube Laminate Structure (Fibers Orientation)..... | 22 |
| 2.4.6 | Effect of Steel and FRP Rebar | 23 |
| 2.4.7 | Effect of Bond..... | 25 |
| 2.4.8 | Effect of Inner Hole | 27 |
| 2.5 | LIGHTWEIGHT HYBRID FRP-CONCRETE COMPOSITE SECTIONS | 28 |
| CHAPTER 3: EXPERIMENTAL PROGRAM..... | | 47 |
| 3.1 | INTRODUCTION..... | 47 |
| 3.2 | FABRICATION OF GFRP TUBES | 47 |
| 3.3 | TESTS ON GFRP TUBES..... | 49 |
| 3.3.1 | Fiber Content | 49 |
| 3.3.2 | Glass Transition Temperature..... | 50 |
| 3.3.3 | Mechanical Performance of GFRP Tubes | 51 |
| 3.4 | TEST VARIABLES..... | 52 |
| 3.5 | BEAM SPECIMENS | 53 |
| 3.6 | FORMWORKS AND CASTING | 54 |
| 3.7 | TEST SETUP AND INSTRUMENTATIONS | 55 |
| CHAPTER 4: FLEXURAL BEHAVIOUR OF FULLY-CFFT RECTANGULAR | | |
| BEAMS | | 75 |
| 4.1 | ABSTRACT..... | 76 |
| 4.2 | INTRODUCTION..... | 77 |
| 4.3 | EXPERIMENTAL PROGRAM | 78 |

| | | |
|---------|--|-----|
| 4.4 | TEST RESULTS AND DISCUSSIONS | 79 |
| 4.4.1 | Shear Strength of Rectangular Fully-CFFT Beams | 80 |
| 4.4.2 | Flexural Behaviour of the Control RC Beams | 81 |
| 4.4.3 | Failure Patterns of Fully-CFFT Beams | 81 |
| 4.4.4 | Effect of Cycling Load..... | 84 |
| 4.4.5 | Flexural Performance of Fully-CFFT Beams | 84 |
| 4.4.5.1 | Effect of Steel Reinforcement in Fully-CFFTs | 85 |
| 4.4.5.2 | Effect of Outer Tube Laminate Structure | 87 |
| 4.4.5.3 | Effect of Outer Tube Thickness..... | 88 |
| 4.4.6 | Cracking Moment of Rectangular Fully-CFFT Beams | 90 |
| 4.5 | ANALYTICAL MODELLING OF RECTANGULAR CFFT BEAMS UNDER FLEXURE..... | 93 |
| 4.5.1 | Description of the Analytical Model..... | 94 |
| 4.5.2 | Constitutive Relationships of Materials..... | 95 |
| 4.5.2.1 | Steel Model..... | 95 |
| 4.5.2.2 | FRP Tube Model | 96 |
| 4.5.2.3 | Concrete Model | 98 |
| 4.5.3 | Procedure of Analysis..... | 101 |
| 4.5.4 | Verification of the Model..... | 102 |
| 4.6 | PARAMETRIC STUDY | 104 |
| 4.6.1 | Effect of Steel Reinforcement Ratio | 104 |
| 4.6.2 | Effect of Tube Stiffness or Laminate Structure | 105 |
| 4.6.3 | Effect of Tube Thickness | 105 |
| 4.6.4 | Effect of Concrete Strength | 106 |
| 4.7 | CONCLUSIONS..... | 106 |

**CHAPTER 5: FLEXURAL BEHAVIOUR OF PARTIALLY-CFFT RECTANGULAR
BEAMS145**

| | | |
|-----|----------------------------|-----|
| 5.1 | ABSTRACT | 146 |
| 5.2 | INTRODUCTION..... | 147 |
| 5.3 | EXPERIMENTAL PROGRAM | 149 |

| | | |
|---|--|------------|
| 5.4 | TEST RESULTS AND DISCUSSIONS | 149 |
| 5.4.1 | Shear Strength of Rectangular Partially-CFFT Beams | 150 |
| 5.4.2 | Flexural Behaviour of RC Beams and Fully-CFFT Beams | 151 |
| 5.4.3 | Failure Pattern of Partially-CFFT Beams | 151 |
| 5.4.4 | Flexural Performance of Rectangular Partially-CFFT Beams | 153 |
| 5.4.4.1 | Effect of the Outer Tube Thickness in Partially-CFFT Beams | 153 |
| 5.4.4.2 | Effect of the Inner Tube Thickness in Partially-CFFT Beams | 155 |
| 5.4.4.3 | Effect of the Inner Tube Laminate Structure in Partially-CFFT Beams .. | 156 |
| 5.4.4.4 | Effect of the Inner Tube Shape in Partially-CFFT Beams | 157 |
| 5.4.5 | Comparison between Fully and Partially-CFFT Beams | 158 |
| 5.4.6 | Strain Behaviour in CFFT Beams | 160 |
| 5.4.7 | Strength to Weight Ratio | 161 |
| 5.4.8 | Cracking Moment (M_{cr}) of Rectangular Partially-CFFT Beams | 163 |
| 5.5 | CONCLUSIONS | 164 |
| CHAPTER 6: DEFLECTION PREDICTION OF RECTANGULAR CFFT BEAMS | | 201 |
| 6.1 | ABSTRACT | 202 |
| 6.2 | INTRODUCTION | 203 |
| 6.3 | REVIEW OF DEFLECTION EQUATIONS | 203 |
| 6.4 | DEFLECTION CALCULATIONS | 205 |
| 6.4.1 | Procedure of Analysis and Assumptions | 209 |
| 6.4.1.1 | At the Pre-Cracking Stage ($M_a \leq M_{cr}$) | 209 |
| 6.4.1.2 | At the Pre-Yielding Stage ($M_{cr} \leq M_a \leq M_y$) | 209 |
| 6.4.1.3 | At the Post-Yielding Stage ($M_y \leq M_a \leq M_u$) | 210 |
| 6.5 | CONCLUSIONS | 211 |
| CHAPTER 7: CONCLUSIONS AND RECOMMENDATIONS | | 221 |
| 7.1 | CONCLUSIONS | 221 |
| 7.2 | RECOMMENDATIONS FOR FUTURE WORK | 225 |
| 7.3 | CONCLUSIONS EN FRANÇAIS | 226 |
| 7.4 | RECOMMANDATIONS POUR DES TRAVAUX FUTURS | 230 |

| | |
|------------------------|------------|
| REFERENCES..... | 233 |
| APPENDIX A..... | 245 |
| APPENDIX B..... | 250 |

LIST OF TABLES

| | |
|--|-----|
| Table 2.1 – Typical properties of structural materials (ISIS Canada Design Manual No.4 2008) | 32 |
| Table 3.1 – Configurations and mechanical properties of fabricated filament-wound GFRP tubes | 57 |
| Table 3.2 – Details of beam specimens | 58 |
| Table 4.1 – Beam specimens and summary of test results | 109 |
| Table 4.2 – Shear forces in fully-CFFT beams..... | 110 |
| Table 4.3 – Details of calculating cracking strength of fully-CFFT beams..... | 111 |
| Table 4.4 – Experiment versus predicted cracking moment for rectangular CFFT beams .. | 112 |
| Table 4.5 – Internal forces and their positions in rectangular CFFT section..... | 113 |
| Table 4.6 – Theoretical versus experimental yield moments of rectangular CFFT beams .. | 114 |
| Table 4.7 – Theoretical versus experimental ultimate moments of rectangular CFFT beams using unconfined concrete model | 115 |
| Table 4.8 – Theoretical versus experimental ultimate moments of rectangular CFFT beams using partially confined concrete model | 115 |
| Table 5.1 – Beam specimens and summary of test results | 166 |
| Table 5.2 – Shear forces in fully and partially-CFFT beams..... | 167 |
| Table 5.3 – Details of calculating cracking strength of partially-CFFT beams..... | 168 |

LIST OF FIGURES

| | |
|--|----|
| Figure 2.1 – Schematic of pultrusion process [http://mdacomposites.org] | 33 |
| Figure 2.2 – Schematic of RTM process [http://mdacomposites.org] | 33 |
| Figure 2.3 – Schematic of VARTM process [http://mdacomposites.org] | 34 |
| Figure 2.4 – Schematic of compression molding process [http://mdacomposites.org] | 34 |
| Figure 2.5 – Schematic of filament winding machine [http://mdacomposites.org]..... | 35 |
| Figure 2.6 – Resin bath types in filament winding process [http://mdacomposites.org]..... | 35 |
| Figure 2.7 – Distribution of composite manufacturing process wise [Beckwith 2006] | 36 |
| Figure 2.8 – Composite manufacturing cost by different processes [Taheri 1996]..... | 36 |
| Figure 2.9 – Field applications of CFFTs [http://google.com] | 37 |
| Figure 2.10 – Moment-curvature response and failure modes of B1 and B2 [Fam and Rizkalla 2002]..... | 38 |
| Figure 2.11 – Effect of concrete strength on load-deflection curves [Mohamed and Masmoudi 2010]..... | 38 |
| Figure 2.12 – Effect of FRP tube thickness on load–deflection curves [Mohamed and Masmoudi 2010]..... | 39 |
| Figure 2.13 – Load-deflection response and failure modes of B3 and B4 [Fam and Rizkalla 2002] | 39 |
| Figure 2.14 – Load-deflection curves for specimens B1 to B7 [Cole and Fam 2006] | 40 |
| Figure 2.15 – Effect of rebar type on load–deflection curves [Mohamed and Masmoudi 2010] | 41 |
| Figure 2.16 – Beam test results of Belzer et al. (2013)..... | 41 |
| Figure 2.17 – Load-deflection behaviour for different beam configurations [Fam and Rizkalla 2002] | 42 |
| Figure 2.18 – Beam test results of Fam et al. (2005)..... | 43 |
| Figure 2.19 – Previous approaches of hybrid composite sections | 44 |
| Figure 2.20 – Proposed cross-section by Elmahdy et al. (2008) | 44 |
| Figure 2.21 – Proposed cross-section by Khennane (2010) | 45 |
| Figure 2.22 – Cross-section examples of DSTB [Idris and Ozbakkaloglu 2014] | 45 |

| | |
|--|-----|
| Figure 3.1 – Filament winding process (Civil Engineering department, Sherbrooke University) | 59 |
| Figure 3.2 – Fibers installment in filament winding process..... | 59 |
| Figure 3.3 – Fiber laminates structure patterns..... | 60 |
| Figure 3.4 – Curing of FRP tubes by applying heat | 60 |
| Figure 3.5 – Removing the mandrel | 61 |
| Figure 3.6 – Final Products of GFRP tubes | 61 |
| Figure 3.7 – Sand coating for GFRP tubes | 62 |
| Figure 3.8 – Fiber content test (ASTM D3171-09) | 62 |
| Figure 3.9 – DSC test (ASTM D3418-08)..... | 63 |
| Figure 3.10 – Coupons tests and instrumentations | 64 |
| Figure 3.11 – Coupons tests results of OR12 ₃₀ and OR16 ₄₅ in axial direction..... | 65 |
| Figure 3.12 – Stress-strain response of steel bar 15M..... | 65 |
| Figure 3.13 – Cross section configurations of the tested beams..... | 66 |
| Figure 3.14 – Reinforcement cages and tubes assembly | 66 |
| Figure 3.15 – Details of beam specimens (dimensions are in mm)..... | 67 |
| Figure 3.16 – Casting process..... | 68 |
| Figure 3.17 – Seven days moisture curing for CFFT beams | 68 |
| Figure 3.18 – Concrete cylinders tests (ASTM C39-12)..... | 69 |
| Figure 3.19 – Typical schematic of test setup and instrumentations (dimensions are in mm)..... | 70 |
| Figure 3.20 – View of beam test setup | 70 |
| Figure 3.21 – Supports..... | 71 |
| Figure 3.22 – Scheme of loading and unloading cycles (rate = 1 mm/min)..... | 71 |
| Figure 3.23 – DPs positions to measure deflection and slippage | 72 |
| Figure 3.24 – LVDTs to measure top and bottom axial strains | 72 |
| Figure 3.25 – Strain gages on steel bars and inner tubes | 73 |
| Figure 3.26 – Strain gages on outer tubes..... | 73 |
| | |
| Figure 4.1 – Moment-slip response of fully-CFFT beams | 116 |
| Figure 4.2 – Typical steel strains and curvature of fully-CFFT beams | 116 |
| Figure 4.3 – Shear forces in fully-CFFT beams | 116 |

| | |
|--|-----|
| Figure 4.4 – Corner failure in pultruded FRP tubes (Belzer et al. 2013)..... | 117 |
| Figure 4.5 – Matrix surface cracks | 117 |
| Figure 4.6 – Failure pattern and moment-deflection response of RC beams..... | 118 |
| Figure 4.7 – Failure pattern and moment-deflection response of fully-CFFT beams OR2 ₃₀ | 119 |
| Figure 4.8 – Failure pattern and moment-deflection response of fully-CFFT beams OR4 ₃₀ | 120 |
| Figure 4.9 – Failure pattern and moment-deflection response of fully-CFFT beams OR8 ₃₀ | 121 |
| Figure 4.10 – Failure pattern and moment-deflection response of fully-CFFT beam OR12 ₃₀ | 122 |
| Figure 4.11 – Failure pattern and moment-deflection response of fully-CFFT beam OR16 ₄₅ | 123 |
| Figure 4.12 – Moment-deflection response of fully-CFFT beams | 124 |
| Figure 4.13 – Normalized moment-curvature response of fully-CFFT beams..... | 125 |
| Figure 4.14 – Proposed effect of steel reinforcement in fully-CFFT beams | 125 |
| Figure 4.15 – Coupons tests results of OR12 ₃₀ and OR16 ₄₅ in axial direction..... | 126 |
| Figure 4.16 – Correlations between M_{cr} , M_y , and M_u of fully-CFFT beams | 127 |
| Figure 4.17 – Proposed analytical model..... | 128 |
| Figure 4.18 – Proposed model for steel | 128 |
| Figure 4.19 – Proposed model for FRP tube..... | 129 |
| Figure 4.20 – Proposed model for concrete | 129 |
| Figure 4.21 – Effect of concrete confinement model | 130 |
| Figure 4.22 – Axial and transverse strains at the top face of the FRP tube in CFFT beams | 131 |
| Figure 4.23 – Theoretical versus experimental moments of CFFT beams | 131 |
| Figure 4.24 – Predicted versus experimental moment-strain response of CFFT beam OR2 ₃₀ | 132 |
| Figure 4.25 – Predicted versus experimental neutral axis depth of CFFT beam OR2 ₃₀ | 132 |
| Figure 4.26 – Predicted versus experimental moment-curvature response of CFFT beam OR2 ₃₀ (Model with partially confined concrete)..... | 133 |
| Figure 4.27 – Predicted versus experimental moment-deflection response of CFFT beam OR2 ₃₀ (Model with partially confined concrete)..... | 133 |
| Figure 4.28 – Predicted versus experimental moment-strain response of CFFT beam OR4 ₃₀ | 134 |

| | |
|--|-----|
| Figure 4.29 – Predicted versus experimental neutral axis depth of CFFT beam OR4 ₃₀ | 134 |
| Figure 4.30 – Predicted versus experimental moment-curvature response of CFFT beam OR4 ₃₀ (Model with partially confined concrete)..... | 135 |
| Figure 4.31 – Predicted versus experimental moment-deflection response of CFFT beam OR4 ₃₀ (Model with partially confined concrete)..... | 135 |
| Figure 4.32 – Predicted versus experimental moment-strain response of CFFT beam OR8 ₃₀ | 136 |
| Figure 4.33 – Predicted versus experimental neutral axis depth of CFFT beam OR8 ₃₀ | 136 |
| Figure 4.34 – Predicted versus experimental moment-curvature response of CFFT beam OR8 ₃₀ (Model with partially confined concrete)..... | 137 |
| Figure 4.35 – Predicted versus experimental moment-deflection response of CFFT beam OR8 ₃₀ (Model with partially confined concrete)..... | 137 |
| Figure 4.36 – Predicted versus experimental moment-strain response of CFFT beam OR12 ₃₀ | 138 |
| Figure 4.37 – Predicted versus experimental neutral axis depth of CFFT beam OR12 ₃₀ | 138 |
| Figure 4.38 – Predicted versus experimental moment-curvature response of CFFT beam OR12 ₃₀ (Model with partially confined concrete)..... | 139 |
| Figure 4.39 – Predicted versus experimental moment-deflection response of CFFT beam OR12 ₃₀ (Model with partially confined concrete)..... | 139 |
| Figure 4.40 – Effect of steel reinforcement on the flexural behaviour of CFFT beams with thin FRP tubes..... | 140 |
| Figure 4.41 – Effect of steel reinforcement on the flexural behaviour of CFFT beams with thick FRP tubes..... | 141 |
| Figure 4.42 – Effect of fiber laminates structure on the flexural behaviour of CFFT beams..... | 142 |
| Figure 4.43 – Effect of FRP tube thickness on the flexural behaviour of CFFT beams..... | 143 |
| Figure 4.44 – Effect of concrete strength on the flexural behaviour of CFFT beams..... | 144 |
| | |
| Figure 5.1 – Moment-slip response in partially-CFFT beams..... | 169 |
| Figure 5.2 – Typical steel strains and curvature of partially-CFFT beams..... | 170 |
| Figure 5.3 – Shear forces in partially-CFFT beams..... | 170 |
| Figure 5.4 – Failure pattern and moment-deflection response of RC beams..... | 171 |

| | |
|---|-----|
| Figure 5.5 – Failure pattern and moment-deflection response of fully-CFFT beams OR2 ₃₀ | 172 |
| Figure 5.6 – Failure pattern and moment-deflection response of fully-CFFT beams OR4 ₃₀ | 173 |
| Figure 5.7 – Failure pattern and moment-deflection response of fully-CFFT beams OR8 ₃₀ | 174 |
| Figure 5.8 – Failure pattern and moment-deflection response of partially-CFFT beam OR2 ₃₀ -IC4 ₃₀ | 175 |
| Figure 5.9 – Failure pattern and moment-deflection response of partially-CFFT beam OR4 ₃₀ -IC4 ₃₀ | 176 |
| Figure 5.10 – Failure pattern and moment-deflection response of partially-CFFT beams OR4 ₃₀ -IC2 ₃₀ | 177 |
| Figure 5.11 – Failure pattern and moment-deflection response of partially-CFFT beams OR8 ₃₀ -IC4 ₃₀ | 178 |
| Figure 5.12 – Failure pattern and moment-deflection response of partially-CFFT beams OR4 ₃₀ -IS2 ₃₀ | 179 |
| Figure 5.13 – Failure pattern and moment-deflection response of partially-CFFT beams OR4 ₃₀ -IS4 ₃₀ | 180 |
| Figure 5.14 – Failure pattern and moment-deflection response of partially-CFFT beams OR4 ₃₀ -IS4 ₆₅ | 181 |
| Figure 5.15 – Failure pattern and moment-deflection response of partially-CFFT beams OR8 ₃₀ -IS4 ₃₀ | 182 |
| Figure 5.16 – Moment-deflection response of partially-CFFT beams with circular voids | 183 |
| Figure 5.17 – Correlations between M_{cr} , M_y , and M_u of partially-CFFT beams with circular voids | 184 |
| Figure 5.18 – Effect of the inner tube thickness in partially-CFFT beams | 185 |
| Figure 5.19 – Typical neutral axis location in partially-CFFT beams | 186 |
| Figure 5.20 – Effect of the inner tube laminates in partially-CFFT beams | 186 |
| Figure 5.21 – Effect of the inner tube shape in partially-CFFT beams | 187 |
| Figure 5.22 – Partially-CFFT beams with circular voids versus fully-CFFT beams | 188 |
| Figure 5.23 – Partially-CFFT beams with square voids versus fully-CFFT beams | 189 |
| Figure 5.24 – Strains in the FRP tube of OR2 ₃₀ | 190 |
| Figure 5.25 – Strains in the FRP tubes of OR2 ₃₀ -IC4 ₃₀ | 190 |
| Figure 5.26 – Strains in the FRP tube of OR4 ₃₀ | 191 |

| | |
|--|-----|
| Figure 5.27 – Strains in the FRP tubes of OR4 ₃₀ -IC2 ₃₀ | 191 |
| Figure 5.28 – Strains in the FRP tubes of OR4 ₃₀ -IC4 ₃₀ | 192 |
| Figure 5.29 – Strains in the FRP tubes of OR4 ₃₀ -IS2 ₃₀ | 193 |
| Figure 5.30 – Strains in the FRP tubes of OR4 ₃₀ -IS4 ₃₀ | 194 |
| Figure 5.31 – Strains in the FRP tubes of OR4 ₃₀ -IS4 ₆₅ | 195 |
| Figure 5.32 – Strains in the FRP tube of OR8 ₃₀ | 196 |
| Figure 5.33 – Strains in the FRP tubes of OR8 ₃₀ -IC4 ₃₀ | 196 |
| Figure 5.34 – Strains in the FRP tubes of OR8 ₃₀ -IS4 ₃₀ | 197 |
| Figure 5.35 – Flexural strength-to-weight ratios of RC beams, fully-CFFT beams, and partially-CFFT beams with circular voids..... | 198 |
| Figure 5.36 – Flexural strength-to-weight ratios of RC beams, fully-CFFT beams, and partially-CFFT beams with square voids..... | 199 |
| | |
| Figure 6.1 – Variation of the effective moment of inertia in fully-CFFT beams..... | 213 |
| Figure 6.2 – Variation of the effective moment of inertia in partially-CFFT beams..... | 213 |
| Figure 6.3 – Variation of the effective moment of inertia due to different steel reinforcement ratios in fully-CFFT beams (from parametric study)..... | 214 |
| Figure 6.4 – Correlations between m and $\rho_f n_f + \rho_s \rho_s$ | 215 |
| Figure 6.5 – Correlations between $\frac{I_e}{I_g}$ and $\frac{M_a}{M_{cr}}$ in the RC beams..... | 215 |
| Figure 6.6 – Correlations between $\frac{I_e}{I_g}$ and $\frac{M_a}{M_{cr}}$ in the fully-CFFT beams OR2 ₃₀ | 216 |
| Figure 6.7 – Correlations between $\frac{I_e}{I_g}$ and $\frac{M_a}{M_{cr}}$ in the fully-CFFT beams OR4 ₃₀ | 216 |
| Figure 6.8 – Correlations between $\frac{I_e}{I_g}$ and $\frac{M_a}{M_{cr}}$ in the fully-CFFT beams OR8 ₃₀ | 217 |
| Figure 6.9 – Correlations between $\frac{I_e}{I_g}$ and $\frac{M_a}{M_{cr}}$ in the fully-CFFT beams OR12 ₃₀ | 217 |
| Figure 6.10 – Correlations between $\frac{I_e}{I_g}$ and $\frac{M_a}{M_{cr}}$ in the fully-CFFT beams OR16 ₄₅ | 218 |

| | |
|--|-----|
| Figure 6.11 – Correlations between $\frac{I_e}{I_g}$ and $\frac{M_a}{M_{cr}}$ in the partially-CFFT beam OR2 ₃₀ -IC4 ₃₀ | 218 |
| Figure 6.12 – Correlations between $\frac{I_e}{I_g}$ and $\frac{M_a}{M_{cr}}$ in the partially-CFFT beam OR4 ₃₀ -IC4 ₃₀ | 219 |
| Figure 6.13 – Correlations between $\frac{I_e}{I_g}$ and $\frac{M_a}{M_{cr}}$ in the partially-CFFT beams OR8 ₃₀ -IC4 ₃₀ | 219 |
| Figure 6.14 – Correlations between $\frac{I_e}{I_g}$ and $\frac{M_a}{M_{cr}}$ in the partially-CFFT beams OR4 ₃₀ -IS4 ₃₀ | 220 |
| Figure 6.15 – Correlations between $\frac{I_e}{I_g}$ and $\frac{M_a}{M_{cr}}$ in the partially-CFFT beams OR8 ₃₀ -IS4 ₃₀ | 220 |
| Figure A.1 – Coupons tests results of OR2 ₃₀ | 245 |
| Figure A.2 – Coupons tests results of OR4 ₃₀ | 245 |
| Figure A.3 – Coupons tests results of OR8 ₃₀ | 246 |
| Figure A.4 – Coupons tests results of OR12 ₃₀ | 246 |
| Figure A.5 – Coupons tests results of OR16 ₄₅ | 247 |
| Figure A.6 – Coupons tests results of IC2 ₃₀ | 247 |
| Figure A.7 – Coupons tests results of IC4 ₃₀ | 248 |
| Figure A.8 – Coupons tests results of IS2 ₃₀ | 248 |
| Figure A.9 – Coupons tests results of IS4 ₃₀ | 249 |
| Figure A.10 – Coupons tests results of IS4 ₆₅ | 249 |
| Figure B.1 – A spreadsheet for analytical study | 250 |

CHAPTER 1

INTRODUCTION

1.1 GENERAL

Engineers and scientists are searching for innovative solutions that provide longer life and require less maintenance than conventional materials and systems. One of such innovations is concrete-filled fiber-reinforced polymer (FRP) tubes (CFFTs). The CFFTs are becoming an attractive and alternative system for many special types of structural applications especially those attacked by corrosive environments such as piles, bridge piers, bridge girders, monopoles, and overhead sign structures. The outer FRP tubes provide corrosion resistant elements, lateral and longitudinal reinforcement, lightweight permanent formworks, in addition to confining the inner concrete core. On the other side, the concrete core supports the tube against local buckling in addition to its role in resisting compressive loads.

Extensive research was developed on CFFTs as columns [Mirmiran et al. 1998, 2001; Fam and Rizkalla 2001; Lam and Teng 2003, 2004; Hong and Kim 2004; Zhu et al. 2006; Teng et al. 2007; Ozbakkaloglu and Oehlers 2008a, 2008b; Mohamed and Masmoudi 2008a, 2008b, 2010a; Mohamed et al. 2010; Park et al. 2011; Abouzied et al. 2012b; Abouzied and Masmoudi 2012, 2013; Ozbakkaloglu 2013a, 2013b; Vincent and Ozbakkaloglu 2013; Idris and Ozbakkaloglu 2013; and others], but comparatively limited research was carried out on CFFTs as beams [Mirmiran et al. 2000; Doval et al. 2001; Fam and Rizkalla 2002; Cole and Fam 2006; Fam et al. 2005; Yu et al. 2006; Mohamed and Masmoudi 2010b, Zakaib and Fam 2012; Belzer et al. 2013] and most of them concentrated on the circular section more than the rectangular section. However, the rectangular section has higher moment of inertia than the circular section in beams. Hence, it has higher flexural stiffness to resist the applied loads and deformations. Moreover, the construction and architectural requirements prefer the rectangular section of beams, rather than the circular beams, due to its stability during

installation and its workability during connecting to other structural members like slabs and columns. To date, only two studies on the flexural behaviour of rectangular CFFT beams have been reported, Fam et al. 2005 and Belzer et al. 2013, and their tested specimens number are relatively low (three beams for Fam et al. 2015 and four beams for Belzer et al. 2013) and none of them reinforced the rectangular CFFTs with steel rebar. These dissertation studies a large number of CFFT rectangular beams with steel rebar (twenty-two CFFT beams). Therefore, this research extends the literature of rectangular CFFTs and represents another step toward the CFFT technique to be fully implemented in the field of civil engineering structures and to introduce simple design inspired by the North American design codes provisions.

Unlike steel or FRP-RC beams, the steel-reinforced CFFT beams can exhibit superior additional flexural capacities in the post-yielding stage. This is attributed to the confining action of the FRP tube on the concrete core to withstand high strains, the FRP tube reinforcement contribution in the axial direction, and the reinforcement action of the steel bars in their strain hardening status. In most tested circular CFFT beams that failed in compression, the compression failure was predominantly governed by the compression failure of the tube flange under longitudinal compressive stresses where the tensile hoop strains (i.e., confinement effect) was insignificant [AASHTO 2012]. Note that, these observations are based on flexural tests of circular CFFTs without steel reinforcement and more investigations are required to verify that observations on rectangular CFFTs with steel rebar.

Analytical models have been developed to predict the flexural capacity and load-deflection response for the circular CFFTs [Cole and Fam 2006; Fam and Son 2008; Mohamed and Masmoudi 2010b]. These models are based on strain compatibility, internal forces equilibrium, and material constitutive relationships. The forces within the CFFT cross section were calculated by integrating the stress over the area of each individual material. Despite the limited number of tested specimens, these models predict well the flexural behaviour of their circular CFFT beams. Their theoretical analysis depends mainly on a computer-based analysis and requires some sophisticated calculation procedures. These proposed models

require also verification and adjustment to be valid for the rectangular CFFT beams, and need to be simplified to be applicable for engineers.

The CFFTs that are completely filled with concrete are not optimal for applications governed by pure bending, because the concrete below the neutral axis is cracked and it contributes slightly to bending resistance and mainly prevents the tube from buckling. As such, the excess weight of the cracked concrete may increase the transportation and installation cost. A number of FRP-concrete hybrid systems have been developed over the years, including both open and closed FRP forms, to reduce the excess weight of the cracked concrete below the neutral axis [Deskovic and Triantafillou 1995; Canning et al.1999; Fam and Rizkalla 2002; Chakrapan 2005; Khennane 2010; Idris and Ozbakkaloglu 2014]. While, limited trials were carried out on filament-wound FRP tubes especially those with rectangular section [Fam et al. 2005].

Fam and Rizkalla (2002) investigated the effect of inner holes by testing circular CFFT beams with outer identical GFRP tubes 168 mm diameter. One beam was totally filled with concrete, one beam had a central hole, and another two beams had similar holes, but they are maintained by concentric and eccentric inner GFRP hollow tubes 89 mm diameter. The results indicated that the strength of the CFFT beam with a central hole was 9% less than that of the fully-CFFT beam. Moreover, providing an inner concentric GFRP hollow tube improved the strength by 7% more than that of the fully beam due to the additional reinforcement. Also, shifting the inner GFRP hollow tube toward the tension side was more effective, where the strength increased by 39% higher than the fully-CFFT beam. Fam et al. (2005) designed a rectangular section, $266 \times 374 \text{ mm}^2$, of filament-wound GFRP tube with an inner rectangular air void. The strength of the voided section reached 78% of that completely filled with concrete. The hollow beam did not reach the target strength, because it failed by inward buckling and fracture of the unsupported concrete flange at the compression side. Idris and Ozbakkaloglu (2014) investigated the flexural behaviour of FRP-high strength concrete (HSC)-steel composite beams by testing double-skin tubular beams (DSTBs) with outer GFRP tubes and a central inner hollow steel section (HSS). The main parameters of the study included the cross-sectional shapes of the inner HSS and the external GFRP tube, concrete strength, presence or absence of concrete filling inside the steel tube, and effects of

using mechanical connectors to enhance the bond between the steel tube and surrounding concrete. The results indicated that DSTBs exhibit excellent load-deflection behaviour with high inelastic deformations and minimal strength degradations (minor increase of flexural strength after yielding). However, relatively large slippage can occur at the concrete-steel tube interface unless the bond is enhanced by mechanical connectors. Regardless the high flexural strength and stiffness of the DSTBs based on the inner steel tube, the weight and the bond remain critical issues in this design and need further investigations.

In this dissertation, the author tries to get benefit of each advantage of each design in the literature and to merge them together to develop a new design of lightweight partially-CFFT beams. This design contains: (1) Outer rectangular GFRP tubes to increase the sectional moment of inertia, to provide flexural and shear reinforcement, and to protect the inner structural elements (concrete and steel) against corrosion, (2) Inner holes shifted toward the tension zone to increase the compression zone area, (3) The holes were provided by inner hollow GFRP tubes to support and confine the concrete at the compression side and to act as reinforcement, (4) Steel rebar is provided at the tension side to increase the stiffness of the section, and (5) The surfaces of tubes adjacent to the concrete were roughened by sand coating to achieve a full composite action.

1.2 RESEARCH OBJECTIVES

The study aims to generate much needed data and to fill research gaps of the rectangular CFFT beams and to represent another step toward the CFFT technique to be fully implemented in the field of civil engineering structures and to introduce simple design inspired by the North American design codes. The study investigates the flexural capacities of rectangular steel-reinforced CFFT beams fully and partially filled with concrete and their corresponding service deflection through testing wide range of GFRP tubes with different thicknesses and configurations. In addition, this study introduces a new design of lightweight partially-CFFT beams. This design contains an outer rectangular filament-wound GFRP tube with an inner hole provided by inner hollow circular or square filament-wound GFRP tubes shifted toward the tension zone of the cross section. The outer GFRP tube itself provides a stay-in-place form, shear and flexural reinforcement, and protects the embedded concrete and

steel reinforcement. The inner tubes were designed to act as flexural reinforcement, to support the concrete core at the compression zone, in addition to reduce the weight of the beam. The space between the tubes is filled with concrete that acts as a compression member and eliminates the buckling of the tubes walls. The CFFT beams are reinforced by longitudinal steel bars at the tension side only to enhance their serviceability by increasing their flexural stiffness. The study is seeking also for that using outer and inner GFRP tubes in addition to steel rebar would make the FRP-concrete-steel composite beam fails gradually with enough warning signs. The combination of FRP and conventional structural materials, steel and concrete, aims to optimize the structural section performance based on their individual distinctive properties.

The objectives of this study have been summarized as follow:

- 1) Experimentally investigate the effect of fiber laminate structure, thickness, and configuration of the outer and inner filament-wound GFRP tubes on the flexural performance of fully and partially-CFFT beams.
- 2) Compare the rectangular CFFT beams with conventional RC beams in terms of strength to weight ratio and ductility.
- 3) Analytically design the reinforced CFFT rectangular beams to predict their flexural capacities (crack, yield, and ultimate moments).
- 4) Examine the North American codes provisions to evaluate the effective moment of inertia required to calculate the deflection and to propose necessary modifications and assumptions.

1.3 METHODOLOGY

This study relies on a comprehensive experimental program involving twenty-four full-scale beam specimens, 3200 mm long and $305 \times 406 \text{ mm}^2$ cross section, which have been tested under a four-point bending setup. These specimens include eight fully-CFFT beams with wide range of tube thickness of 3.4 mm to 14.2 mm, fourteen partially-CFFT beams with different outer and inner GFRP tubes configurations, and two conventional steel-reinforced concrete (RC) beams as control specimens.

The research program was conducted in a combined experimental and analytical study to achieve the research objectives through the following aspects:

- 1) Fabrication of the GFRP tubes by filament-winding process in the Civil Engineering Department at the University of Sherbrooke and carrying out all necessary tests to evaluate the physical and mechanical properties of the fabricated filament-wound GFRP tubes.
- 2) Fabrication of twenty-four full-scale beam specimens and testing them over a simply supported span under a four-point bending setup.
- 3) Experimental study was conducted to investigate the flexural performance of the fully and partially-CFFT beams according to the test variables.
- 4) Analytical study was conducted to predict the flexural capacities and behaviour based on linear strain compatibility and failure patterns.
- 5) Analytical study was conducted to examine and modify Branson's equation to predict well the effective moment of inertia and deflection of the reinforced CFFT beams at the pre-yielding stage and the post-yielding stage.

1.4 THESIS OUTLINES

Chapter 1 defines the problem and presents the research significance, objectives of the research project, and the methodology that was adopted.

Chapter 2 provides a literature review concerning the previous work on the flexural behaviour of CFFT beams reporting the main factors influencing the flexural performance, and the available models for lightweight beams. It reports also a background of different techniques to manufacture FRP composite tubes.

Chapter 3 describes the experimental work program in details. It presents the test matrix, used material, fabrication of the GFRP tubes, casting process, test procedure, test setup, and measuring devices.

Chapter 4 presents the experimental results of eight fully-CFFT beams with wide range of tube thickness, and two controls RC beams. The results indicate outstanding performance of

the fully-CFFT beams in terms of strength and ductility. The fully-CFFT beams attain flexural strength and ductility 444% and 1432% higher than that of the RC beams, respectively. The results indicate that increasing the tube thickness changes the pattern of failure from tension to compression. Moreover, a strain compatibility/equilibrium model was developed to predict the moment-curvature response of the section. The model addresses the issues of confinement and tension stiffening of concrete. The curvature along the span of the flexural member was integrated to predict the deflection. The analytical results match well the experimental results in terms of moment, deflection, strains, and neutral axis responses. Then, a parametric study was carried out to enrich the experimental data. The contents of this chapter have been submitted to the Journal of Engineering Structures. The paper is titled “Flexural behaviour of rectangular FRP-tubes filled with reinforced concrete: experimental and theoretical studies”.

Chapter 5 presents experimental investigations on the proposed new design of lightweight partially-CFFT beams addressing the effect of the inner tube thickness, laminates and shape on the flexural performance of partially-CFFT beams. The results indicate superior performance of the proposed design compared to the RC beams. The strength-to-weight ratio of the partially-CFFT beams attained higher values than that of the corresponding fully-CFFT beams. Moreover, the general failure pattern of the partially-CFFT beams was gradual in compression unlike the sudden tension failure of the fully-CFFT beams. The contents of this chapter have been published in two journals. First, a paper titled “Structural Performance of New Fully and Partially Concrete-Filled Rectangular FRP-Tube Beams” has been published in Elsevier Construction and Building Materials Journal. Second, a paper titled “New High-Performance Rectangular FRP-Tube Beams Partially Filled with Concrete” has been accepted in ACI–special publication.

Chapter 6 predicts the deflection of such new design of rectangular CFFT hybrid beams inspired with Branson’s equation. A new power and assumptions were developed into Branson’s equation to predict well the effective moment of inertia of the section. These assumptions consider the effect of the GFRP tube strength, thickness, configuration, and steel reinforcement. In addition, they predict well the deflection in the pre-yielding and post-yielding stages of the hybrid FRP-concrete-steel CFFT rectangular beams. The contents of

this chapter have been submitted to the Journal of Structural Engineering ASCE. The paper title is “Effective moment of inertia of rectangular FRP-tube beams fully or partially filled with reinforced concrete”.

The last Chapter of the thesis is **Chapter 7**, which presents general conclusions obtained from the experimental and theoretical results throughout the thesis. In addition, this chapter suggests recommendations for future work.

CHAPTER 2

LITERATURE REVIEW

2.1 INTRODUCTION

In recent years, the application of concrete-filled fiber-reinforced polymer (FRP) tubes (CFFTs) has been used for different structural applications. The most highly developed application to date is the use of CFFTs as pier column and as fender piles in marine structures. The FRP tube provides lightweight structural component, permanent formwork, non-corrosive characteristics, and saving of construction time and effort. Moreover, it provides axial and lateral reinforcement and confinement for the concrete core. On the other side, the concrete core provides support for the tube against buckling in addition to its role to resist the compressive loads. Extensive research was carried out on CFFTs as columns [Mirmiran et al. 1998, 2001; Fam and Rizkalla 2001; Lam and Teng 2003, 2004; Hong and Kim 2004; Zhu et al. 2006; Teng et al. 2007; Ozbakkaloglu and Oehlers 2008a, 2008b; Mohamed and Masmoudi 2008a, 2008b, 2010a; Mohamed et al. 2010; Park et al. 2011; Abouzied et al. 2012b; Abouzied and Masmoudi 2012, 2013; Ozbakkaloglu 2013a, 2013b; Vincent and Ozbakkaloglu 2013; Idris and Ozbakkaloglu 2013; and others], but comparatively limited research was carried out on CFFTs as beams [Mirmiran et al. 2000; Doval et al. 2001; Fam and Rizkalla 2002; Cole and Fam 2006; Mohamed and Masmoudi 2010b, Fam et al. 2005; Yu et al. 2006; Zakaib and Fam 2012; Belzer et al. 2013]. These studies concentrated extensively on the circular section more than the rectangular ones. However, the rectangular section should behave more effective than the circular one in bending. Since concrete has low tensile strength compared to its high compressive strength, it is completely cracked below the neutral axis in the section under flexure. Then, the role of cracked part is limited to support the tube walls against buckling. Since this heavy weight increases the cost of building construction and transportation, many researchers tried to design beam sections with inner voids to reduce the undesired excessive weight of the beams.

The high performance of FRP composites especially the filament-wound tubes encourages researchers to use them with conventional materials like steel and concrete to produce lightweight composite sections for beams. This chapter introduces description of the FRP composites materials and manufacturing processes, and a literature review of previous work on CFFTs as beams. Finally, it presents previous trials to make lightweight beams using the FRP composites.

2.2 FRP COMPOSITE MATERIALS

Fiber-reinforced polymer (FRP) composites consist mainly of fibers and resin matrix. Fibers, which are the main load-carrying component, are bonded together with a resin matrix. The matrix not only coats the fibers and protects them from mechanical abrasion, but also transfers stresses between the fibers. Moreover, it transfers inter-laminar and in-plane shear in the composite, and provides lateral support to fibers against buckling when subjected to compressive loads. Additives and fillers may be added for curing or enhancing mechanical and/or physical properties. The use of FRP composite material was pioneered by the aerospace industry in the 1940s, primarily because of its many desirable properties, such as high performance, high strength-to-weight and high stiffness-to-weight ratios, high-energy absorption, and outstanding corrosion and fatigue damage resistance. Now, its use is increasing for civil engineering infrastructure such as buildings and bridges. Table 2.1 indicates the physical and mechanical properties of the most used fibers and resins compared to conventional steel and concrete materials.

2.2.1 Fibers

There are three important categories of fibers: glass, carbon and aramid fibers. Presently, glass fibers are used widely across all industries, although carbon fiber and aramid fiber composites are mostly found in aerospace, automotive and sporting goods equipments [Chakrapan 2005].

2.2.1.1 Glass Fibers

Glass fiber or fiberglass is a material made from extremely fine fibers of glass, and it is the largest reinforcement measured in sales. Glass fiber was invented in 1938 by Russell Games Slayter of Owens-Corning as a material to be used as insulation. Ever since then, glass fiber has become widely used as insulation and composite reinforcement material. Based on the composition and the application, glass fibers can be classified in several types. The most commonly used glass fiber type for composite applications is E-glass (electrical glass) and S-glass (structural or high-strength glass). E-glass has good mechanical properties and high electrical insulation. S-glass is also used in composite materials where high tensile strength is desired, however, this material comes at a much higher cost. Glass fibers are excellent thermal and electrical insulators and are the most inexpensive of the high-performance fibers. Hence, their extensive use is in buildings and the electric power industry as insulation materials.

2.2.1.2 Carbon Fibers

Carbon fibers are used in structural engineering applications today in FRP strengthening sheets, strips, and fabrics, and in FRP pre-stressing tendons. Carbon fiber is a solid semi crystalline organic material consisting of atomic level of planar two-dimensional arrays of carbon atoms. Due to their two dimensional atomic structure, carbon fibers are considered to be orthotropic, having different properties in the longitudinal direction of the atomic array than in the transverse direction. The longitudinal axis of the fiber is parallel to the graphitic planes and gives the fiber its high longitudinal modulus and strength. Carbon fibers are very durable and perform very well in hot and moist environments and when subjected to fatigue loads. They do not absorb moisture. They have a negative or very low coefficient of thermal expansion in their longitudinal direction, giving them excellent dimensional stability. They are, however, thermally and electrically conductive. Compared with glass fibers, carbon fibers have lower density but higher tensile strength and elastic modulus. These properties make carbon fiber an ideal reinforcement for composite materials used in aircraft components, high-performance vehicles, sporting equipment, wind generator blades, and other high performance applications.

2.2.1.3 Aramid Fibers

Aramid fibers were used to produce the first generation of FRP pre-stressing tendons in the 1980s in Europe and Japan. However, few manufacturers still produce aramid FRP reinforcing bars or tendons. Aramid fibers consist of aromatic polyamide molecular chains. They were first developed, and patented, by DuPont in 1965 under the trade name Kevlar. A combination of their relatively high price, difficulty in processing, high moisture absorption, low melting temperatures, and relatively poor compressive properties have made them less attractive for FRP parts for structural engineering applications. Their advantages include extremely high tenacity and toughness, and consequently they are used in many industrial products either in bare fabric form or as reinforcements for FRP composites where energy absorption is required. Moreover, they are the lightest of the high performance fibers.

2.2.2 Polymer Resins

There are two types of polymeric matrices widely used for FRP composites; namely, thermoplastic and thermosetting. Thermoplastic polymers are made from molecules in a linear structural form. These are held in place by weak secondary bonds, which can be destroyed by heat or pressure. After cooling, these matrices gain a solid shape. Although it can degrade their mechanical properties, thermoplastic polymers can be reshaped by heating as many times as necessary. Thermosetting polymers are used more often than thermoplastic. They are low molecular-weight liquids with very low viscosity, and their molecules are joined together by chemical cross-links. Hence, they form a rigid three-dimensional structure that once set, cannot be reshaped by applying heat or pressure. Thermosetting polymers are processed in a liquid state to obtain good wet-out of fibers. These materials have good thermal stability, chemical resistance, and undergo low creep and stress relaxation. However, these polymers have relatively low strain to failure, resulting in low impact strength. Two major disadvantages are their short shelf life and long manufacturing time. Some commonly used thermosetting polymers are polyesters, vinyl esters and epoxies [Chakrapan 2005].

2.2.2.1 Polyester Resin

Polyester resin is widely used to make pultruded FRP profiles for use in structural engineering. It is also used to make some FRP rebar. When greater corrosion resistance is desired in FRP parts, higher-priced vinyl ester resins are generally recommended, although the corrosion resistance of some polyester resins may be as good as that of vinyl ester resins. Polyester resins can also be used for FRP strengthening for structures. However, epoxy resins are preferred at this time for FRP strengthening applications because of their adhesive properties, low shrinkage, and environmental durability.

2.2.2.2 Epoxy Resin

Epoxy resins are used in many FRP products for structural engineering applications. Most carbon fiber-reinforced pre-cured FRP strips for structural strengthening are made with epoxy resins. In addition, epoxy resin adhesives are used to bond pre-cured FRP strips to concrete (and other materials) in the FRP strengthening process. Epoxy resins are also used extensively in FRP strengthening applications, because, the epoxy resin is applied to dry fiber sheets or fabrics in the field, and then it is cured in situ acting as both the matrix for the FRP composite and as the adhesive to attach the FRP composite to the substrate. Epoxy resins have also been used to manufacture FRP tendons for pre-stressing concrete and FRP stay cables for bridges. They are not used extensively to produce larger FRP profiles, due to their higher costs and the difficulty entailed in processing large pultruded FRP parts.

2.2.2.3 Vinyl Ester Resin

In the last twenty years, vinyl ester resins have become attractive polymer resins for FRP products for structural engineering due to their good properties especially their corrosion resistance and their ease of processing. Today, vinyl ester resins are used widely to make the majority of FRP rebar sold in the world and FRP pultruded profiles. Most manufacturers of pultruded profiles make profiles of identical shape in both polyester and vinyl ester resin series. Vinyl ester resins have also been used to make FRP strengthening strips and FRP rods for near-surface-mounting applications. They are generally replacing polyester resins in FRP

products in structural engineering due to their superior environmental durability in alkaline environments.

2.2.3 Fillers

Fillers are used in polymers for a variety of reasons, namely to reduce cost, improve processing, control density, thermal conductivity, thermal expansion, electrical properties, magnetic properties, flame retard, and to improve mechanical properties. Each filler type has different properties depending on its particle size, shape and surface chemistry. In general, the fillers can change the performance of polymer composites by changing the color, viscosity, barrier properties, curing rate, electrical and thermal properties, surface finish, shrinkage, etc.

2.3 FRP COMPOSITE MANUFACTURING PROCESSES

The earliest method of making composites was by manual layup, where each layer of the composites is put manually one above the other to produce the final layout. This consumes much time and needs a lot of skilled labor. This method was made easier using prepregs, which are fibers pre-impregnated with resin. Major advantages of the manual set up are that it has high versatility, but the accuracy is dependent on the skill of the worker and can yield goods with high volume fractions. Its major disadvantages are that it is slow, yields low production rates and there are health and safety issues, such as physical contact with the resin and its fumes [Taheri 1996]. Due to the development in manufacturing technology, there are many ways of making composites. Even though each technique is different, but they all have the following goals [<http://mdacomposites.org>]:

- 1) Arrange fibers in the desired orientation and stacking sequence. This ensures the appropriate fiber orientation, and specifies the amount of fiber in each layer of the composite, so it governs the strength and stiffness of the composite.
- 2) Ensure adequate wetting of fibers. Adequate wetting of the fibers is important to allow the right amount of resin in between the fibers to have an appropriate fiber-resin ratio. This is also crucial to the strength and stiffness of the composite.

- 3) Curing of resin. Curing enables the bonding of each layer of the composite to each other, thus unifying the product.
- 4) Minimization of the amount of voids. One of the most important factors in composite manufacturing is the removal of voids or air gaps between two successive layers of fibers. The voids reduce the stress bearing capacity of the fibers.

2.3.1 Pultrusion Process

Pultrusion is an automated continuous composite manufacturing process. The major application of the pultrusion process is in the fabrication of composite parts that have a prismatic cross section profile. Pultrusion process is suited ideally for mass scale production. In this process, fibers are pulled through a resin bath to coat the reinforcement with the resin. Then excess resin is removed, as fibers are passed through heated die. Die completes the curing of the resin and controls the shape of the section. The major advantages of the pultrusion process are its capability to produce in high volume and being a very highly automated process. Its major disadvantages are the expensive die costs and its inability to produce products non-prismatic geometries [Hazra 2011]. Figure 2.1 shows a schematic of pultrusion process.

2.3.2 Resin Transfer Molding (RTM) Process

In this process, layers of fibers or prepregs are placed between male and female molds, and then they are pressurized and injected with resin. The resin is injected to fill all voids within the mold and thus penetrates and wets all surfaces of the reinforcing materials. A wide variety of reinforcement materials can be used. This process offers low waste and reduces machining cost of the finished product. The process can be automated. The major limitations of this process are manufacturing of complex shapes requires many trials, errors to ensure proper wetting, and the mold designing is complex [Hazra 2011]. Figure 2.2 shows the schematic of RTM process.

2.3.3 Vacuum Assisted Resin Transfer Molding (VARTM) Process

Conceptually, this process is similar to RTM, but it is different on many accounts. First, VARTM is a single side process under a sealed enclosure and instead of the positive pressure used in RTM, vacuum is applied to the mold and sucked into the fabric-fiber. In this process, wetting of the fiber is dependent on the permeability of the preformed laminate and architecture of the fiber. Viscosity of the resin has to be low. This process is very safe from health hazard point of view as the entire system is under vacuum and can yield very high quality products. Typical applications of VARTM include production of train seats, marine, complex aircraft and automotive parts [Hazra 2011]. Figure 2.3 shows a schematic of VARTM process.

2.3.4 Compression Molding Process

Compression molding process, as shown in Figure 2.4, is used in manufacturing sheet molding compound composites and bulk molding compound. This process consists of three stages, namely charging, compressing and ejecting. The material to be molded is preheated and placed in a mold in the charging stage. Then pressure and additional heat is applied in the compression stage. Finally, the finished product is removed from the mold after sufficient curing time. Major applications of the compression moldings are automotive components such as fenders, bumpers, and leaf springs. The major disadvantages of this process are that it cannot produce long fiber composite parts and mold costs cannot be justified for low production volumes. Also, resins with high shrinkage rates can cause waviness, ripples, sink marks and rough surfaces on the product [Hazra 2011].

2.3.5 Filament Winding Process

Filament winding is a type of composite manufacturing process, where controlled amount of resin and oriented fibers are wound around a rotating mandrel and cured to produce the required composite part. It was initially used to produce pressure vessels, water and chemical tanks. The development stage of filament winding goes back to dry wire winding of rocket motor cases, which requires reinforcement. Today, the applications include aircraft fuselages,

wing sections, helicopter rotor shafts, high-pressure pipelines, sports goods and structural applications of all types [Balya 2004]. The major advantages of the winding process are that filament winding machines are computer numerically controlled machines, highly automated and may be setup and operated in a matter of minutes, and capable of producing accurate repetitive fiber orientation. Moreover, it uses continuous lengths of fibers. Hence, sections with very high strength-to-weight and stiffness-to-weight ratios can be manufactured [Mallick 2007]. However, the process has some limitations such as difficulty in placing fibers parallel to the axis of the mandrel, high mandrel cost, and special treatment on the external mandrel surface needed to ensure evenness. One primary tool used in the filament winding process is a precision ground mandrel that the fiber and resin are wound upon it. The mandrel is supported horizontally between a head and tail stoke. The tail stoke is free, but head stoke is driven by required angle and speed, using a computer program. As the mandrel rotates, a carriage travels along the mandrel and delivers fiber with a given position and tension. Carriage motion is also controlled by the computer in connection with head stoke rotation.

Fibers pass through a resin bath after tensioning system and gets wet before winding operation. When a pre-impregnated fiber or prepreg is used, wetting is not performed. Tensioning system is an important part of filament winding. This importance gets critical when winding at high angles. Since tension changes the friction force between fiber and the mandrel, it should be kept at a certain value during winding operation. Fiber tension also affects the volumetric ratio of composite at a given point. Excessive resin, due to a low tension, can result in decreased mechanical properties. Therefore, tensioning systems should be capable of rewinding a certain value of fiber. This condition occurs when fiber band reverses at the end of tube, while winding at low angles. Wetting can be done by two commonly used bathing type; drum bath and dip bath. Drum bath provide less fiber damage than dip bath. This is especially important when using carbon fibers. On the other hand, dip bath provides a better wetting action and mainly used with aramid or glass fibers. If fibers are not wetted in a desired way, air bubbles can be trapped between them and can cause voids in the composite part. Therefore, drum baths can be heated for a better wetting action. Lowering resin viscosity, reducing fiber speed, and increasing fiber path on the drum are other methods

used for better wetting action. If heated resin is to be used, dip baths are preferred since drum surface cools as it leaves the resin bath.

The rotating mandrel can be a part of the produced composite part (a pressure vessel) or can be removed from the composite part. If it will be removed, a press should be used for removing. All mandrels, which will be removed, should have low thermal expansions in order to reduce residual stresses after curing action. In addition, surface finish is an important point, since an interface between the composite part and the mandrel is generally not permitted. If a concave part is needed on the filament-wound part, a female mold can be used. In addition, excessive wet fiber can be used in order to fill the concave parts. Metal or composite parts can be mounted on mandrel in order to guide winding action such as pin-rings or end-domes, which must be removable or collapsible. Sharp edges should be avoided in order not to cut fibers. Winding angle is the angle between the fibers and a line on the mandrel surface, which is parallel to mandrel axis. A maximum value, which is close to 90° , can be approximated. Very low winding angle values need some arrangements at the ends of the mandrel, such as pin-rings [Balya 2004].

Filament winding process is considered the second largest process for manufacturing composites as illustrated by the statistics in Figure 2.7. In addition, the process has acceptable moderate cost for composite manufacturing, especially FRP tubes, comparing with other methods as shown in Figure 2.8.

2.4 CONCRETE-FILLED FRP TUBES UNDER FLEXURE

2.4.1 General Review

Concrete-filled FRP tubes (CFFTs) have been used in the field as bridge piers, marine piles, and girders as shown in Figure 2.9. They also have a great potential in other applications such as poles, and overhead highway signs. CFFTs demonstrate excellent durability in corrosive environments such as the tidal zones of marine piles. The CFFT system combines hollow FRP tubes and concrete in a very effective way such that both materials are effectively utilized. The FRP tube acts as a permanent formwork for concrete, a barrier against corrosive environments, and as hoop and axial reinforcement. On other hand, the

concrete core provides support for the tube, preventing it from buckling locally, and contributes to the internal compressive resistance force [Qasrawi 2007]. While circular CFFTs have been extensively studied in bending and under axial loads, very limited studies have been conducted on rectangular, open or closed, FRP-concrete hybrid systems [Fam et al. 2005]. Generally, the circular CFFT beams experienced better performance than the conventional reinforced concrete (RC) beams in terms of flexural strength and ductility. Unlike steel or FRP-RC beams, the steel-reinforced CFFT beams can exhibit superior additional flexural capacities in the post-yielding stage. This was attributed mainly to the FRP tube contributed in the flexural reinforcement and it forced the concrete core to withstand higher strains. The next sections display the previous work on CFFTs under flexure with respect to some important parameters, which help the current research program, as the effect of concrete core, fiber laminate structure, FRP tube thickness, using reinforcement steel or FRP bars, and inner voids.

2.4.2 Effect of Inner Concrete Core

Fam and Rizkalla (2002) tested hollow circular GFRP tube of 100 mm diameter, B1, and compared it to another one that completely filled with concrete, B2, under flexure. Figure 2.10 shows the moment-curvature behaviour of the hollow and concrete-filled GFRP filament-wound tubes, B1 and B2, respectively. Figure 2.10 indicates that the strength and stiffness are significantly increased by filling the tube with concrete. The strength gain was 212%. The presence of concrete has contributed to the stiffness and moment resistance of the section in the compression zone of the beam. The concrete also provided internal support to the tube and prevented its local buckling at the compression side. Figure 2.10 also shows the failure mode of B1, which failed due to local buckling and crushing of the hollow tube, while B2 had flexural tension failure due to rupture of the fibers in the tension side.

2.4.3 Effect of Concrete Strength

Based on many research on CFFT columns, the ultimate strength of the confined concrete is mainly dependent on the stiffness of the GFRP tubes, and the confinement effectiveness is reduced as the concrete strength increases [Mandal et al. 2005], but this matter may be

different in case of CFFT beams and needs more investigations. Mohamed and Masmoudi (2010b) tested circular CFFTs under pure bending. Through many test variables, they tested six CFFT beams with two batches of concrete, 30 and 45 MPa, to study the effect of concrete strength on the flexural strength of CFFT beams. Figure 2.11(a, b) shows the load–deflection responses of six beams that contained identical internal reinforcement ratio of steel or FRP bars. The two figures indicated that the initial and post-cracking flexural stiffness of the three reinforced CFFT beams constructed from concrete of normal strength of 30 MPa, were similar to that of the three reinforced CFFT beams constructed from concrete of medium strength of 45 MPa. Figure 2.11(a) indicates that the beam reinforced with steel bars (A45S) does not have gain in the strength as compared with beam A30S. Also, Figure 2.11(b) indicates that the increase in the flexural strength for beams reinforced with GFRP bars is not significant with increasing the concrete strength from 30 MPa (A30G and B30G) to 45 MPa (A45G and B30G), Specimen A45G and B30G having only 4.8% and 14% higher strength than that of A30G and B30G, respectively. On the other hand, the increase in the energy absorption (area under load-deflection curve) is not significant as compared with the increase in the concrete compressive strength 50% (from 30 to 45 MPa) for the tested CFFT beams. The increase in the energy absorption is limited to 3%, for the beams reinforced with steel bars, with increasing the concrete compressive strength from 30 to 45 MPa. The corresponding value for the beams reinforced with FRP bars is 11%. It can be concluded that the flexural behaviour of the six reinforced CFFT beams tested in that study were not significantly affected with increasing the concrete compressive strength from 30 to 45 MPa. This is attributed to two factors: (1) the six CFFT beams failed in flexure due to the tensile rupture of the FRP tubes and FRP or steel bars at the tension side of the beams, (2) the FRP tubes confined the concrete core of the beams, as evident from the final failure mode, the concrete core inside the FRP tube at the compression side did not experience crushes or spalls as compared with failure mode of the spiral-steel beams.

2.4.4 Effect of Tube Thickness

Tests by Mirmiran et al. (2000) involved circular beams with shear span to depth (a/D_o) ratio of about 2, with two different reinforcement ratios (ρ), 7.2% and 43.2%, characterized as under and over reinforced beams, respectively. The under reinforced beams consisted of

symmetric $\pm 55^\circ$ glass fiber plies, while the over reinforced beams comprised of symmetric glass fiber plies with 0° and $\pm 45^\circ$ orientations, where all angles are measured with respect to the longitudinal axis of the tube. As expected, the over reinforced beams failed in compression, while the under reinforced beams failed by tensile rupture of the tube at tension side.

Fam and Rizkalla (2002) tested twenty circular CFFT beams with a/D_o ratios ranging between 2.67 to 7.4, reinforcement ratios from 3.8% to 12.3%, and a wide range of fibers stacking sequence. All tested beams failed in flexure, except one with 0° fibers failed by splitting due to horizontal shear. In addition, they found that the higher the thickness of the FRP tube, the lower the gain in flexural strength and stiffness resulting from the concrete fill. The load-deflection behaviour of CFFTs was almost linear, and the stiffness depended largely on the tube properties after cracking. It was also noted that CFFTs with thicker tubes or a higher percentage of fibers in the axial direction tended to fail in compression, and that the absence of fibers in the hoop direction could also lead to compression failure, because the hoop fibers tend to support the longitudinal fibers and prevent them from buckling at the micro scale, as indicated earlier.

Mohamed and Masmoudi (2010b) tested two circular CFFTs beams, with the same diameter of 213 mm and laminate structure of 90° and $\pm 60^\circ$, filled with the same batch of concrete with unconfined compressive strength of 45 MPa, but differ in the tube thickness. One GFRP tube of Type B had thickness of 6.40 mm, which is equal to 2.2 times the thickness of the other tube of Type A with thickness of 2.90 mm. The reinforcement ratio of the tube Type B is 120% more than that of Type A. Figure 2.12 presents the load-deflection curves showing the effect of the FRP tube thickness. Figure 2.12 indicates that the beam constructed from the tube Type B (B45G) experienced 33.3% higher strength than that of beam constructed from the tube Type A (A45G). At all load levels, the beam of tube Type B experienced lower deflection than that of the beam of tube Type A. Despite the increase in strength and stiffness due to increasing the thickness, the authors concluded that the increase in the flexural strength (20 to 30%) is not significant as compared to the increase in the FRP tube reinforcement ratio (120%). This is attributed to the fact that the increase in the flexural strength is mainly resulted from the contribution of the excess thickness of the FRP tubes in

the tension side only. This unexpected conclusion could be attributed to that their tubes laminate structure had high angles, 90° and $\pm 60^\circ$, which are not effective for flexural reinforcement which needs more fibers in the longitudinal direction than in hoop direction. While for axial loading the high angles is preferred for confinement process. Hence, the thickness of the tubes cannot increase the performance of the FRP tubes alone. There should be a relation between the thickness and laminate structure and type of loading (axial or bending).

2.4.5 Effect of Tube Laminate Structure (Fibers Orientation)

Winding angle is the angle between the fibers and the line on the mandrel surface, which is parallel to mandrel axis. This angle is controlled during fabrication of the FRP tubes in filament winding process. There are two common types of laminate orientation, circumferential and helical windings. Circumferential, or hoop, winding is a special form of helical winding and is used to deposit fibers close to 90° to the longitudinal axis and is generally applied to the cylindrical or straight portion of the mandrel and generate a single layer of fibers. Helical winding is used to lay the fibers at angles from 5° to 80° to the longitudinal axis. These fibers are wound on the mandrel surface in alternating positive and negative orientations and result in a double layer of wound material [Frank 1995]. Very low winding angles need some arrangements at the ends of the mandrel, such as pin-rings, to hold the fibers in their designed orientation and to prevent their sliding during fabrication. Generally, the fibers in the circumferential direction are utilized to provide confinement on the concrete, while the fibers in the axial direction provide flexural and axial strength and stiffness. The laminate structure of FRP tubes could be optimized by controlling the sequence of the hoop and helical winding and consequently the proportions of fibers contribution in the hoop and axial directions, respectively, to suit the application. For flexural members, larger stiffness would be required in the axial direction. While for axial members, larger stiffness is required in the hoop direction as well as a minimum Poisson's ratio in order to produce the maximum confinement of concrete [Fam and Rizkalla 2003]. Kaynak (2005) conducted a split-disk test for specimens produced with five different winding angle to investigate the processing parameters of continuous filament-wound GFRP tubes. The results indicated that both hoop tensile strength and hoop tensile modulus of elasticity depend strongly on the fiber

direction of specimens. Specimens having 90° and $\pm 65^\circ$ had much higher values compared to those having $\pm 45^\circ$, $\pm 25^\circ$ and 0° .

Fam and Rizkalla (2002) compared the load-deflection behaviour of two concrete-filled GFRP tubes beams which are similar in size and wall thickness, but different in laminate structure. Beam B3 had only one third of the fibers content wound at an angle of 15° with the longitudinal axis and the other two thirds are placed on the hoop direction at 82° . Beam B4 had all the fibers content wound at 30° with the longitudinal axis. The two different laminate structures resulted in an effective elastic modulus for beam B3 of about 80% of that of beam B4, as shown in Figure 2.13. The relative stiffness after cracking is almost proportional to the relative effective elastic modulus of the tubes in the axial direction. Although the two beams achieved similar flexural strength, the failure modes were quite different. B4 behaved in a nonlinear way and developed a gradual compression failure due to matrix cracking and fiber buckling in the compression zone. This is attributed to the absence of fibers in the hoop direction to confine the other layers. The beam B3 failed in tension and behave in semi linear way. It should be noted that B3 has only 33% of the fibers oriented in the axial direction, which is relatively low for flexural members and causes early axial cutting of fibers under flexure at the tension side.

2.4.6 Effect of Steel and FRP Rebar

Cole and Fam (2006) fabricated and tested seven circular CFFT beam specimens, B1 to B7, to determine the effect of longitudinal internal rebar, including steel, GFRP and CFRP. Identical GFRP tubes were used in this study with tube thickness of 8 mm and inner diameter of 203 mm, and had mostly fibers in the hoop direction to simulate spiral reinforcement. Specimens B1 and B2 were RC control specimens with conventional steel circular ties and spirals, respectively. B3 was CFFT reinforced with the same amount of longitudinal steel bars as B1 and B2. B4 to B7 had the same outer GFRP tube as B3 but differ in the type and ratio of reinforcement. Figure 2.14(a) shows the gain in strength and ductility due to confining the circular RC beams with GFRP tube. It indicated the superior performance of the GFRP tubes compared to steel spirals, because they confine a larger area of concrete and contribute as longitudinal reinforcement. The effect of reinforcement ratio is shown in Figure

2.14(b) by comparing specimens B3 and B4 of 3.2 and 1.6% steel reinforcement ratios, respectively, and specimens B5 and B6 of 3.2 and 1.1% GFRP rebar reinforcement ratios, respectively. Specimen B4 exhibited the same general behaviour as B3 but was 28% lower in strength and 44% lower in stiffness, due to the lower reinforcement ratio. The steel-reinforced CFFT specimens maintained a large residual load after initial failure that was caused by rupture of the tube in tension, and then followed by crushing of the tube in compression, and finally the tube fractures in the hoop direction on the compression side, indicating significant confinement. Specimen B5 showed 53% higher strength and 33% higher stiffness than B6. Both Specimens B5 and B6 exhibited the same longitudinal tension failure of the tube, immediately followed by rupture of the bottom layer of GFRP rebar. Figure 2.14(b) also shows that the load capacities of Specimens B3 and B5 were similar due to the similar tensile strengths of steel and GFRP rebar which have the same bar cross section, where B5 had only 5% higher strength. The stiffness of B3 after cracking was twice that of B5, due to the difference in Young's moduli of steel and GFRP rebar. The most important difference, however, is in ductility. B3 exhibited great ductility, with sequential failure and residual strength at very large deflection (220 mm). B5, however, exhibited a rather linear behaviour, until the load dropped completely when the GFRP rebar failed at 74 mm deflection, just after the tensile failure of the GFRP tube, at a deflection of 70 mm. Also shown in the same figure, the behaviour of B6 and B7 with GFRP and CFRP rebar of the same cross-sectional area, respectively. Specimen B7 had 32% higher stiffness and 43% higher strength than B6. This is attributed to the substantial difference in tensile strength and modulus of GFRP and CFRP rebar. The failure mode for both specimens was longitudinal tensile failure of the tube followed by rupture of the bottom layer of FRP rebar, almost simultaneously. It is also worth noting that Specimen B7 achieved similar strength to Specimens B3 and B5 of larger size steel and GFRP rebar, respectively, due to the superior properties of CFRP. From these comparisons, it appears that in reinforced CFFTs FRP rebar does not show significant structural advantage over steel rebar. Additionally, steel rebar is enclosed inside the tube and protected from corrosion induced by external environmental conditions. In fact, the comparable failure strains of GFRP tube and FRP rebar is rather a disadvantage as it results in a sudden and complete failure of the system. Conversely, the ductile steel rebar has allowed the GFRP tube to fail in a sequential manner over an extended

range of deflections, and thereby offers significant ductility and adequate warning signs of failure. The authors also concluded that using longitudinal steel reinforcement is superior to FRP reinforcement because the FRP bars fail at a strain very similar to that of the tube, thus not allowing the system to exhibit any extra ductility.

Mohamed and Masmoudi (2010b) found the same results of Cole and Fam (2006) when testing circular CFFT beams reinforced with steel and GFRP bars of the same cross-sectional area. The load–deflection curves for their specimens are shown in Figure 2.15. Specimen A30S that has steel rebar was compared to A30G that has GFRP bars noting that the two specimens were cast using the same type of the FRP tube and concrete batch. The FRP-reinforced CFFT beam (A30G) behaved in linear way until failure in tension in a brittle manner, unlike the steel-reinforced CFFT beam (A30S) which failed in a ductile manner. The behaviour of A30G showed no yielding compared to A30S. The figures also indicated that A30S experienced lower deflection, higher stiffness and 64% higher strength than A30G. This increase in the flexural strength is attributed to the difference in the Young modulus between the steel and the GFRP bars, and this increase approximately equals the cube root of axial stiffness ratio between the glass and the steel bars $\sqrt[3]{\rho_f E_f / \rho_s E_s}$. On the other hand, the post-cracking flexural stiffness for the beam reinforced with steel bars was higher than that of the beam reinforced with GFRP bars. The average ratio between the post-cracking flexural stiffness of the steel-and-GFRP-reinforced CFFT beams was approximately 3.9, which was approximately the same as the ratio of the modulus of elasticity of steel to that of GFRP bars as it was 4.1. Moreover, the ductility of A30S was 5.6 times the ductility of A30G.

2.4.7 Effect of Bond

Bond development is one of the basic aspects of structural behaviour, since the transmission of load from reinforcement to concrete relies on it. Therefore, the quality of bond has a prominent influence on crack formation, hence affects the spacing between cracks and crack width, and consequently affects the tension stiffening which is related to deflection calculations. The FRP tube in the case of concentrically loaded column provides hoop confinement, and therefore, the mechanical bond between FRP and concrete is not important. For flexural loads, the FRP tube plays an important role. It confines the concrete in the

compression zone and acts as the flexural and shear reinforcement at the same time. This requires the development of the full composite action between FRP tube and concrete. Therefore, a mechanical bond is necessary [Samaan 1997]. AASHTO LRFD guide specifications for design of concrete-filled FRP tubes for flexural and axial members (2012) explicitly mentioned that CFFTs under flexure should be detailed, fabricated, and constructed such that full composite action is achieved between the tube and concrete. To enhance mechanical bond between the FRP tube and concrete and achieve the full composite action there are some common methods like sand coating, resin ribs, shear connector, and internal crossing bars. When flexural tests on CFFTs without internal reinforcement are carried out, excessive slip may occur between the concrete core and FRP tube. This slip may adversely affect the composite action of the system unless special measures are taken, such as roughening the inner surface of the tube [Fam and Rizkalla 2002]. Iftekhar (2004) tested CFFTs as deep beam and short beam under flexure and fatigue. He concluded that slippage is probably the most important factor that dominates the fatigue behaviour and fatigue life of CFFT beams. Fatigue life is directly related to the amount of slippage that occurs between the concrete core and the FRP tube. Slippage reduces the composite action in fatigue loading at a much greater rate when compared with static and quasistatic response. If internal rebar is used and no bond enhancing is done, slip measured at both ends may be very small and can be neglected [Cole and Fam 2006].

Belzer et al. (2013) tested twelve beam specimens of four different configurations to examine the bond effect on the flexural behaviour of rectangular CFFT tubes. Each beam was 3.5 m long with cross section dimensions of 152 mm wide by 203 mm deep with flange and web thicknesses of 9.5 mm and 6.4 mm, respectively. Three beams of each configuration type were tested to establish repeatability of the results. The concrete-to-GFRP tube adhesive used in this research was a wet cure epoxy that co-cures with wet concrete. The four configurations, shown in Figure 2.16(a), include: empty GFRP tube (A), concrete-filled GFRP tube (B), concrete-filled GFRP tube with epoxy bonding of the flanges (C), and concrete-filled GFRP tube with epoxy bonding of all interior surfaces (D). The test specimens were fabricated by using paint rollers to apply the epoxy adhesive to the appropriate interior surfaces of the partially coated beams (C) and fully coated beams (D).

Relative displacement (slip) between the pultruded GFRP tube and concrete core was monitored at the end of each specimen and shown in Figure 2.16(b). It is observed that the unbonded specimens (B) showed the initiation of slip at low loads with the displacement continuing to grow linearly throughout the test. This slip is initiated when the mechanical bond (friction) between the concrete and tube is overcome. The partially bonded specimens (C) showed the initiation of slip at higher loads with C-2 showing no slip and C-3 showing slip associated with failure. Finally, the fully bonded tubes (D) showed no slip with the exception of D-3 that showed slip at failure. As expected due to the composite action, the fully bonded configuration (D) shows the highest strength and stiffness, followed by the partially bonded tube (C), and then the unbonded tube (B), and finally the empty tube (A), as shown in Figure 2.16(c). Moreover, the fully bonded configuration (D) achieves nearly 80% of the full capacity of the tube from the ultimate longitudinal tensile strain measurements from the coupon testing, while the unbonded tube (B) achieved only 58% of the tube flexural capacity.

2.4.8 Effect of Inner Hole

Fam and Rizkalla (2002) investigated the effect of inner hole in concrete-filled GFRP tubes as a trial to reduce the own dead weight of such beams. All the beams had identical outer GFRP tubes, beam 5 had a central hole, designed to provide a concrete wall thickness equivalent to the depth of the compression zone of the completely filled beam 4. Beams 6 and 7 had similar holes, but they are maintained by inner GFRP tubes, both concentric and eccentric. The load-deflection behaviour of beams 4, 5, 6, and 7 is compared in Figure 2.17. The figure also compares the strength and strength-to-self weight ratio of the beams in the form of a bar graph. The strength of beam 5 is only 9% less than that of beam 4, while its strength to weight ratio is 35% higher. Therefore, the designer could achieve comparable flexural strength of the totally filled tube by providing a central hole to reduce the dead weight, provided that the concrete wall thickness is equal to or larger than the depth of the compression zone of a similar tube totally filled with concrete. Providing an inner GFRP tube, as in beam 6, improves the strength and stiffness as compared to beam 5, due to the additional reinforcement. Also, shifting the inner tube toward the tension side, as in beam 7, is more effective; however, this non axisymmetric configuration is only convenient if the

direction of the applied load is constant, as for the case of bridge girders. The load-deflection behaviour is almost linear, with typical reduction in the stiffness after cracking.

Fam et al. (2005) studied beams of rectangular filament-wound GFRP tubes, totally and partially filled with concrete under flexure. The beam section was optimized by providing a central hole to reduce the self-weight of the beam. In this case, the concrete was cast with a void offset towards the tension side of the tube such that the concrete is optimally used for compression, shear and stability of the FRP tube. The GFRP tubes were fabricated using a combined filament winding and hand lay-up technique and were composed of E-glass fibers and epoxy resin with a fiber volume fraction of 60%. The stacking sequence for the flanges is shown in Figure 2.18(a). The $[45^\circ]$ and $[90^\circ]$ layers were composed through the filament winding process and were mainly provided for shear resistance and possible confinement of concrete. The longitudinal $[0^\circ]$ layers were only provided in the upper and lower flanges of the section using hand lay-up of bidirectional glass fibers sheets to provide longitudinal flexural reinforcement. The inner surface of the tubes was roughened by coarse sand coated to prevent slippage. The load-deflection behaviour of the two different configurations of test beams B1 and B2 is shown in Figure 2.18(b). The results showed that both beams had identical flexural stiffness. Although the flexural strength of B2 is 22% lower than that of B1, the dead weight of B2 is 56% lighter than B1, resulting in an overall strength to weight ratio for B2, 77% higher than B1. B1 failed in tension where the GFRP bottom flange ruptured. While B2 failed in compression and suffered outward buckling of the tube flange in addition to inward buckling of the relatively thin concrete flange inside the tube as shown in Figure 2.18(c).

2.5 LIGHTWEIGHT HYBRID FRP-CONCRETE COMPOSITE SECTIONS

In terms of initial costs, FRP composites are, however, still too expensive to compete with other conventional materials (steel and concrete) used in civil engineering applications. To make the best use of materials, combinations of FRP and conventional materials have to be investigated. CFFTs that are completely filled with concrete are not optimal for applications

that are governed by pure bending, such as bridge girders, light poles, and highway overhead sign structures. This is because in such applications the concrete section is cracked below neutral axis, and the concrete core contributes slightly to bending resistance and mainly prevents the tube from buckling and holding reinforcement bars (if exist) in their position. Therefore, there have been studies on a composite system that has concrete in the compressive portion and voided FRP parts below the neutral axis of the beam. The advantages of the combination between these materials to form hybrid FRP-concrete composite system are identified as:

- 1) Lightweight, high strength and corrosion resistant.
- 2) Potential reduction of transport costs for finished members.
- 3) Cost of manufacture can be comparable to the conventional material for a large number of elements.
- 4) Cost can be paid off after several years in service.

Figure 2.19(a) shows the hybrid composite section of Deskovic (1995). He designed a simple beam with a GFRP box section with a layer of concrete on top and a layer of CFRP on the bottom. Experimental tests were performed on large-scale specimens and the results showed good agreement with those from the finite element models. A preliminary design procedure was proposed for the hybrid section based on stiffness, strength and ductility requirements. Canning et al. (1999) designed a beam section as shown in Figure 2.19(b). The beam consisted of a concrete section in the compressive region, a GFRP composite sandwich foam core web section and a GFRP flange interleaved with high-strength unidirectional carbon fiber tape. The beam was designed such that the neutral axis was situated at the soffit of the concrete to prevent tensile forces developing in the concrete. In an attempt to achieve composite action between the concrete and GFRP composite, indents were placed in the vertical faces of the shuttering. During the loading test, certain areas of the shuttering separated from the concrete prematurely; however, the indents did provide continued partial composite action to failure. The failure of the beam occurred by flexural crushing of the concrete followed by failure of the webs in shear. Chakrapan (2005) worked on a project to overcome economic issue, which is one of the major barriers of the use of FRP in civil engineering. He designed a hybrid composite section shown in Figure 2.19(c). According to

the full-scale tests results, the assumption of plane sections remain plane in the region of predominantly bending was shown to be valid. This implied that the principles of flexural design for conventional beams could be used for this duplex section.

Elmahdy et al. (2008) proposed a section composed of a pultruded GFRP hollow box reinforced with externally bonded steel-reinforced polymer (SRP) or CFRP sheets on the bottom flange to carry the tensile stresses. A 54 mm thin layer of ultra-high performance concrete (UHPC) was cast on top of the section to carry the compressive stresses. Composite action between the GFRP section and the UHPC slab was ensured through shear stud connectors and moisture-insensitive epoxy adhesive applied on the top flange of the GFRP section before casting the UHPC slab. The configuration of the section and the tests setup is shown in Figure 2.20. The test results concluded that the flexural capacity of GFRP box sections was increased significantly to about 3.7 times that of the GFRP box alone. The presence of UHPC on the top side of the beam supports the top GFRP flange and helps avoid the buckling of this flange under high compression stresses. Also, the high deflection of the GFRP box section is greatly reduced by the addition of the high stiffness materials (UHPC, SRP, and CFRP). The strain distribution across the depth of the proposed hybrid beam remained linear until failure. Hence, the proposed simplified analysis technique can be used with confidence to predict the beam behaviour.

Indeed, these previous designs (Deskovic, Canning, Chakrapan, and Elmahdy) use “in-house” technology to build the GFRP box, which has the potential of increasing the initial cost of the beam. Additionally, the concrete is not fully confined as to take advantage of its increased ductility and strength under confining stresses [Khennane 2008]. Khennane (2010) proposed a new hybrid FRP-concrete beam design shown in Figure 2.21. The new proposed beam design will consist of a GFRP pultruded profile, a high performance concrete (HPC) block, CFRP strip laminate and an outer GFRP laminate wrap with fibers orientated at $\pm 45^\circ$. The addition of the outer laminate serves three purposes. Its principal role is to confine the concrete as to achieve a ductile behaviour. Confining the whole section will also ensure a composite behaviour between the concrete and the pultruded profile, thus eliminating the risk of deboning failure. Finally, its third role is to improve the shear strength of the pultruded profile. The use of HPC instead of normal concrete will result in an overall increase in the

stiffness of the beam, in addition to a reduction in its depth. According to Khennane (2010), these features of this hybrid beam design will allow for longer spans of bridges, increasing girder-to-girder spacing, and shallower sections.

Idris and Ozbakkaloglu (2014) investigated the flexural behaviour of FRP-high strength concrete (HSC)-steel composite beams by testing double-skin tubular beams (DSTBs) with outer FRP tubes and a central inner hollow steel section (HSS) as shown in Figure 2.22. The main parameters of study included the cross-sectional shapes of the inner HSS and the external FRP tube, concrete strength, presence or absence of concrete filling inside the steel tube, and effects of using mechanical connectors to enhance the bond between the steel tube and surrounding concrete. The results indicated that DSTBs exhibit excellent load-deflection behaviours with high inelastic deformations and minimal strength degradations (slightly increase of flexural strength after yielding). However, relatively large slippage can occur at the concrete-steel tube interface unless the bond is enhanced by mechanical connectors. Regardless the high flexural strength and stiffness of the DSTBs based on the inner steel tube, the weight and the bond remain critical issues in this design and need further investigations.

Table 2.1 – Typical properties of structural materials (ISIS Canada Design Manual No.4 2008)

| Material | Mass Density (kg/m ³) | Tensile Strength (MPa) | Modulus of Elasticity (GPa) | Elongation at Failure (%) | Maximum Long-Term Temperature Use (°C) |
|--|-----------------------------------|------------------------|-----------------------------|---------------------------|--|
| E-Glass Fibers | 2590 | 3450 | 72 | 4.8 | 200 |
| S-Glass Fibers | 2540 | 4300 | 87 | 5.0 | 200 |
| Pan-Type Carbon Fibers | 1790 | 3650 | 230 | 1.4 | 400 |
| Pitch-Based Carbon Fibers | 2040 | 2400 | 380 | 0.5 | 1000 |
| Aramid Fibers | 1480 | 3620 | 130 | 2.8 | 200 |
| Polyester Matrix | 1220 | 50 - 65 | 3.0 | 2 - 3 | 120 |
| Vinyl ester Matrix | 1170 | 70 - 80 | 3.5 | 4 - 6 | 140 |
| Epoxy Matrix | 1100 - 1450 | 50 - 90 | 3.0 | 2 - 8 | 120 - 200 |
| Steel Rebar | 8000 | 500 | 200 | 20 | 300 |
| Portland Cement Concrete 20-60 MPa | 2450 | 2 - 5 | 20-40 | < 0.05 | 100 - 200 (70 During The Cure) |
| Portland Cement Concrete with Polymer 60 MPa | 2140 | 5 | 25-30 | < 0.05 | 100 |

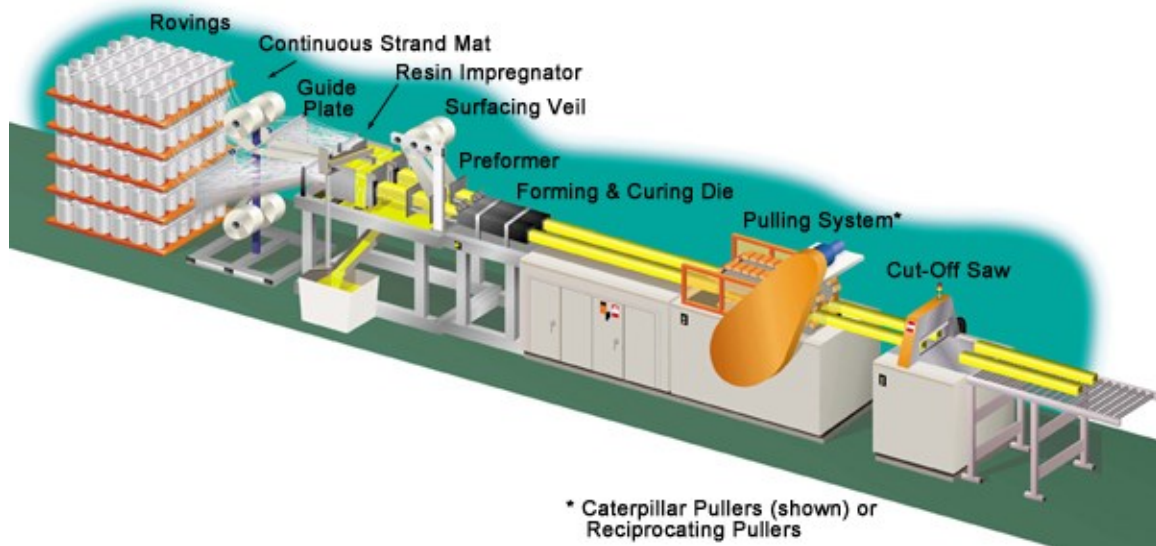


Figure 2.1 – Schematic of pultrusion process [<http://mdacomposites.org>]

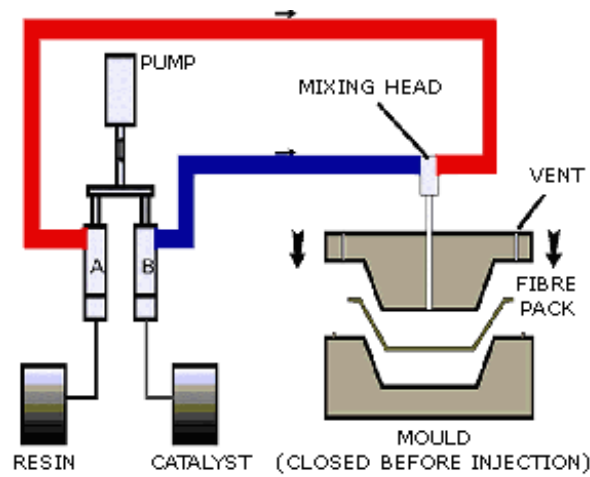


Figure 2.2 – Schematic of RTM process [<http://mdacomposites.org>]

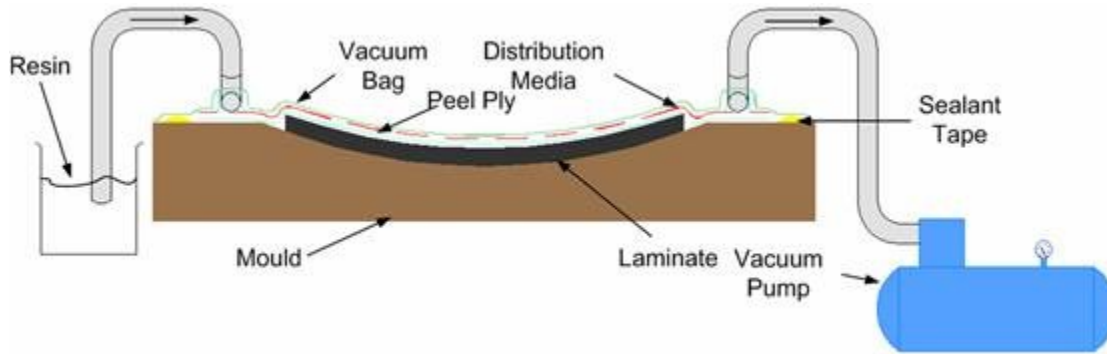


Figure 2.3 – Schematic of VARTM process [<http://mdacomposites.org>]

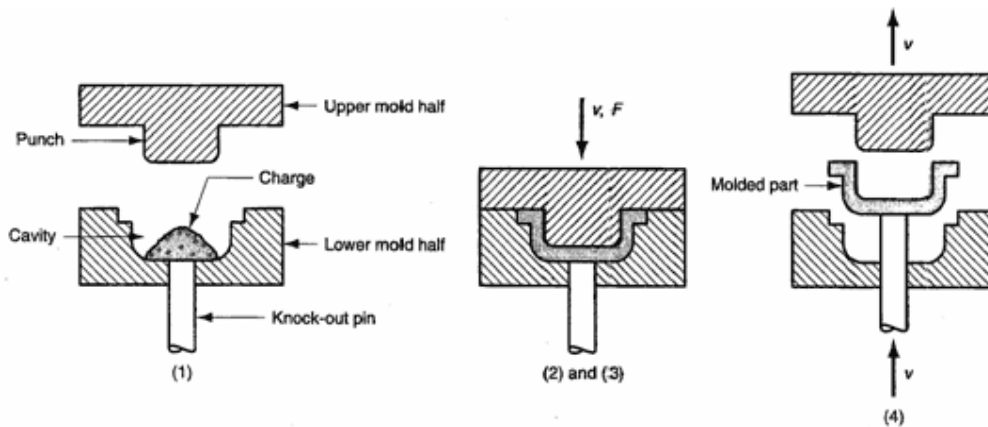


Figure 2.4 – Schematic of compression molding process [<http://mdacomposites.org>]

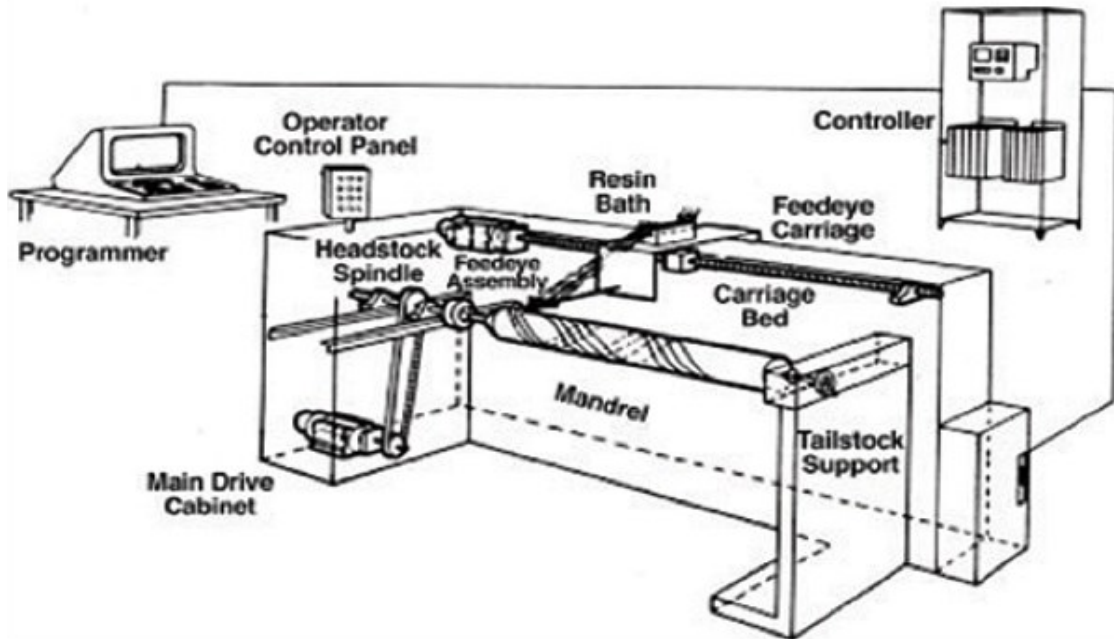
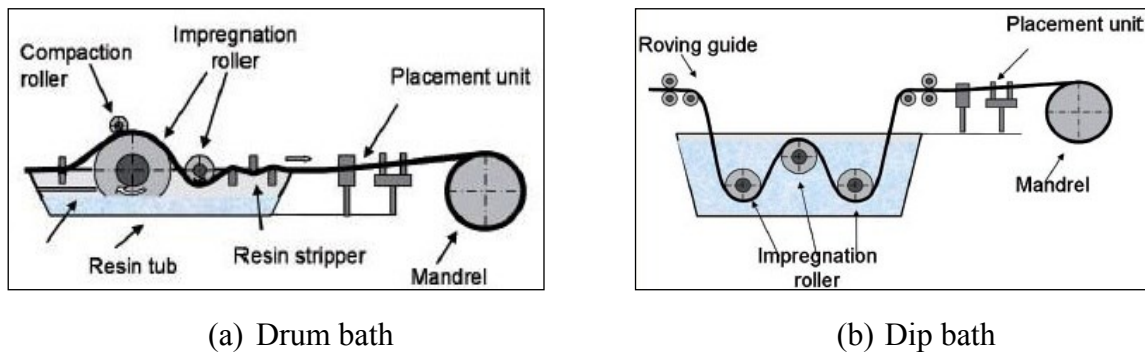


Figure 2.5 – Schematic of filament winding machine [<http://mdacomposites.org>]



(a) Drum bath

(b) Dip bath

Figure 2.6 – Resin bath types in filament winding process [<http://mdacomposites.org>]

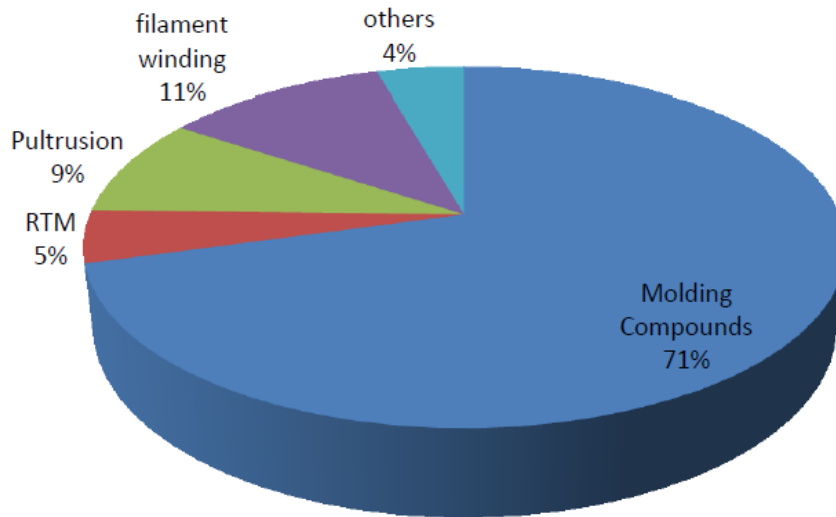


Figure 2.7 – Distribution of composite manufacturing process wise [Beckwith 2006]

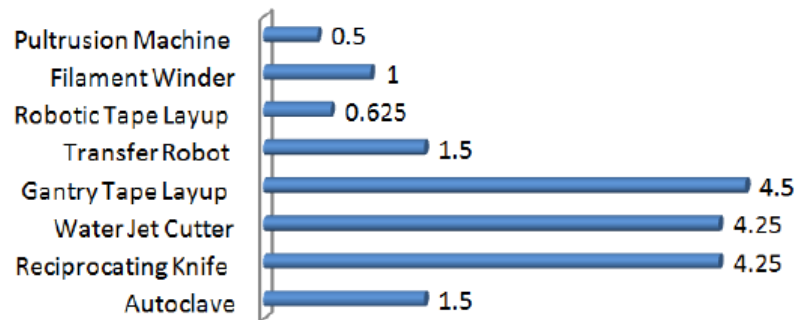


Figure 2.8 – Composite manufacturing cost by different processes [Taheri 1996]



(a) CFFT columns in bridges



(b) CFFTs in Marine structures



(c) CFFT arches

Figure 2.9 – Field applications of CFFTs [<http://google.com>]

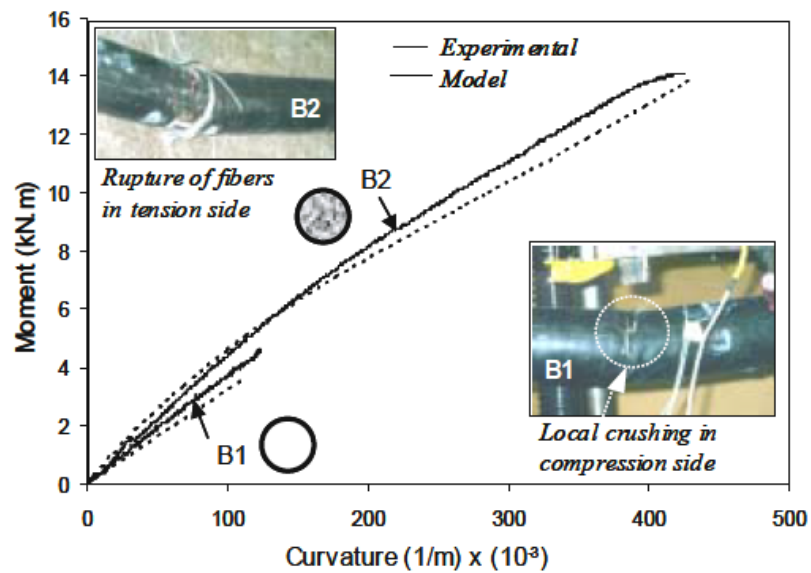


Figure 2.10 – Moment-curvature response and failure modes of B1 and B2 [Fam and Rizkalla 2002]

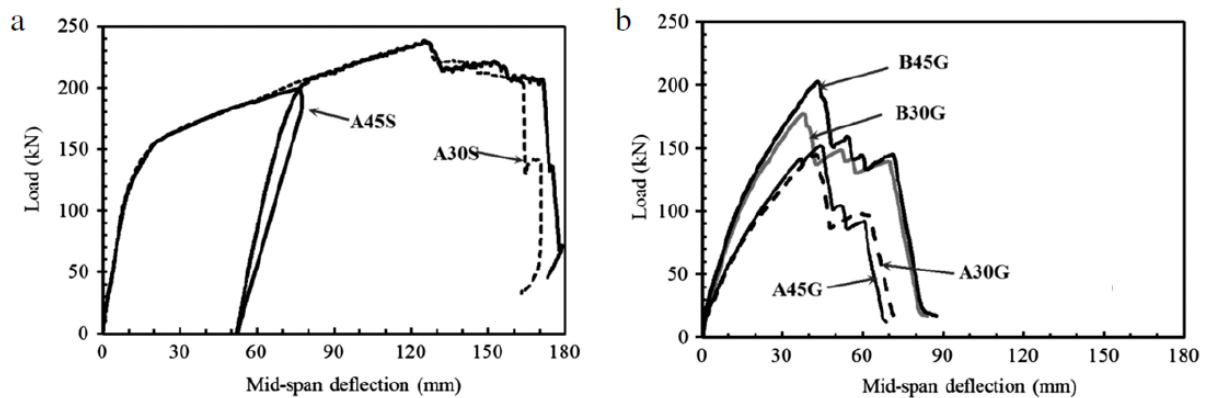


Figure 2.11 – Effect of concrete strength on load-deflection curves [Mohamed and Masmoudi 2010]

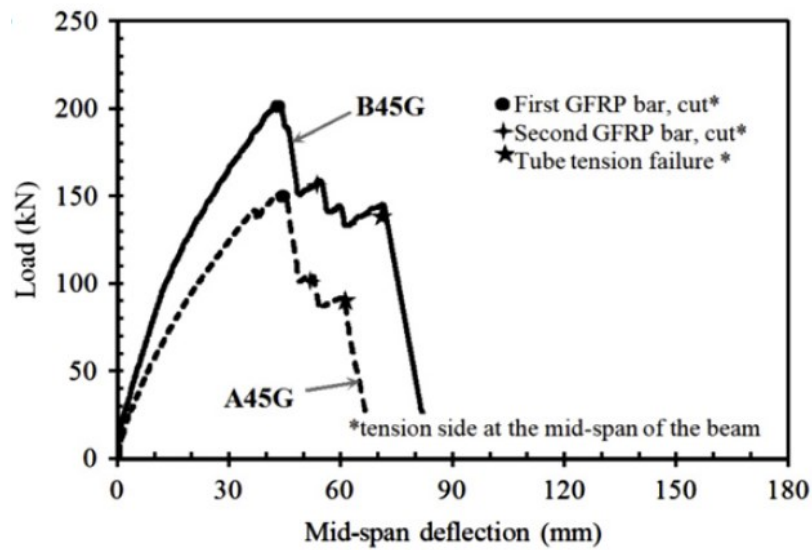


Figure 2.12 – Effect of FRP tube thickness on load–deflection curves [Mohamed and Masmoudi 2010]

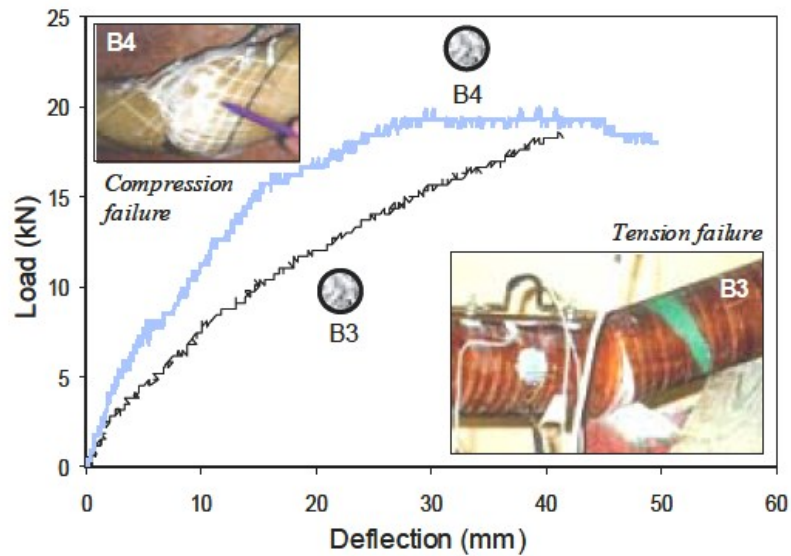
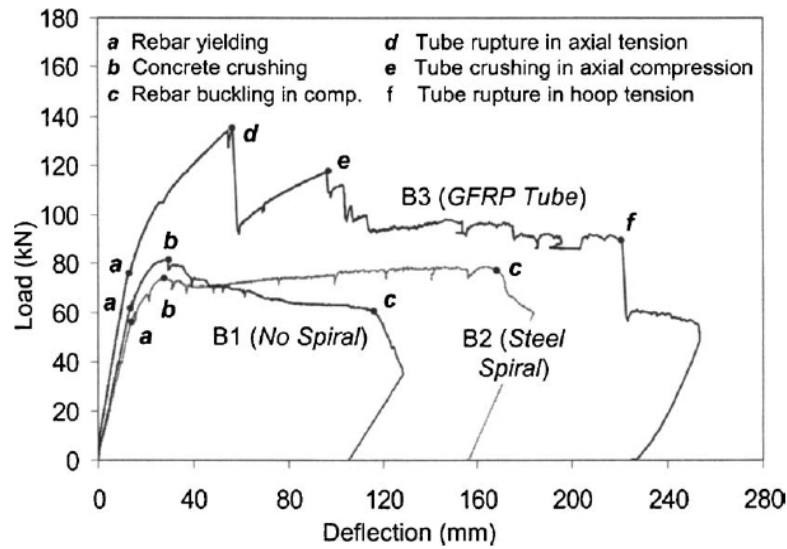
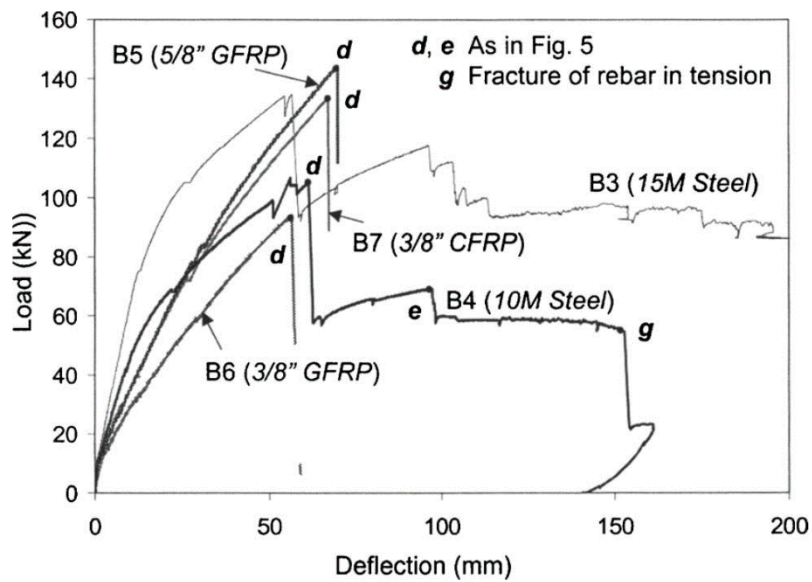


Figure 2.13 – Load-deflection response and failure modes of B3 and B4 [Fam and Rizkalla 2002]



(a) Effect of confining RC beams



(b) Effect of rebar type and ratio

Figure 2.14 – Load-deflection curves for specimens B1 to B7 [Cole and Fam 2006]

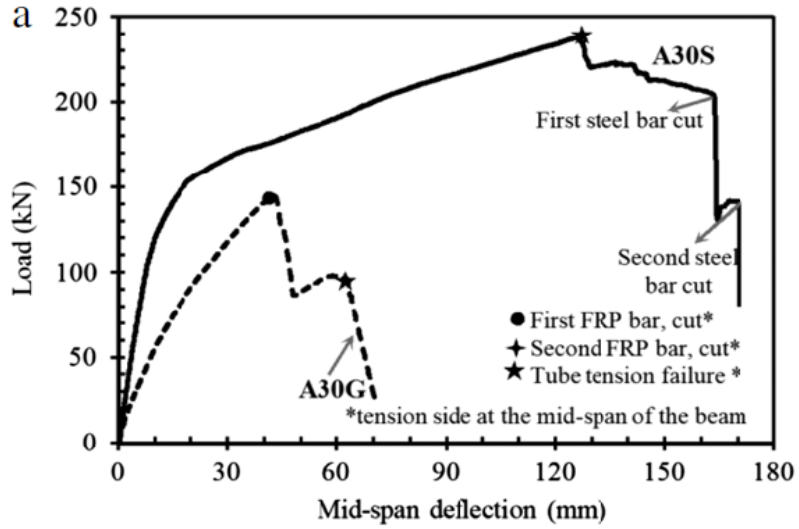
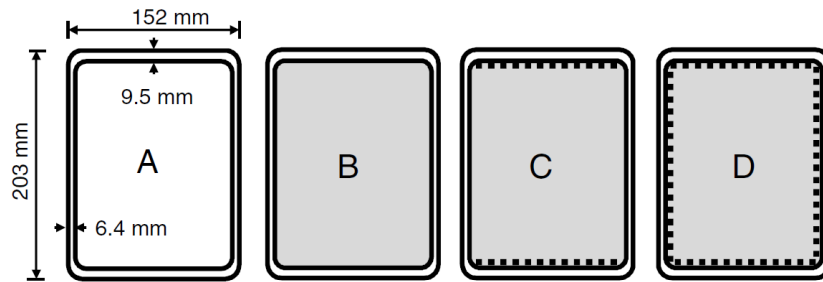
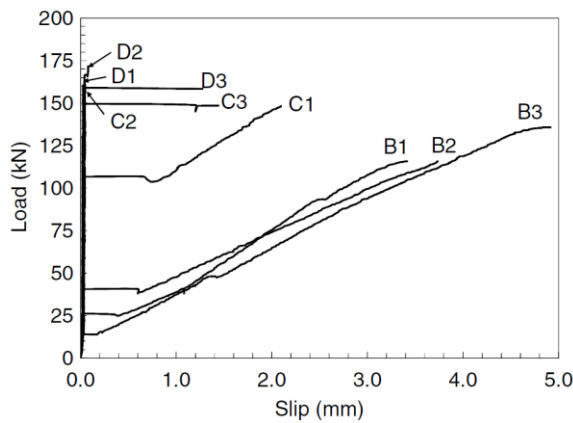


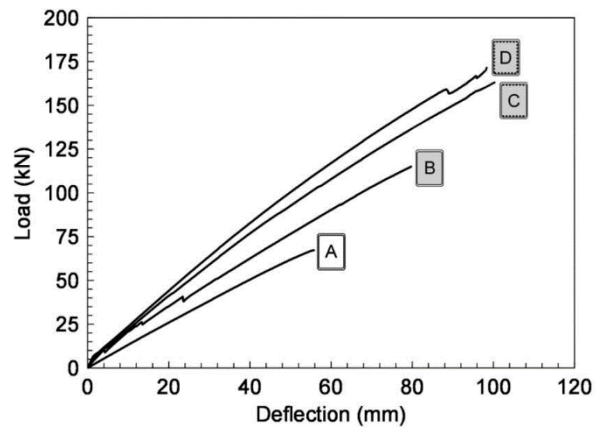
Figure 2.15 – Effect of rebar type on load–deflection curves [Mohamed and Masmoudi 2010]



(a) Beams configurations



(b) Load-slip response



(c) Load-deflection response

Figure 2.16 – Beam test results of Belzer et al. (2013)

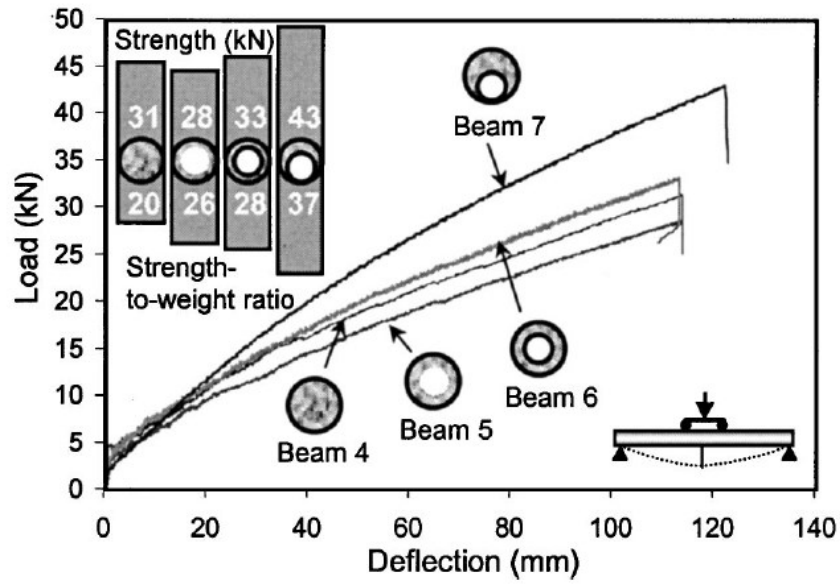
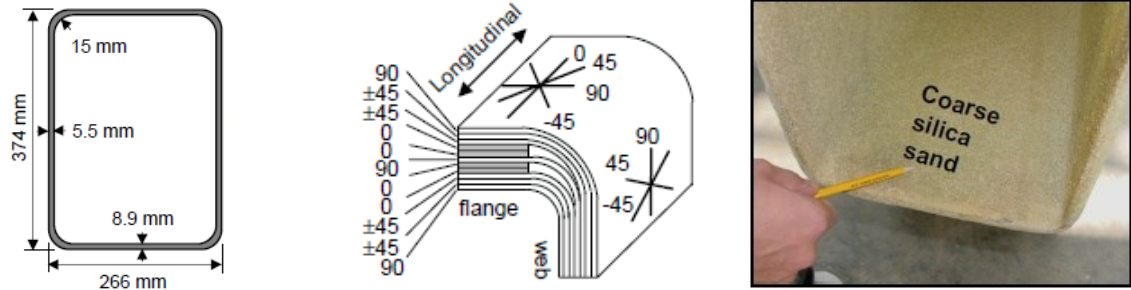
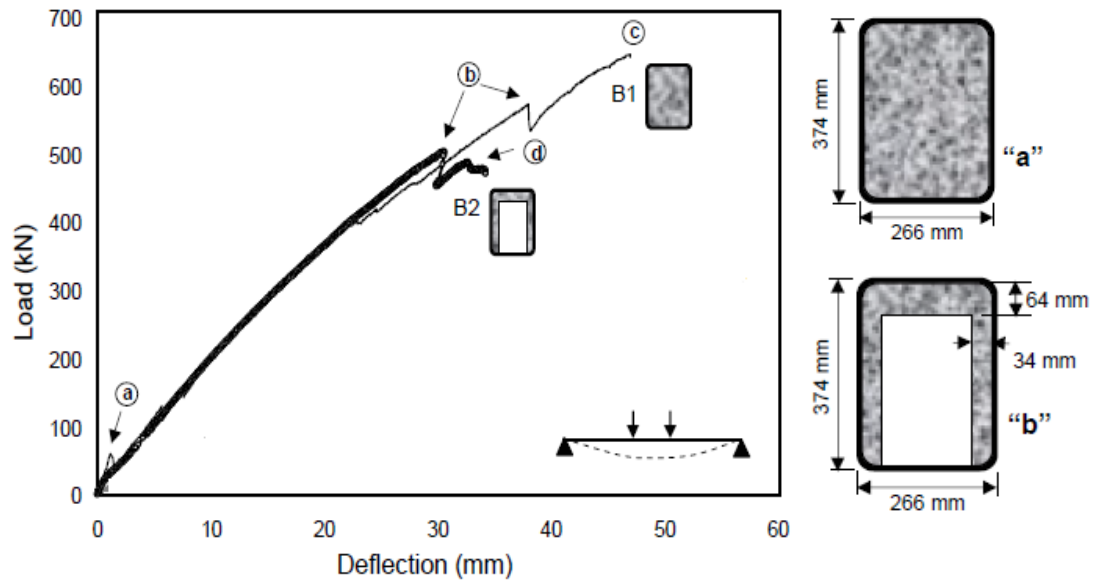


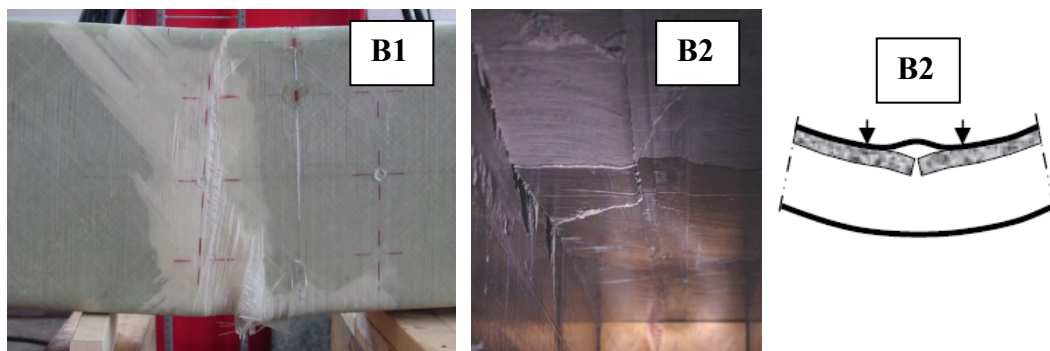
Figure 2.17 – Load-deflection behaviour for different beam configurations [Fam and Rizkalla 2002]



(a) GFRP tube details



(b) Load-deflection response



(c) Failure modes of tested beams

Figure 2.18 – Beam test results of Fam et al. (2005)

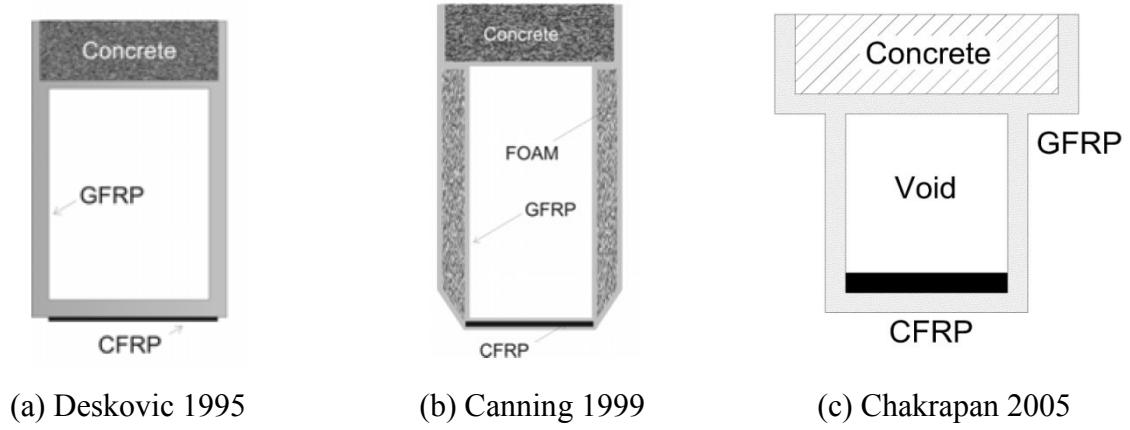


Figure 2.19 – Previous approaches of hybrid composite sections

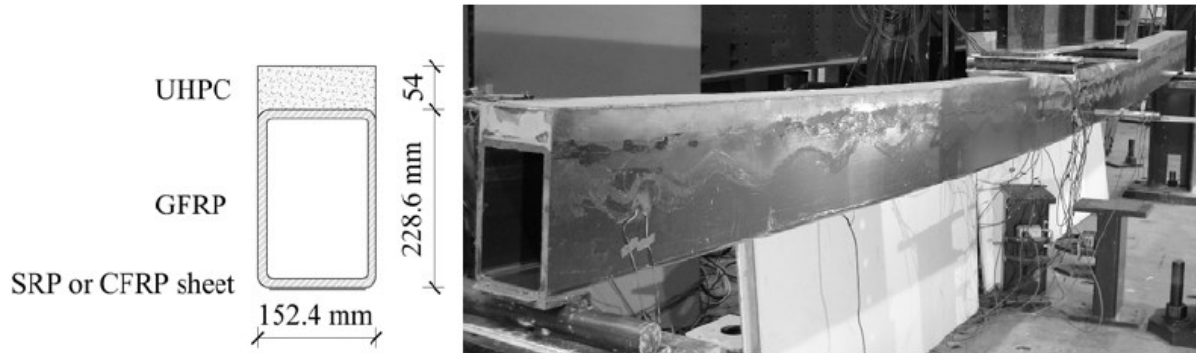


Figure 2.20 – Proposed cross-section by Elmahdy et al. (2008)

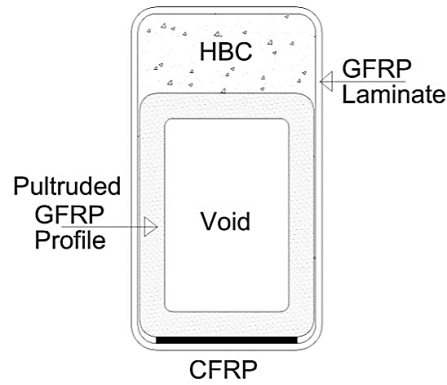


Figure 2.21 – Proposed cross-section by Khennane (2010)

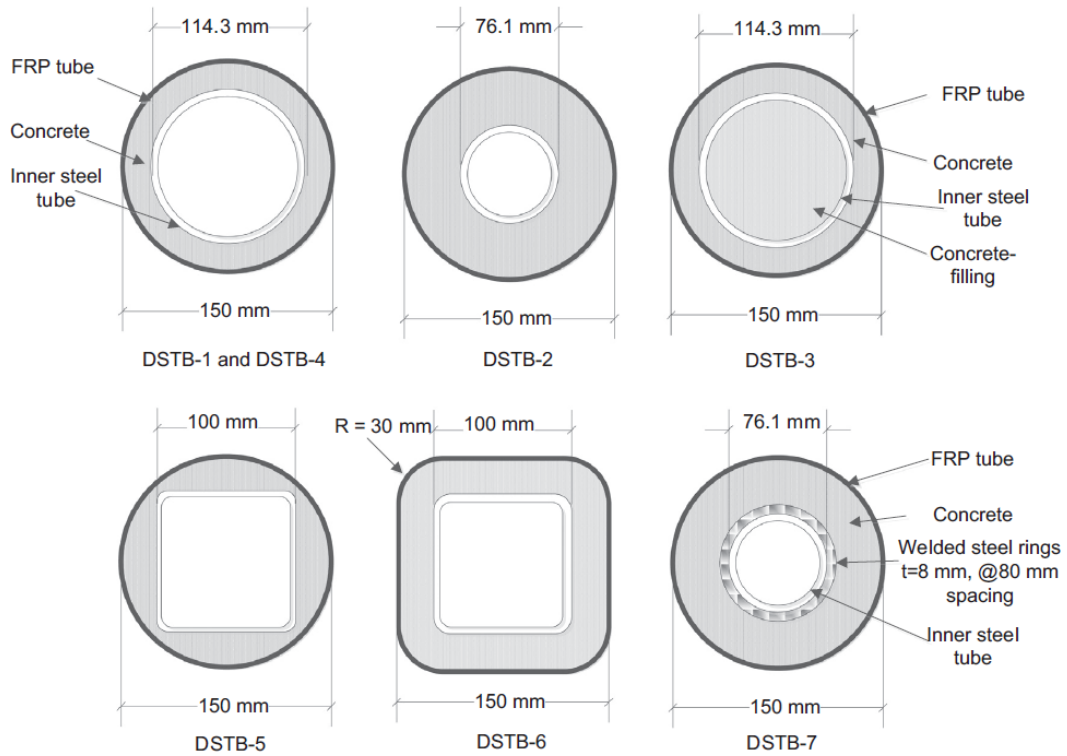


Figure 2.22 – Cross-section examples of DSTB [Idris and Ozbakkaloglu 2014]

CHAPTER 3

EXPERIMENTAL PROGRAM

3.1 INTRODUCTION

This dissertation aims to generate much needed data and to fill research gaps of rectangular concrete-filled fiber-reinforced polymer (FRP) tubes (CFFTs) and to design lightweight durable hybrid composite beams by providing inner voids into the tubes to form partially-CFFTs. The experimental program investigated the flexural behaviour of twenty-four full-scale beam specimens including fully-CFFT beams, partially-CFFT beams, and conventional steel-reinforced concrete (RC) beams. Several sizes and configurations of FRP tubes, composed of typical E-glass fibers and vinyl ester resin, were fabricated by filament winding process in the Civil Engineering department at Sherbrooke University. The fabricated GFRP tubes were tested by standard tests to verify their quality control and to measure their physical and mechanical properties. Rectangular GFRP tubes were used as outer jackets. While, circular and square hollow tubes were used as inner tubes in the partially-CFFT beams. All the beams were cast with normal-weight concrete and reinforced with steel rebar. The beams were tested over a simply supported span under a four-point bending load. The details of the used materials, beam specimens, fabrication process, test setup, and instrumentations are presented in this chapter.

3.2 FABRICATION OF GFRP TUBES

In the filament winding process, the placement of the fibers is controlled and can be oriented in either the hoop direction and/or inclined to the axial direction as needed to develop the necessary strength properties in the hoop or axial directions. Hence, the filament-wound FRP tubes can provide flexural reinforcement and shear reinforcement in the axial and transverse direction of the CFFT beams, respectively. This was one of the reasons for choosing to

fabricate the FRP tubes in the current study by filament-winding process. Different sizes and configurations of GFRP tubes were fabricated for this study at the laboratory of Composites for Infrastructures at Civil Engineering department at Sherbrooke University using the filament winding process as shown in Figure 3.1. The FRP tubes were composed of E-glass fibers and vinyl ester resin. The fibers type is a single end roving of Fiber E-glass. Based on the manufacturer data, the fibers have a nominal texture of 1100 gm/km, a maximum tensile strength of 2400 MPa, and modulus of elasticity of 80 GPa. Vinyl ester resin was used. Based on the manufacturer data, the resin has a density of 1170 kg/m³, a maximum tensile strength of 70 MPa, and a modulus of elasticity of 3.5 GPa. Table 1 lists the configurations and details of the fabricated filament-wound GFRP tubes. All the outer tubes have identical rectangular cross sections with internal dimensions of 305×406 mm² and round corners of 25 mm radius to avoid any damage due to stress concentration at the corners. While circular tubes with an internal diameter of 218 mm and square tubes with internal cross section of 203×203 mm² and round corners of 12.5 mm radius were used as inner hollow tubes in the partially-CFFT beams.

The filament-winding process starts with a large number of fibers rovings pulled from a series of creels into a liquid resin bath. Just before entering the resin bath, the rovings are gathered into a band by passing through a stainless steel comb as shown in Figure 3.2(a). After the rovings are immersed into the resin, they are pulled through a wiping device that removes the excess resin and controls the resin coating thickness around each roving as shown in Figure 3.2(b). Once the rovings have been impregnated and wiped, they are gathered together in a flat band using a comp followed by a ring called payout located on the carriage of the winding machine as shown in Figure 3.2(c).

The traversing speed of the carriage and the winding speed of the mandrel are controlled by computer to create the desired winding angle patterns. Two winding patterns were used, as shown in Figure 3.3(a, b): (1) a circumferential pattern at 90° to provide shear reinforcement and to prevent buckling of the longitudinal fibers, and (2) helical patterns at 30°, 45°, and 65° to provide axial stiffness and strength for the CFFT beam, in addition to their contribution as shear reinforcement. The helical patterns were used to designate the fabricated tubes. For

example; OR4₃₀ refers to an **O**uter **R**ectangular tube has **4** layers of a helical pattern at **30°**. While IS4₆₅ refers to an **I**nnner **S**quare tube has **4** layers of a helical pattern at **65°**.

After completion of the filament winding process, the composite structure is subjected to heat to be cured as shown in Figure 3.4. The optimum curing period and temperature were determined after series of tests to achieve sufficient degrees of polymerization [Abouzieed et al. 2011, 2012a, 2012b]. The last step was pulling the mandrel out of the cured composite tube as shown in Figure 3.5. While supporting the composite tube, the mandrel is attached to an extractor carriage and slowly removed from the center of the tube. After pulling out the mandrel and cleaning the surface of the composite tubes, standard tests were carried out to evaluate the physical and mechanical properties of the final products shown in Figure 3.6. Then, the tubes were cut to the required length of the beam prototypes. The inner surface of the outer tubes and the outer surface of the inner tubes (surfaces in contact with concrete) were sand coated by a layer of vinyl ester resin and coarse sand particles to produce a rough texture in order to enhance the bond between the concrete core and the tubes to achieve a full composite action (see Figure 3.7).

3.3 TESTS ON GFRP TUBES

After curing, standard tests were carried out to evaluate the quality and the physical and mechanical properties of the fabricated filament-wound GFRP tubes. The most important physical properties measured were the percentage of fiber in the composite, and the glass transition temperature of the composite for quality issues. While to measure the mechanical performance of the tubes, tension and compression tests were carried out on identical coupons to obtain the tensile and compressive strength in the axial and transverse (hoop) directions. More details about each test and its specimens are illustrated in the following sections.

3.3.1 Fiber Content

Pyrolysis is chemical decomposition of material components by the action of heat. According to ASTM D3171 (2009), small samples of tube walls are burned in the pyrolysis oven, shown

in Figure 3.8(a), to a high temperature (550°C) which makes the resin to evaporate and leave the fiber alone (see Figure 3.8(c)). The fiber content (W_f) is the ratio of the final mass of the sample after pyrolysis (M_f) and its initial mass before pyrolysis (M_i) as given in Eq. (3.1). Then, the content of resin matrix (W_m) can be estimated from Eq. (3.2). Note that the balance used had an accuracy of 0.001 gm. Three samples at least of each manufactured tube were tested and the average fiber content values are listed in Table 3.1.

$$W_f(\%) = \frac{M_f}{M_i} \times 100 \quad (3.1)$$

$$W_m(\%) = (M_i - M_f/M_i) \times 100 \quad (3.2)$$

3.3.2 Glass Transition Temperature

The glass transition temperature (T_g) is the temperature at which the material begins to soften. This test is carried out by Differential-Scanning-Calorimeter (DSC Q10) shown in Figure 3.9(a), which is equipped with a digital acquisition and data processing. According to ASTM D3418 (2008), the test was carried out on five small cubic samples 2 to 3 mm long for each tube. The temperature of the device increases by several hundred degrees and during that time, the system can evaluate a large number of factors for the sample as its temperature, thermal stability, and its melting and crystallization temperatures. For each sample, a typical graph is obtained, as shown in Figure 3.9(b), which indicates the glass transition temperature (T_g) by the crest of the curve. The obtained results agreed with the manufacturer data where T_g for resin was about 120 °C. To verify if the fabricated tubes had been fully cured or not yet, the degree of polymerization is calculated by applying in Eq. (3.3) and (3.4). Where, ΔH_{pp} is the heating at the end of polymerization, X is the value in J/g determined by the DSC device and equals the area under the bubble, and ΔH_r is the heating temperature of resin predetermined by the manufacturer and equals to 237.2 °C. Based on these calculations in early step of tubes fabrication, the temperature and period of curing was justified at 60 °C for 24 hours to obtain good quality of tube products with a degree of polymerization equivalent to 95% or more.

$$\Delta H_{pp} = X \times \left(\frac{100}{100 - \% \text{ fiber}} \right) \quad (3.3)$$

$$\text{Degree of Polymerization} = 100 \times \left(1 - \frac{\Delta H_{pp}}{\Delta H_r} \right) \quad (3.4)$$

3.3.3 Mechanical Performance of GFRP Tubes

The mechanical performance of the fabricated filament-wound GFRP tubes is verified by measuring the tensile and compressive strength in the axial and transverse (hoop) direction of the tubes. The tests are performed using MTS press machine shown in Figure 3.10(a). One of the machine jaws is fixed and connected to a data acquisition system to measure loads, displacements and strains. The other is movable and connected to the drive system of travel. An extensometer is placed on the specimen in order to measure the corresponding strains.

For the rectangular and square GFRP tubes, coupon specimens were cut according to ASTM D638 (2010) type I or III, based on the specimen thickness, forming coupons with dog bone shape as shown in Figure 3.10(b). This shape is performed to ensure the rupture position to be at the mid-length of each coupon and far from the machine jaws. For the circular GFRP tubes, ring specimens were cut according to ASTM D2290 (2014) with a width of 25.4 mm and 4 mm half circle grooves 180° apart as shown in Figure 3.10(c) to ensure that the maximum stresses (rupture position) to be near the strain gages position. For each specimen, the average width and thickness of the critical central part were measured to get the effective sectional area to calculate the effective stress.

For the rectangular and square tubes, at least five identical coupon specimens in the axial direction of the tube were tested under tension following ASTM D3039/D3039M (2014), and another five coupons were tested under compression following ASTM D695 (2010). The same numbers and tests were carried out in the transverse direction also. For compression tests, an anti-buckling guide was used to prevent buckling of the coupons as shown in Figure 3.10(e). The same previous tests were carried out to measure the tensile and compressive strength in the axial direction only of the circular tubes. While the split disk test was carried out on five identical rings to measure the mechanical properties in the hoop direction of the

circular tubes according to ASTM D2290 (2014) as shown in Figure 3.10(f). Figure 3.10(d, e, f) shows typical failure patterns of the coupons tests.

The results of the tensile and compressive strength in each direction are listed in Table 3.1. The stress-strain relationships for each tube in both directions (axial and hoop) are indicated in Appendix A. Typical axial stress-strain curves for outer rectangular tubes are shown in Figure 3.11. This figure compares between two outer tubes, OR12₃₀ and OR16₄₅, which contain two different stacking sequences. The results indicate two major points:

- 1) Reducing the winding angle from 45° to 30° increased significantly the axial strength and stiffness of the filament-wound GFRP tubes,
- 2) The filament-wound GFRP tubes behaved in a nonlinear way, especially with high winding angles 45°.

3.4 TEST VARIABLES

The objectives of this research were achieved by testing twenty-four full-scale beams, including rectangular fully and partially-CFFT beams with steel rebar and conventional RC beams. Several test variables were considered as follows:

- 1) Effect of fiber laminate orientation and thickness of the outer tube on the flexural behaviour of fully-CFFT beams.
- 2) Effect of the outer tube thickness on the flexural behaviour of partially-CFFT beams.
- 3) Effect of fiber laminate structure and thickness of the inner hollow tube on the flexural behaviour of partially-CFFT beams.
- 4) Effect of the inner hollow tube shape on the flexural behaviour of partially-CFFT beams.
- 5) Effect of steel rebar on the flexural strength and failure mode of fully and partially-CFFT beams.
- 6) Comparing strength-to-weight ratios of fully and partially-CFFT beams with conventional RC beams.

- 7) Analytical study to develop design equations to investigate the experimental results in terms of flexural capacities and deformations.

The conclusions of these studied parameters will be collected and analyzed to form a new durable lightweight hybrid composite beam with acceptable strength that can be used in structures, bridges, and ready structural elements industry.

3.5 BEAM SPECIMENS

Twenty-four full-scale beams, 3200 mm long, were fabricated for this study, including eight fully-CFFT beams, fourteen partially-CFFT beams, and two control RC beams, as shown in Table 3.2. Note that some beams had an identical beam to verify the results of this non-homogenous hybrid composite section and to check the quality control of the fabricated beams especially the tubes were manufactured by the author in the laboratory. The beam specimens were identified by the GFRP tube(s) components used to form each beam. A fully-CFFT beam that contains only one outer tube is identified as OR2₃₀, for example. While a partially-CFFT beam that contains outer and inner tubes is identified as OR2₃₀-IC4₃₀, for example.

All the tested beams were reinforced at the tension side with deformed steel bars 4-15M as flexural reinforcement with a concrete cover of 38 mm. A standard tension test ASTM A615 (2009) was carried out on three specimens of steel bar 15M (see Figure 3.12). The average yield tensile strength (f_y) and the average ultimate tensile strength (f_{su}) were 467 and 610 MPa, respectively, while the average ultimate plastic strain at rupture was 0.164. The average modulus of elasticity E_s was around 200 GPa and the plastic hardening modulus was about 2 GPa ($\approx 0.01E_s$).

Figures 3.13 and 3.14 indicate the cross section configuration, steel cages, and tubes assembly for the beam specimens. Conventional RC beams were tested as control beams to investigate the confinement effect of the rectangular CFFT beams and to compare their strength-to-weight ratio to that of rectangular fully and partially-CFFT beams. Accordingly, the RC beams were reinforced with the same flexural reinforcement 4-15M at the tension

side and 2-10M as top steel reinforcement, and steel stirrups 10M@150mm as shear reinforcement. For the partially-CFFT beams, the inner hollow GFRP tubes were 2900 mm long, but their hollow part was 2400 mm long centered with their length to keep solid parts at the supports region to prevent any shear failure or web buckling during the test at this region. This was done by moving the end block 250 mm inward the hollow tubes. The steel bars and the inner hollow tubes were held together by strong plastic straps, in addition all the assembly was held in its designed position by spacers and screws to hold it to the outer tubes. A cut (window) at the bottom end of the inner tube was formed to prevent air bubbles formation inside the bottom solid part of the inner tube during the casting, since the CFFT beams would be cast on inclined formwork. Finally, perpendicular hooks at 90° and 200 mm long were formed in the steel bars to provide adequate development length and to eliminate any slippage between the concrete core and the outer tube. Figure 3.15 indicates also the reinforcement and section details of each beam type.

3.6 FORMWORKS AND CASTING

The RC beams were cast horizontally in a wooden box formwork, while the tubes were fixed on inclined frames and the concrete was poured into them from top end gates as shown in Figure 3.16. Supporting the tubes against movement and blocking their ends were enough to start the casting process, because the tubes worked as a stay-in-place formwork. All the beams were cast with a ready-mixed normal weight concrete. The mix proportions for cubic meter of concrete includes 380 kg of cement, 152 litre of water, 1070 kg of limestone aggregate with a maximum size of 14 mm, 718 kg of sand. One litre of superplasticizer of polycarboxylate-based high range water reducing admixture, with a specific gravity of 1.7 and solid content of 32%, was added to the mixture before casting the tubes to enhance the concrete workability. The RC beams had been cured in a conventional way by spraying water for 7 days. The CFFT beams were covered tightly with plastic sheets and the moisture that surrounded the beams (under the cover) had been kept at high level for 7 days, as shown in Figure 3.17.

After 28 days of casting, concrete cylinder tests were performed according to ASTM C39 (2012) for every batch. At least five concrete cylinders were tested under compression

machine, shown in Figure 3.18(a), to get the compressive strength of the concrete cylinders. While three cylinders were tested under MTS machine, shown in Figure 3.18(b), with attached vertical strain extensometers to draw the actual stress-strain curve of the concrete cylinders as shown in Figure 3.18(c). The average unconfined compressive strength for the cylindrical concrete specimens at 28 days old (f'_c) is listed in Table 3.2. Based on the stress-strain curves of the concrete cylinders, the experimental modulus of elasticity E_{co} is compatible with Eq. 3.5 proposed by the Canadian codes CSA-S806 (2012) and CSA-S6 (2014).

$$E_{co} = 4500\sqrt{f'_c} \quad (3.5)$$

3.7 TEST SETUP AND INSTRUMENTATIONS

The beams were tested using a four-point bending setup over a simply supported span of 2920 mm long and the distance between the applied concentrated loads was 720 mm centered with the beam length as shown in Figures 3.19, 3.20 and 3.21. These lengths give a span-to-depth ratio of 7.3 and shear span-to-depth ratio of 2.75. As such, it is believed that the beams tested in this study are governed by flexure [Cole 2005].

The beams were loaded under displacement control using MTS machine with a capacity of 10000 kN. The beams were loaded in scheme of loading, unloading, and reloading cycles until the failure, as shown in Figure 3.22. Note that, the rate was constant for all loading and unloading cycles and equals 1 mm/min. The cycles depended on a pre-calculated deflection value at yielding of the embedded steel reinforcement that equals 15 mm. Hence, the maximum displacement limits of the loading cycles were at $0.5\Delta_y$, Δ_y , $2\Delta_y$, and finally at $4\Delta_y$. Afterthought, the last loading cycle continues until failure. The unloading cycles started from the end of each loading cycles and finished at the closer of a minimum displacement limit or zero load value of the machine to avoid releasing the load from the beam and to save time of testing. The unloading and reloading scheme was intended for the assessment of stiffness at various load levels and to evaluate the ductility of such CFFT beam system.

Three displacement potentiometers (DPs) were used to monitor the deflection profile along the beam length, as shown in Figure 3.23(a). In addition, two DPs were located at the ends of the beam to record any relative displacement (slippage) between the concrete core and the tube, if occurred, as shown in Figure 3.23(b).

Linear variable differential transducers (LVDTs) were attached at the beams top and bottom faces of the tubes, as shown in Figure 3.24, to monitor the extreme axial compressive and tensile strains. Before casting, electrical strain gages, 10 mm long, were bonded on the steel reinforcing bars at the most critical section at the mid-span as shown in Figure 3.25(a). In addition, axial and transverse strains gages, 10 mm long, were bonded directly on the inner tubes surfaces at their top and bottom faces and at the mid-height of their web as shown in Figure 3.25(b). Before test, axial and transverse strains gages, 10 mm long, were bonded directly on the outer tubes surfaces at their top and bottom faces, corners, and at different levels along the beam depth (at $H/3$) as shown in Figure 3.26(a). The objective of the strain gages measurements is to draw the strain profile and to record the confining action around the section. Finally, strain rosettes were located at the center of the shear span and the mid-height to investigate the shear response of the beam as shown in Figure 3.26(b). The load, deflection, and strains were recorded automatically during the tests using a data acquisition system that record the readings every 0.5 second.

Table 3.1 – Configurations and mechanical properties of fabricated filament-wound GFRP tubes

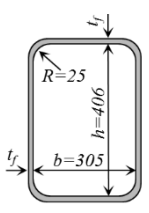

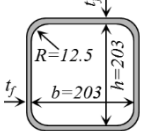
| Tube | Cross Section (mm) | Stacking sequence | %Fibers (By weight) | t_f (mm) | Mechanical properties | Axial direction | | | Hoop direction | | | |
|--------------------|---|--|---------------------|------------|-----------------------|-----------------|----------------|------------------------|----------------|----------------|------------------------|----------|
| | | | | | | E_{lo} (GPa) | F_{lo} (MPa) | ϵ_{lo} (mm/m) | E_{tr} (GPa) | F_{tr} (MPa) | ϵ_{tr} (mm/m) | |
| OR2 ₃₀ |  | [90°, ±30°, 90°] | 62 | 3.4 | Ten. Test | 14.3±2.2 | 158.2±19.9 | 15.7±4.6 | 16.0±1.3 | 256.9±25.7 | 21.8±2.1 | |
| | | | | | Comp. test | 14.0±2.9 | -92.2±9.0 | -7.0±0.7 | 17.8±1.7 | -174.9±8.9 | -10.4±1.4 | |
| OR4 ₃₀ | | [90°, ±30°, 90°, ±30°, 90°] | 61 | 5.7 | Ten. Test | 14.5±1.2 | 173.3±9.0 | 15.3±1.9 | 14.4±0.5 | 249.0±24.9 | 23.9±3.2 | |
| | | | | | Comp. test | 15.5±1.2 | -165.2±6.5 | -12.5±1.1 | 14.5±0.7 | -292.5±17.9 | -23.9±3.5 | |
| OR8 ₃₀ | | [90°, ±30° ₂ , 90°, ±30° ₂ , 90°] | 59 | 8.7 | Ten. Test | 16.2±1.1 | 197.2±15.7 | 18.9±1.8 | 13.7±0.9 | 168.0±5.8 | 19.2±1.2 | |
| | | | | | Comp. test | 17.7±1.2 | -188.5±9.2 | -11.8±0.5 | 13.8±1.0 | -210.8±12.7 | -17.8±0.9 | |
| OR12 ₃₀ | | [90°, ±30° ₆ , 90°] | 59 | 9.9 | Ten. Test | 18.6±0.6 | 241.9±12.8 | 15.3±0.9 | 13.4±0.9 | 125.2±8.8 | 16.6±2.1 | |
| | | | | | Comp. test | 20.1±1.7 | -175.9±12.4 | -9.5±1.2 | 12.2±0.5 | -217.1±15.7 | -24.0±2.7 | |
| OR16 ₄₅ | | [90°, ±45° ₄ , 90°, ±45° ₄ , 90°] | 58 | 14.2 | Ten. Test | 10.5±1.7 | 100.0±14.0 | 22.7±6.0 | 13.0±0.9 | 163.9±2.5 | 24.5±2.1 | |
| | | | | | Comp. test | 11.1±1.4 | -110.0±6.3 | -20.7±0.9 | 12.2±1.0 | -170.6±7.3 | -21.4±2.3 | |
| IC2 ₃₀ | |  | [90°, ±30°, 90°] | 74 | 2.1 | Ten. Test | 17.5±2.0 | 228±16.5 | 17.6±2.3 | 25.1±1.2 | 312±16.7 | 12.3±0.7 |
| | | | | | | Comp. test | 20.3±0.7 | -121±6.6 | -7.2±0.5 | --- | --- | --- |
| IC4 ₃₀ | [90°, ±30° ₂ , 90°] | | 75 | 3.1 | Ten. Test | 16.9±2.2 | 217.1±14.6 | 17.3±2.1 | 23.3±1.9 | 298.1±14 | 13.1±1.0 | |
| | | | | | Comp. test | 20.4±0.8 | -130.6±4.3 | -8.0±0.5 | --- | --- | --- | |
| IS2 ₃₀ |  | [90°, ±30°, 90°] | 63 | 2.9 | Ten. Test | 16.9±1.1 | 142±11 | 13.0±1.5 | 16.6±0.8 | 157.2±9.3 | 10.4±1.0 | |
| | | | | | Comp. test | 13.4±1.3 | -118±7.6 | -12.0±1.8 | 20±3.2 | -163.4±22 | -9.3±2.8 | |
| IS4 ₃₀ | | [90°, ±30° ₂ , 90°] | 62 | 4.7 | Ten. Test | 16.5±3.5 | 147.9±7.9 | 14.2±3.2 | 15.2±1.5 | 119.9±8.9 | 9.3±1 | |
| | | | | | Comp. test | 12.5±1.1 | -118.1±5.3 | -13.1±1.7 | 14.4±0.7 | -203±10.4 | -15.1±1.3 | |
| IS4 ₆₅ | | [90°, ±65° ₂ , 90°] | 60 | 4.2 | Ten. Test | 4.7±1.8 | 24.6±4.1 | 10.1±3.2 | 22.6±1.2 | 336.5±12.0 | 13.7±1.2 | |
| | | | | | Comp. test | 5.2±1.7 | -63.5±6.3 | -18.2±3.8 | 20.9±1.9 | -271.1±10.1 | -12.3±1.3 | |

Table 3.2 – Details of beam specimens

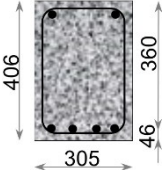
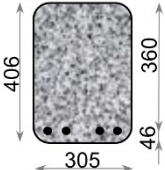
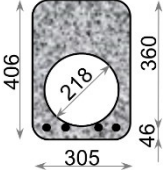
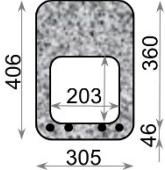
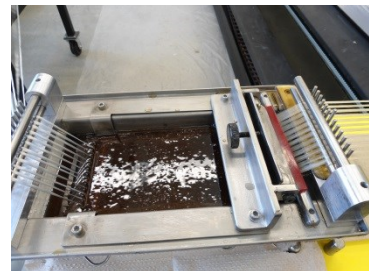
| Group | Beam ID | Section Configuration (mm) | Steel reinforcement | Outer tube | Inner tube | Concrete strength (MPa) |
|--------------------------------|---|---|---|--------------------|-------------------|-------------------------|
| RC beam | RC #1 |  | Top 2-10M Bot. 4-15M Ties 10M/150 mm | --- | --- | 41.7 |
| | RC #2 | | | | | 41.7 |
| Fully CFFT beams | OR2 ₃₀ #1 |  | Bot. 4-15M | OR2 ₃₀ | --- | 49.7 |
| | OR2 ₃₀ #2 | | | OR2 ₃₀ | --- | 49.7 |
| | OR4 ₃₀ #1 | | | OR4 ₃₀ | --- | 48.7 |
| | OR4 ₃₀ #2 | | | OR4 ₃₀ | --- | 48.7 |
| | OR8 ₃₀ #1 | | | OR8 ₃₀ | --- | 41.7 |
| | OR8 ₃₀ #2 | | | OR8 ₃₀ | --- | 41.7 |
| | OR12 ₃₀ | | | OR12 ₃₀ | --- | 48.7 |
| | OR16 ₄₅ | | | OR16 ₄₅ | --- | 48.7 |
| CFFT beams with circular voids | OR2 ₃₀ -IC4 ₃₀ |  | Bot. 4-15M | OR2 ₃₀ | IC4 ₃₀ | 49.7 |
| | OR4 ₃₀ -IC4 ₃₀ | | | OR4 ₃₀ | IC4 ₃₀ | 49.7 |
| | OR4 ₃₀ -IC2 ₃₀ #1 | | | OR4 ₃₀ | IC2 ₃₀ | 49.7 |
| | OR4 ₃₀ -IC2 ₃₀ #2 | | | OR4 ₃₀ | IC2 ₃₀ | 49.7 |
| | OR8 ₃₀ -IC4 ₃₀ #1 | | | OR8 ₃₀ | IC4 ₃₀ | 41.7 |
| | OR8 ₃₀ -IC4 ₃₀ #2 | | | OR8 ₃₀ | IC4 ₃₀ | 41.7 |
| CFFT beams with square voids | OR4 ₃₀ -IS2 ₃₀ #1 |  | Bot. 4-15M | OR4 ₃₀ | IS2 ₃₀ | 48.7 |
| | OR4 ₃₀ -IS2 ₃₀ #2 | | | OR4 ₃₀ | IS2 ₃₀ | 48.7 |
| | OR4 ₃₀ -IS4 ₃₀ #1 | | | OR4 ₃₀ | IS4 ₃₀ | 48.7 |
| | OR4 ₃₀ -IS4 ₃₀ #2 | | | OR4 ₃₀ | IS4 ₃₀ | 48.7 |
| | OR4 ₃₀ -IS4 ₆₅ #1 | | | OR4 ₃₀ | IS4 ₆₅ | 48.7 |
| | OR4 ₃₀ -IS4 ₆₅ #2 | | | OR4 ₃₀ | IS4 ₆₅ | 48.7 |
| | OR8 ₃₀ -IS4 ₃₀ #1 | | | OR8 ₃₀ | IS4 ₃₀ | 49.7 |
| | OR8 ₃₀ -IS4 ₃₀ #2 | | | OR8 ₃₀ | IS4 ₃₀ | 49.7 |



Figure 3.1 – Filament winding process (Civil Engineering department, Sherbrooke University)



a) Fibers roving on creels

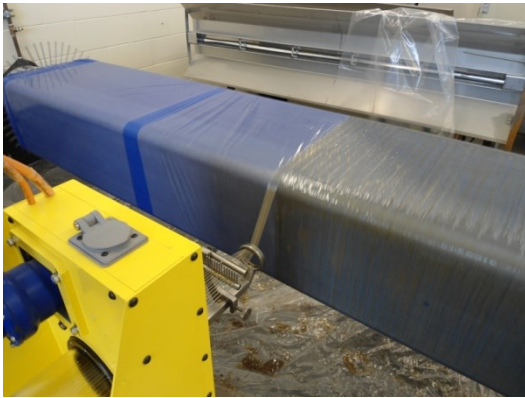


b) fiber impregnation into resin dip path

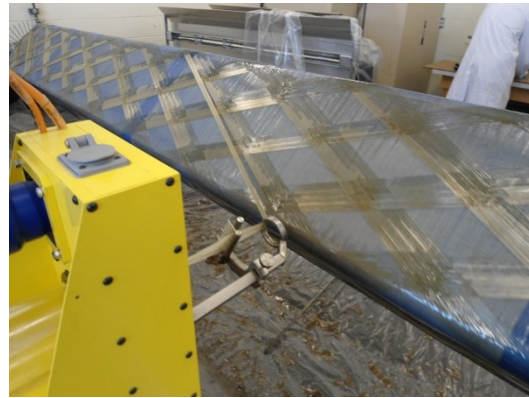


c) Gathering fibers by payout

Figure 3.2 – Fibers installment in filament winding process



(a) Circumferential pattern



(b) Helical pattern

Figure 3.3 – Fiber laminates structure patterns



Figure 3.4 – Curing of FRP tubes by applying heat



Figure 3.5 – Removing the mandrel



Figure 3.6 – Final Products of GFRP tubes



(a) Sand coating the outer surface of inner tubes



(b) Sand coating the inner surface of outer tubes

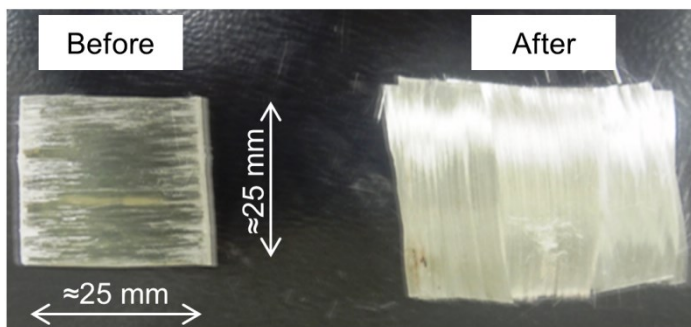
Figure 3.7 – Sand coating for GFRP tubes



(a) Pyrolysis oven



(a) Balance

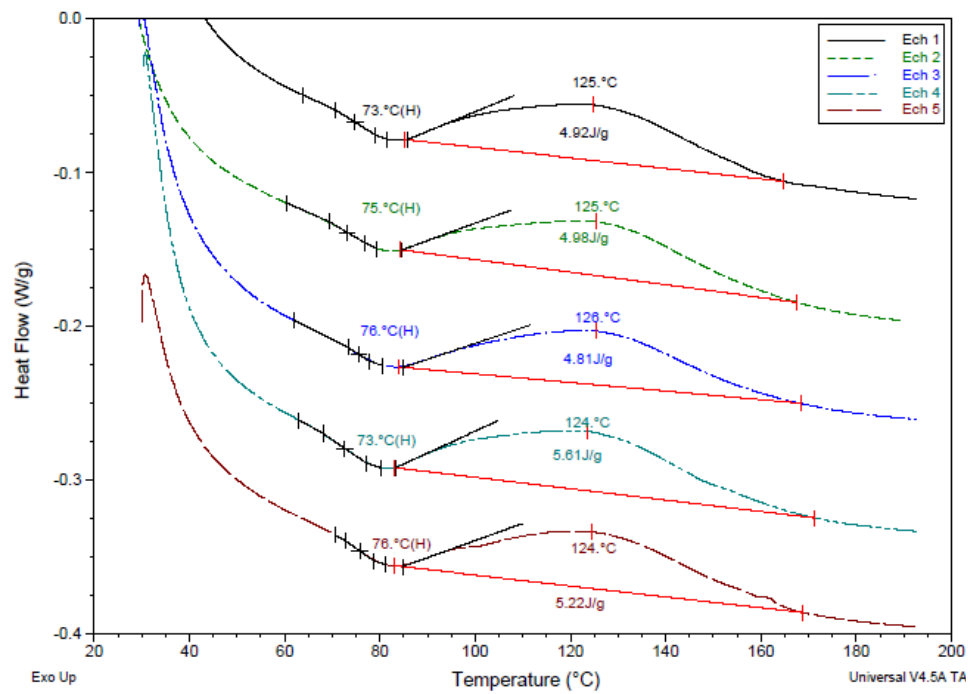


(c) Sample dimension and status

Figure 3.8 – Fiber content test (ASTM D3171-09)



(a) DSC Q10 device

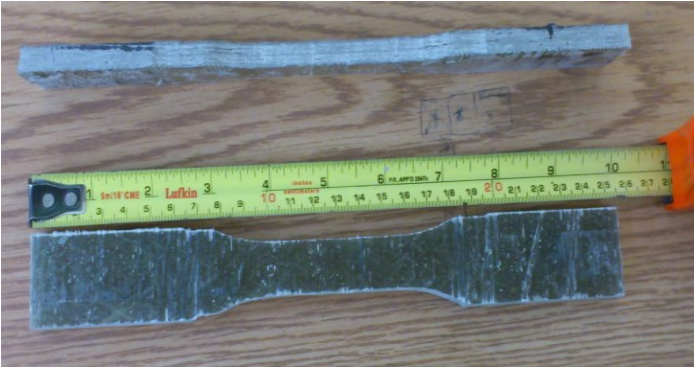


(b) Typical DSC curves

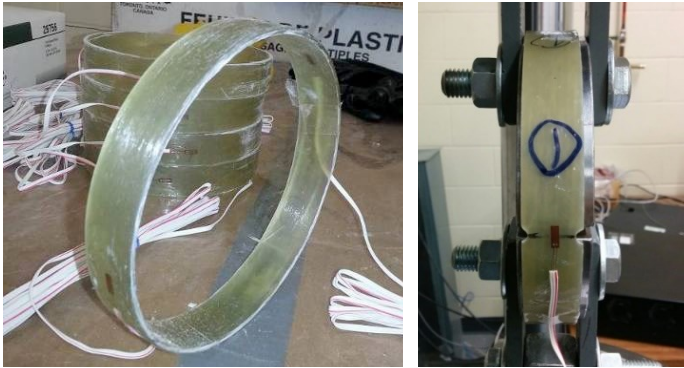
Figure 3.9 – DSC test (ASTM D3418-08)



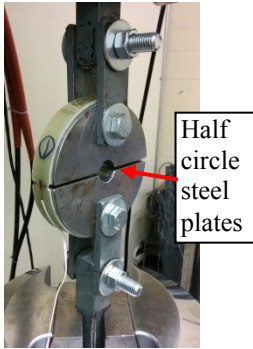
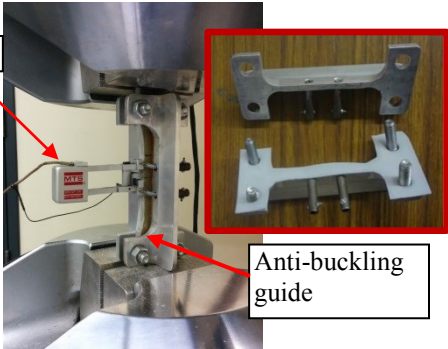
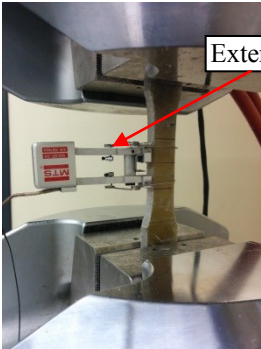
(a) MTS press 810



(b) Dog-bone shape of coupons



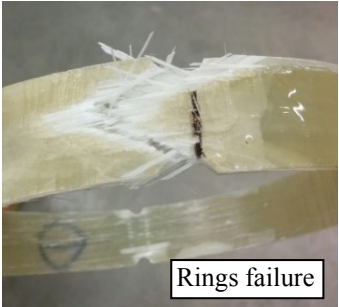
(c) Rings for split-disc test



Coupons tension failure



Coupons Compression failure



Rings failure

(d) Tension test

(e) Compression test

(f) Split disk test

Figure 3.10 – Coupons tests and instrumentations

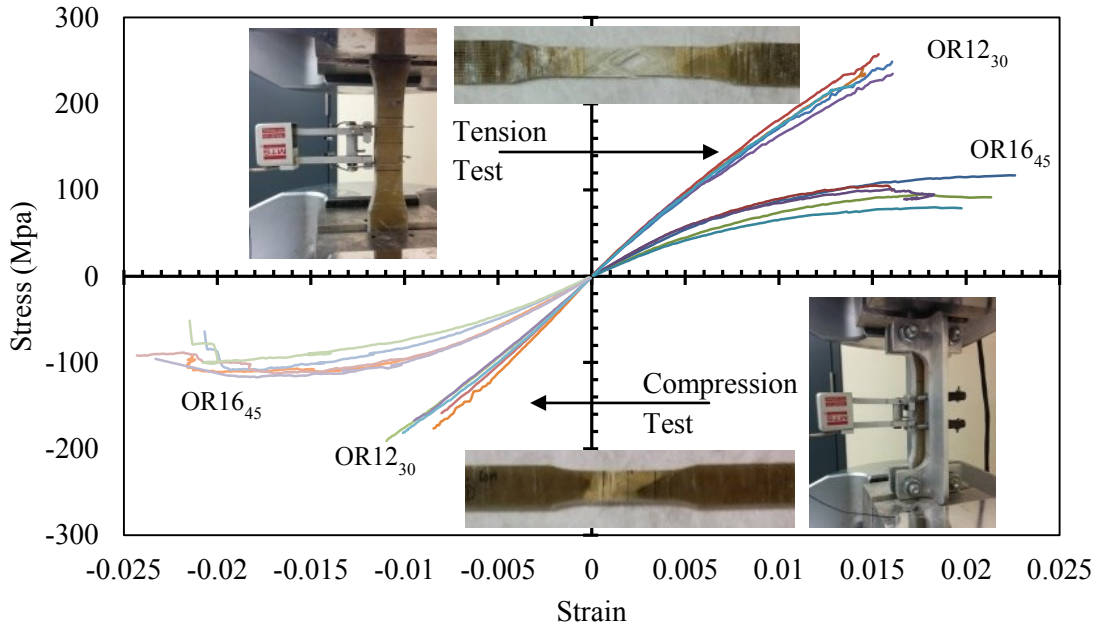


Figure 3.11 – Coupons tests results of OR12₃₀ and OR16₄₅ in axial direction

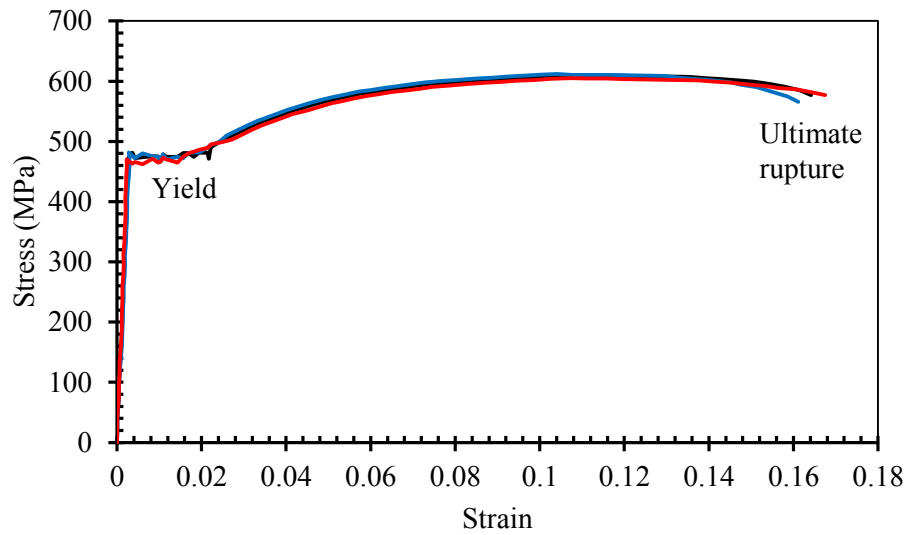


Figure 3.12 – Stress-strain response of steel bar 15M

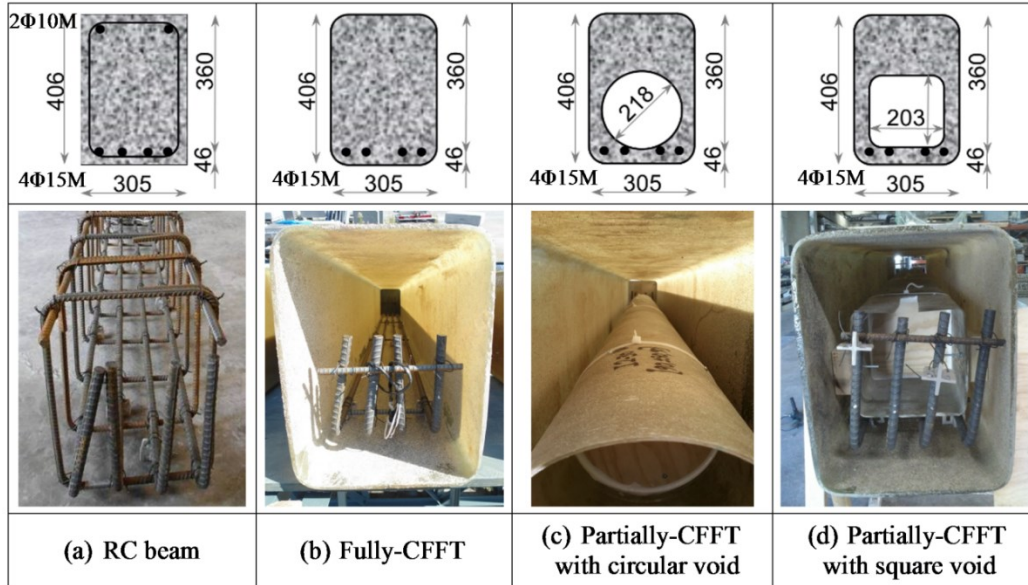


Figure 3.13 – Cross section configurations of the tested beams

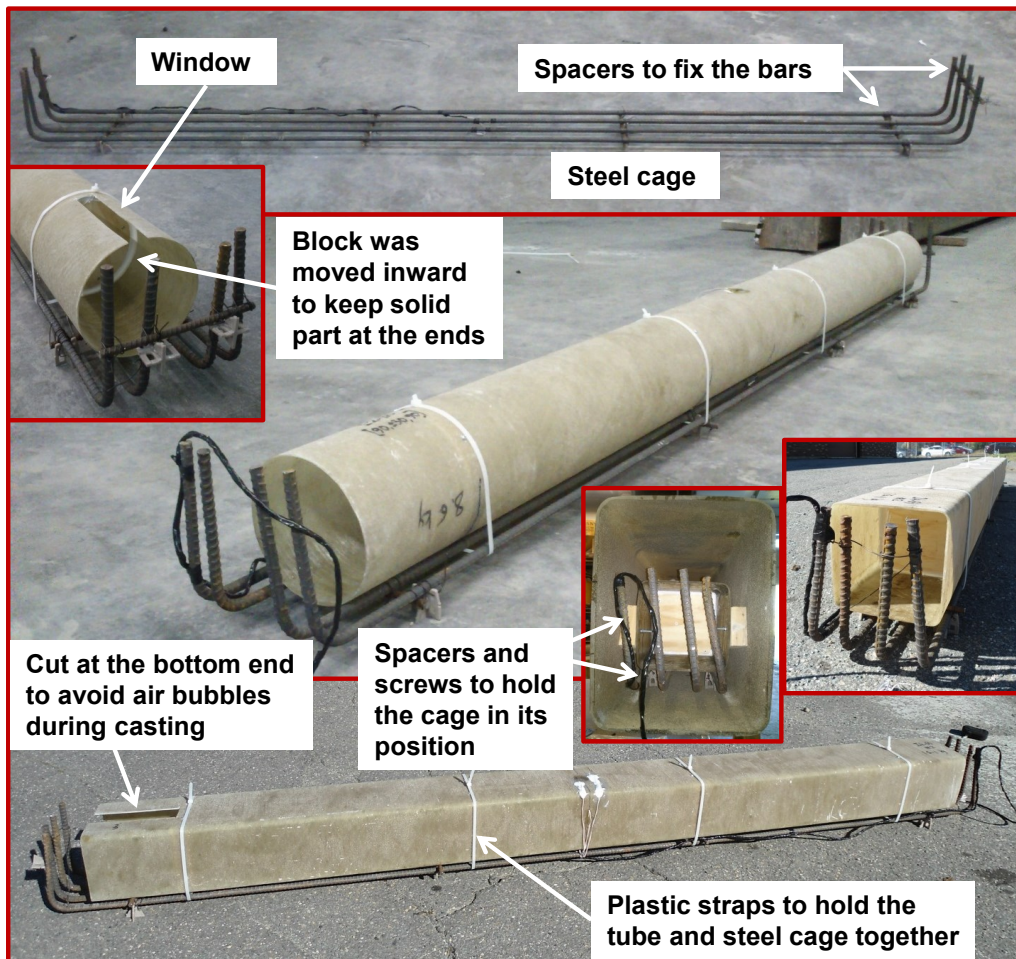


Figure 3.14 – Reinforcement cages and tubes assembly

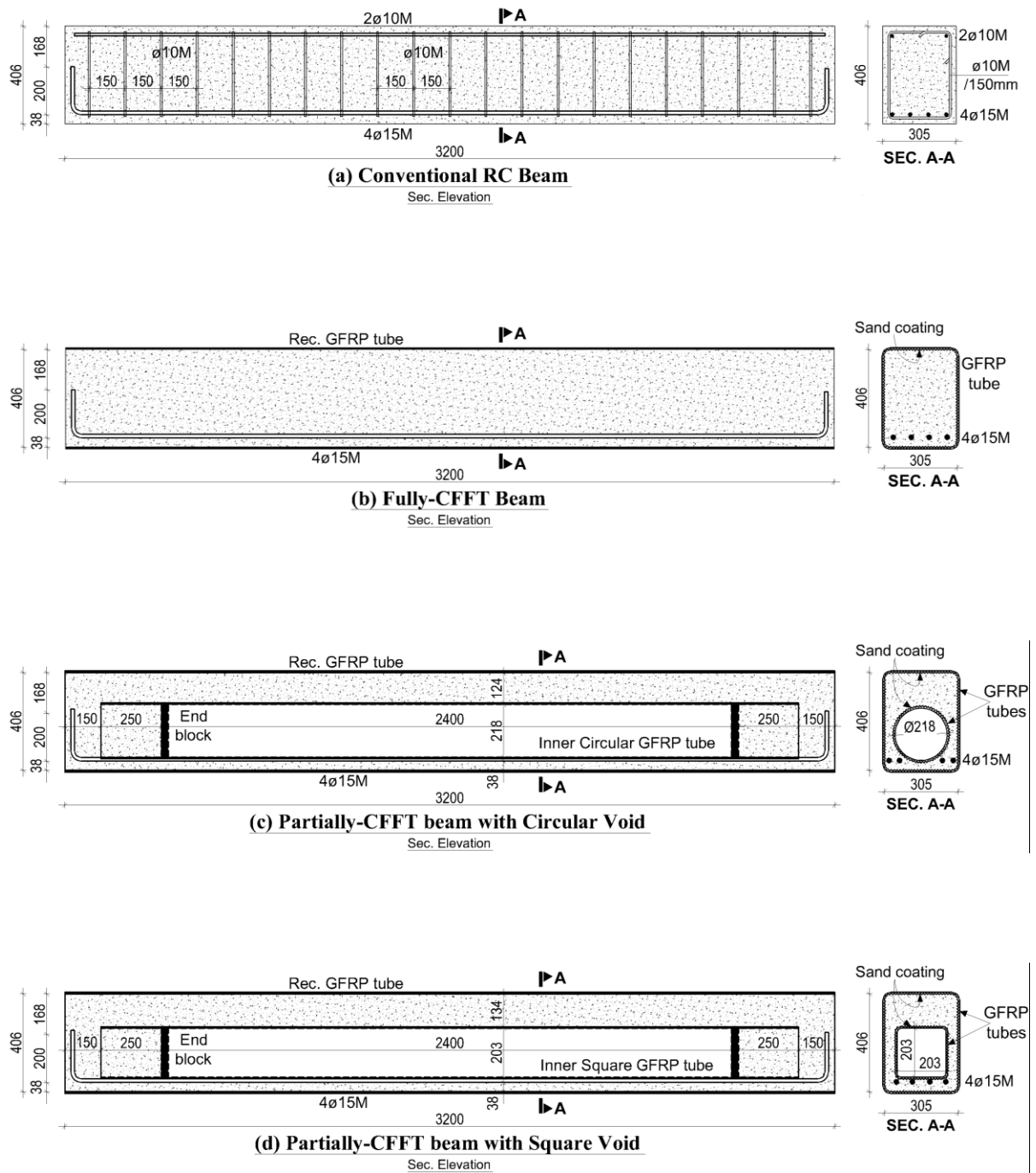


Figure 3.15 – Details of beam specimens (dimensions are in mm)



(a) Wooden formwork for RC beams



(b) Inclined frames for CFFT beams

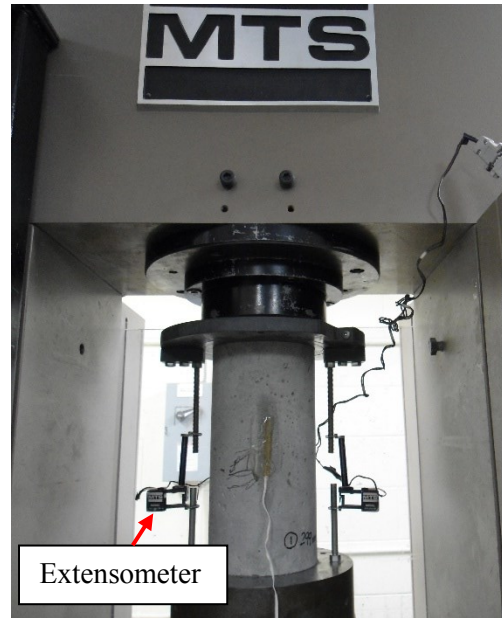
Figure 3.16 – Casting process



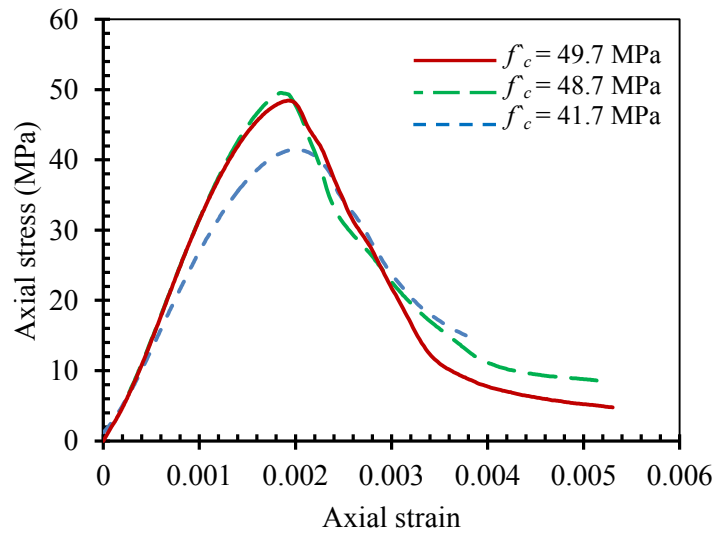
Figure 3.17 – Seven days moisture curing for CFFT beams



(a) Compression machine



(b) Compression test by MTS machine



(c) Typical axial stress-strain response of concrete cylinder for every batch

Figure 3.18 – Concrete cylinders tests (ASTM C39-12)

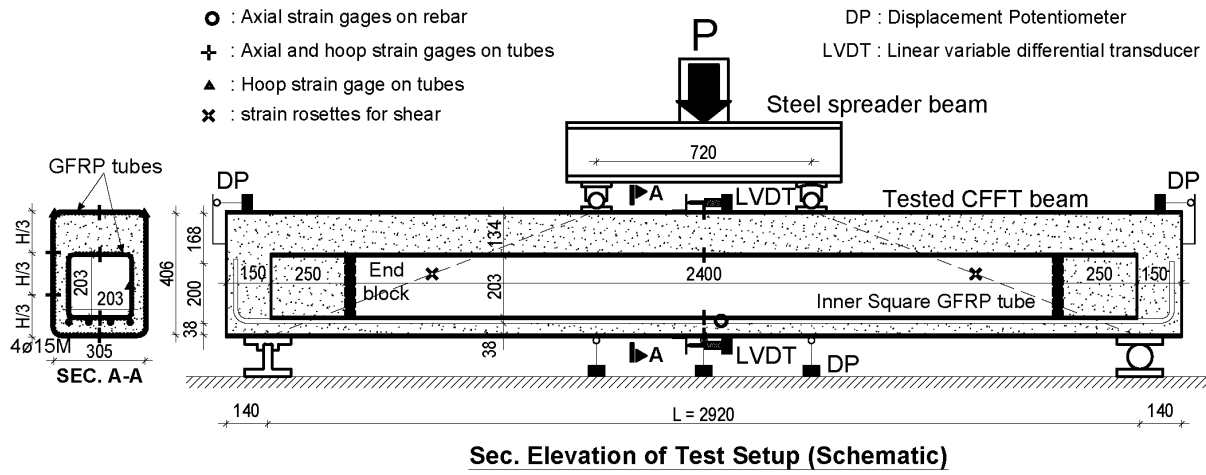
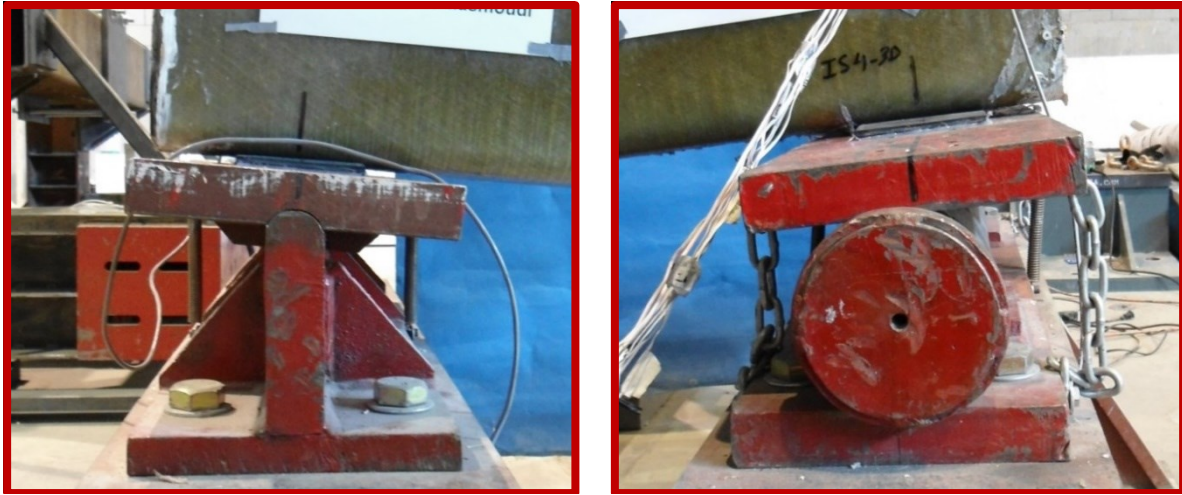


Figure 3.19 – Typical schematic of test setup and instrumentations (dimensions are in mm)



Figure 3.20 – View of beam test setup



(a) Hinged support

(b) Roller support

Figure 3.21 – Supports

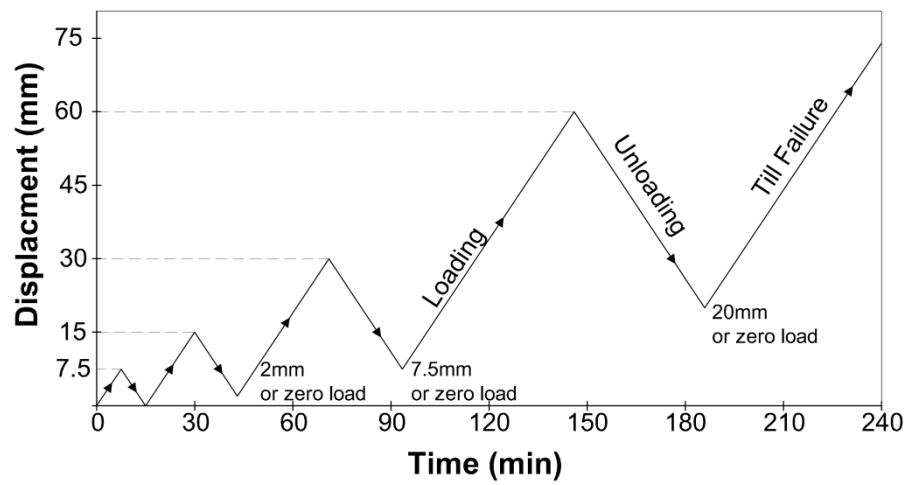
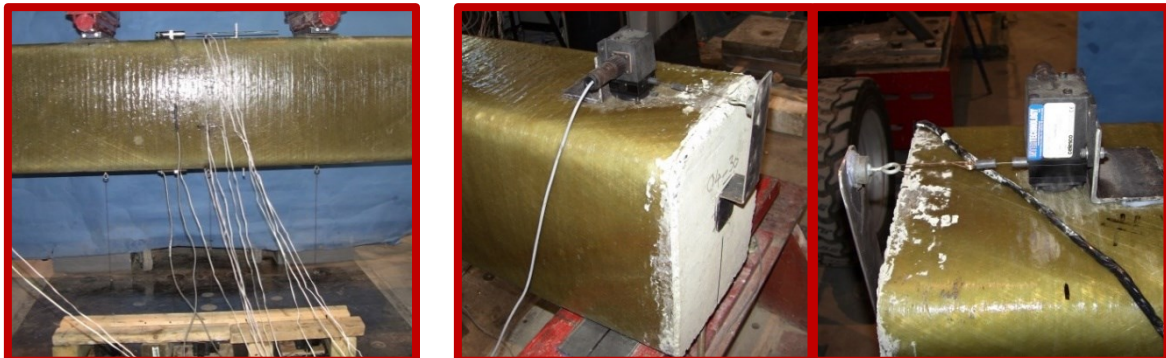


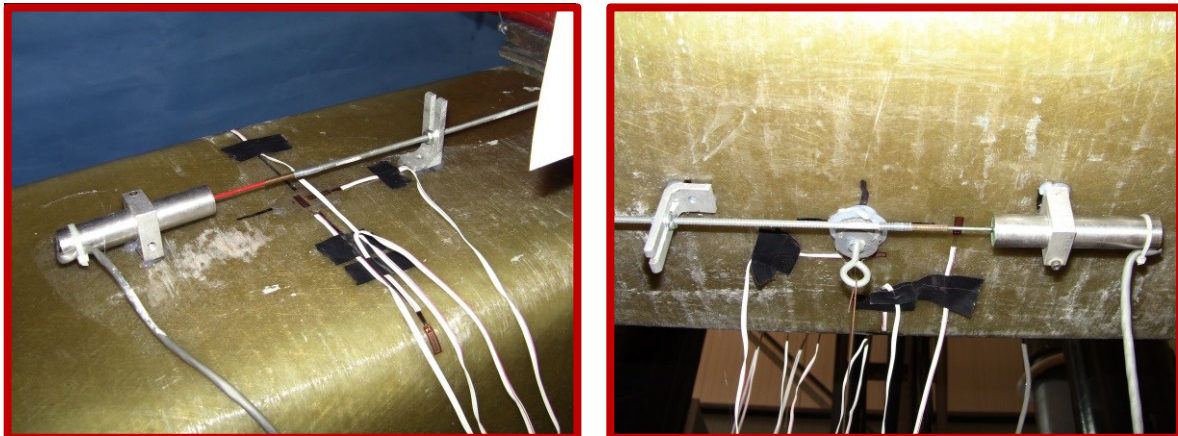
Figure 3.22 – Scheme of loading and unloading cycles (rate = 1 mm/min)



(a) Bottom DPs
to measure deflection

(b) End DPs
to measure slippage

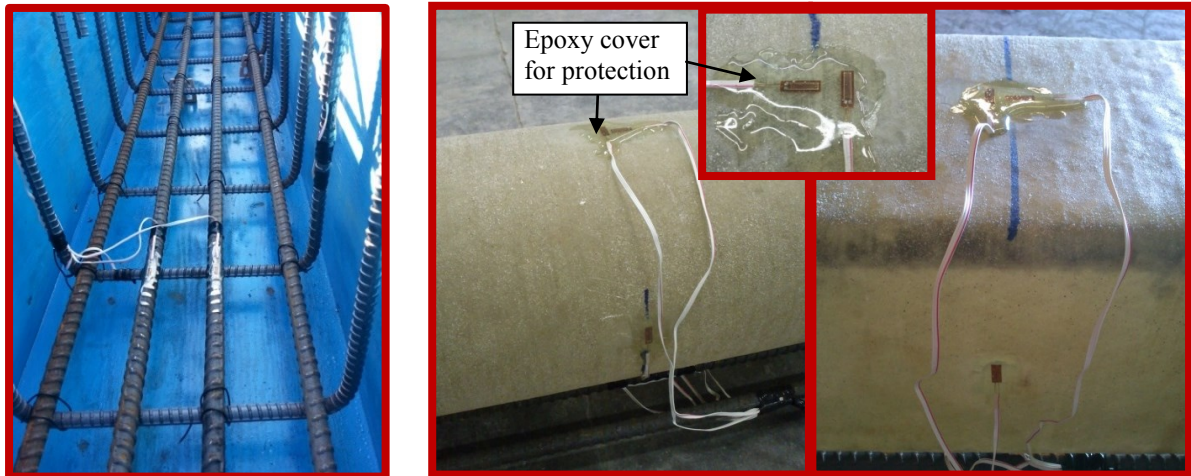
Figure 3.23 – DPs positions to measure deflection and slippage



(a) Top LVDT

(b) Bottom LVDT

Figure 3.24 – LVDTs to measure top and bottom axial strains



(a) Strain gages on steel bars

(b) Strain gages on inner tubes

Figure 3.25 – Strain gages on steel bars and inner tubes



(a) Axial and hoop strain on outer tube

(b) Strain rosette at middle of shear span

Figure 3.26 – Strain gages on outer tubes

CHAPTER 4

FLEXURAL BEHAVIOUR OF FULLY-CFFT RECTANGULAR BEAMS

Foreword

Authors and Affiliation

- Ahmed Abouzied: PhD candidate, Department of Civil Engineering, Sherbrooke University, Sherbrooke, Quebec, Canada, J1K 2R1.
E-mail: ahmed.abouzied@usherbrooke.ca
- Radhouane Masmoudi: Professor, Department of Civil Engineering, Sherbrooke University, Sherbrooke, Quebec, Canada, J1K 2R1.
E-mail: radhouane.masmoudi@usherbrooke.ca

Journal Title: Journal of Engineering Structures

Submitted at: January 2016.

Acceptance Status: in review.

Reference: A. Abouzied and R. Masmoudi, (2016). "Flexural behaviour of rectangular FRP-tubes filled with reinforced concrete: experimental and theoretical studies", *Elsevier Journal of Engineering Structures*, ENGSTRUCT-S-16-00088.

4.1 ABSTRACT

This chapter investigates experimentally and analytically the flexural behaviour of rectangular fully concrete-filled fiber-reinforced polymer (FRP) tube (CFFT) beams with steel rebar. Eight full-scale CFFT beams, 3200 mm long and $305 \times 406 \text{ mm}^2$ cross section, were tested under a four-point bending load and were compared to two control steel-reinforced concrete (RC) beams. The main objectives are to study the effect of several parameters as the outer tubes thickness and fiber laminates on the flexural behaviour of such hybrid FRP-concrete-steel beams. The experimental results indicate an outstanding performance of the CFFT beams in terms of strength and ductility compared to the RC beams since their flexural strength and ductility attained values 444% and 1432% higher than that of the RC beams, respectively. A strain compatibility/equilibrium model was developed to predict the moment-curvature response of the CFFT section addressing the issue of confinement and tension stiffening of concrete. The analytical results match well the experimental results in terms of moments, curvature, strains, and neutral axis location. Based on the model, the deflection can be predicted by integrating the curvatures along the span of the flexural member.

Keywords: Beams, Fiber-Reinforced Polymer, Filament-Wound, Concrete-Filled FRP Tubes, Flexural behaviour, Deflection.

4.2 INTRODUCTION

Fiber-reinforced polymer (FRP) composite materials have recently been used in the field of civil engineering constructions especially in corrosive environments. One of the innovative applications is the concrete-filled FRP tubes (CFFTs) which are becoming an alternative for different structural applications due to their high performance and durability. Extensive research was developed on CFFTs as columns [Mirmiran et al. 1998, 2001; Fam and Rizkalla 2001; Lam and Teng 2003, 2004; Hong and Kim 2004; Zhu et al. 2006; Teng et al. 2007; Ozbakkaloglu and Oehlers 2008a, 2008b; Mohamed and Masmoudi 2008a, 2008b, 2010a; Mohamed et al. 2010; Park et al. 2011; Abouzied et al. 2012b; Abouzied and Masmoudi 2012, 2013; Ozbakkaloglu 2013a, 2013b; Vincent and Ozbakkaloglu 2013; Idris and Ozbakkaloglu 2013; and others], but comparatively limited research was carried out on CFFTs as beams [Mirmiran et al. 2000; Doval et al. 2001; Fam and Rizkalla 2002; Cole and Fam 2006; Mohamed and Masmoudi 2010b, Fam et al. 2005; Yu et al. 2006; Zakaib and Fam 2012; Belzer et al. 2013] and most of them concentrated on the circular section more than the rectangular one. However, the rectangular section has higher moment of inertia than the circular section. Hence, it has higher flexural stiffness to resist the applied loads and deformations. Moreover, the construction and architectural requirements prefer the rectangular section of beams, rather than the circular beams, due to its stability during installation and its workability during connecting to other structural members like slabs and columns. To date, only two studies on the flexural behaviour of rectangular CFFT beams have been reported, Fam et al. (2005) and Belzer et al. (2013). However, none of them reinforced the rectangular CFFTs with steel rebar or analytically studied the deflection response of the composite section.

Most of the tested circular CFFT beams failed in compression [AASHTO 2012]. This compression failure was predominantly governed by the compression failure of the tube flange under longitudinal compressive stresses where the tensile hoop strains (i.e., confinement effect) were insignificant [AASHTO 2012]. This notice is based on flexural tests of circular CFFTs without steel reinforcement. More investigations are required to verify that notice on rectangular CFFTs with steel rebar. Unlike steel-or-FRP-RC beams, the

steel-reinforced CFFT beams can exhibit superior additional flexural capacities in the post-yielding stage [Abouzied and Masmoudi 2014, 2015a, 2015b, 2015c]. This is attributed to the confining action of the FRP tube on the concrete core to withstand higher strains, and the FRP tube reinforcement contribution in the axial direction, in addition to the reinforcement action of the steel bars in their plastic hardening status. New design equations are required to get benefit of the outstanding flexural capacity at the post-yielding stage, and simultaneously, equations to predict the expected deflection with reasonable accuracy.

Analytical models have been developed to predict the flexural capacity and load-deflection response for circular CFFTs [Cole and Fam 2006; Fam and Son 2008; Mohamed and Masmoudi 2010b]. These models are based on strain compatibility, internal forces equilibrium, and material constitutive relationships. The forces within the CFFT cross section were calculated by integrating the stress over the area of each individual material. Despite the limited number of tested specimens, these models predict well the flexural behavior of their circular CFFT beams. Their theoretical analysis depends mainly on a computer-based analysis and requires some sophisticated calculation procedures. Also, these proposed models require verification and adjustment to be valid for the rectangular CFFT beams, and need to be simplified to be applicable for engineers.

The main objective of this chapter is to investigate the experimental results of beam tests carried out on fully CFFT-beams in the current experimental program indicated in the previous Chapter 3. This objective is accomplished by expressing the experimental results of eight fully-CFFT beams that compared to two control RC beams. Further analysis and discussion were carried out to investigate the effect of each test variable as outer tubes thickness and laminates, and steel reinforcement. Also, this chapter attempts to establish a theoretical basis for the development of design procedure inspired by the North American design codes provisions.

4.3 EXPERIMENTAL PROGRAM

In this chapter, ten full-scale rectangular beams, including eight fully-CFFT beams and two conventional RC beams, were tested under a four-point bending load and compared together.

Table 4.1 presents the details of the beam specimens studied in this chapter. The detailed description of the experimental program was illustrated in Chapter 3.

4.4 TEST RESULTS AND DISCUSSIONS

The objective of this study is to evaluate the flexural behaviour of rectangular fully-CFFT beams with steel rebar. This objective was accomplished as the shear failure was avoided and all the tested beams failed at the pure flexure zone and the full composite action between the hybrid section structural components was accomplished to avoid any undesired slippage failure. Figure 4.1 plots the correlation between the applied moment and the slip at the two ends of the tested CFFT beams. Almost no slip readings between the concrete core and the tubes were recorded until the ultimate load, even after the ultimate failure the maximum slip measured did not exceed 0.2 mm, which can be neglected. Therefore, a full composite action was achieved. This is attributed to the roughened surface of the tubes by sand coating and the presence of the deformed steel bars with hooks that hold the concrete core in its place.

The applied moment was calculated by multiplying the concentrated load ($P/2$) with the shear span (a), while the deflection was measured at the mid-span. Although the concrete core was hidden behind the tubes surface and it was difficult to see the first crack, the cracking moment (M_{cr}) was evaluated from the readings of the steel strain and the curvature response change as shown in Figure 4.2. The experimental yielding moment (M_y) was evaluated from the yielding plateau of the moment-strain response of the embedded steel at the tension side as shown in Figure 4.2. Table 4.1 summarizes the beam test results as the flexural moments at the first crack, yield and ultimate moments, the ultimate mid-span deflection (at the peak), the failure mode, and the ductility. The ductility was evaluated by the energy absorption determined as the area under the moment-deflection curve until the peak load.

Generally, the two identical beams in each group behaved almost typically and their average results are used in the comparisons. The following sections provide detailed comparisons and discussions for the test results including the effect of the test parameters.

4.4.1 Shear Strength of Rectangular Fully-CFFT Beams

The fabricated filament-wound FRP tubes were designed to have adequate fibers in their transverse direction. Therefore, the tube itself acts as continuous shear reinforcement around the cross section perimeter of the CFFT beam. Accordingly, it was not applicable to add steel ties inside the CFFT section.

Although none of the CFFT beams failed in shear, the contribution of the FRP tube in resisting shear, V_f , can be approximately evaluated from the measured nominal shear force, V_n , at the ultimate flexural failure reduced by the concrete contribution in shear, V_c , which is calculated according to ACI-318 (2014), as indicated in Eq. 4.1 and Eq. 4.2.

$$V_f = V_n - V_c \quad (4.1)$$

$$V_c = 0.17\lambda\sqrt{f'_c} b_w d \quad (4.2)$$

In the current study, $b_w d$ is approximated as the area of the concrete core, A_c , and the factor λ equals the unit for the normal weight concrete.

Assuming a diagonal shear crack at 45° as shown in Figure 4.3, the shear resisting force in the FRP tube webs produces vertical tensile stresses in the FRP webs, F_f , which can be calculated as:

$$F_f = \frac{0.5V_f \cos 45^\circ}{t_f d_{eff}} \quad (4.3)$$

Where, d_{eff} is the effective straight depth of the rectangular GFRP tube web excluding the rounded corners.

Table 4.2 lists the shear forces calculations in the fully-CFFT beams. The calculated stresses in the outer FRP tube, F_f , were compared to the allowable tensile strength in the transverse direction of the rectangular GFRP tubes, F_{tr} , evaluated experimentally from the coupons tests (See Chapter 3, Table 3.1). The results indicate that the developed tensile stresses in the FRP

tubes due to the shear forces are relatively very low compared to the tensile strength of the FRP tubes in the transverse direction, since the ratio F_f / F_{tr} did not exceed 31%. These results indicate the effective shear reinforcement action of the filament-wound FRP tube.

4.4.2 Flexural Behaviour of the Control RC Beams

Figure 4.6 presents the typical failure pattern of the RC beams, which failed in tension under flexure. The first crack happened at an average moment 30.5 kN.m. Then, multiple vertical flexural cracks were formed especially at the pure moment zone and no complete diagonal cracks at the shear zone were noticed until yielding of the bottom steel reinforcement that happened at an average moment 114.5 kN.m. After yielding, the stiffness of the beam was almost dissipated resulting in a yielding plateau with almost no increase in the flexural strength. This plateau continued due to the plastic hardening of the steel. At the meantime, the compressive strain at the top extreme of concrete was increasing until crushing at maximum compressive strain 0.0035 corresponding to a mid-span deflection of 29 mm.

4.4.3 Failure Patterns of Fully-CFFT Beams

All the tested CFFT beams failed under flexure without any signs of shear failure, web buckling, or slippage between the concrete core and the tubes. The corners of the rectangular filament-wound FRP tubes indicated stability until the end of the tests without any separation. This gives an advantage point for the filament-wound FRP tubes in rectangular CFFT beams versus the pultruded FRP rectangular tubes that fail commonly due to corner separation as shown in Figure 4.4. The good failure performance of the filament-wound FRP tubes is attributed to existence of transverse fibers that eliminates buckling of the axial fibers and connects strongly the tube flanges with the tube webs preventing their separation at the corners. Accordingly, the flexural reinforcement action of the filament-wound tubes in their axial direction can be fully utilized until high levels of loading until the axial rupture of the fibers due to flexure. In contrast, the pultruded FRP tubes fail early at the corners eliminating the full utilization of the tube elements, flanges and webs, which are still active without any rupture as shown in Figure 4.4.

Based on this study, the filament-wound FRP tubes are recommended in rectangular CFFT beams more than the pultruded FRP tubes because:

- 1) The filament-wound FRP tubes control the strength of the tubes in both the axial and transverse direction by controlling the amount of flexural and shear reinforcement, in addition to its confining action.
- 2) The filament-wound FRP tubes improve the stability of the CFFT beams against any undesired secondary failure like shear failure and corners separation, which occurs commonly in the pultruded FRP tubes.

In the studied rectangular CFFT beams, insignificant micro surface cracks were formed in the matrix, as shown in Figure 4.5. However, these cracks were hard to be observed unless applying direct light on the tubes surface. These cracks were vertical with different heights according to their position along the beam length. In other words, their height is directly related to the moment profile along the beam span. They were formed when the matrix tensile stresses exceeds the maximum allowable stress of the resin matrix, which was 70 MPa according to the manufacturer data.

Figures 4.7 to 4.11 present the failure patterns and the moment-deflection response of the rectangular fully-CFFT beams OR2₃₀, OR4₃₀, OR8₃₀, OR12₃₀, and OR16₄₅.

The CFFT beams OR2₃₀, which have the least tube thickness of 3.4 mm, failed in tension under flexure with axial rupture of fibers at the tension side, as shown in Figure 4.7(c), with a sudden loss of the flexural strength.

The CFFT beams OR4₃₀, which have a tube thickness of 5.7 mm, experienced also a tension failure under flexure. However, there was inflate at the compression flange before failure load and minor signs of outward buckling as shown in Figure 4.8(b).

The failure of the CFFT beams OR8₃₀, which have a tube thickness of 8.7 mm, started with inflate followed by outward buckling of the compression tube flange with a limited drop in the flexural strength. Accordingly, the flexural stiffness decreased. Nevertheless, OR8₃₀ continued to resist the loads depending mainly on the tube bottom flange at the tension side

and the confined concrete at the compression side. Shortly thereafter, an axial rupture of fibers at the tension side happened with a sudden loss of the flexural strength, as shown in Figure 4.9(c).

The CFFT beam OR12₃₀, which has a tube thickness of 9.9 mm, failed in compression under flexure beginning with inflate followed by outward buckling of the compression tube flange with a limited drop of strength, but the beam could not resist any additional loads afterwards. Although the tension flange was still active, the strength was decreasing gradually. Meanwhile, a transverse rupture of fibers was increasing at the compression side. This may be attributed to the low percentage of the transverse fibers in the GFRP tube OR12₃₀ (two layers of 90° circumferential pattern). Finally, at high level of deformation and curvature, its tensile flange failed with axial rupture of fibers at the tension side with a significant drop of strength, as shown in Figure 4.10(c).

The CFFT beam OR16₄₅, which has the maximum tube thickness of 14.2 mm, failed in compression beginning with inflate and outward buckling of the compression tube flange with a limited loss of the flexural strength. The CFFT beam OR16₄₅ continued to resist the loads, but shortly thereafter, it failed in tension by axial rupture of fibers at the tension side, as shown in Figure 4.11(c). The failure pattern of OR16₄₅ could be considered similar to that of OR8₃₀.

Generally, rectangular CFFT beams with steel rebar fail gradually in a sequential manner (yielding of steel, buckling of compressed tube flange, and finally rupture of the fibers). It can be noticed that even after the ultimate failure, the reinforced CFFT beams keep a residual strength due to the existence of the steel that has a high plastic strain (see the horizontal yielding plateau after the ultimate in Figures 4.7, 4.8, and 4.9), unlike the FRP-concrete composite beams that commonly lose their flexural strength entirely after the failure of their FRP reinforcement elements.

Based on the noticed pattern of failure of the tested fully-CFFT beams, the CFFT beams OR2₃₀ and OR4₃₀ could be considered as under-reinforced beam section, while OR12₃₀ could be considered as over-reinforced beam section, while OR8₃₀ and OR16₄₅ could be considered

as balanced sections. Accordingly, the failure pattern of the fully-CFFT beams changes from tension to compression failure with increasing the FRP tube thickness. Note that, the laminates structure is also an important parameter beside the tube thickness.

4.4.4 Effect of Cycling Load

The beams were loaded under quasi-static loading in scheme of loading, unloading, and reloading cycles until failure, as shown in Figure 3.22 in Chapter 3. Note that the loading rate was constant for all loading and unloading cycles and equals 1 mm/min. The cycles depended on pre-expected deflection values at yielding of the embedded steel reinforcement, Δ_y . The beams were unloaded at $0.5\Delta_y$, Δ_y , $2\Delta_y$, and finally at $4\Delta_y$. The last loading cycle continues until failure. Despite the lower flexural stiffness and strength of the conventional RC beam compared to the CFFT beams, it behaved like the CFFT beams under the quasi-static loading. Before yielding of steel reinforcement (the first and second cycle), there was insignificant effect of unloading-reloading cycles at the fully-CFFT beams. Since, both steel and GFRP tube were still elastic. Note that, the unloading-reloading stiffness was almost the same and there were no gaps in the deflection response at the first and second cycles end. After yielding of the embedded steel and becoming plastic, the stiffness of the unloading-reloading cycles was decreasing gradually within the third and fourth cycle for each CFFT beams. At the third cycle, which occurred mostly before the ultimate failure, there was insignificant gap in the deflection response (< 1 mm). At the fourth cycles this gap increases to 3 to 4 mm, if the cycle occurs before the ultimate peak failure as shown in Figures 4.7, 4.8 and 4.11. This gap increases significantly if the cycle occurs after the ultimate peak failure as shown in Figure 4.10.

4.4.5 Flexural Performance of Fully-CFFT Beams

The objectives of the following sections are to highlight the performance of the rectangular fully-CFFT beams compared to the conventional RC beams. Further comparisons and discussion are illustrated to study the effect of steel reinforcement, FRP tube thickness, and fibers laminates structure in the fully-CFFT beams. To facilitate the analysis, the reloading cycles are eliminated from the curves and the outer envelopes are used in the comparisons.

Figure 4.12 indicates the effect of confining the conventional RC beams with filament-wound GFRP tubes, where it plots the moment-deflection responses of the fully-CFFT beams OR2₃₀, OR4₃₀, OR8₃₀, OR12₃₀, and OR16₄₅ compared to that of the RC beams which have the same cross section and tension steel reinforcement. The results of the tested rectangular fully-CFFT beams indicated the significant gain in strength, stiffness, and ductility compared to the RC beam. The results indicate that the yield moment M_y of the CFFT beams was significantly greater than that of the RC beam, and increases with increasing the FRP tube thickness. The ultimate flexural capacities (M_u) of the CFFT beams are very impressive. For example, the average M_u of the CFFT beams OR2₃₀, which have a tube thickness of 3.4 mm, attained 197% the flexural strength of the RC beams. While, M_u of the CFFT beam OR16₄₅, which has a tube thickness of 14.2 mm, attained 544% the flexural strength of the RC beams. The results indicate also that the ductility of the CFFT beams is significantly greater than that of the RC beam. For example, the ductility of the fully-CFFT beam OR16₄₅ attains about 15 times that of the RC beam.

The overall behaviour of the fully-CFFT beams is considered as nonlinear as shown in Figure 4.12. Before cracking, the beams start with a great flexural stiffness due to the massive gross sectional inertia. After the first crack and until yielding of the embedded reinforcement steel (pre-yielding stage), there was a difference in the flexural stiffness among the CFFT beams, due to the different thickness and stiffness of the GFRP tubes. After yielding of the steel bars (post-yielding stage), the flexural stiffness decreased, as expected, because of the low modulus of elasticity of the GFRP tubes material. Nevertheless, the flexural strength of the CFFT beams was increasing gradually until failure depending on the axial tensile strength of the GFRP tube at the tension side in addition to the hardened steel, and the compressive strength of both the confined concrete and the axial compressive strength of the GFRP tube flange at the compression side.

4.4.5.1 Effect of Steel Reinforcement in Fully-CFFTs

The results indicate that the hybrid steel-concrete-FRP composite system of the fully-CFFT beams made the behaviour of the rectangular CFFT beams to contain three stages, pre-cracking stage, post-cracking (pre-yielding) stage, and post-yielding stage. Even after the

ultimate failure, the results show that the CFFT beams can keep a residual strength because of the existence of the steel that has a high plastic strain.

Fam et al. (2005) studied rectangular filament-wound GFRP tubes with fiber stacking sequence of $[90^\circ, \pm 45^\circ_2, 90^\circ, \pm 45^\circ_2, 90^\circ]$ filled with concrete and their flanges were strengthened by additional four axial glass fiber sheets by hand layup technique. The tensile strength of their tubes web and flange was 152 and 315 MPa, respectively. They tested two CFFT beams completely filled with concrete, B1 and B3, but the beams had different cross section area. B1 had a cross section area of $266 \times 374 \text{ mm}^2$, while B3 had a cross section area of $164 \times 271 \text{ mm}^2$. B1 is chosen to be compared with the tested CFFT beams in the current study due to its cross section dimension and FRP reinforcement ratio are close to the current study. This aims to study the effect of steel reinforcement on the flexural behaviour of rectangular CFFT beams. The comparison is carried out by comparing the moment-curvature ($M-\psi$) responses of the CFFT beams, as shown in Figure 4.13, since the compared beams have different size and spans. The moment was normalized with respect to the width B and the depth H of the cross section, while the curvature, which is calculated from the axial strains along the beam depth, was normalized with respect to the depth H .

Despite the steel reinforcement ratio (ρ_s) is comparatively small in this study, Figure 4.13 shows that providing the CFFT section with steel rebar increased significantly the initial flexural stiffness of the CFFT beams compared to Fam et al. (2005). In addition, there is ascending strength at the post-yielding of the reinforced CFFT beams. That means for the same flexural strength the hybrid section will have smaller deflection compared to the section that contains FRP tube only. This behaviour is obviously seen when comparing the CFFT beam OR8₃₀ to B1, since the two beams have almost the same FRP ratio (ρ_f).

The results of the CFFT beam OR8₃₀ compared to B1 of Fam et al. (2005) indicate also that the failure of the fully-CFFT beams occurs once the curvature (or the axial strains) attains a maximum allowable value. For example, if only the steel rebar increases in OR8₃₀, it can be proposed that (see Figure 4.14):

- 1) The initial flexural stiffness will increase at the pre-yielding stage.

- 2) The yield moment will increase.
- 3) The flexural stiffness will remain the same at the post-yielding stage.
- 4) The ultimate flexural strength will increase.
- 5) The ultimate failure will occur at the same curvature value as in the current study.

4.4.5.2 Effect of Outer Tube Laminate Structure

The effect of outer tube laminate structure is investigated by comparing the flexural results of the CFFT beams OR12₃₀ and OR16₄₅ as shown in Figure 4.12. OR16₄₅ has fibers orientation angle of 45°, while OR12₃₀ has fibers orientation angle of 30°. Moreover, OR16₄₅ has more fibers layers and higher tube thickness compared to OR12₃₀. See Table 3.1 in Chapter 3 for more details about the fibers laminate structure.

The results indicate that the primary flexural stiffness of OR16₄₅ is slightly smaller than that of OR12₃₀, but after yielding, the flexural stiffness of OR16₄₅ is significantly affected by its fiber laminates structure and become significantly lower than that of OR12₃₀. However, OR16₄₅ attained higher flexural strength than OR12₃₀. The results indicate also a clear nonlinear behaviour of OR16₄₅ at the post-yielding stage compared to that of OR12₃₀. To interpret those results, the coupons test results of these two CFFT beams should be discussed as shown in Figure 4.15. As seen in Figure 4.15, increasing the fibers orientation angle from 30° to 45° reduced the axial strength and the modulus of elasticity of the FRP tube material. The lower modulus of elasticity of OR16₄₅ interprets the lower flexural stiffness of the CFFT beam OR16₄₅ especially at the post-yielding stage compared to that of OR12₃₀. In addition, the nonlinear behaviour of OR16₄₅ coupons causes its flexural behaviour to be obviously nonlinear more than that of OR12₃₀. Of course, the effect of the FRP tube material becomes more significant at the post yielding stage, because at this stage, the contribution of the FRP tube is more significant compared to the other structural elements in the section (crushed concrete and hardened steel).

At the post yielding stage, the FRP tube strength and stiffness governs the flexural capacity and behaviour the CFFT beams. In other words, the compressive strength besides the buckling resistance of the tube compression flange can govern the ultimate strength, or the

tensile strength of the tube tension flange can govern the ultimate strength, whichever is reached first. The axial internal force of the FRP tube can be calculated by multiplying the ultimate axial stress of the coupons (F_{lo}) with the cross section area of the tube flange ($b \times t_f$). It was found that the calculated axial force of OR16₄₅ is lower than that of OR12₃₀. So, what is the reason that OR16₄₅ attained higher flexural strength? The author thinks that the high thickness and the excessive fibers in the transverse direction of OR16₄₅ resisted the buckling of the compression flange and permitted it to withstand higher compressive strains and consequently higher flexural strength than OR12₃₀. However, the tube OR12₃₀, which has higher axial strength and tube thickness of 9.9 mm, failed early once the buckling occurred at the compression flange of the tube. Note that, OR12₃₀ has two layers only of transverse fibers at 90° circumferential pattern causing early buckling of the axial fibers at the compression flange. Accordingly, it can be concluded that buckling of the compression flange governs the ultimate capacity of the over-reinforced CFFT beams.

4.4.5.3 Effect of Outer Tube Thickness

To study the effect of increasing the outer tube thickness, the comparison will concentrate on the results of the fully-CFFT beams OR2₃₀, OR4₃₀, OR8₃₀, and OR12₃₀ excluding OR16₄₅ to eliminate the buckling resistance. The results indicate the significant gain in strength, stiffness, and ductility of the rectangular fully-CFFT beams compared to the conventional RC beams (see Table 4.1). For example, confining the RC beam with a tube of 3.4 mm thickness, as in OR2₃₀, enhanced the ultimate flexural strength and ductility by 97% and 297% higher than that of the RC beam, respectively. The CFFT beams OR4₃₀, which have a tube of 5.7 mm thickness, attained ultimate flexural strength and ductility 204% and 694% higher than that of the RC beam, respectively. The CFFT beams OR8₃₀, which have a tube of 8.7 mm thickness, attained ultimate flexural strength and ductility 327% and 1052% higher than that of the RC beam, respectively. While, the CFFT beam OR12₃₀, which has the maximum tube thickness of 9.9 mm, attained an ultimate flexural strength and ductility 344% and 465% higher than the RC beam, respectively. As seen in OR12₃₀, the gain decelerated in strength and decreased in ductility. It can be concluded that the ductility increases with increasing the tube thickness until reaching a limit between under-and-over-reinforced sections. After this limit, the flexural strength and the ductility decrease due to the

compression failure of the fully-CFFT beam. It is evident that the compression failure of the compression tube flange governs the enhancement in strength and ductility in the fully-CFFT beams. This behaviour is illustrated in Figure 4.16, which plots the correlations between the flexural moments at different stages (first crack, yield, ultimate) compared to the normalized strength of the FRP tubes represented by their reinforcement ratio $\rho_f (=A_f/A_c)$ multiplied by their modular ratio $n_f (=E_f/E_{co})$. Note that, E_f is taken as the average modulus of elasticity from the compression and tension coupons tests in the axial direction of the GFRP tubes.

The results of M_{cr} , shown in Table 4.1, indicate minor difference among the fully-CFFT beams and the average M_{cr} of them is 45.8 kN.m. While, M_y of the fully-CFFT beams is significantly greater than that of the RC beam, and increases with increasing the FRP tube thickness. Figure 4.16(a) indicates a linear increase of M_y with increasing the tube thickness. It is rational due to the excess contribution of the elastic GFRP tube material as flexural reinforcement in the cracked section.

Figure 4.16(b) indicates a non-linear increase of M_u until a certain limit that separates the under-and-over-reinforced sections. This limit is also clearly shown in Figure 4.16(c), which mainly represents the post yielding stage by comparing M_u/M_y to the tube strength where at this stage the reinforcement action of the GFRP tube is effective and significant. This limit is close to the results of OR8₃₀ confirming its balanced failure behaviour. Note that, the buckling of the tube compression flange affects the flexural capacity and eliminate the confinement efficiency. This non-linear response indicates that increasing the thickness of the tube does not mean increasing the ultimate capacity of the CFFT beam, but there is an optimum FRP reinforcement ratio and fibers distribution to achieve the maximum capacity.

This optimum ratio is near to the results of OR8₃₀ where $\rho_f = 10\%$ and $\frac{\text{Axial fibers}}{\text{Transverse fibers}} = \frac{1}{1}$.

Figure 4.16 shows also the results position of the fully-CFFT beam OR16₄₅ that has a GFRP tube thickness of 14.2 mm. However, this thickness is non-practical because of the high cost of the GFRP tubes. The results of OR16₄₅ at the first crack-to-yield stage (pre-yielding stage), shown in Figure 4.16(a), indicate compatibility with the other beams results. It is rational, because the flexural strength at this stage depends on the tensile strength of steel

rebar and the GFRP tube and there have not been buckling or confinement yet. On the other hand, Figures 4.16(b, c) indicate the non-compatibility of OR16₄₅ results with the other CFFT beams. It is attributed to the high gain in the flexural strength of OR16₄₅ due to the resistance of the early buckling of the compression flange ($\frac{\text{Axial fibers}}{\text{Transverse fibers}} = \frac{1}{1.3}$).

Based on the results of the current study and shown in Figure 4.16, the flexural moments at different stages (first crack, yield, and ultimate) could be estimated by regression analysis if one of them is known, for example M_{cr} , as following:

$$M_y = M_{cr} [30.32(\rho_f n_f) + 2.85] \quad (4.4)$$

$$M_u = M_{cr} [-3543.47(\rho_f n_f)^2 + 430.33(\rho_f n_f) - 1] \quad (4.5)$$

$$M_u = M_y [-1001.93(\rho_f n_f)^2 + 100.73(\rho_f n_f) + 0.18] \quad (4.6)$$

4.4.6 Cracking Moment of Rectangular Fully-CFFT Beams

One of the advantages of the CFFT system is that the outer FRP tube acts as a jacket that protects the inner structural elements, such as concrete and steel, against corrosion even if the inner concrete core is cracked. Therefore, there is no worry about the concrete cracks for the durability and appearance requirements. However, it is important for effective design of FRP-concrete composite structure to study the cracking behaviour for serviceability requirements related to deflection and crack width control. Therefore, the cracking moment (M_{cr}) is evaluated for the current study of rectangular fully-CFFT beams. Although the concrete core was hidden behind the tubes surface and it was difficult to see the first crack, the cracking moment (M_{cr}) was evaluated from the readings of the steel strain, bottom strains of the FRP tube, or the curvature response change as shown in Figure 4.2. The results of M_{cr} indicate minor difference among the fully-CFFT beams with changing their tube thickness, and the average M_{cr} of them is 45.8 kN.m, which is greater than that of the RC beam by 51%. This increase could be attributed to many factors:

- 1) The FRP tubes contributed positively in the gross section inertia I_g , however, this contribution is comparatively limited due to the low FRP modular ratio,

- 2) The full composite action (the bond) due to the roughened tubes surfaces delayed the generation of the cracks,
- 3) The concrete expansion during curing was restrained by the tube inducing chemical pre-stressing on the concrete [Fam and Rizkalla 2002], and
- 4) Confining the concrete with FRP tubes restrained it against crack propagation.

Table 4.3 presents analysis of the experimental results at the first crack of the rectangular fully-CFFT beams. This analysis seeks to estimate accurately the cracking capacity of such type of beams, and consequently the yield and ultimate capacity can be estimated approximately by Eq. (4.5) and Eq. (4.6), respectively. The experimental M_{cr} and the moment of inertia of the gross transformed section, I_g , were used to develop an expression for the modulus of rupture of concrete (f_{cr}) using the following equations:

$$I_g = I_c + (n_s - 1)I_s + n_f I_f \quad (4.7)$$

$$f_{cr} = M_{cr} Y_t / I_g \quad (4.8)$$

Where I_c , I_s , and I_f are the local moment of inertia of the concrete, steel, and FRP tube, respectively. Y_t is the distance of the extreme tension fiber of concrete from the centroid. n_s is the steel modular ratio ($n_s = E_s/E_{co}$), while n_f is the FRP modular ratio ($n_f = E_f/E_{co}$). E_s is the elasticity modulus of steel that equals 200 GPa. E_{co} is the elasticity modulus of concrete calculated as $E_{co} = 4500\sqrt{f'_c}$. E_f is the elasticity modulus of the FRP tube, which is approximated as the average of the axial elasticity modulus in tension and compression.

The North American codes as ACI building code ACI-318 (2014), Canadian code CSA-S806 (2012), and CSA-S6 (2014) use Eq. (4.9) to predict the modulus of rupture of concrete. They also recommend calculating I_g for concrete section only neglecting reinforcement. The coefficient k equals 0.62 in ACI-318, while it equals 0.6 and 0.4 in the Canadian codes CSA-S806 and CSA-S6, respectively.

$$f_{cr} = k\lambda\sqrt{f'_c} \dots (\lambda = 1.0 \text{ for normal-weight concrete}) \quad (4.9)$$

Based on the North American codes formula, the coefficient k can be estimated for each beam based on the experimental f_{cr} and f'_c as shown in Eq. (4.10). Note that, the analysis considers the gross moment of inertia considering the total section elements (concrete + steel + tube) transformed to concrete, $I_{g(Total)}$, and the gross moment of inertia for concrete only neglecting reinforcement, $I_{g(Conc.)}$.

$$k = f_{cr} / \sqrt{f'_c} \quad (4.10)$$

The results in Table 4.3 indicate that an average value of $k = 0.8$ can be proposed in case of calculating $I_{g(Conc.)}$ for concrete section only neglecting reinforcement. This value is about 30% higher than the values proposed by the codes ACI-318 and CSA-S806, and 100% higher than the value proposed by the code CSA-S6. This indicates high cracking strength of the CFFT beams. Note that, the average proposed value for k is 0.69 in case of considering all reinforcement and tubes in calculating $I_{g(Total)}$.

Table 4.4 presents comparisons between the experimental results of M_{cr} and the predicted values of M_{cr} based on the American code ACI-318. The predicted results of M_{cr} indicate that the ACI assumption to neglect the reinforcement in calculating I_g underestimates the experimental results and is very conservative compared to considering reinforcement in calculating I_g . Accordingly, it is recommended to consider the reinforcement in calculating I_g . Rationally, this conclusion is also investigated for the other two Canadian codes since their coefficient k is lower than that of the ACI building code.

To date only two studies investigated the cracking strength of CFFTs, Fam and Rizkalla (2002) and Mohamed and Masmoudi (2010b), however they tested circular CFFT beams. Fam and Rizkalla (2002) evaluated $k = 1.0$ based mainly on the experimental results of large-scale circular CFFT beams without reinforcement. While Mohamed and Masmoudi (2010b) evaluated $k = 0.94$ based on experimental investigation on the flexural behaviour of circular CFFT beams with a diameter of 213 mm and were reinforced with steel or FRP bars with high reinforcement ratios. Note that, both previous literatures calculated the coefficient k based on the gross moment of inertia of the transformed section including reinforcement and FRP tube. By applying the k values of their tests, the predicted results overestimate the

current experimental results as shown in Table 4.4. Based on the results in the current study, a value for $k = 0.69$ was assumed in case of calculating the gross moment of inertia for the total section elements (concrete + steel + FRP tube) transformed to concrete. As seen, there is a difference in the coefficient k value compared to the literatures. Accordingly, it can be concluded that the value of the coefficient k depends on different parameters as:

- 1) The cross section size. Where, the small size has higher cracking strength due to the effective confinement of the tube and the higher reinforcement ratio ($A_{tube}/A_{concrete}$).
- 2) The section shape. Where, the rectangular section has a higher gross inertia, compared to the circular section, and consequently a lower cracking strength for the same M_{cr} .
- 3) The reinforcement ratio including the compression reinforcement and the FRP tube.
- 4) The fiber laminates that governs the FRP tube axial stiffness.
- 5) The roughness of the tube surfaces adjacent to the concrete. In other meaning, the bond between the concrete and the tube.

4.5 ANALYTICAL MODELLING OF RECTANGULAR CFFT BEAMS UNDER FLEXURE

Unlike steel-or-FRP-RC beams, the steel-reinforced concrete-filled FRP tube (CFFT) beams can exhibit superior additional flexural capacities in the post-yielding stage. This is attributed to the confining action of the FRP tube on the concrete core to withstand high strains, and the FRP tube reinforcement contribution in the axial direction, in addition to the reinforcement action of the steel bars in their plastic hardening status. The expected failure types of CFFT beams are: (1) tension failure by axial rupture of fibers at the tension side due to exceeding the allowable axial tensile strains at the tension side of the FRP tube, (2) compression failure by transverse rupture of fibers at the compression side due to confining the concrete, or (3) compression failure due to buckling of FRP tube flange under the axial compressive strains.

Analytical models have been developed to predict the flexural capacity and load-deflection response for the circular CFFTs [Fam 2000; Cole and Fam 2006; Fam and Son 2008; Mohamed and Masmoudi 2011]. These models are based on strain compatibility, internal forces equilibrium, and material constitutive relationships. The forces within the CFFT cross

section were calculated by integrating the stress over the area of each individual material. Despite the limited number of their tested specimens, these models predict well the flexural behaviour of their circular CFFT beams. Their theoretical analysis depends mainly on a computer-based analysis and requires some sophisticated calculation procedures. Also, these proposed models require verification and adjustment to be valid for the rectangular CFFT beams, and need to be simplified to be applicable for engineers.

Based on many research on circular CFFT beams that failed in compression, the compression failure was predominantly governed by the compression failure of the tube flange under longitudinal compressive stresses where the tensile hoop strains (i.e., confinement effect) was insignificant [AASHTO 2012]. Accordingly, AASHTO (2012) proposed the unconfined stress-strain relationship of concrete proposed by Popovics (1973) with an extended strain softening beyond the usual ultimate compressive strain to be used in calculating the ultimate moment capacity of circular CFFTs based on equilibrium and strain compatibility. However, the experimental results in this dissertation indicate that some rectangular CFFT beams that failed in compression pronounced confinement issues at the compression side. Accordingly, AASHTO assumption about neglecting confinement in CFFTs needs to be verified in case of rectangular CFFT beams.

In the following sections, analytical study has been developed to predict theoretically the moment-curvature response of the fully-CFFT beams. Then, the curvatures along the span of the beams are integrated to predict the deflection. The analytical model accounts for the material non-linearity and tension stiffening of concrete in the tension side. In addition, the model addresses the confinement of concrete in the compression side. Comparison between the experimental results and the theoretical results have been carried out in terms of moment-curvature response, moment-deflection response, strain profile along the beam depth, and the neutral axis position.

4.5.1 Description of the Analytical Model

An analytical model based on strain compatibility/equilibrium was developed to predict theoretically the flexural behaviour of rectangular CFFT beams as shown in Figure 4.17. The

cross section is assumed as a complete rectangular section neglecting the round corners. The overall section width is $B = b + 2t_f$ and the overall section height is $H = h + 2t_f$ where b and h are the inner section width and height, respectively. The effective width of the tube flange is b , while the effective height of the tube web is h . The model is based on the assumption that plain sections remain plain after deformation, which means linear strain distribution along the depth of the CFFT section subjected to bending. This model assumes also full bond between the concrete core, steel bars, and the GFRP tubes (no slip). The bottom strain, ε_{bot} , is related to the axial tensile strain of the GFRP tube. While the top strain, ε_{top} , is related to the axial compressive strains of the GFRP tube. The stresses in the GFRP tube are based on the stress–strain curves obtained from the coupon tests. The model assumes a linear behaviour of the FRP tube in both tension and compression. Two models for concrete in compression are examined in this study, unconfined and partially confined models. In addition, the tensile strength and tension stiffening of concrete in tension are considered. A cracked section analysis is performed using a layer-by-layer approach for the non-linear materials (concrete) in order to sum the forces along the cross-section depth using numerical integration. The depth of the compression zone, c , is the distance between the neutral axis and the inner edge of the tube top flange. By assuming c and the strains at any level (steel level or tube top and bottom faces), the internal tension and compression forces along the cross section can be determined. This iterative process is continued until equilibrium of the tension and compression forces is achieved. Then, the nominal theoretical moment (M_{th}) can be determined by calculating the total moments of the internal forces around the neutral axis. More details about the materials models and calculations are illustrated in the following sections.

4.5.2 Constitutive Relationships of Materials

4.5.2.1 Steel Model

The steel was modeled by a bilinear model in two parts: (1) a linear elastic part up to the yield strain ($\varepsilon_s = f_y / E_s = 0.0023$), (2) a yield plateau up to the ultimate plastic strain with a zero plastic hardening elasticity modulus, as shown in Figure 4.18. Based on tensile tests on steel bars in Chapter 3, the yield strength of steel, f_y , equals 467 MPa, the modulus of

elasticity equals 200 GPa, and the maximum hardening strain is 0.16. The internal tension force in steel, T_s , is calculated as:

$$T_s = E_s \cdot \varepsilon_s \cdot A_s \quad (4.11)$$

Where $E_s \cdot \varepsilon_s \leq f_y$ and it acts at a distance from the neutral axis, YT_s , equals:

$$YT_s = d - c \quad (4.12)$$

4.5.2.2 FRP Tube Model

The parts of the rectangular FRP tube above and below the neutral axis were considered effective in resisting the compression and tension forces, respectively. The stress-strain response of the GFRP tubes obtained from coupon tests reflected a nonlinear stress-strain response as shown in Appendix A. Nonlinearity could result from the multilayer laminate, the fiber orientation, stacking sequence, that lead to a progressive laminate failure, and resin, which is a nonlinear material. For easy analysis, a linear stress distribution for the FRP material was assumed with maximum limits for strength and strains as shown in Figure 4.19. The upper limits for the strength and strains equal F_{lo} and ε_{lo} , which were obtained from coupons test results given in Table 3.1 in Chapter 3. Note that, these limits are different in tension and compression. Accordingly, the secant modulus was used to model the FRP tube as follow:

$$E_{ten} = \frac{F_{lo(ten)}}{\varepsilon_{lo(ten)}} \quad (4.13)$$

$$E_{comp} = \frac{F_{lo(comp)}}{\varepsilon_{lo(comp)}} \quad (4.14)$$

Where, E_{ten} is the secant modulus of the FRP tube in tension and E_{comp} is the secant modulus of the FRP tube in compression.

Due to assumption of linear stress distribution and the regular geometry of the tube flanges and webs, the internal forced can be integrated directly without dividing it to layers as follow.

The internal compression force in the tube flange, $C_{Tube\ flange}$, is calculated as:

$$C_{Tube\ flange} = bt_f E_{comp} \left(\frac{\varepsilon_{cc} + \varepsilon_{top}}{2} \right) \quad (4.15)$$

Where, $E_{comp} \left(\frac{\varepsilon_{cc} + \varepsilon_{top}}{2} \right) \leq F_{lo(comp)}$. This force act at a distance from the neutral axis equals:

$$YC_{Tube\ flange} = c + \frac{t_f}{2} \quad (4.16)$$

The internal compression force in the tube two webs, $C_{Tube\ webs}$, is calculated as:

$$C_{Tube\ webs} = ct_f E_{comp} \varepsilon_{cc} \quad (4.17)$$

Where, $E_{comp} \varepsilon_{cc} \leq F_{lo(compression)}$. This force act at a distance from the neutral axis equals:

$$YC_{Tube\ webs} = \frac{2c}{3} \quad (4.18)$$

The internal tension force in the tube flange, $T_{Tube\ flange}$, is calculated as:

$$T_{Tube\ flange} = bt_f E_{ten} \left(\frac{\varepsilon_{bot} + \varepsilon_{ct}}{2} \right) \quad (4.19)$$

Where, $E_{ten} \left(\frac{\varepsilon_{bot} + \varepsilon_{ct}}{2} \right) \leq F_{lo(ten)}$. This force act at a distance from the neutral axis equals:

$$YT_{Tube\ flang} = h - c + \frac{t_f}{2} \quad (4.20)$$

The internal tension force in the tube two webs, $T_{Tube\ webs}$, is calculated as:

$$T_{Tube\ webs} = (h - c)t_f E_{ten} \varepsilon_{ct} \quad (4.21)$$

Where, $E_{ten} \varepsilon_{ct} \leq F_{lo(ten)}$. This force act at a distance from the neutral axis equals:

$$YT_{Tube\ webs} = \frac{2}{3}(h - c) \quad (4.22)$$

4.5.2.3 Concrete Model

Two models for concrete in compression are examined in this study as shown in Figure 4.20. The first concrete model is an unconfined concrete model with extended strain softening using Popovics's model (1973) as suggested by AASHTO (2012). This model was suggested due to its accurate representation of the material nonlinearity. Popovics's model to get the compressive stress f_c at corresponding strain ε_c is indicated as follow:

$$f_c = \frac{f'_c (\varepsilon_c / \varepsilon'_c)^r}{r - 1 + (\varepsilon_c / \varepsilon'_c)^r} \quad (4.23)$$

Where, f'_c is the unconfined compressive strength of concrete cylinders, r is a factor given as:

$$r = \frac{E_{co}}{E_{co} - E_{sec}} \quad (4.24)$$

Where E_{sec} is the secant modulus of concrete determined as:

$$E_{sec} = \frac{f'_c}{\varepsilon_c} \quad (4.25)$$

E_{co} is the tangent modulus of concrete ($E_{co} = 4500\sqrt{f'_c}$). The maximum compressive strain ϵ'_c is taken as 0.002 based on the compressed cylinder test results as mentioned in Chapter 3.

The second concrete model is a partially confined concrete model, which is based on a function similar to the Popovics's model up to f'_c followed by plastic behaviour with constant compressive strength f'_c as shown in Figure 4.20. This model was chosen to present intermediate level of confinement that is adequate for beams, instead of full confinement models that are adequate for columns.

The experimental results of the CFFT beams indicated enhancement in the tensile strength of concrete, which is attributed to many factors as the roughness of the FRP tube that eliminated the cracks propagation and the pre-stressing action of the tubes on the concrete during curing process. Accordingly, it is suggested to consider the tensile strength and tension stiffening for concrete in the model. The tensile strength of concrete, f_{cr} , is determined as:

$$f_{cr} = 0.62\sqrt{f'_c} \text{ (MPa)} \quad (4.26)$$

The corresponding tensile strain, ϵ_{cr} , is determined as:

$$\epsilon_{cr} = \frac{f_{cr}}{E_{co}} \quad (4.27)$$

For $\epsilon_c \geq \epsilon_{cr}$, the model proposed by Collins and Mitchell (1997) has been adopted as follows:

$$f_c = \frac{\alpha_1 \alpha_2 f_{cr}}{1 + \sqrt{500(\epsilon_c - \epsilon_{cr})}} \quad (4.28)$$

α_2 is a factor accounting for the nature of loading and was taken as 0.7 for repeated loading. α_1 is a factor accounting for the bond characteristics. The bond factor ranges in value from zero to 1.0, where zero indicates unbonded reinforcement and the tension stiffening is completely ignored, while 1.0 indicates the maximum level of tension stiffening due to a

perfectly bonded reinforcement [Collins and Mitchell 1997]. Accordingly, α_l was taken as 1.0 because of the full composite action achieved in the tested CFFT beams.

Due to non-linearity of the concrete material in compression and in tension, the concrete parts above and below the neutral axis are divided into n number of strips, which have the same thickness h_i . Where $h_i = c / n$ for the strips in the compression zone and $h_i = (h - c) / n$ for the strips in the tension zone. Note that, increasing the numbers of strips, n , increase the accuracy of the model. The centroid of each strip, i , is located at its mid-thickness. Then, the distance from each compression strip to the neutral axis, YC_i , and the distance from each tension strip to the neutral axis, YT_i , are calculated as:

$$YC_i = \frac{c}{n}(i - 0.5) \dots\dots \text{for strips in the compression zone} \quad (4.29)$$

$$YT_i = \frac{h - c}{n}(i - 0.5) \dots\dots \text{for strips in the tension zone} \quad (4.30)$$

The strain at mid-thickness of each strip is calculated as:

$$\varepsilon_{ci} = \varepsilon_{cc} \frac{YC_i}{c} \dots\dots \text{for strips in the compression zone} \quad (4.31)$$

$$\varepsilon_{ti} = \varepsilon_{ct} \frac{YT_i}{h - c} \dots\dots \text{for strips in the tension zone} \quad (4.32)$$

These strain values are retrieved in Eq. 4.23 and 4.28 to obtain the corresponding compressive stress or tensile stress in concrete, respectively. The internal compression or tension force, C_{ci} or T_{ci} , inside each strip is calculated as:

$$C_i = f_{ci} b h_i \dots\dots (f_{ci} \text{ from Eq.4.23}) \quad (4.33)$$

$$T_i = f_{ti} b h_i \dots\dots (f_{ti} \text{ from Eq.4.28}) \quad (4.34)$$

The total compression and tension forces of the concrete are calculated as:

$$C_c = \sum_{i=1}^{i=n} C_i \quad (4.35)$$

$$T_c = \sum_{i=1}^{i=n} T_i \quad (4.36)$$

4.5.3 Procedure of Analysis

The internal tension and compression forces along the cross section and their distances from the neutral axis are arranged in Table 4.5. The procedure of analysis can be summarized in the following steps:

- 1) Specify the tube dimensions, thickness, material properties, location and area of rebar, and number of concrete strips, n .
- 2) Assume a value for the compressive strain at the top face of FRP tube, ε_{top} .
- 3) Assume a value for the compression zone depth c .
- 4) Calculate the strains at steel rebar (ε_s), top face of concrete (ε_{cc}), bottom face of concrete (ε_{ct}), and the bottom face of the FRP tube (ε_{bot}). Note that, the yield of rebar occurs if ε_s exceeds the allowable yield strain of the steel. Tension failure of the CFFT beam occurs if ε_{bot} exceeds the allowable tensile strains of the FRP coupons in the axial direction. Compression failure of the CFFT beam occurs if ε_{top} exceeds the allowable compressive strains of FRP coupons in the axial direction.
- 5) For each concrete strip in compression or tension, compute the strains at its mid-thickness (ε_{ci} or ε_{ti}) and the corresponding compressive or tensile stresses.
- 6) Calculate the total compressive and tensile forces in concrete, rebar, and FRP tube.
- 7) Check for equilibrium by satisfying the condition that the absolute value of the difference between the total compression force and the total tension force is less than the allowable tolerance accepted for the difference ($\Sigma C = \Sigma T$).
- 8) If the equilibrium is not satisfied, go to step 3 and assume another value for c . The process is repeated until the equilibrium is satisfied.
- 9) Once the equilibrium is satisfied, the internal moments are calculated for all the internal forces around the neutral axis as $M_{theo} = \Sigma(F_i \cdot Y_i)$, and the corresponding

$$\text{curvature is calculated as } \psi = \frac{\varepsilon_{top}}{c + t_f}.$$

- 10) Go to step 2 to enter a new strain value for ε_{top} and repeat the process till the complete moment-curvature response is constructed.

Once the moment-curvature response of the section ($M-\psi$) is obtained, the moment-deflection response of the member ($M-\Delta$) can be estimated. The deflection is calculated by integrating the curvatures along the span using the moment-area method. For a four-point bending, it is given by the following equation:

$$\Delta = \iint \psi dx dx = \frac{\psi}{24} (3L^2 - 4a^2) \quad (4.37)$$

Where L is the span between the supports and a is the shear span.

The previous steps were easily developed in a spreadsheet as shown in Appendix B.

4.5.4 Verification of the Model

This section presents the predicted flexural behaviour in terms of moment-curvature, moment-deflection, and moment-strain behaviour as well as the neutral axis depth for the fully-CFFT beams OR2₃₀, OR4₃₀, OR8₃₀, and OR12₃₀.

The effect of using the unconfined or confined concrete models can be investigated from Figure 4.21. It plots the predicted versus the experimental neutral axis depth of the CFFT considering the unconfined and confined concrete material models as well as tension stiffening being considered or ignored.

Despite considering or ignoring the tension stiffening of concrete, the partially confined model of concrete indicates good prediction for the flexural behavior of the tested CFFT beams. While, the unconfined concrete model can be used only in the FRP tubes that have small tube thickness. For example, the CFFT beam OR2₃₀, which has a tube of 3.4 mm thickness, the response of the unconfined and confined concrete model was identical until the ultimate predicted moment in spite of considering or ignoring the tension stiffening. In the CFFT beam OR4₃₀ that has a tube of 5.7 mm thickness, the predicted response using the unconfined concrete model matches that uses the partially confined model until

approximately 90% of the ultimate moment. In the CFFT beams OR8₃₀ and OR12₃₀, the response that uses the unconfined concrete model was not able at all to predict well their flexural response and deviates from the experimental results at about 60% of the ultimate moments. These theoretical results confirm the experimental results indicated in Figure 4.22 that indicates excessive transverse strains at the top face of the CFFT beams OR8₃₀ and OR12₃₀ proving the confinement presence unlike the CFFT beams OR2₃₀ and OR4₃₀.

Until yield (pre-yielding stage), both unconfined and confined concrete model give the same results since the confinement has not been activated yet ($\varepsilon_{top} < \varepsilon'_c$). This is confirmed by the calculated and the experimental compressive strains at the top face of the tubes since they do not exceed 0.0012. In addition, the experimental transverse strains do not exceed Poisson's ratio effect as shown in Figure 4.22. Table 4.6 lists the theoretical and experimental yield moments of the CFFT beams and the tension stiffening of the concrete is considered or ignored. The predicted yield moments are in good agreement with the experimental results. However, the tension stiffening of concrete indicates a minor effect on the theoretical yield moments. The results indicate that the tension stiffening contribution is directly proportional to the FRP tube thickness. This contribution can be considered in thick tubes, and should be ignored in thin tubes. It is attributed to the thick tubes confine well the inner concrete core and prevent it from excessive cracks unlike the thin tubes. In general, ignoring the tension stiffening of concrete in the pre-yielding stage underestimates the experimental results and achieves safe design. Figure 4.23 indicates the good agreement of the theoretical versus experimental yield moments.

At post-yielding stage, the effects of confinement and the tension stiffening become significant. Therefore, Tables 4.7 and 4.8 list the predicted versus experimental ultimate moments of the CFFT beams and the confinement and tension stiffening of the concrete issues are considered. As seen in the tables, using the unconfined concrete model is conservative especially in the thick tubes. While, using the partially confined concrete model agrees with the experimental results. Figure 4.23 indicates the good agreement of the theoretical versus experimental yield moments especially when using the partially confined concrete model. Accordingly, the analytical results justify the use of the partially confined concrete model in modelling the fully-CFFT rectangular beams. Figures 4.24 to 4.39 show

the experimental versus the analytical moment-strain, variation of the neutral axis depth, moment-curvature, and moment-deflection of the CFFT beams. Note that these figures plot the predicted results that use the partially confined concrete model only and the tension stiffening being considered or ignored. Generally, good agreement is observed. However, in the thin FRP tubes, OR2₃₀ and OR4₃₀, ignoring the tension stiffening shows better agreement with the experimental profiles of strains, curvature, and deflection than considering it.

4.6 PARAMETRIC STUDY

A parametric study has been performed using the proposed analytical model to study extensively the effect of steel reinforcement ratio, tube stiffness, tube thickness, and concrete strength. Figures 4.40 to 4.44 show the predicted moment-strain, variation of the neutral axis depth, moment-curvature, and moment-deflection for virtual CFFT beams to study the considered parametric variables. Note that, these figures plot the predicted results that use the partially confined concrete model only and the tension stiffening being ignored for safe design.

4.6.1 Effect of Steel Reinforcement Ratio

The effect of steel reinforcement was studied in thin GFRP tube of 4 mm thickness (Figure 4.40), and in another thick GFRP tube of 14 mm thickness (Figure 4.41). The axial stiffness of both GFRP tubes was 14 GPa, and the concrete compressive strength was 49 MPa. The steel reinforcement ratio (A_s / bh) was changing from zero to 0.02. Note that, the ratio 0.02 was chosen to be more than the balanced reinforcement ratio in conventional RC beams.

Figure 4.40 shows that increasing the steel reinforcement ratio increases the initial flexural stiffness at the pre-yielding stage, the yield moments, and the ultimate moments. The location of the neutral axis changes significantly with changing the steel reinforcement ratio (the higher reinforcement ratio, the closer neutral axis to the center of the section). As expected, after yielding of steel, the flexural stiffness decreased due to the low axial stiffness of the GFRP tubes. For the same FRP tube, the flexural stiffness at the post-yielding stage is similar for different steel reinforcement ratios. This is attributed to the FRP tube is the only

reinforcement member that provide flexural rigidity at the post-yielding stage. The same results were observed for the thick GFRP tube when increasing the wall thickness from 4 mm to 14 mm as shown in Figure 4.41. These conclusions were proposed later in Figure 4.14 when comparing the experimental results of the reinforced CFFT beams with that of Fam et al. (2005). See section 4.4.5.1.

4.6.2 Effect of Tube Stiffness or Laminate Structure

The stiffness of the filament-wound GFRP tubes is governed mainly by the fiber laminates structure. This means, for the same tube thickness and layers, increasing the percentage of the fibers in the axial direction increases the axial stiffness of the filament-wound GFRP tube. Four percentages of axial stiffness of GFRP tubes were studied in Figure 4.42. The thickness of the GFRP tube is 10 mm. the steel reinforcement ratio is 0.006 (4-15M at the tension side). The concrete compressive strength is 49 MPa.

The results indicate that the flexural stiffness at the pre-yielding stage was increasing slightly with increasing the GFRP tube unlike in case of increasing steel reinforcement. However, at the post-yielding stage, the stiffer the GFRP tube increases significantly the flexural stiffness of the CFFT beam since it is the main reinforcement element at the post-yielding stage. Generally, increasing the axial stiffness increases the overall strength and stiffness of the CFFT beam, however, the failure mode could be changed. Low axial stiffness of the tubes means low axial fibers compared to the transverse fibers. Therefore, the excessive transverse fibers can resist the early buckling of the axial fibers and the compression flange. This confirms the results of the CFTT beam OR16₄₅. The neutral axis location was changing slightly with changing the GFRP tube axial stiffness.

4.6.3 Effect of Tube Thickness

Three thicknesses of GFRP tubes were studied as shown in Figure 4.43. The steel reinforcement ratio is 0.006 (4-15M at the tension side). The concrete compressive strength is 49 MPa. The axial stiffness of both GFRP tubes was 14 GPa.

The results indicate similar conclusions as in case of studying the axial stiffness effect of the GFRP tube. Generally, increasing the tube thickness increases the overall strength and stiffness of the CFFT beam. The results indicate that the flexural stiffness at the pre-yielding stage was increasing with increasing the GFRP tube. At the post-yielding stage, the stiffer the GFRP tube increases significantly the flexural stiffness of the CFFT beam. The thin tube fails in tension since its axial strain at the bottom increases rapidly. The neutral axis location was moving downward with increasing the GFRP tube thickness.

4.6.4 Effect of Concrete Strength

The effect of concrete strength was studied by varying the concrete compressive strength for the same reinforcement ratio, tube thickness, and laminate structure as shown in Figure 4.44. The steel reinforcement ratio is 0.006 (4-15M at the tension side). The axial stiffness of both GFRP tubes was 14 GPa. The thickness of the tube is 4 mm to highlight the concrete contribution that increases in thin tubes. The partially confined model of concrete was used and the tension stiffening was ignored. Three concrete batches with compressive strength of 30, 49, and 70 MPa were studied. The results show that the concrete has insignificant effect on the flexural behaviour at the pre-yielding stage. However at the post-yielding stage, there is a minor increase in the flexural strength and stiffness with increasing the concrete strength.

4.7 CONCLUSIONS

Eight full-scale rectangular concrete-filled FRP tubes (CFFTs) with steel rebar and two conventional steel-reinforced concrete (RC) beams were tested under a four-point bending. The experimental results were investigated to evaluate the flexural performance of this hybrid FRP-concrete-steel CFFT beams. In addition, theoretical investigations were developed to predict the flexural capacities through different stages of loading.

The main concluded points of this study are as follows:

- 1) The rectangular CFFT beams experience significantly higher ductility, higher stiffness, and superior strength than the RC beams.

- 2) The failure pattern of the fully-CFFT beams changes from tension to compression failure with increasing the FRP tube thickness.
- 3) Rectangular CFFT beams with steel rebar fail gradually in a sequential manner (yielding of steel, buckling of compressed tube flange, and finally rupture of the fibers). Even after the peak load, the CFFT beams can keep a residual strength because of the existence of the steel that withstands high strains and elongation.
- 4) The flexural strength of fully-CFFT beams increases with increasing the FRP tube thickness until certain limit that separates the under-reinforced and over-reinforced CFFT section. After this limit, buckling of the compression flange of the FRP tube governs the ultimate capacity of over-reinforced CFFT beams. Based on this study, equations are proposed to estimate approximately the flexural moments at different stages (first crack, yield, and ultimate).
- 5) The compression failure in CFFT beams is governed by the buckling of the compression flange of the tubes, which can be resisted by increasing the transverse fibers percentage in the filament-wound FRP tubes.
- 6) The reinforced CFFT rectangular beams experience high cracking strength and the concrete modulus of rupture (f_{cr}) suggested by ACI-318 could be increased by 30% if the gross moment of inertia I_g is calculated neglecting reinforcement.
- 7) The analytical model proposed in this study is capable of predicting well the moment-curvature, moment strains, neutral axis depth, and moment-deflection responses of fully-CFFT rectangular beams. The confinement and tension stiffening issues of concrete are considered in the model.
- 8) Using partially confined model for concrete with plastic strain up to the ultimate compressive strain of the FRP tube indicated better agreement with the experimental results than using the unconfined concrete model proposed by AASHTO guidelines (2012).
- 9) Concrete tension stiffening contribution is directly proportional to the FRP tube thickness. This contribution can be considered in thick tubes, and should be ignored in thin tubes. However, ignoring the tension stiffening of concrete underestimates the experimental results and achieves safe design.

- 10) Using steel reinforcement in the CFFT beams is very significant. It increases the overall flexural stiffness and strength and decreases the deflection of such type of FRP-concrete composite beams.

Table 4.1 – Beam specimens and summary of test results

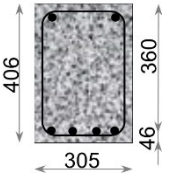
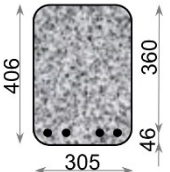
| Group | Beam ID | Section Configuration (mm) | Steel reinforcement | Outer tube | Inner tube | Concrete strength (MPa) | Moment (kN.m) | | | Ultimate Deflection (mm) | Ductility (kN.m ²) | Failure mode |
|------------------|----------------------|--|---|--------------------|------------|-------------------------|---------------|-------|-------|--------------------------|--------------------------------|--------------|
| | | | | | | | M_{cr} | M_y | M_u | | | |
| RC beams | RC #1 |  | Top 2-10M Bot. 4-15M Ties 10M/150 mm | --- | --- | 41.7 | 30 | 113 | 132 | 29 | 3.1 | Tension |
| | RC #2 | | | | | | 41.7 | 31 | 116 | | | |
| Fully CFFT beams | OR2 ₃₀ #1 |  | Bot. 4-15M | OR2 ₃₀ | --- | 49.7 | 43 | 152 | 249 | 52 | 10.2 | Tension |
| | OR2 ₃₀ #2 | | | OR2 ₃₀ | --- | 49.7 | 43 | 150 | 267 | 69 | 14.3 | Tension |
| | OR4 ₃₀ #1 | | | OR4 ₃₀ | --- | 48.7 | 46 | 161 | 404 | 89 | 27.0 | Tension |
| | OR4 ₃₀ #2 | | | OR4 ₃₀ | --- | 48.7 | 44 | 168 | 392 | 77 | 22.2 | Tension |
| | OR8 ₃₀ #1 | | | OR8 ₃₀ | --- | 41.7 | 48 | 204 | 559 | 82 | 33.0 | Balanced |
| | OR8 ₃₀ #2 | | | OR8 ₃₀ | --- | 41.7 | 45 | 210 | 560 | 92 | 38.4 | Balanced |
| | OR12 ₃₀ | | | OR12 ₃₀ | --- | 48.7 | 50 | 245 | 581 | 45 | 17.5 | Comp. |
| | OR16 ₄₅ | | | OR16 ₄₅ | --- | 48.7 | 50 | 235 | 712 | 97 | 47.5 | Balanced |

Table 4.2 – Shear forces in fully-CFFT beams

| Fully-CFFT Beam | t_f (mm) | f'_c (MPa) | V_n (kN) ($=M_u/a$) | V_c (kN) ($=0.17\sqrt{f'_c}A_c$) | V_f (kN) ($=V_n-V_c$) | F_f (MPa) | Exp. F_{tr} (MPa) | $\frac{F_f}{F_{tr}} \times 100$ (%) |
|----------------------|------------|--------------|----------------------------|---|------------------------------|-------------|---------------------|-------------------------------------|
| OR2 ₃₀ #1 | 3.4 | 49.7 | 226.4 | 148.4 | 78.0 | 22.8 | 243 | 9.4 |
| OR2 ₃₀ #2 | 3.4 | 49.7 | 242.7 | 148.4 | 94.3 | 27.6 | 243 | 11.4 |
| OR4 ₃₀ #1 | 5.7 | 48.7 | 367.3 | 146.9 | 220.4 | 38.5 | 214 | 18.0 |
| OR4 ₃₀ #2 | 5.7 | 48.7 | 356.4 | 146.9 | 209.5 | 36.6 | 214 | 17.1 |
| OR8 ₃₀ #1 | 8.7 | 41.7 | 508.2 | 135.9 | 372.2 | 42.6 | 164 | 26.0 |
| OR8 ₃₀ #2 | 8.7 | 41.7 | 509.1 | 135.9 | 373.2 | 42.7 | 164 | 26.0 |
| OR12 ₃₀ | 9.9 | 48.7 | 528.2 | 146.9 | 381.3 | 38.3 | 125 | 30.7 |
| OR16 ₄₅ | 14.2 | 48.7 | 647.3 | 146.9 | 500.4 | 35.1 | 169 | 20.8 |

Table 4.3 – Details of calculating cracking strength of fully-CFFT beams

| Beam | t_f (mm) | f'_c (MPa) | Exp. M_{cr} (kN.m) | Neglecting reinforcement | | | | Considering reinforcement | | | | | |
|----------------------|---------------|-----------------|-------------------------|--------------------------|-----------------------------|-------------------|---------------|---------------------------|-----------------------------|-------------------|------|---------------|------|
| | | | | Y_t (mm) | I_g (mm ⁴) | f_{cr} (MPa) | k | Y_t (mm) | I_g (mm ⁴) | f_{cr} (MPa) | k | | |
| OR2 ₃₀ #1 | 3.4 | 49.7 | 43.4 | 203 | 1.7×10 ⁹ | 5.18 | 0.73 | 198 | 1.86×10 ⁹ | 4.61 | 0.65 | | |
| OR2 ₃₀ #2 | 3.4 | 49.7 | 42.5 | 203 | 1.7×10 ⁹ | 5.07 | 0.72 | 198 | 1.86×10 ⁹ | 4.52 | 0.64 | | |
| OR4 ₃₀ #1 | 5.7 | 48.7 | 45.7 | 203 | 1.7×10 ⁹ | 5.45 | 0.78 | 198 | 1.91×10 ⁹ | 4.74 | 0.68 | | |
| OR4 ₃₀ #2 | 5.7 | 48.7 | 44.5 | 203 | 1.7×10 ⁹ | 5.31 | 0.76 | 198 | 1.91×10 ⁹ | 4.61 | 0.66 | | |
| OR8 ₃₀ #1 | 8.7 | 41.7 | 48.5 | 203 | 1.7×10 ⁹ | 5.79 | 0.90 | 198 | 1.98×10 ⁹ | 4.85 | 0.75 | | |
| OR8 ₃₀ #2 | 8.7 | 41.7 | 45.1 | 203 | 1.7×10 ⁹ | 5.38 | 0.83 | 198 | 1.98×10 ⁹ | 4.51 | 0.70 | | |
| OR12 ₃₀ | 9.9 | 48.7 | 49.8 | 203 | 1.7×10 ⁹ | 5.94 | 0.85 | 198 | 2.03×10 ⁹ | 4.85 | 0.69 | | |
| OR16 ₄₅ | 14.2 | 48.7 | 49.6 | 203 | 1.7×10 ⁹ | 5.92 | 0.85 | 198 | 1.94×10 ⁹ | 5.07 | 0.73 | | |
| | | | | | | | Average $k =$ | 0.80 | | | | Average $k =$ | 0.69 |

Table 4.4 – Experiment versus predicted cracking moment for rectangular CFFT beams

| CFFT beam | Exp. M_{cr} (kN.m) | M_{cr} (Predicted) (kN.m) | | | | | | M_{cr} (Exp.) / M_{cr} (Predicted) | | | | | |
|----------------------|----------------------|-----------------------------|----------------|----------------|--------------------|---------------------------------|----------------|--|----------------|----------------|--------------------|---------------------------------|----------------|
| | | ACI 318 | | Fam & Rizkalla | Mohamed & Masmoudi | Proposed coefficient (new k) | | ACI 318 | | Fam & Rizkalla | Mohamed & Masmoudi | Proposed coefficient (new k) | |
| | | $k=0.62$ | | $k=1$ | $k=0.94$ | $k=0.69$ | $k=0.8$ | $k=0.62$ | | $k=1$ | $k=0.94$ | $k=0.69$ | $k=0.8$ |
| | | $I_{g(Total)}$ | $I_{g(Conc.)}$ | $I_{g(Total)}$ | $I_{g(Total)}$ | $I_{g(Total)}$ | $I_{g(Conc.)}$ | $I_{g(Total)}$ | $I_{g(Conc.)}$ | $I_{g(Total)}$ | $I_{g(Total)}$ | $I_{g(Total)}$ | $I_{g(Conc.)}$ |
| OR2 ₃₀ #1 | 43.4 | 41.1 | 36.6 | 66.3 | 62.3 | 45.8 | 47.3 | 1.06 | 1.19 | 0.65 | 0.70 | 0.95 | 0.92 |
| OR2 ₃₀ #2 | 42.5 | 41.1 | 36.6 | 66.3 | 62.3 | 45.8 | 47.3 | 1.03 | 1.16 | 0.64 | 0.68 | 0.93 | 0.90 |
| OR4 ₃₀ #1 | 45.7 | 41.7 | 36.3 | 67.3 | 63.2 | 46.4 | 46.8 | 1.10 | 1.26 | 0.68 | 0.72 | 0.98 | 0.98 |
| OR4 ₃₀ #2 | 44.5 | 41.7 | 36.3 | 67.3 | 63.2 | 46.4 | 46.8 | 1.07 | 1.23 | 0.66 | 0.70 | 0.96 | 0.95 |
| OR8 ₃₀ #1 | 48.5 | 40.1 | 33.7 | 64.6 | 60.7 | 44.6 | 43.6 | 1.21 | 1.44 | 0.75 | 0.80 | 1.09 | 1.11 |
| OR8 ₃₀ #2 | 45.1 | 40.1 | 33.7 | 64.6 | 60.7 | 44.6 | 43.6 | 1.13 | 1.34 | 0.70 | 0.74 | 1.01 | 1.04 |
| OR12 ₃₀ | 49.8 | 44.5 | 36.3 | 71.7 | 67.4 | 49.5 | 46.8 | 1.12 | 1.37 | 0.69 | 0.74 | 1.01 | 1.06 |
| OR16 ₄₅ | 49.6 | 42.3 | 36.3 | 68.3 | 64.2 | 47.1 | 46.8 | 1.17 | 1.37 | 0.73 | 0.77 | 1.05 | 1.06 |
| Average | | | | | | | | 1.11 | 1.29 | 0.69 | 0.73 | 1.00 | 1.00 |
| SD | | | | | | | | 0.06 | 0.10 | 0.04 | 0.04 | 0.05 | 0.08 |

Table 4.5 – Internal forces and their positions in rectangular CFFT section

| Internal Force ID | Expression of the force | Distance from the neutral axis |
|--------------------------------------|---|--|
| Tension force in steel | $T_s = E_s \cdot \varepsilon_s \cdot A_s$ | $YT_s = d - c$ |
| Tension force in tube flange | $T_{Tube\ flang} = bt_f E_{ten} \left(\frac{\varepsilon_{bot} + \varepsilon_{ct}}{2} \right)$ | $YT_{Tube\ flang} = h - c + \frac{t_f}{2}$ |
| Tension force in tube webs | $T_{Tube\ webs} = (h - c)t_f E_{ten} \varepsilon_{ct}$ | $YT_{Tube\ webs} = \frac{2}{3}(h - c)$ |
| Tension force in concrete strips | $T_i = f_{ci} b h_i$ $T_c = \sum_{i=1}^{i=n} T_i$ | $YT_i = \frac{h - c}{n} (i - 0.5)$ |
| Compression force in tube flange | $C_{Tube\ flang} = bt_f E_{comp} \left(\frac{\varepsilon_{cc} + \varepsilon_{top}}{2} \right)$ | $YC_{Tube\ flang} = c + \frac{t_f}{2}$ |
| Compression force in tube two webs | $C_{Tube\ webs} = ct_f E_{comp} \varepsilon_{cc}$ | $YC_{Tube\ webs} = \frac{2c}{3}$ |
| Compression force in concrete strips | $C_i = f_{ci} b h_i$ $C_c = \sum_{i=1}^{i=n} C_i$ | $YC_i = \frac{c}{n} (i - 0.5)$ |

Table 4.6 – Theoretical versus experimental yield moments of rectangular CFFT beams

| CFFT Beam | M_y (exp.) (kN.m) | <i>Unconfined or partially confined concrete model</i> | | | |
|----------------------|------------------------|--|--|------------------------------------|--|
| | | <i>Considering tension stiffening</i> | | <i>Ignoring tension stiffening</i> | |
| | | M_y (th.) (kN.m) | $\frac{M_y \text{ (exp.)}}{M_y \text{ (th.)}}$ | M_y (th.) (kN.m) | $\frac{M_y \text{ (exp.)}}{M_y \text{ (th.)}}$ |
| OR2 ₃₀ #1 | 152 | 171 | 0.89 | 149 | 1.02 |
| OR2 ₃₀ #2 | 150 | 171 | 0.88 | 149 | 1.01 |
| OR4 ₃₀ #1 | 161 | 189 | 0.85 | 161 | 1.00 |
| OR4 ₃₀ #2 | 168 | 189 | 0.89 | 161 | 1.04 |
| OR8 ₃₀ #1 | 204 | 206 | 0.99 | 188 | 1.08 |
| OR8 ₃₀ #2 | 210 | 206 | 1.02 | 188 | 1.12 |
| OR12 ₃₀ | 245 | 239 | 1.03 | 215 | 1.14 |
| | | <i>Average</i> | 0.94 | | 1.06 |
| | | <i>SD</i> | 0.07 | | 0.06 |

Table 4.7 – Theoretical versus experimental ultimate moments of rectangular CFFT beams using unconfined concrete model

| CFFT Beam | M_u (exp.) (kN.m) | Unconfined confined concrete model | | | |
|----------------------|---------------------|------------------------------------|--|-----------------------------|--|
| | | Considering tension stiffening | | Ignoring tension stiffening | |
| | | M_u (th.) (kN.m) | $\frac{M_u(\text{exp.})}{M_u(\text{th.})}$ | M_u (th.) (kN.m) | $\frac{M_u(\text{exp.})}{M_u(\text{th.})}$ |
| OR2 ₃₀ #1 | 249 | 260 | 0.96 | 240 | 1.04 |
| OR2 ₃₀ #2 | 267 | 260 | 1.03 | 240 | 1.11 |
| OR4 ₃₀ #1 | 404 | 319 | 1.27 | 318 | 1.27 |
| OR4 ₃₀ #2 | 392 | 319 | 1.23 | 318 | 1.23 |
| OR8 ₃₀ #1 | 559 | 440 | 1.27 | 427 | 1.31 |
| OR8 ₃₀ #2 | 560 | 440 | 1.27 | 427 | 1.31 |
| OR12 ₃₀ | 581 | 489 | 1.19 | 496 | 1.17 |
| | | <i>Average</i> | 1.17 | | 1.21 |
| | | <i>SD</i> | 0.13 | | 0.10 |

Table 4.8 – Theoretical versus experimental ultimate moments of rectangular CFFT beams using partially confined concrete model

| CFFT Beam | M_u (exp.) (kN.m) | Partially confined concrete model | | | |
|----------------------|---------------------|-----------------------------------|--|-----------------------------|--|
| | | Considering tension stiffening | | Ignoring tension stiffening | |
| | | M_u (th.) (kN.m) | $\frac{M_u(\text{exp.})}{M_u(\text{th.})}$ | M_u (th.) (kN.m) | $\frac{M_u(\text{exp.})}{M_u(\text{th.})}$ |
| OR2 ₃₀ #1 | 249 | 265 | 0.94 | 239 | 1.04 |
| OR2 ₃₀ #2 | 267 | 265 | 1.01 | 239 | 1.12 |
| OR4 ₃₀ #1 | 404 | 359 | 1.13 | 336 | 1.20 |
| OR4 ₃₀ #2 | 392 | 359 | 1.09 | 336 | 1.17 |
| OR8 ₃₀ #1 | 559 | 498 | 1.12 | 488 | 1.15 |
| OR8 ₃₀ #2 | 560 | 498 | 1.12 | 488 | 1.15 |
| OR12 ₃₀ | 581 | 615 | 0.94 | 589 | 0.99 |
| | | <i>Average</i> | 1.05 | | 1.12 |
| | | <i>SD</i> | 0.08 | | 0.08 |

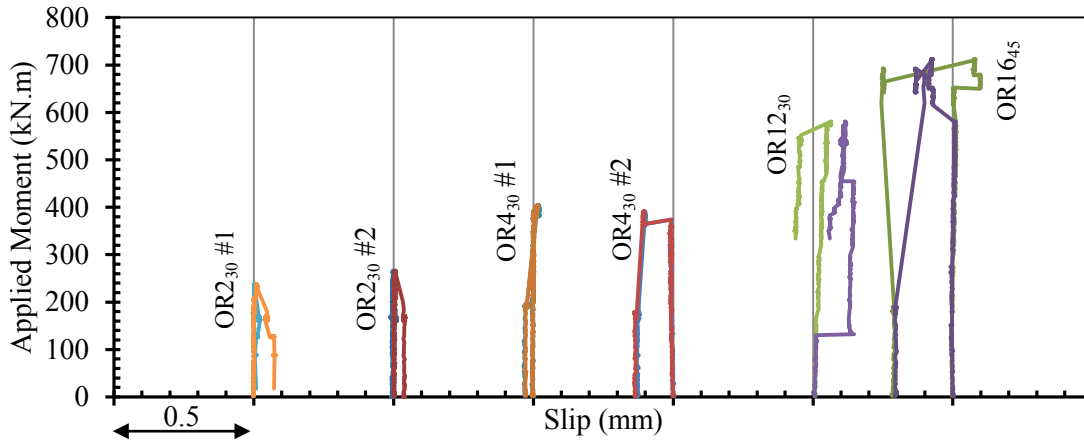
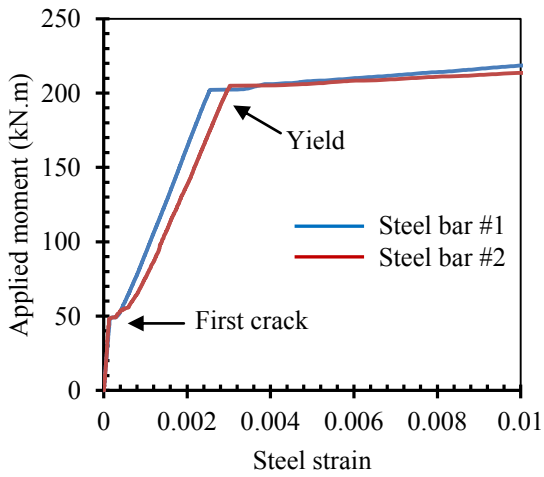
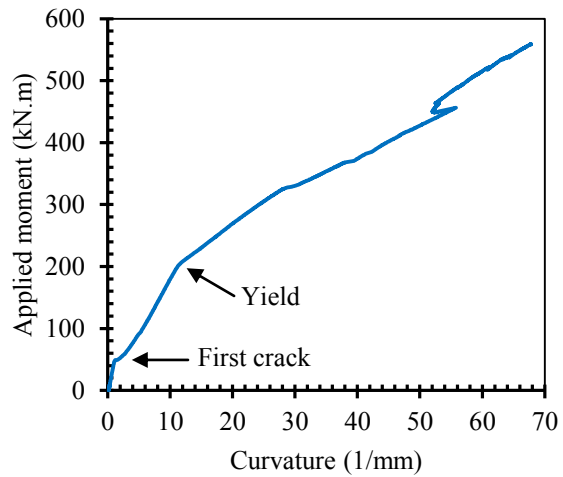


Figure 4.1 – Moment-slip response of fully-CFFT beams



(a) Steel strains of OR8₃₀ #1



(b) Curvature of OR8₃₀ #1

Figure 4.2 – Typical steel strains and curvature of fully-CFFT beams

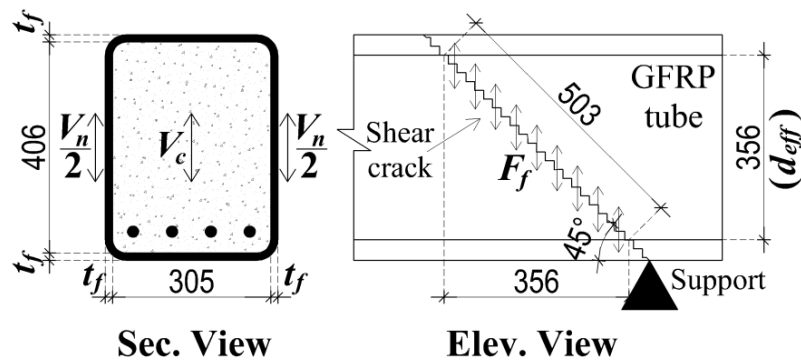
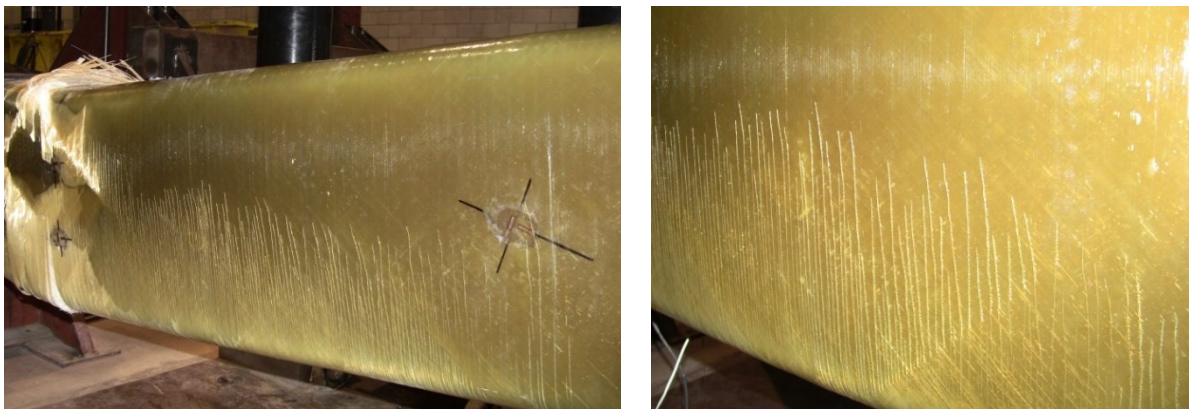


Figure 4.3 – Shear forces in fully-CFFT beams



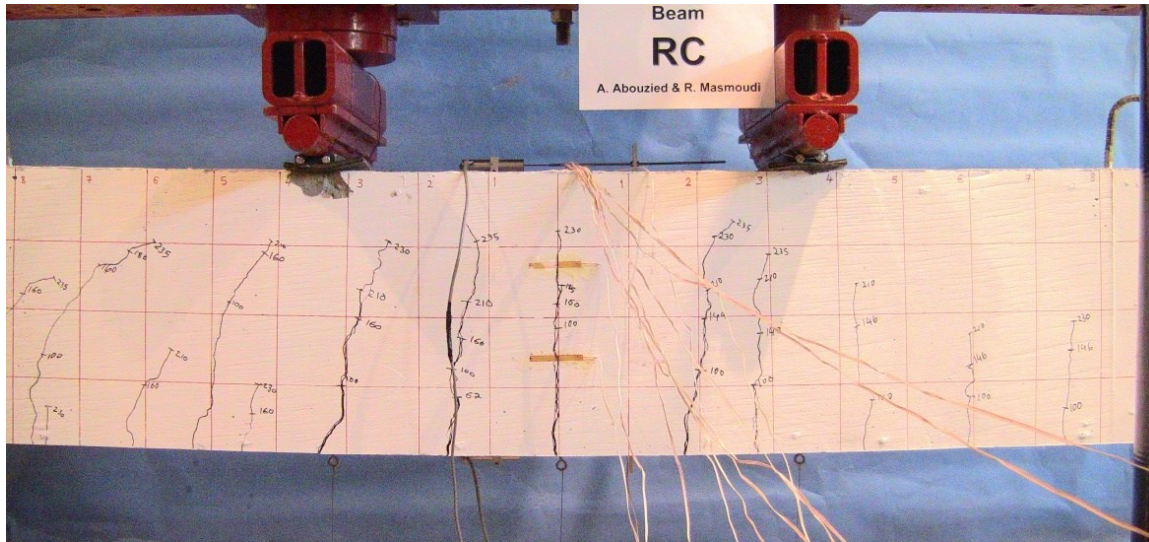
Figure 4.4 – Corner failure in pultruded FRP tubes (Belzer et al. 2013)



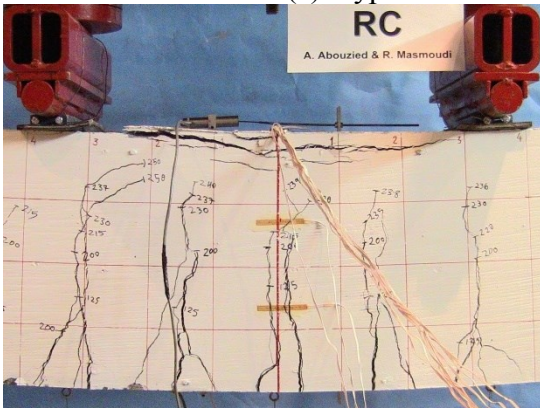
(a) Surface cracks of matrix

(b) Near view of surface cracks

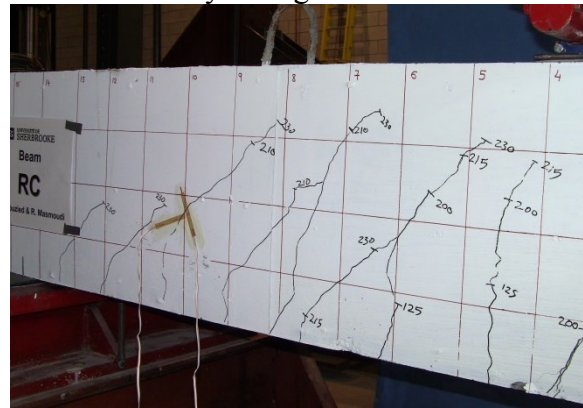
Figure 4.5 – Matrix surface cracks



(a) Typical tension failure due to steel yielding



(b) Final failure



(c) Typical shear cracks near supports

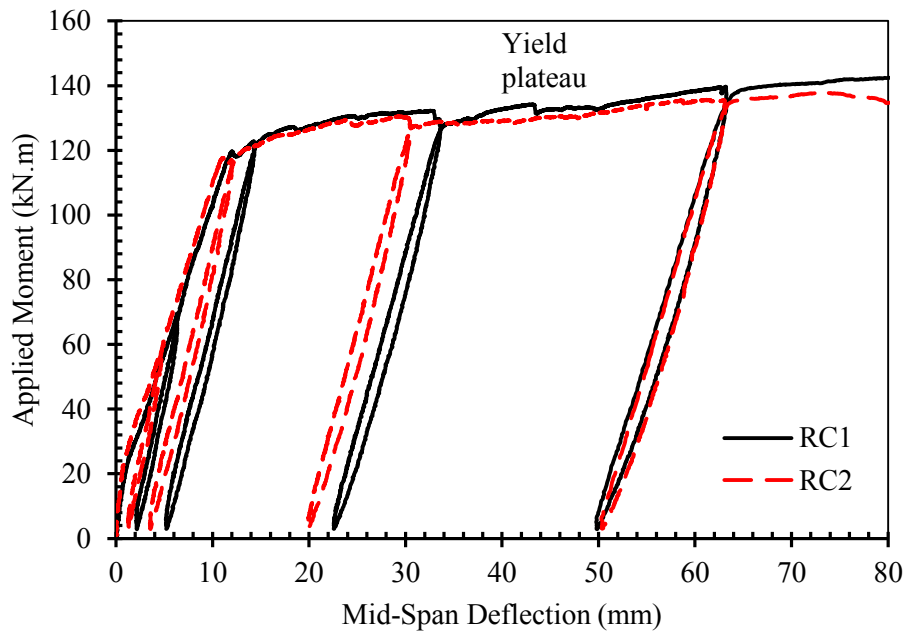
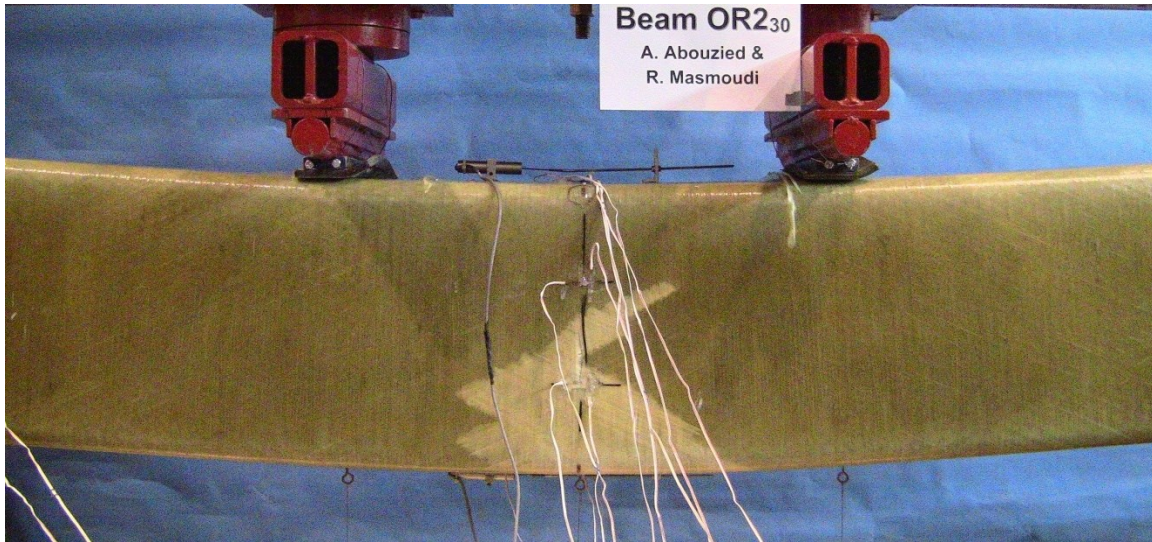


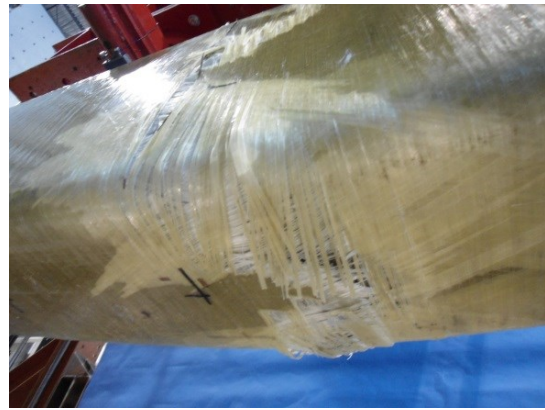
Figure 4.6 – Failure pattern and moment-deflection response of RC beams



(a) Elevation view



(b) Top view



(c) Bottom view

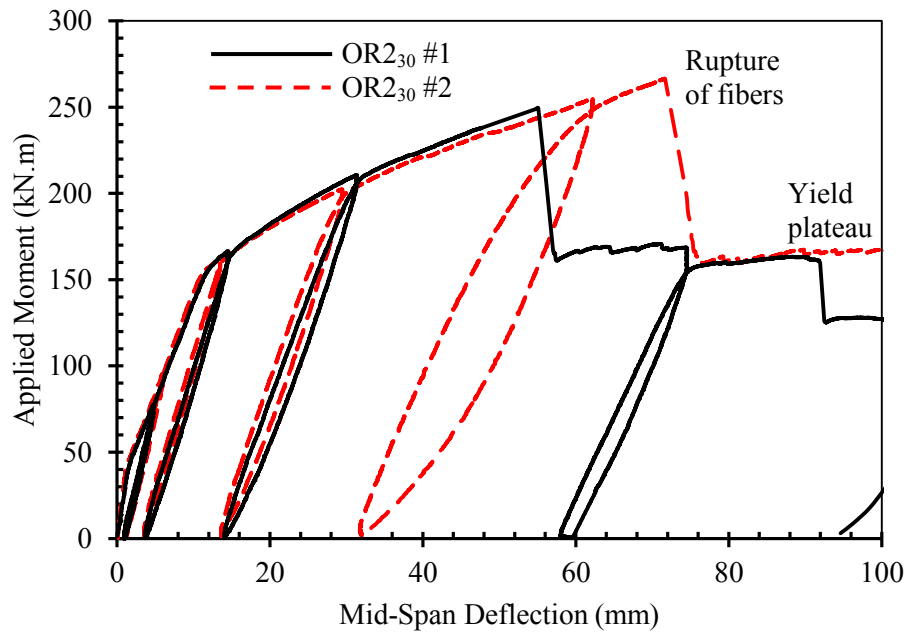
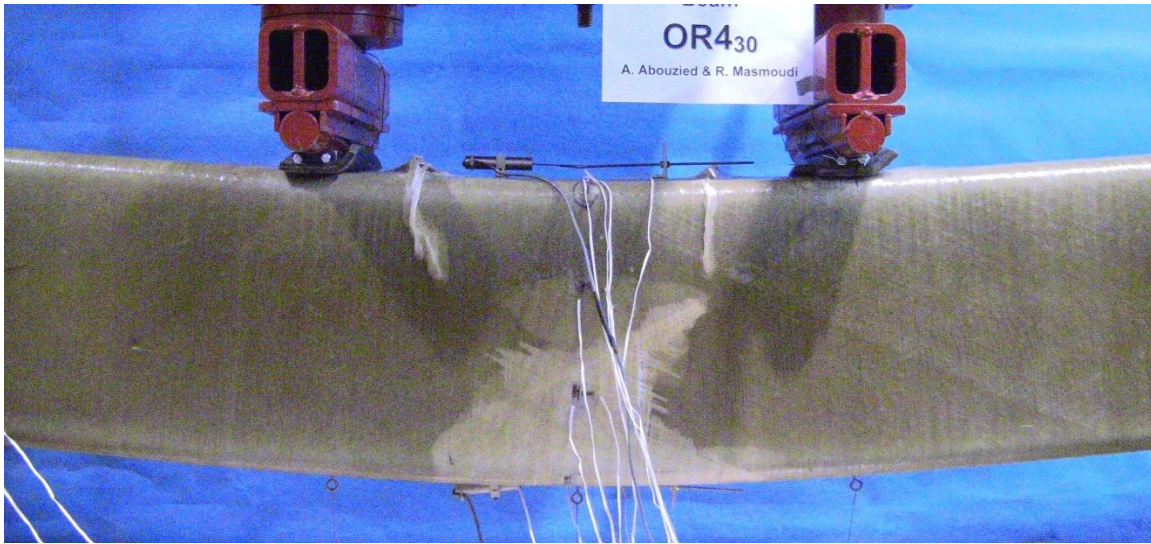


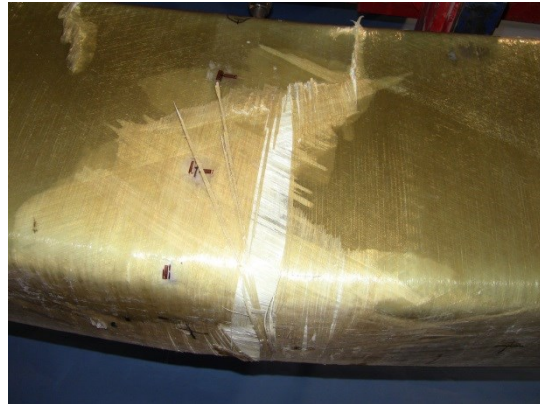
Figure 4.7 – Failure pattern and moment-deflection response of fully-CFFT beams OR2₃₀



(a) Elevation view



(b) Top view



(c) Bottom view

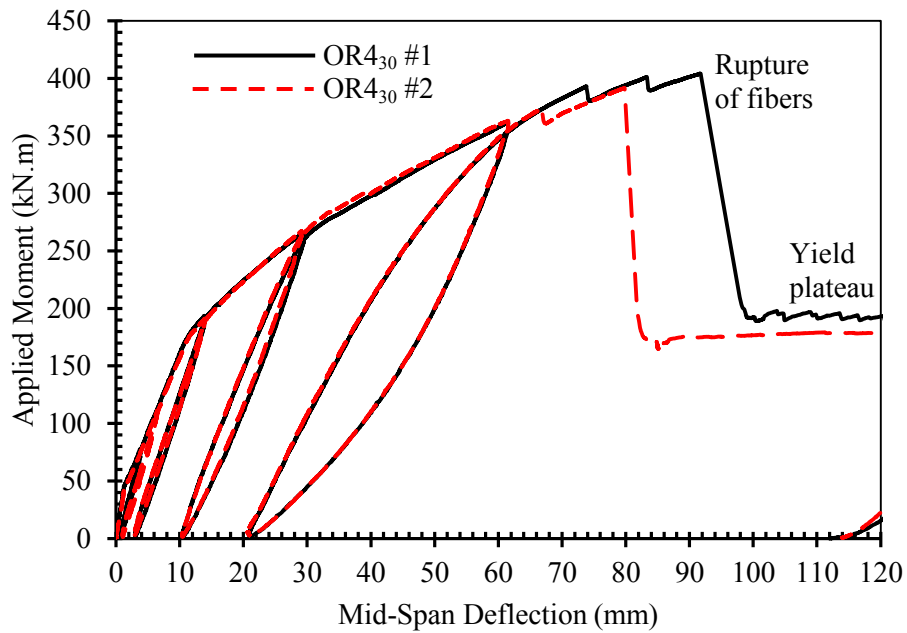
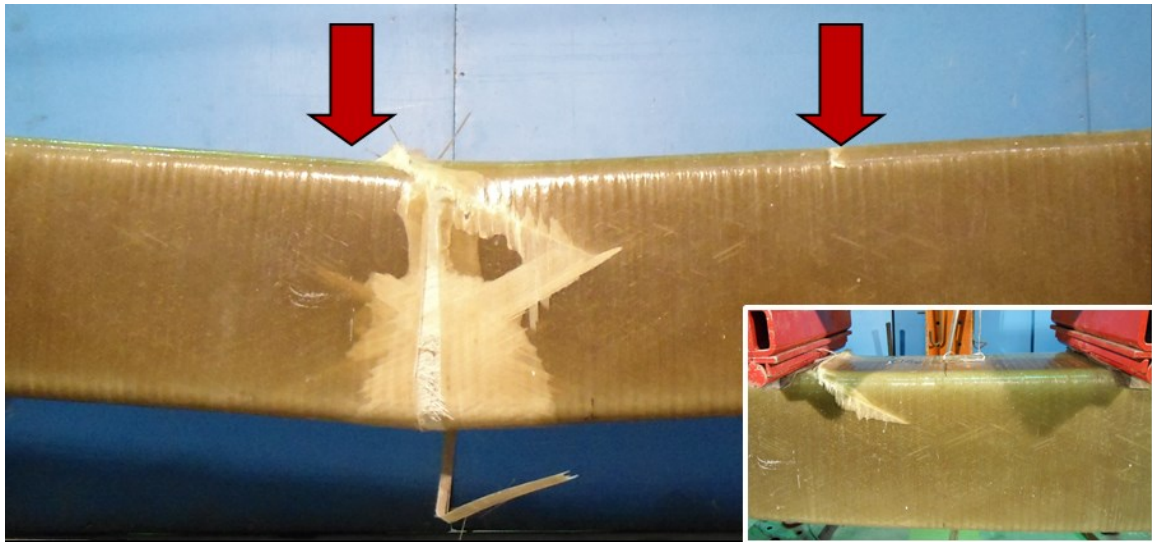
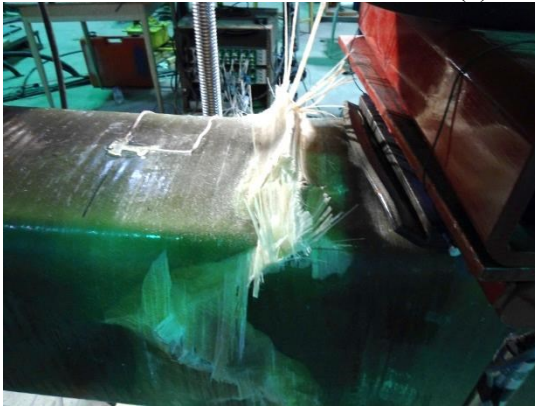


Figure 4.8 – Failure pattern and moment-deflection response of fully-CFFT beams OR430



(a) Elevation view



(b) Top view



(c) Elevation view

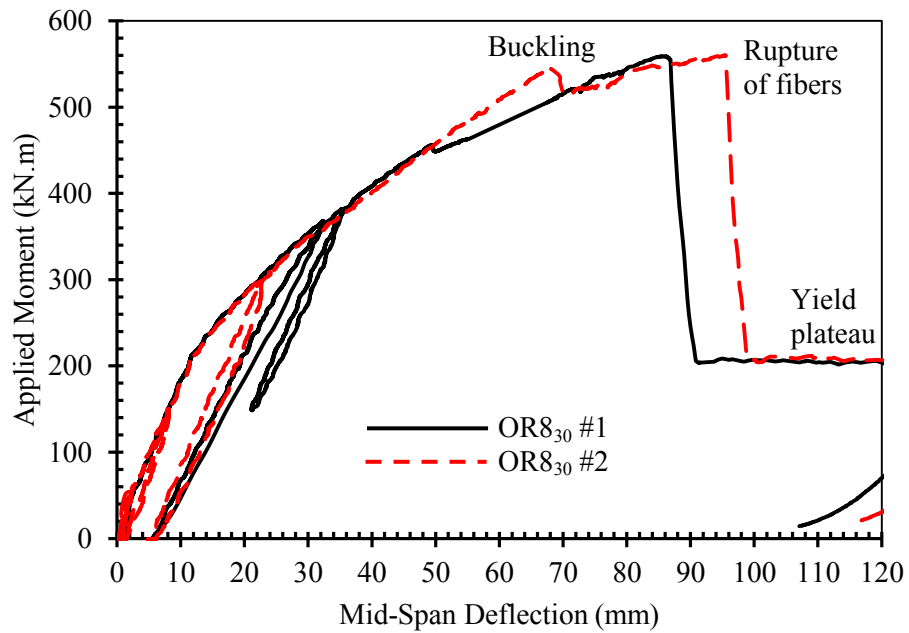
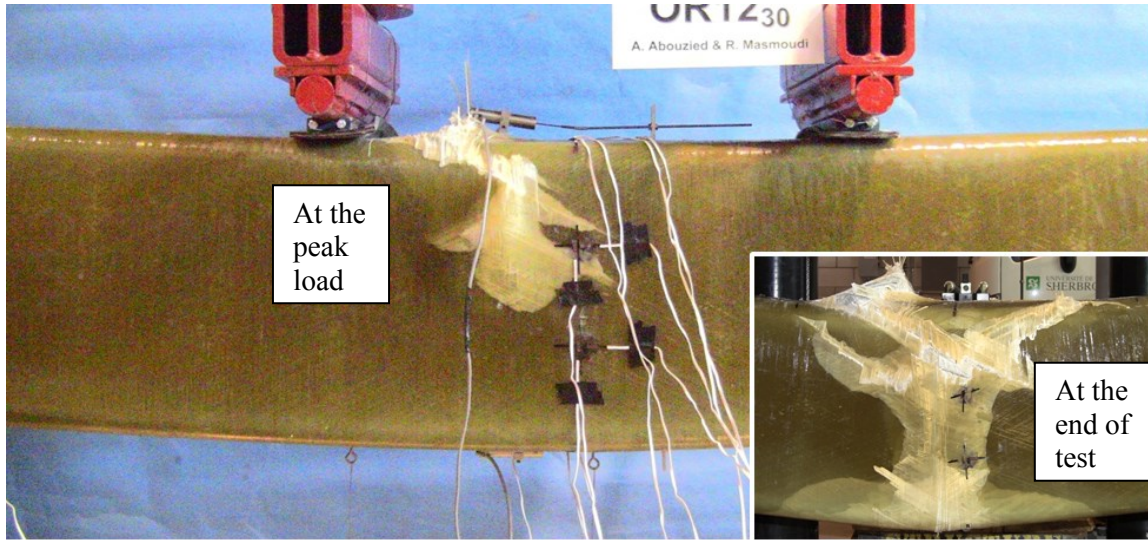
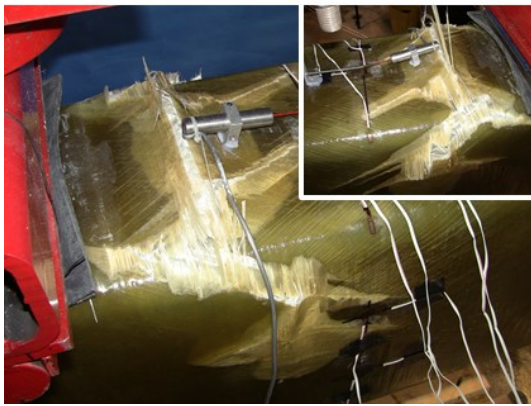


Figure 4.9 – Failure pattern and moment-deflection response of fully-CFFT beams OR8₃₀



(a) Elevation view



(b) Top view



(c) Bottom view

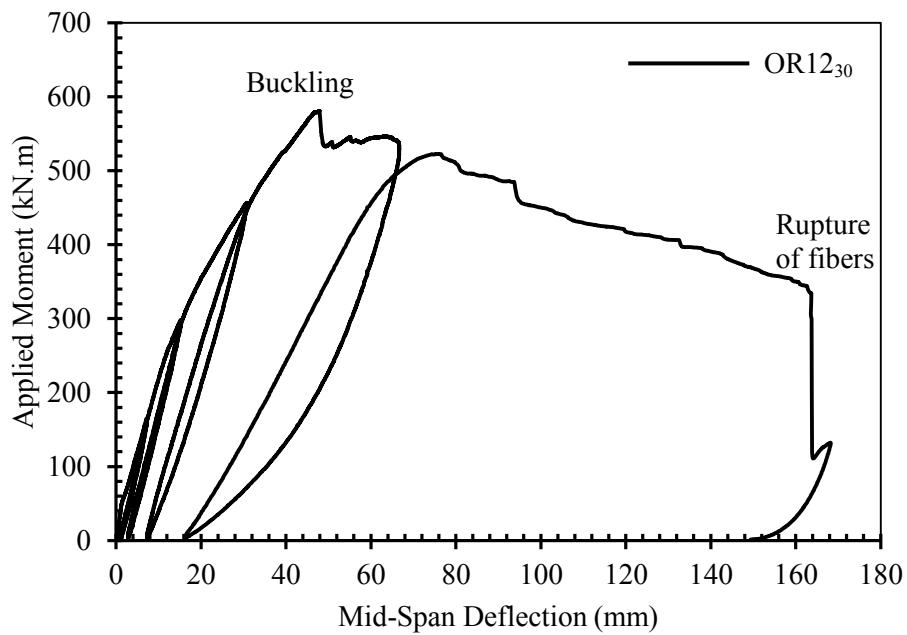
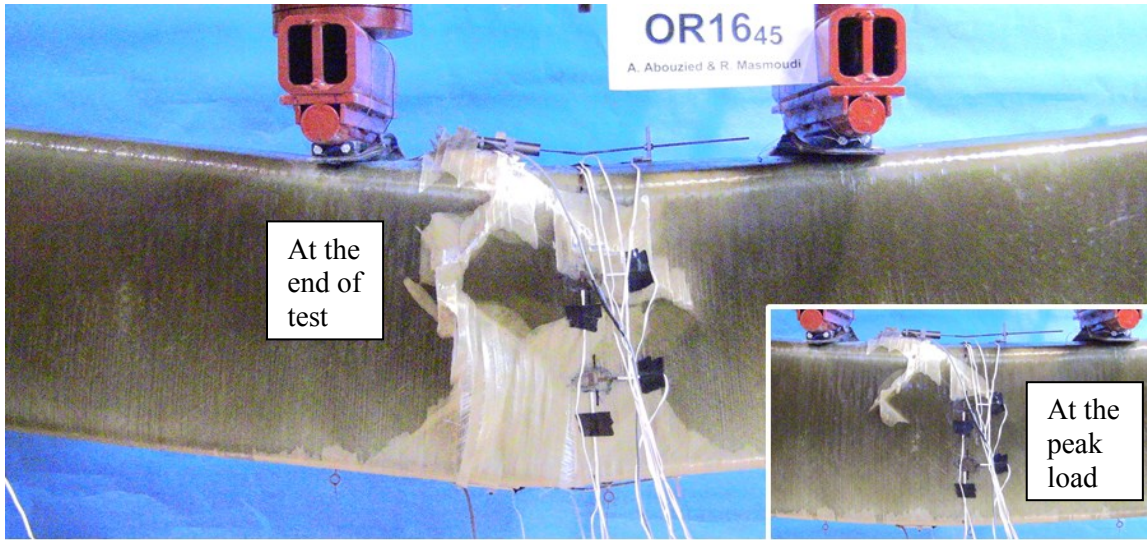
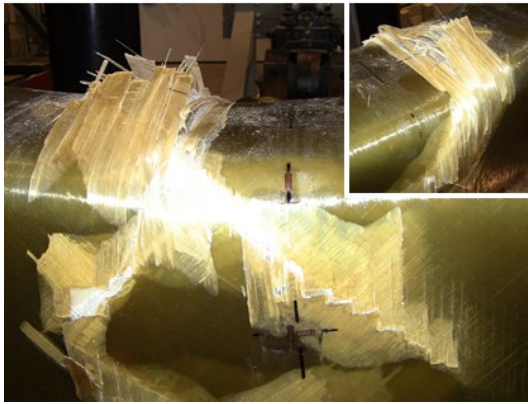


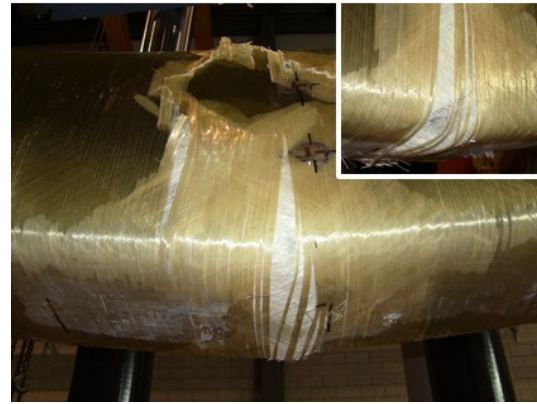
Figure 4.10 – Failure pattern and moment-deflection response of fully-CFFT beam OR12₃₀



(a) Elevation view



(b) Top view



(c) Bottom view

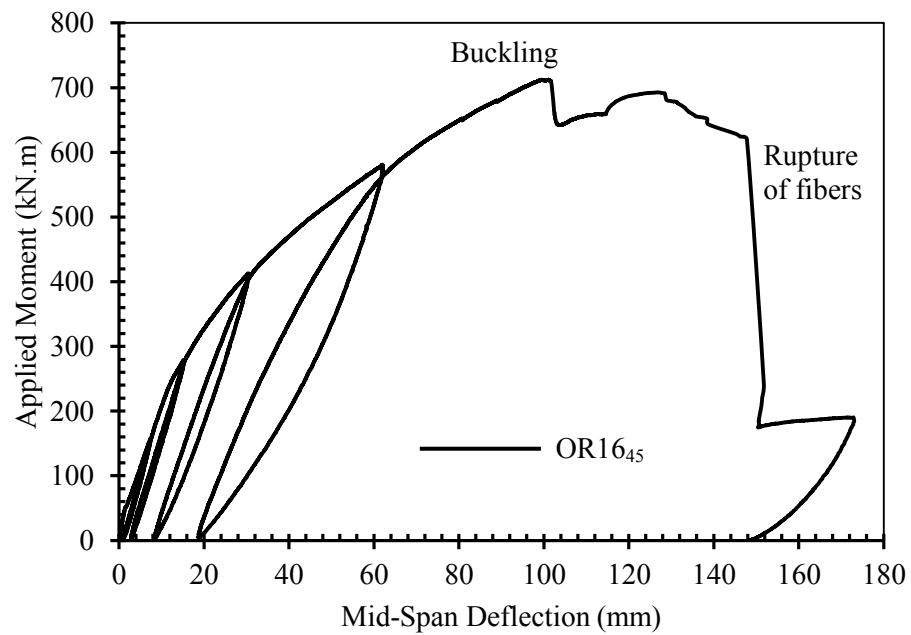


Figure 4.11 – Failure pattern and moment-deflection response of fully-CFFT beam OR1645

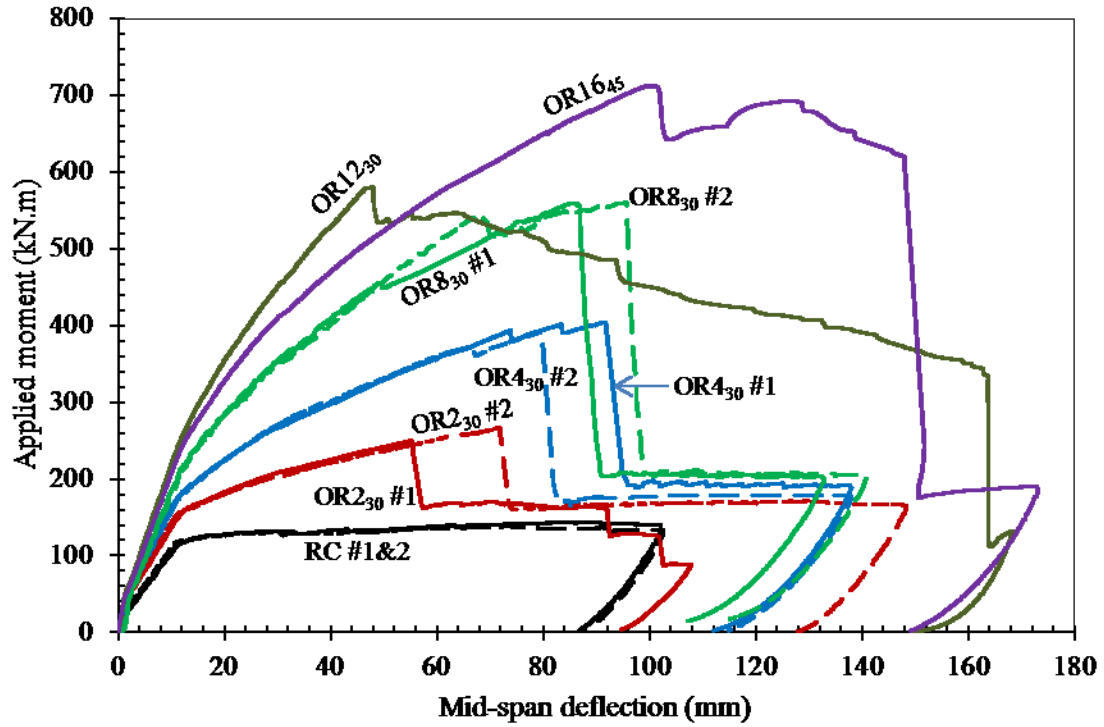


Figure 4.12 – Moment-deflection response of fully-CFFT beams

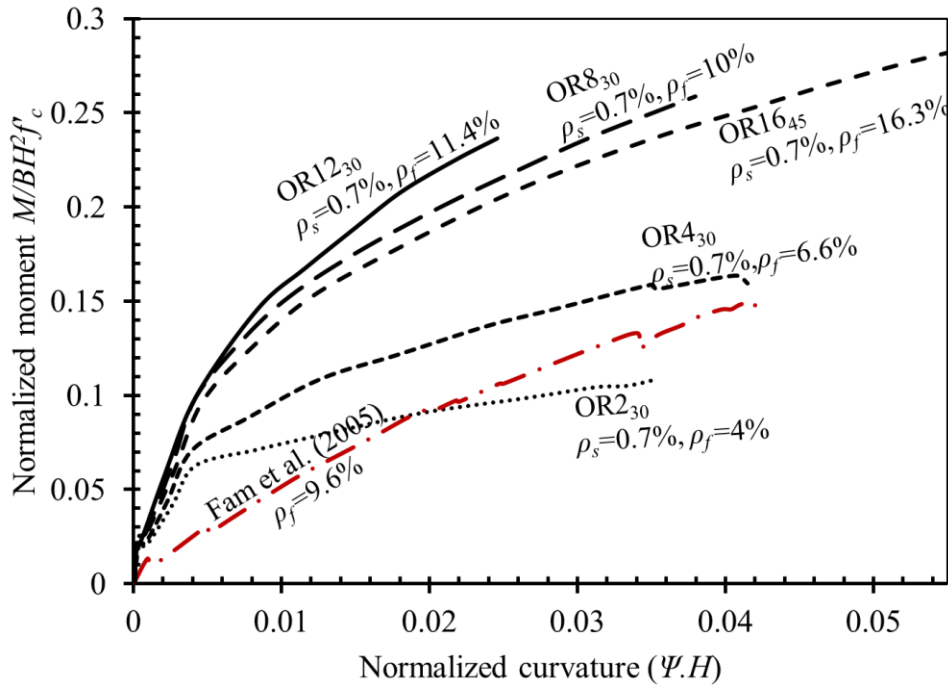


Figure 4.13 – Normalized moment-curvature response of fully-CFFT beams

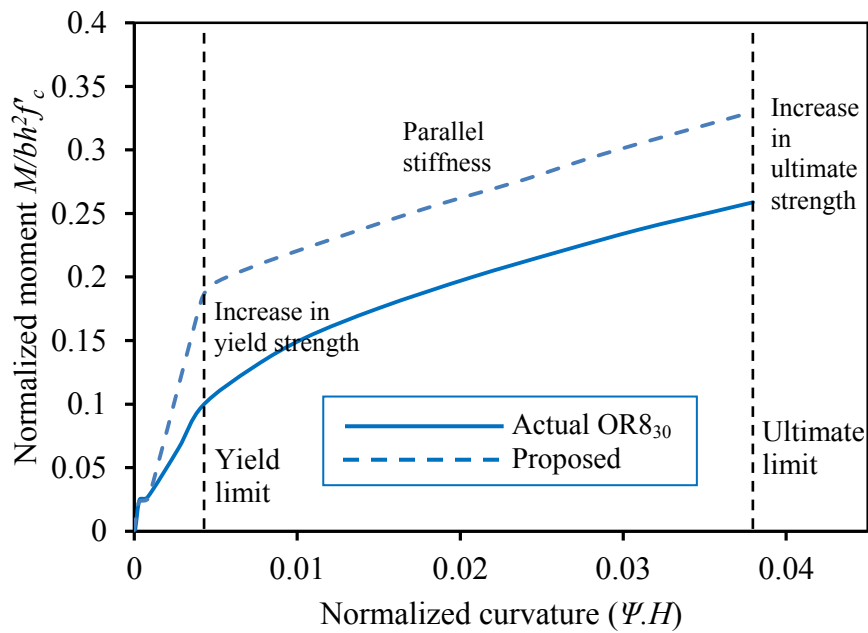


Figure 4.14 – Proposed effect of steel reinforcement in fully-CFFT beams

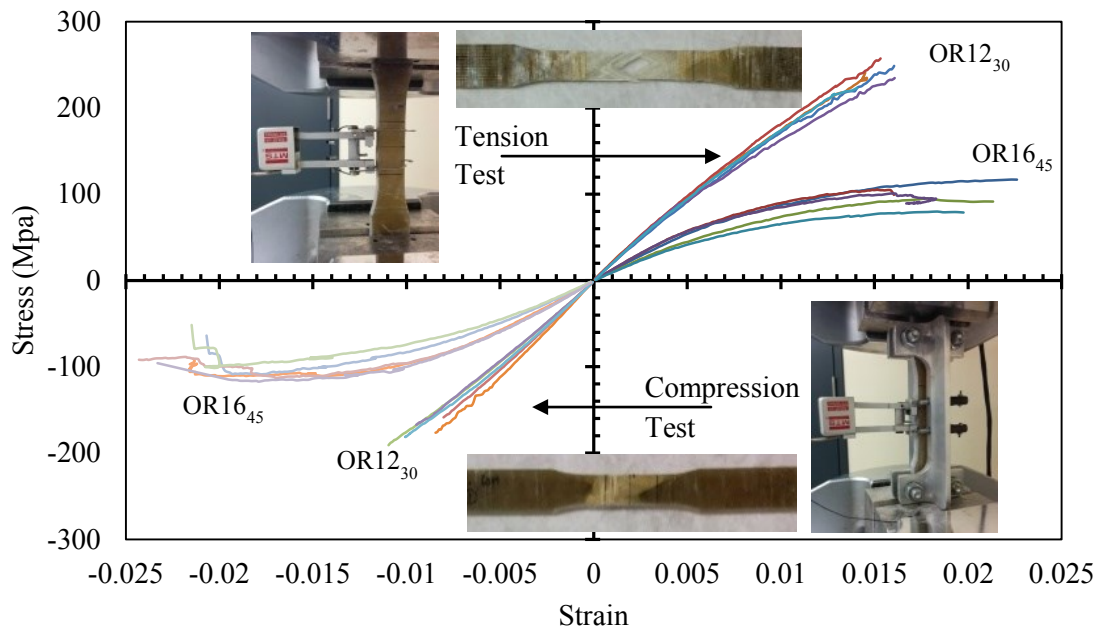
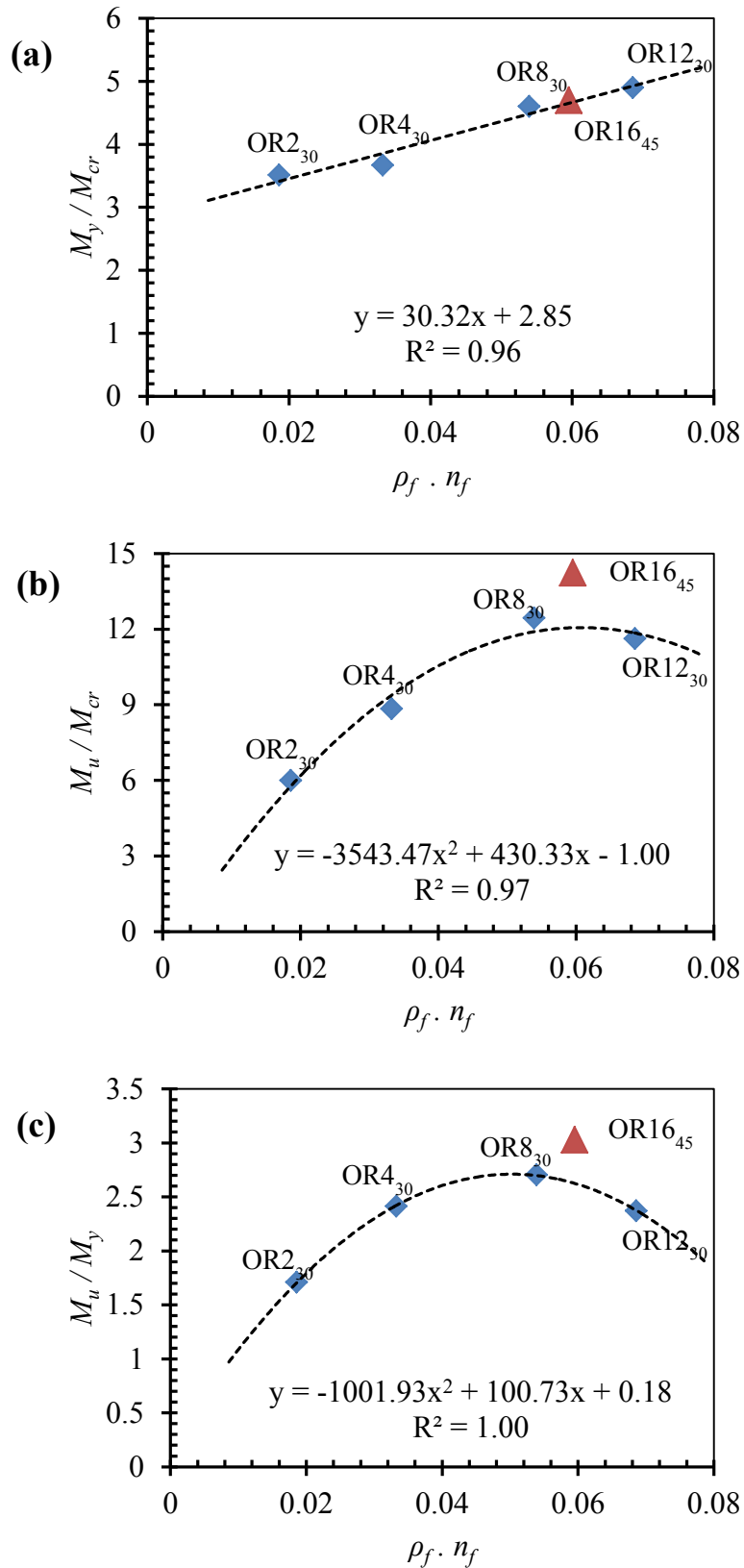


Figure 4.15 – Coupons tests results of OR12₃₀ and OR16₄₅ in axial direction

Figure 4.16 – Correlations between M_{cr} , M_y , and M_u of fully-CFFT beams

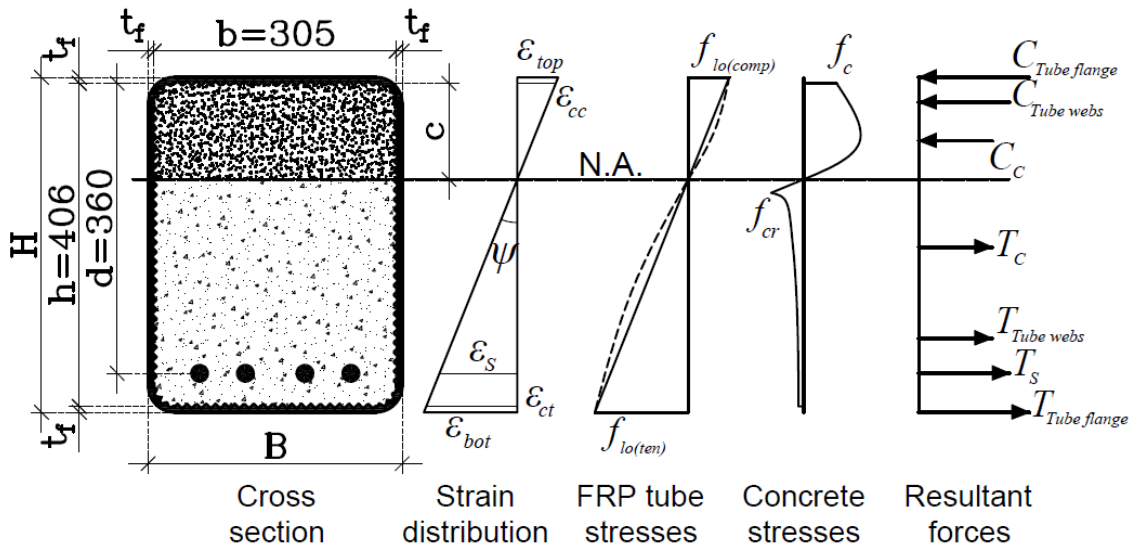


Figure 4.17 – Proposed analytical model

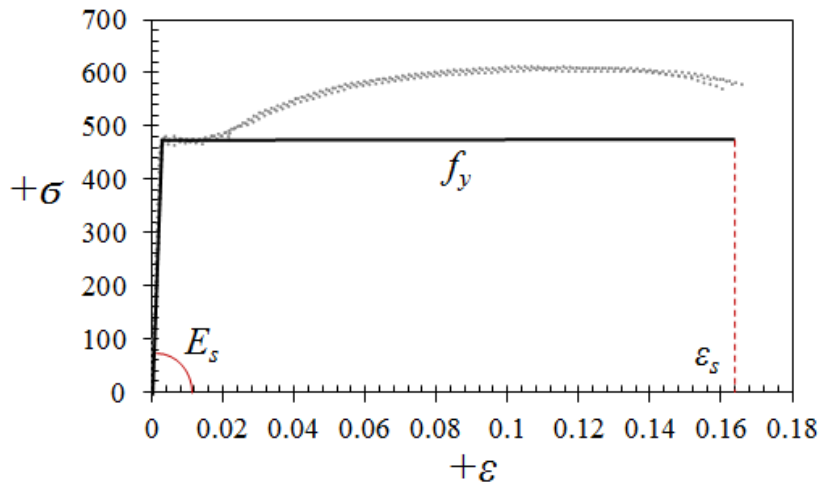


Figure 4.18 – Proposed model for steel

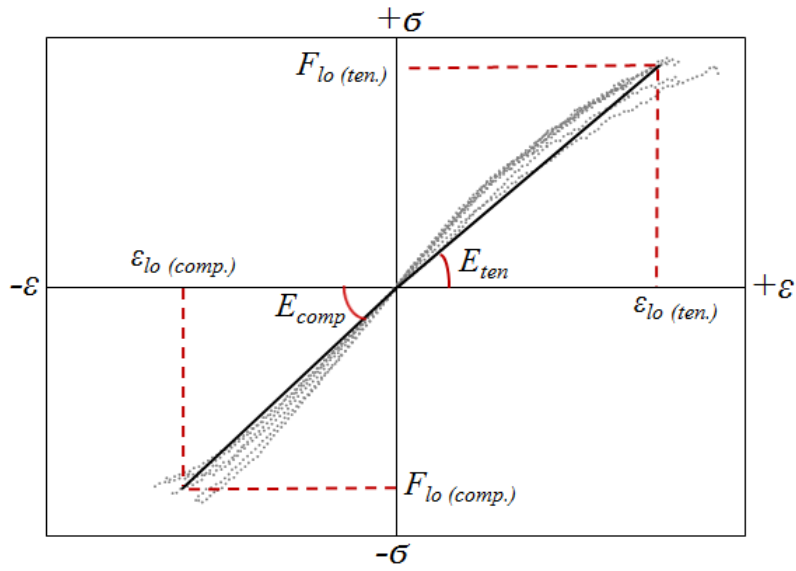


Figure 4.19 – Proposed model for FRP tube

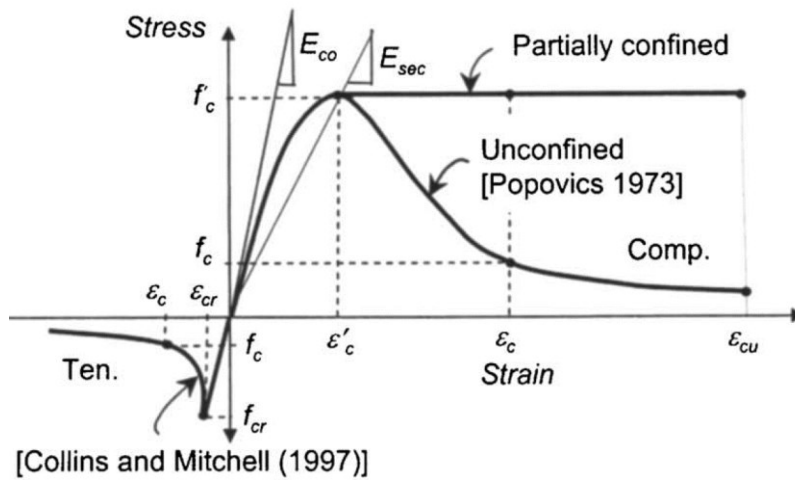


Figure 4.20 – Proposed model for concrete

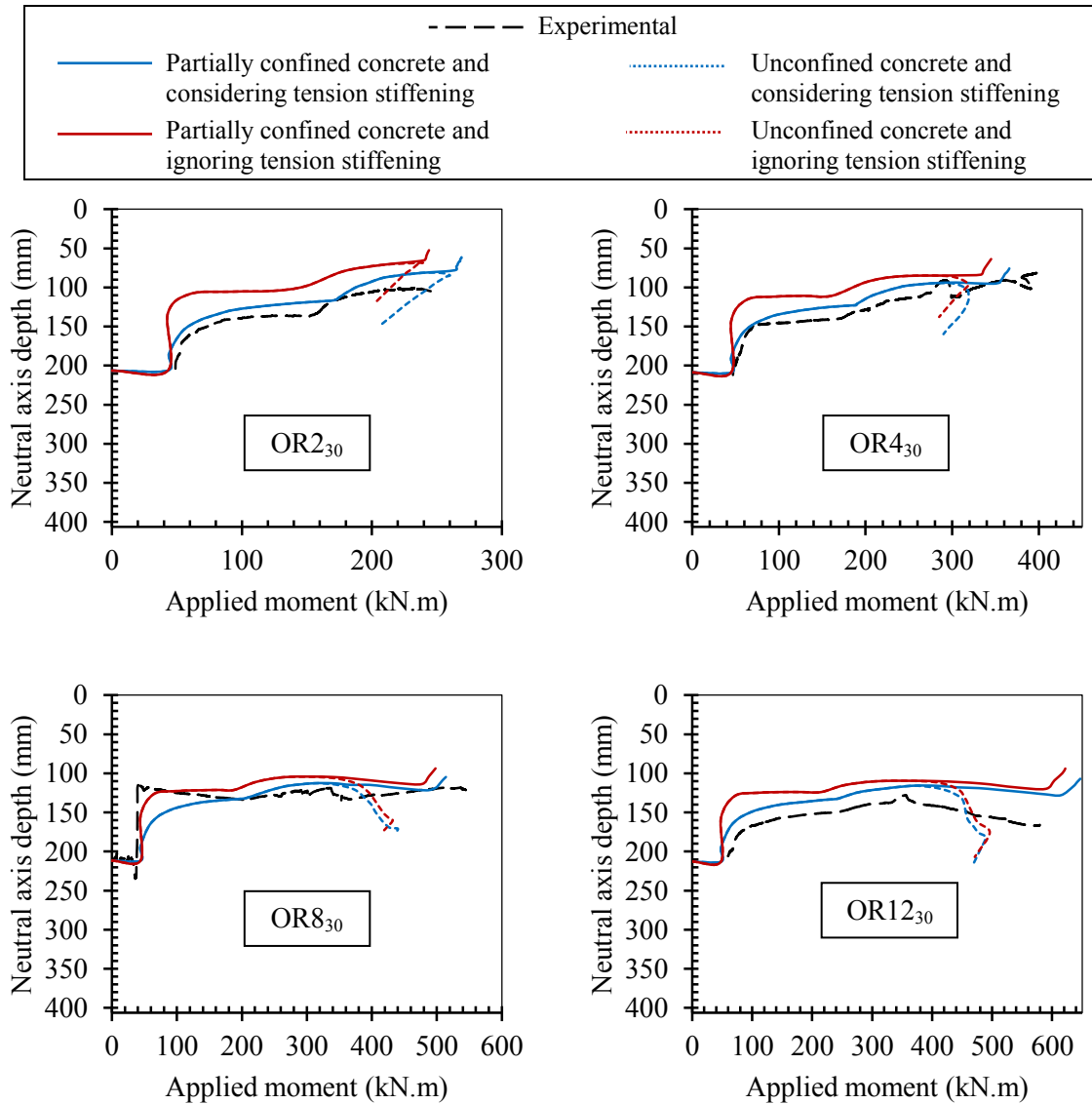


Figure 4.21 – Effect of concrete confinement model

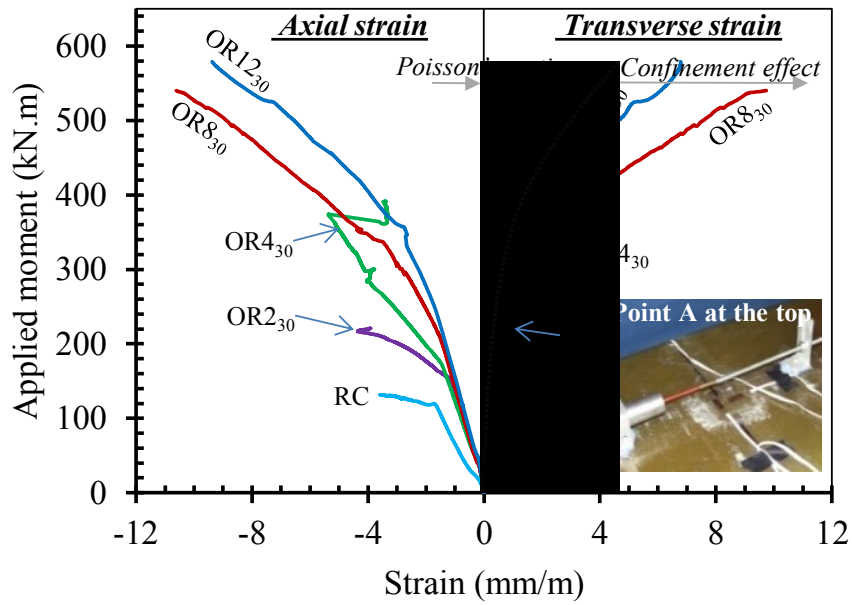


Figure 4.22 – Axial and transverse strains at the top face of the FRP tube in CFFT beams

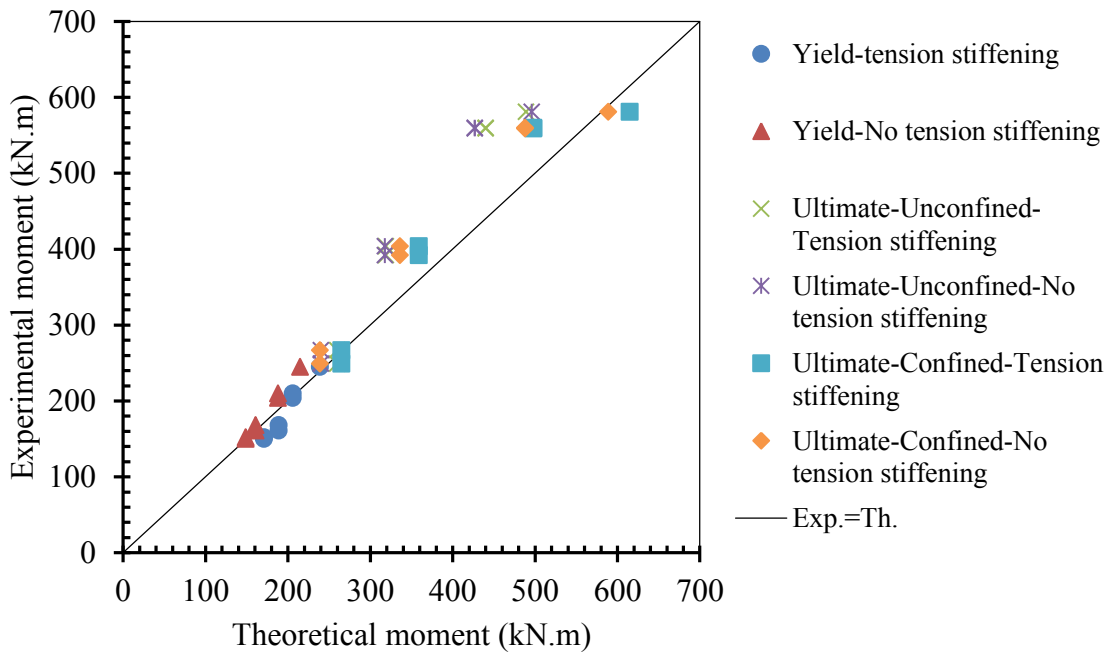


Figure 4.23 – Theoretical versus experimental moments of CFFT beams

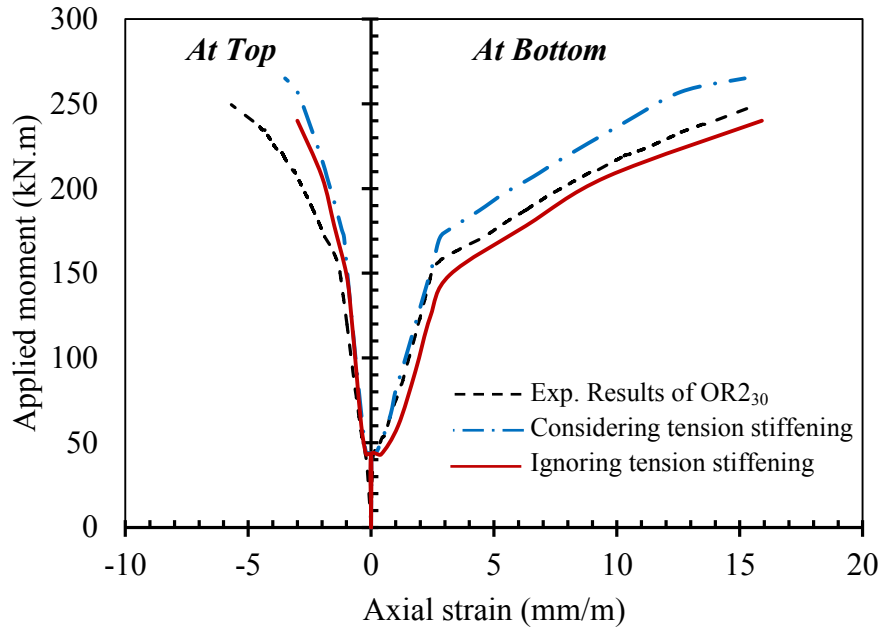


Figure 4.24 – Predicted versus experimental moment-strain response of CFFT beam OR2₃₀
(Model with partially confined concrete)

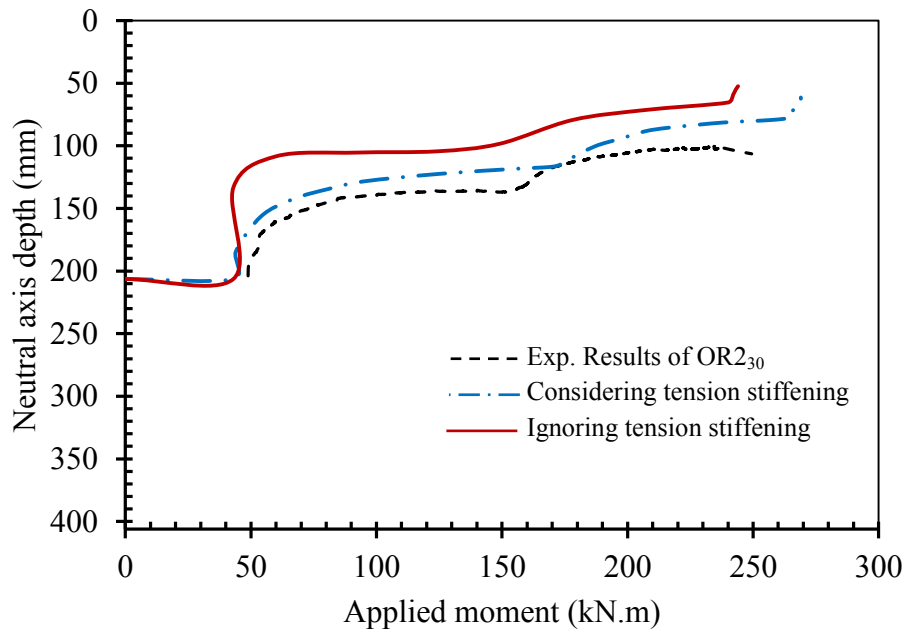


Figure 4.25 – Predicted versus experimental neutral axis depth of CFFT beam OR2₃₀
(Model with partially confined concrete)

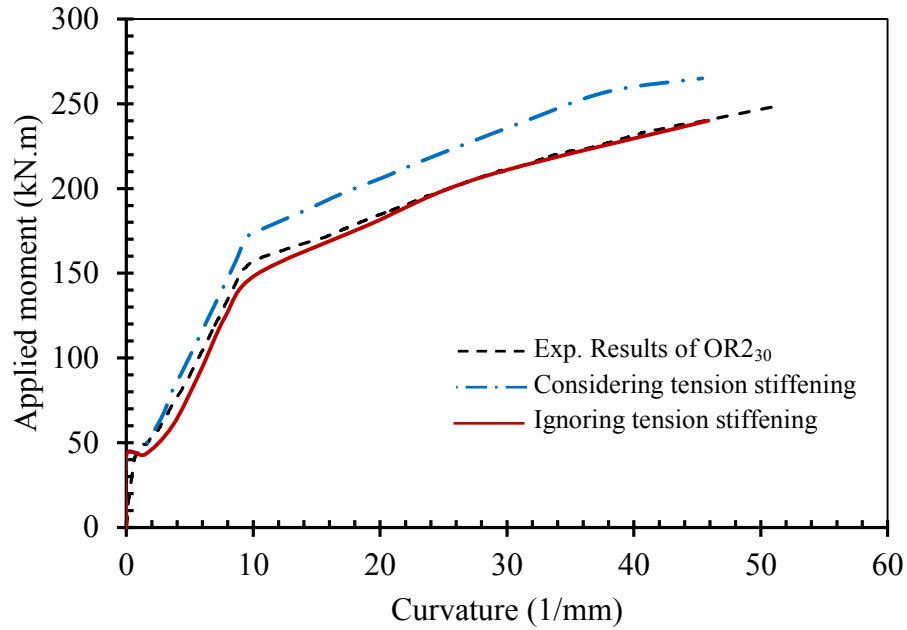


Figure 4.26 – Predicted versus experimental moment-curvature response of CFFT beam OR₂₃₀ (Model with partially confined concrete)

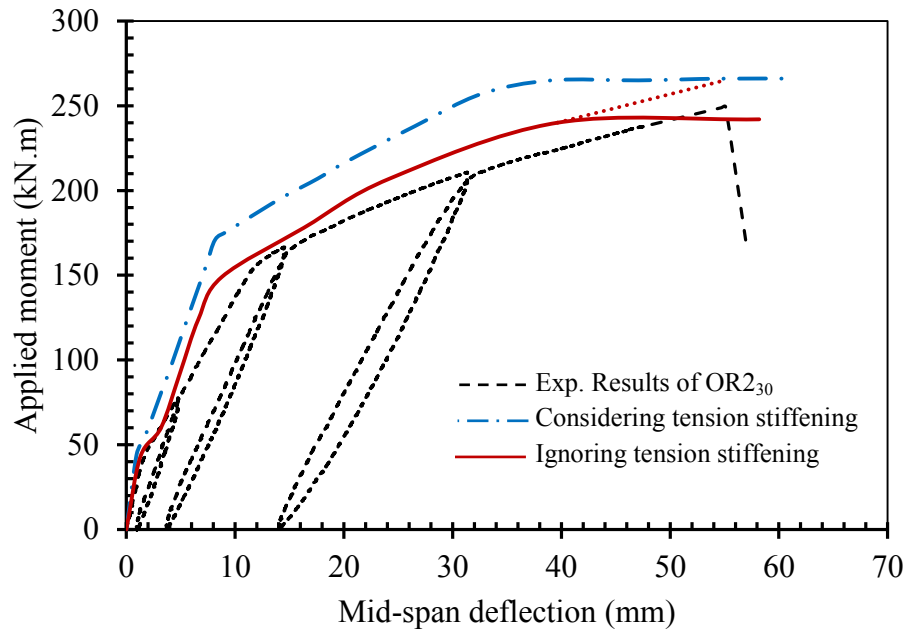


Figure 4.27 – Predicted versus experimental moment-deflection response of CFFT beam OR₂₃₀ (Model with partially confined concrete)

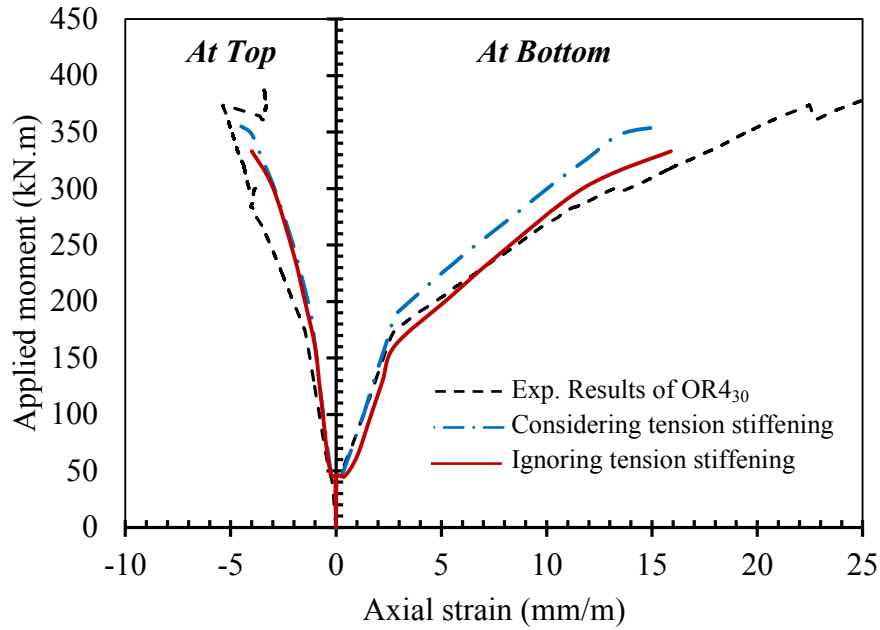


Figure 4.28 – Predicted versus experimental moment-strain response of CFFT beam OR4₃₀
(Model with partially confined concrete)

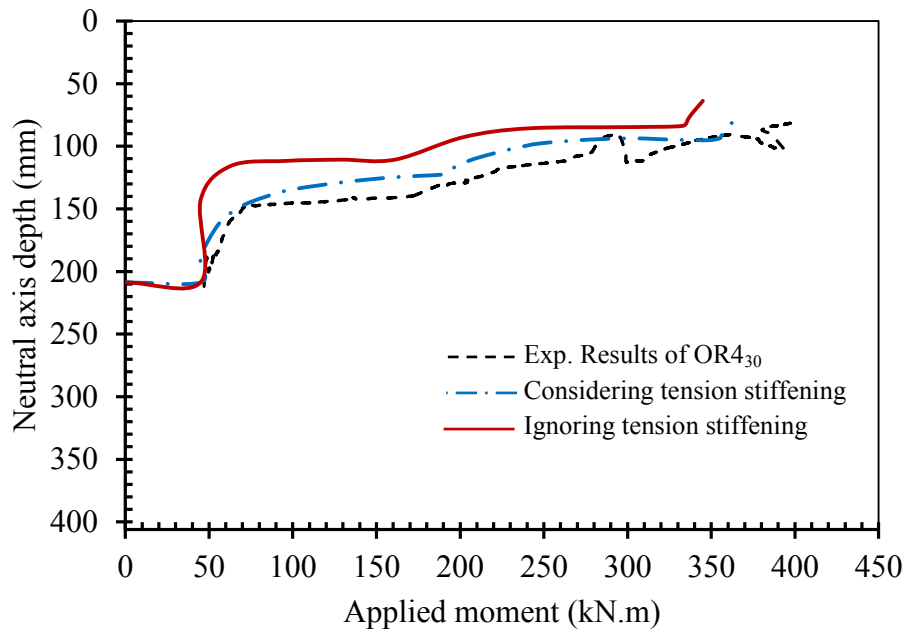


Figure 4.29 – Predicted versus experimental neutral axis depth of CFFT beam OR4₃₀
(Model with partially confined concrete)

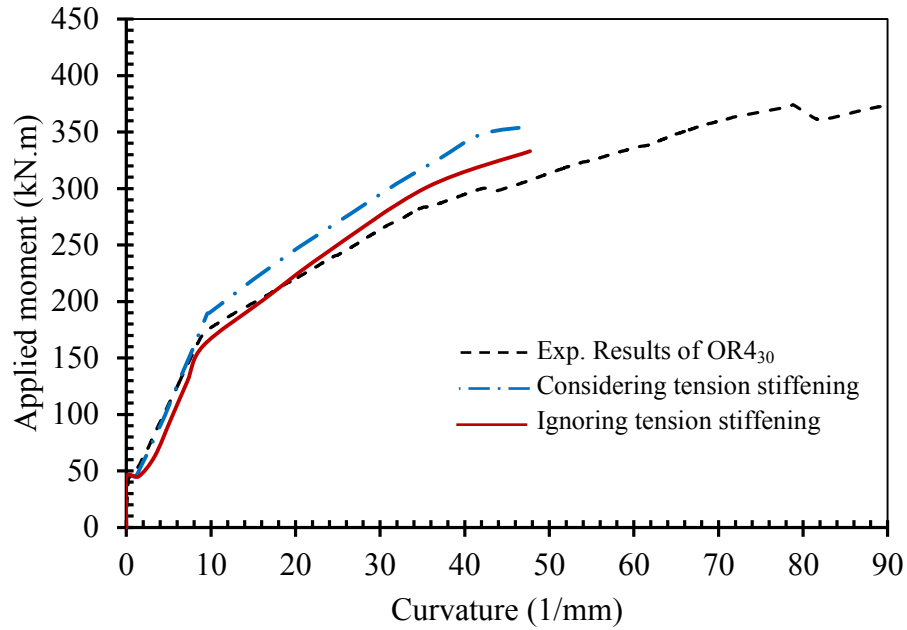


Figure 4.30 – Predicted versus experimental moment-curvature response of CFFT beam OR₄₃₀ (Model with partially confined concrete)

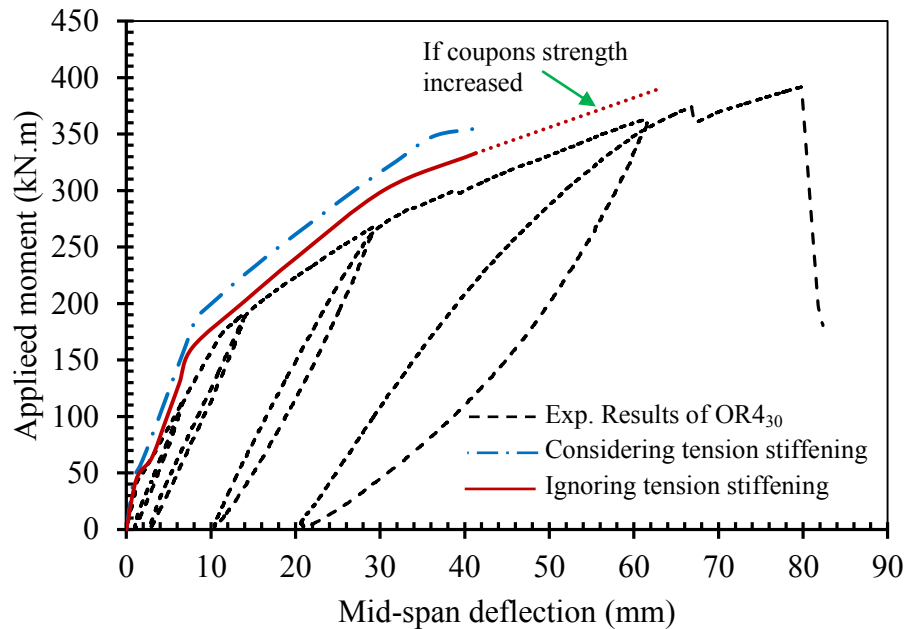


Figure 4.31 – Predicted versus experimental moment-deflection response of CFFT beam OR₄₃₀ (Model with partially confined concrete)

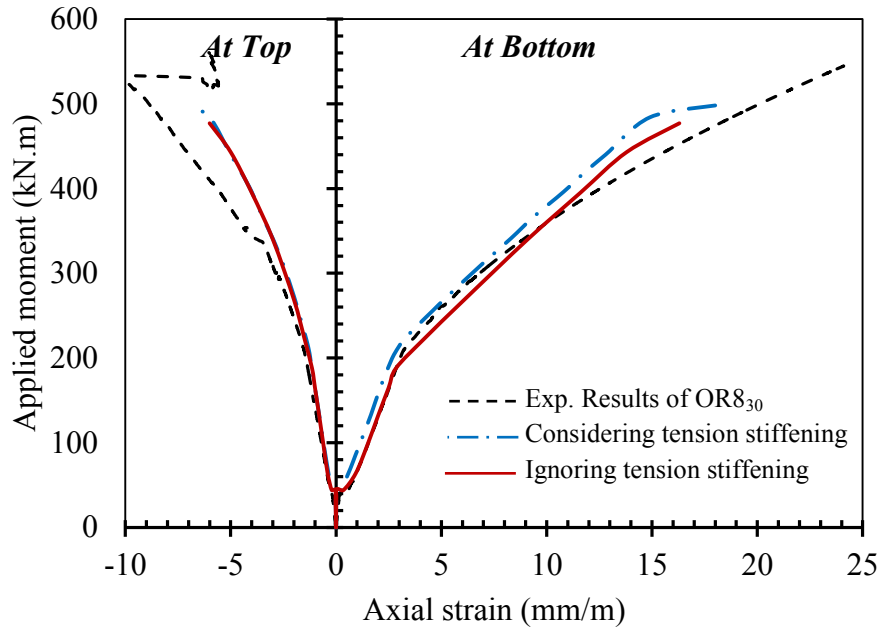


Figure 4.32 – Predicted versus experimental moment-strain response of CFFT beam OR8₃₀
(Model with partially confined concrete)

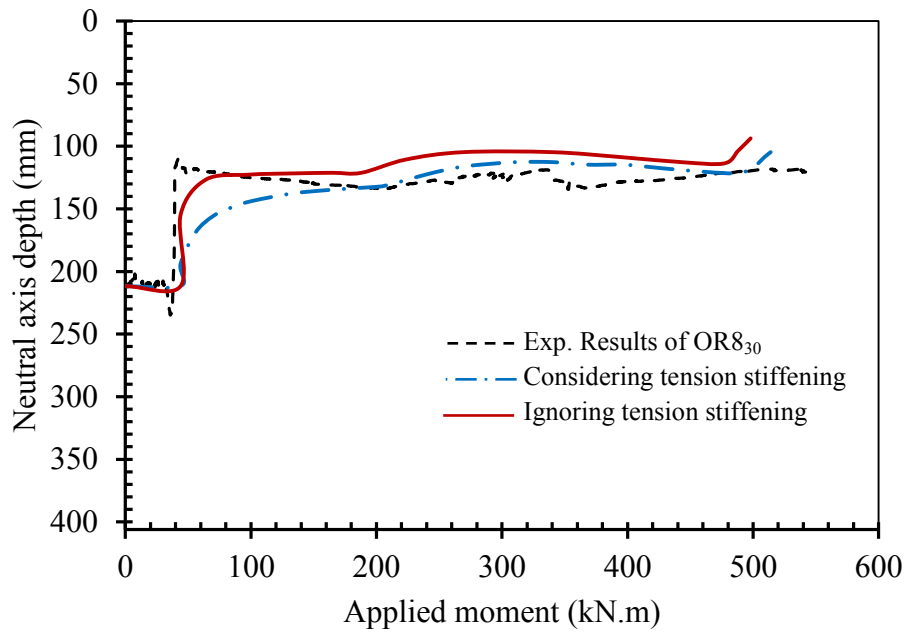


Figure 4.33 – Predicted versus experimental neutral axis depth of CFFT beam OR8₃₀
(Model with partially confined concrete)

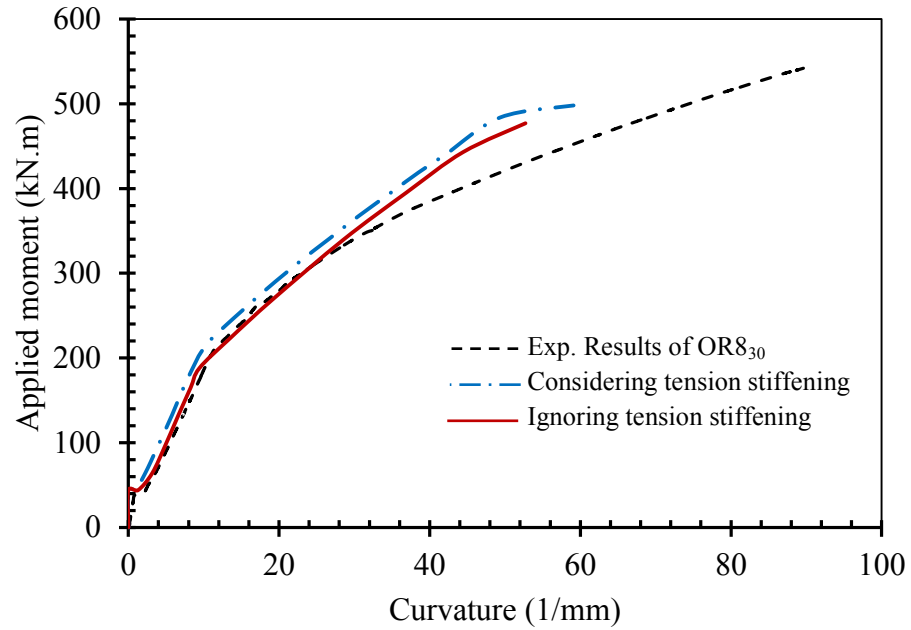


Figure 4.34 – Predicted versus experimental moment-curvature response of CFFT beam OR8₃₀ (Model with partially confined concrete)

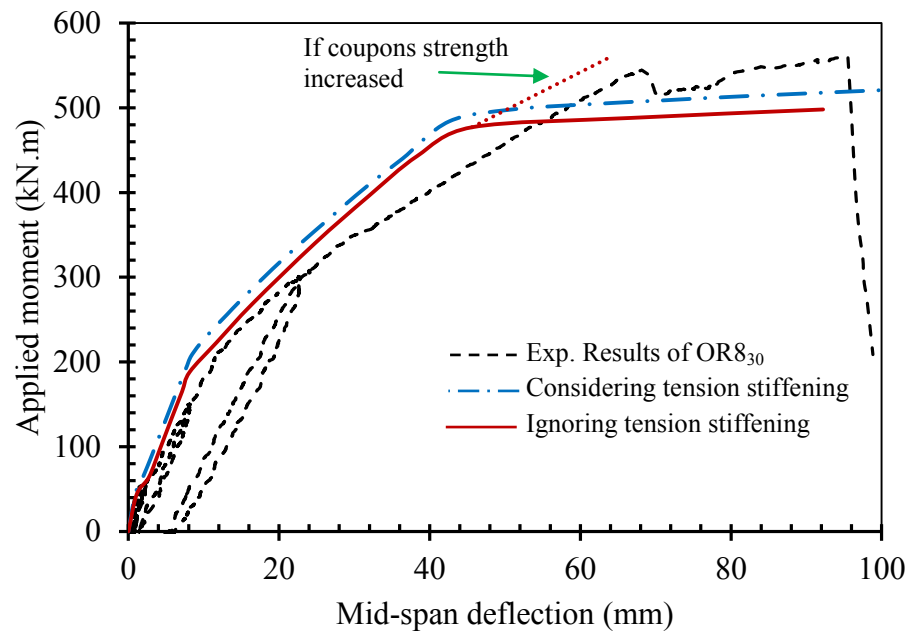


Figure 4.35 – Predicted versus experimental moment-deflection response of CFFT beam OR8₃₀ (Model with partially confined concrete)

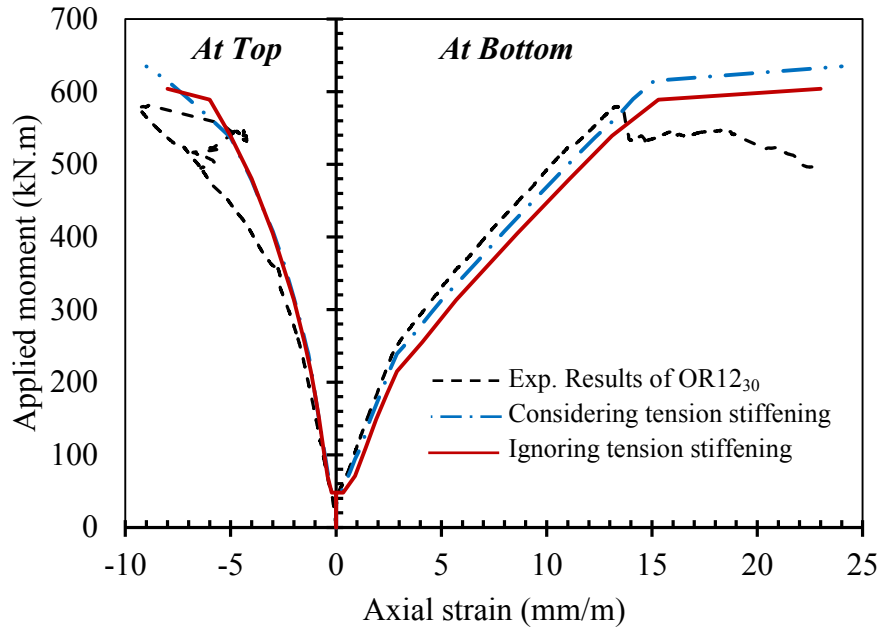


Figure 4.36 – Predicted versus experimental moment-strain response of CFFT beam OR12₃₀
(Model with partially confined concrete)

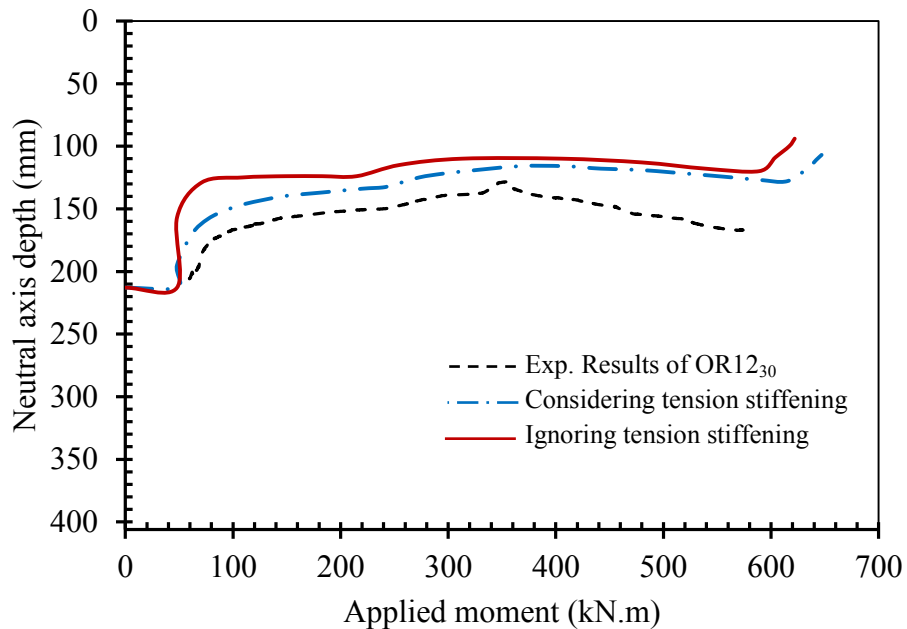


Figure 4.37 – Predicted versus experimental neutral axis depth of CFFT beam OR12₃₀
(Model with partially confined concrete)

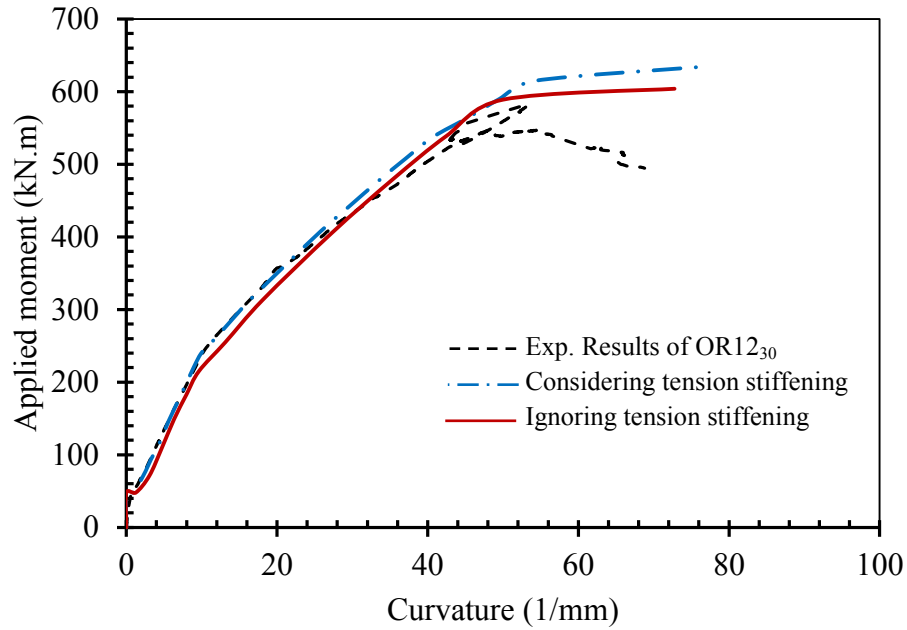


Figure 4.38 – Predicted versus experimental moment-curvature response of CFFT beam OR12₃₀ (Model with partially confined concrete)

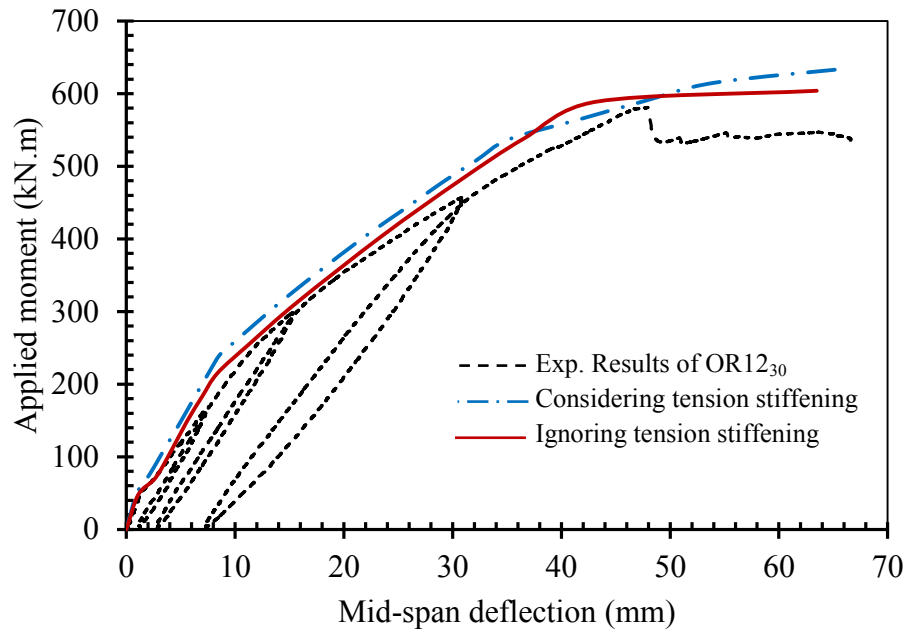


Figure 4.39 – Predicted versus experimental moment-deflection response of CFFT beam OR12₃₀ (Model with partially confined concrete)

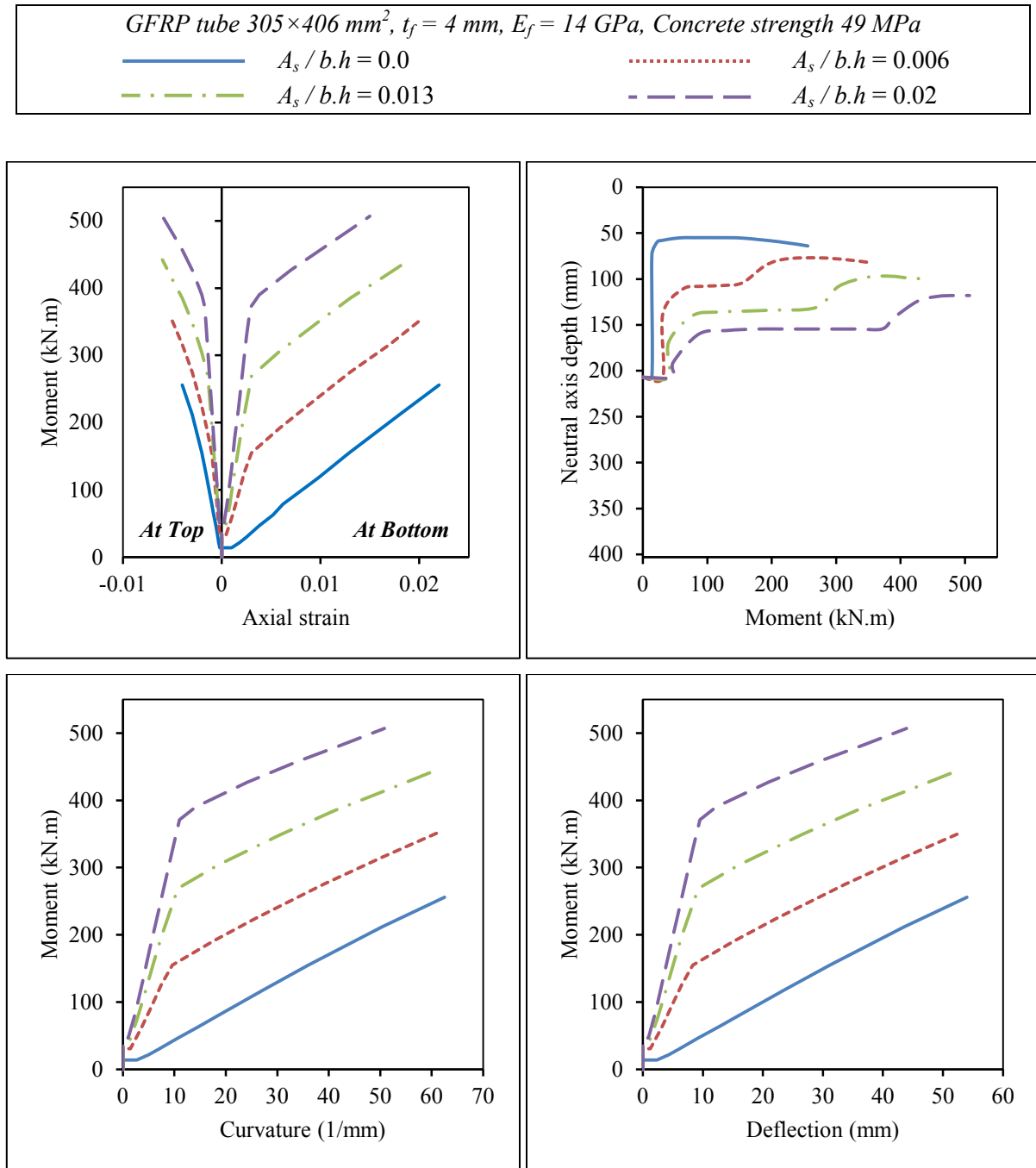


Figure 4.40 – Effect of steel reinforcement on the flexural behaviour of CFFT beams with thin FRP tubes

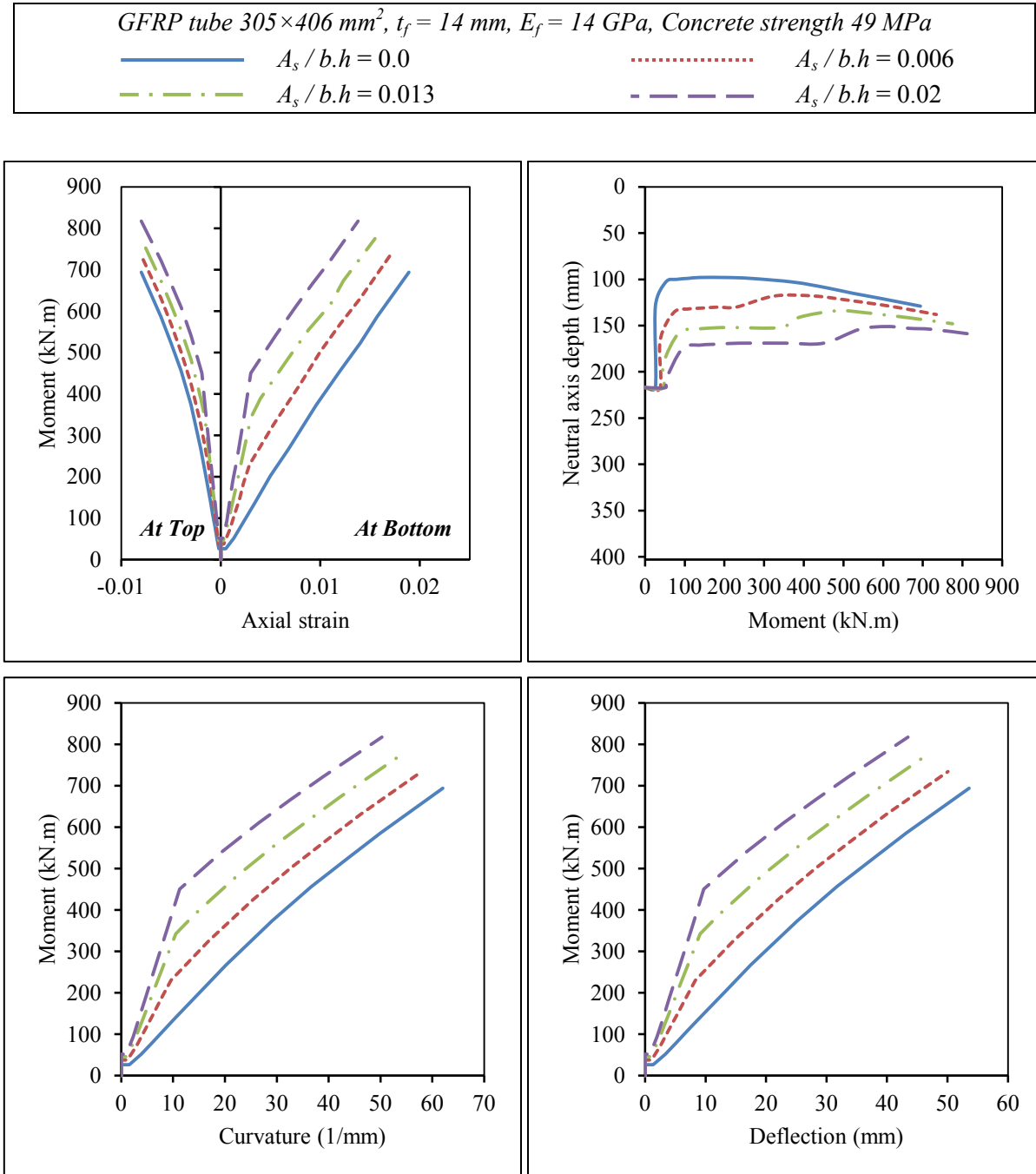


Figure 4.41 – Effect of steel reinforcement on the flexural behaviour of CFFT beams with thick FRP tubes

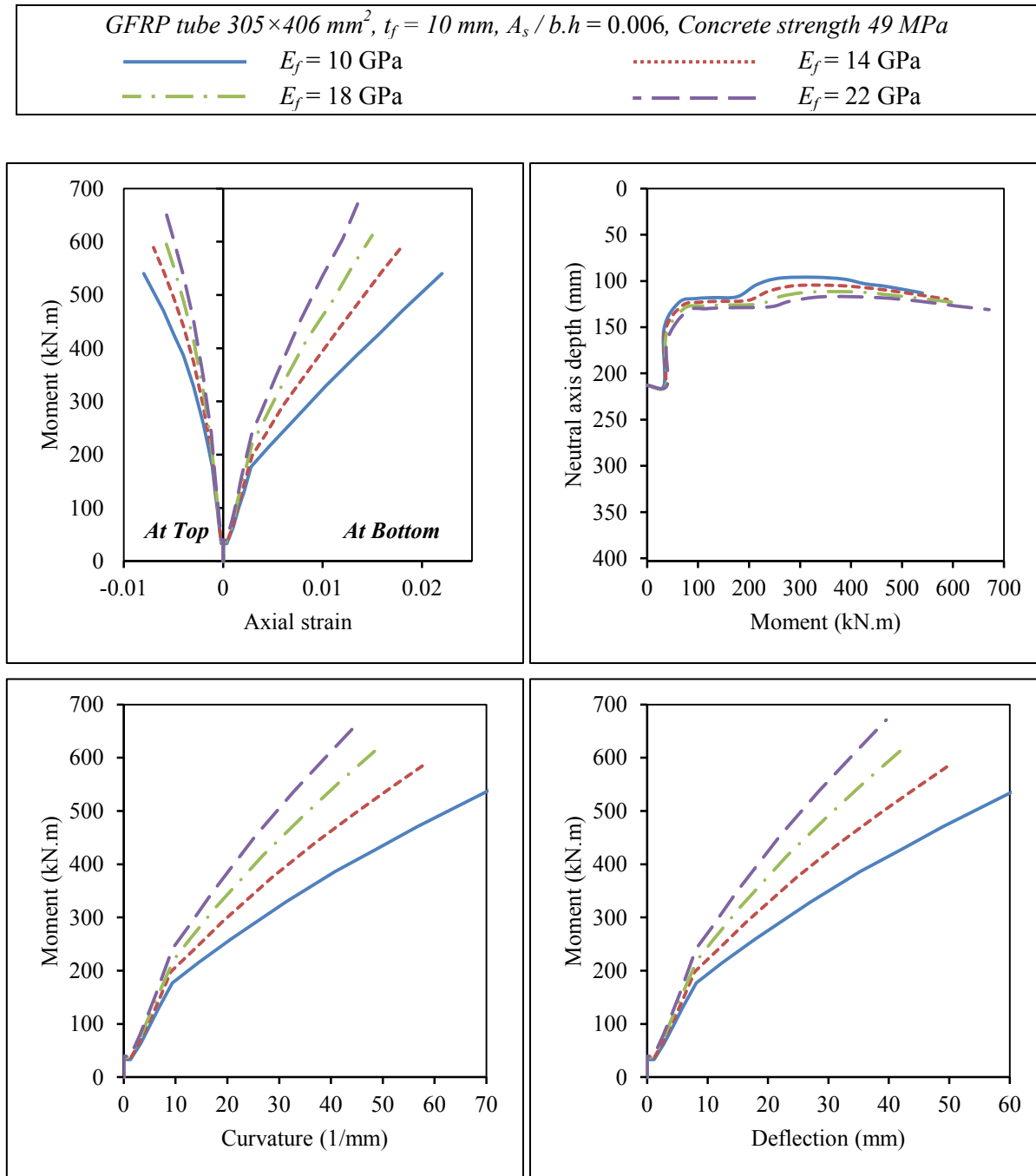


Figure 4.42 – Effect of fiber laminates structure on the flexural behaviour of CFFT beams

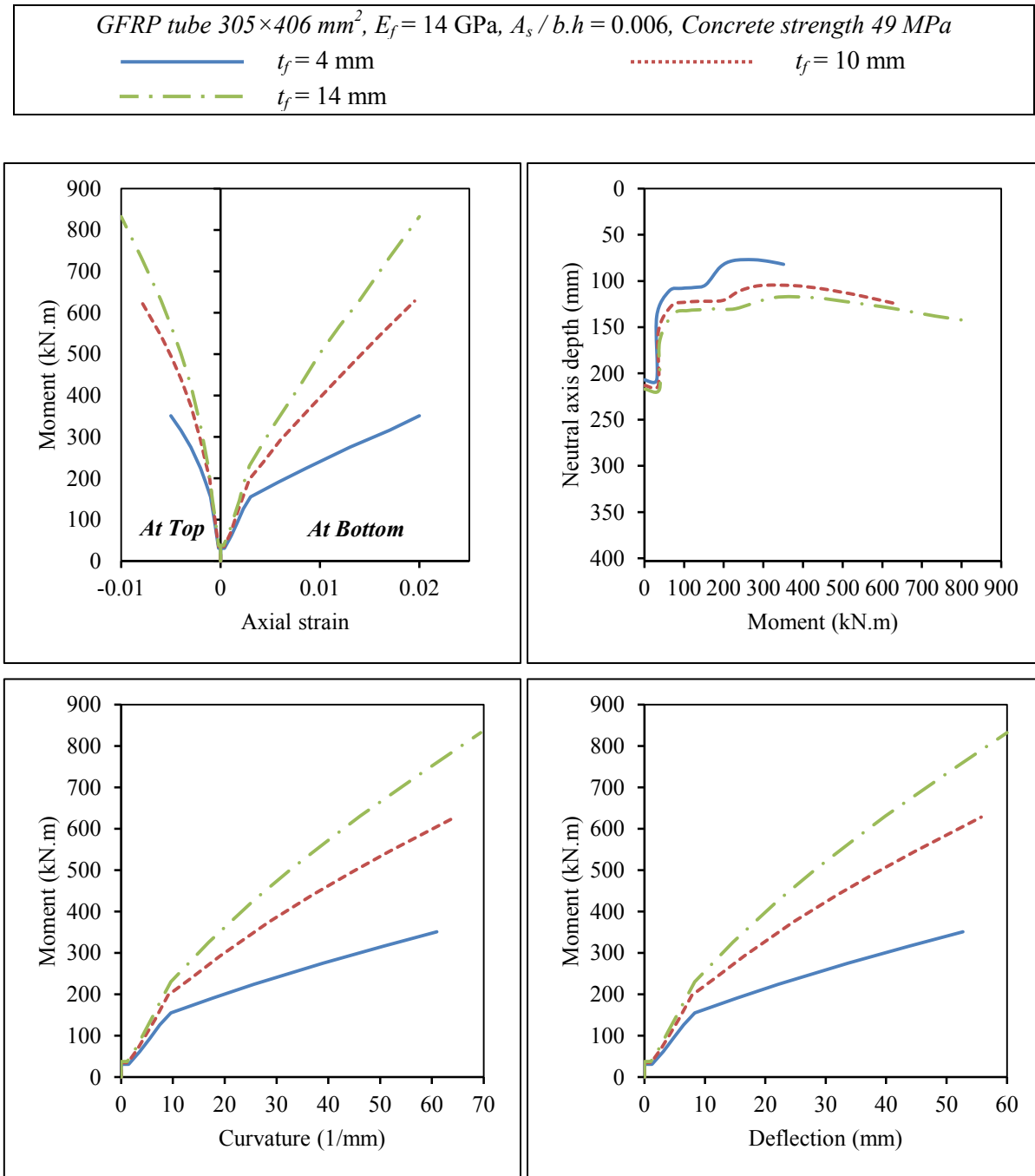


Figure 4.43 – Effect of FRP tube thickness on the flexural behaviour of CFFT beams

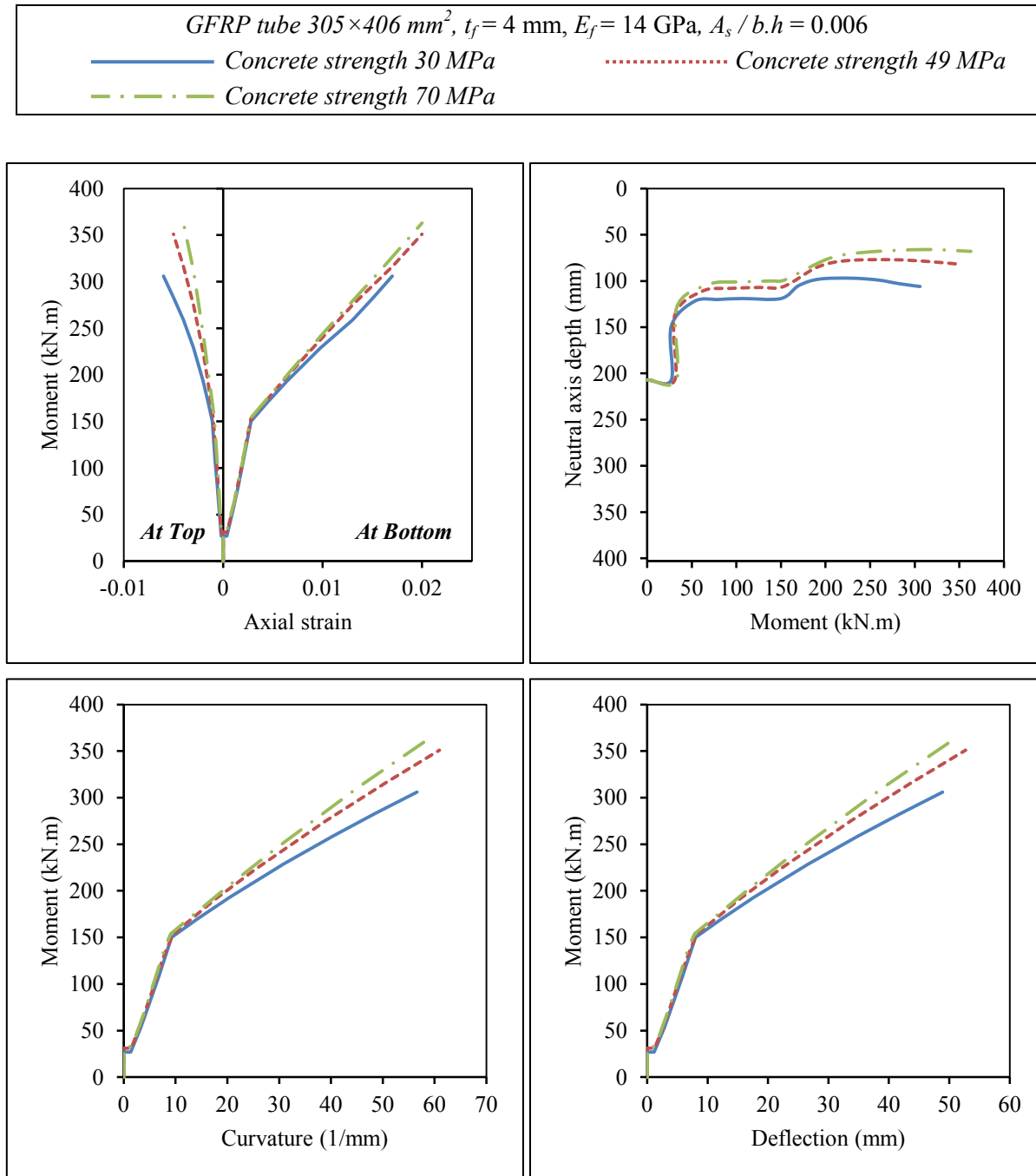


Figure 4.44 – Effect of concrete strength on the flexural behaviour of CFFT beams

CHAPTER 5

FLEXURAL BEHAVIOUR OF PARTIALLY-CFFT RECTANGULAR BEAMS

Foreword

Authors and Affiliation

- Ahmed Abouzied: PhD candidate, Department of Civil Engineering, Sherbrooke University, Sherbrooke, Quebec, Canada, J1K 2R1.
E-mail: ahmed.abouzied@usherbrooke.ca
- Radhouane Masmoudi: Professor, Department of Civil Engineering, Sherbrooke University, Sherbrooke, Quebec, Canada, J1K 2R1.
E-mail: radhouane.masmoudi@usherbrooke.ca

Journal Title: Elsevier–Construction and Building Materials Journal

Acceptance Status: Published online October 2015.

Reference: A. Abouzied and R. Masmoudi, 2015, “Structural performance of new fully and partially concrete-filled rectangular FRP-tube beams”, *Elsevier–Construction and Building Materials Journal*, Vol.101: 652–660.

Journal Title: ACI–Special Publication

Acceptance Status: Accepted for publication.

Reference: A. Abouzied and R. Masmoudi, (2016). “New high-performance rectangular FRP-tube beams partially filled with concrete”, *ACI–Special Publication*, SP-15.

5.1 ABSTRACT

This chapter investigates experimentally the flexural behaviour of fiber-reinforced polymer (FRP) double skin tubular beams partially filled with concrete and reinforced with steel rebar. This new design of hybrid FRP-concrete-steel composite beam contains outer rectangular filament-wound FRP tubes with inner hollow circular or square FRP tubes shifted toward the tension zone in addition to steel rebar at the tension side only. These inner tubes were provided inside the beam to eliminate the excess weight of the cracked concrete at the tension side and to enhance the confining action of corresponding rectangular fully-CFFT beams. Twenty-two full-scale beams, including fourteen partially-CFFT beams, six control fully-CFFT beams, and two control conventional steel-reinforced concrete (RC) beams, were tested under a four-point bending. Several parameters as the outer and inner tubes thickness, fiber laminates, and void shape were investigated to study their effects on the flexural strength and behaviour of such lightweight hybrid beams. The results indicate outstanding performance of the rectangular fully and partially-CFFT beams in terms of strength and ductility compared to the RC beams. The strength-to-weight ratio of the partially-CFFT beams attained higher values than that of corresponding fully-CFFT beams. The inner tubes act positively in reinforcing the partially-CFFT beams and confining the concrete core at the compression side and changed the failure to be gradual with warning signs unlike the fully-CFFT beams. The inner circular void pronounced better performance than the square inner void.

Keywords: Beams, Fiber-Reinforced Polymer, Filament-Wound, Concrete-Filled FRP Tubes, Flexural behaviour, Confinement.

5.2 INTRODUCTION

Concrete-filled fiber-reinforced polymer (FRP) tubes (CFFTs) are becoming an attractive alternative system for many special types of structural applications especially those attacked by corrosive environments such as piles, bridge piers, bridge girders, monopoles, and overhead sign structures. The outer FRP tube provides corrosion resistant element, lateral and longitudinal reinforcement, lightweight permanent formwork, in addition to confining the inner concrete core. On the other side, the concrete core provides support for the tube against local buckling in addition to its role to resist compressive loads.

CFFTs that are completely filled with concrete are not optimal for applications governed by pure bending, because the concrete below the neutral axis is cracked and it contributes slightly to bending resistance and mainly prevents the tube from buckling. As such, the excess weight of the cracked concrete may increase transportation and installation cost. A number of FRP-concrete hybrid systems have been developed over the years, including both open and closed FRP forms, to reduce the excess weight of the cracked concrete below the neutral axis [Deskovic and Triantafillou 1995; Canning et al.1999; Fam and Rizkalla 2002; Chakrapan 2005; Khennane 2010; Idris and Ozbakkaloglu 2014]. While, limited trials were carried out on filament-wound FRP tubes especially those with rectangular section [Fam et al. 2005].

Fam and Rizkalla (2002) investigated the effect of inner holes by testing circular CFFT beams with outer identical GFRP tubes 168 mm diameter. One beam was totally filled with concrete, one beam had a central hole, and another two beams had similar holes, but they are maintained by concentric and eccentric inner GFRP hollow tubes 89 mm diameter. The results indicated that the strength of the CFFT beam with a central hole was 9% less than that of the fully-CFFT beam. Moreover, providing an inner concentric GFRP hollow tube improved the strength by 7% more than that of the fully beam due to additional reinforcement. Shifting the inner GFRP hollow tube toward the tension side was more effective, where the strength increased by 39% higher than the fully CFFT beam.

Fam et al. (2005) designed a rectangular section, $266 \times 374 \text{ mm}^2$, of filament-wound GFRP tube with an inner rectangular air void. The strength of the voided section reached 78% of that completely filled with concrete. The hollow beam did not reach the target strength, because it failed by inward buckling and fracture of the unsupported concrete flange at the compression side.

Idris and Ozbakkaloglu (2014) investigated the flexural behaviour of FRP-high strength concrete (HSC)-steel composite beams by testing double-skin tubular beams (DSTBs) with outer GFRP tubes and a central inner hollow steel section (HSS). The main parameters of the study included the cross-sectional shapes of the inner HSS and the external GFRP tube, concrete strength, presence or absence of concrete filling inside the steel tube, and effects of using mechanical connectors to enhance the bond between the steel tube and surrounding concrete. The results indicated that DSTBs exhibit excellent load-deflection behaviours with high inelastic deformations and minimal strength degradations (slightly increase of flexural strength after yielding). However, relatively large slippage can occur at the concrete-steel tube interface unless the bond is enhanced by mechanical connectors. Regardless the high flexural strength and stiffness of the DSTBs based on the inner steel tube, the weight and the bond remain critical issues in this design and need further investigations.

In this study, the author tries to get benefit of each advantage of each design in the previous literature and to merge them together to develop a new design of partially-CFFT beams. This design contains:

- 1) Outer rectangular FRP tubes to increase the sectional moment of inertia, to provide flexural and shear reinforcement, and to protect the inner structural elements (concrete and steel) against corrosion.
- 2) Inner holes shifted toward the tension zone to increase the compression zone area.
- 3) The holes were provided by inner hollow FRP tubes to support and confine the concrete at the compression side and act as reinforcement.
- 4) Steel rebar was provided at the tension side to increase the stiffness and strength of the section.

- 5) The surfaces of tubes adjacent to concrete were roughened by sand coating to achieve a full composite action.

The main objective of this chapter is to investigate the experimental results of beam tests carried out on partially-CFFT beams in the current experimental program indicated in Chapter 3. This objective is accomplished by expressing the experimental results in terms of moment-deflection response, patterns of failure, strain behaviour, and strength-to-weight ratio. Further analysis and discussion is carried out to investigate the effect of each test variable as outer tubes thickness and laminates, inner tube thickness, inner hollow tubes shapes, inner tubes laminates, and steel reinforcement.

5.3 EXPERIMENTAL PROGRAM

In this chapter, twenty-two full-scale rectangular beams, including fourteen partially-CFFT beams, six fully-CFFT beams, and two conventional RC beams, were tested under a four-point bending setup. Table 5.1 presents the details of the beam specimens studied in this chapter. The detailed description of the experimental program was illustrated in Chapter 3.

5.4 TEST RESULTS AND DISCUSSIONS

The objective of this study is to evaluate the flexural behaviour of new design of rectangular partially-CFFT beams with steel rebar. This objective was accomplished as the shear failure and slippage failure were avoided and all the tested beams failed by flexure. Figure 5.1 plots the correlation between the applied moment and the slip at the two ends of the tested partially-CFFT beams. Note that, the results of the fully-CFFT beam were discussed in details in Chapter 4. Almost no slip readings between the concrete core and the tubes were recorded until the ultimate load, even after the ultimate failure the maximum slip measured did not exceed 0.2 mm, which can be neglected. Therefore, a full composite action was achieved. This is attributed to the roughened surface of the tubes by sand coating and the presence of the deformed steel bars with hooks that hold the concrete core in its place.

The applied moment was calculated by multiplying the concentrated load ($P/2$) with the shear span (a), while the deflection was measured at the mid-span. Although the concrete core was hidden behind the tubes surface, the cracking moment (M_{cr}) was evaluated from the readings of the steel strains, axial strains of the tube bottom face, or the curvature response change as shown in Figure 5.2. The experimental yielding moment (M_y) was evaluated from the yielding plateau of the moment-strain response of the embedded steel at the tension side as shown in Figure 5.2(a). Table 5.1 summarizes the beam test results as the flexural moments at the first crack, yield moment, ultimate moment (at the peak), the ultimate mid-span deflection (at the peak), the failure mode, and the ductility. The ductility was evaluated by the energy absorption determined as the area under the moment-deflection curve until the peak load. Generally, the two identical beams in each group behaved almost typically and their average results are used in the comparisons. The following sections provide detailed comparisons and discussions for the test results including the effect of the test parameters.

5.4.1 Shear Strength of Rectangular Partially-CFFT Beams

This dissertation concentrates mainly on the flexural behaviour of rectangular CFFT beams, so the beams and tests setup was designed to avoid any shear failure at the supports. The fabricated filament-wound GFRP tubes were designed to have adequate fibers in their transverse direction. Therefore, the tube itself acts as continuous shear reinforcement around the cross section perimeter of the CFFT beam. Nevertheless, it is important to investigate the shear strength carefully in case of partially-CFFT beams because of presence of inner voids.

Although none of the fully or partially-CFFT beams failed in shear, the contribution of the FRP tube in resisting shear, V_f , can be approximately evaluated from the measured nominal shear force, V_n , at the ultimate flexural failure reduced by the concrete contribution in shear, V_c , which is calculated according to ACI-318 (2014), as follows:

$$V_f = V_n - V_c \quad (5.1)$$

$$V_c = 0.17\lambda\sqrt{f'_c}b_w d \dots\dots \lambda = 1 \quad (5.2)$$

In the current study, $b_w d$ is approximated as the area of the concrete core, A_c , excluding the inner void area and the factor λ equals the unit for the normal weight concrete.

Assuming a diagonal shear crack at 45° , as shown in Figure 5.3, the shear resisting force in the FRP tube webs produces vertical tensile stresses in the GFRP tube webs, F_f , which can be calculated as:

$$F_f = \frac{0.5V_f \cos 45^\circ}{t_f d_{eff}} \quad (5.3)$$

Where, d_{eff} is the effective straight depth of the rectangular GFRP tube webs excluding the rounded corners. Table 5.2 lists the shear forces calculations in the tested fully and partially-CFFT beams. The calculated stresses in the outer GFRP tube, F_f , were compared to the allowable tensile strength in the transverse direction of the rectangular GFRP tubes, F_{tr} , evaluated experimentally from the coupons tests (see Table 3.1 in Chapter 3). The results indicate that the developed tensile stresses in the GFRP tubes due to the shear forces are relatively very low compared to the tensile strength of the GFRP tubes in the transverse direction, since the ratio F_f / F_{tr} did not exceed 23% and 26% in case of partially-CFFT beams and fully-CFFT beams, respectively. These results indicate effective shear reinforcement action of the filament-wound GFRP tube.

5.4.2 Flexural Behaviour of RC Beams and Fully-CFFT Beams

See Chapter 4.

5.4.3 Failure Pattern of Partially-CFFT Beams

All the tested partially-CFFT beams failed by flexure without any signs of shear failure, web buckling, or slippage between the concrete core and the tubes. Figures 5.8 to 5.15 present the failure patterns of the partially-CFFT beams OR2₃₀-IC4₃₀, OR4₃₀-IC4₃₀, OR4₃₀-IC2₃₀, OR8₃₀-IC4₃₀, OR4₃₀-IS2₃₀, OR4₃₀-IS4₃₀, OR4₃₀-IS4₆₅, and OR8₃₀-IS4₃₀.

All the partially-CFFT beams, with circular or square voids, failed in typical way by flexure in compression. Generally, the failure pattern of the partially-CFFT beams was not sudden like the fully-CFFT beams (see Figures 5.4 to 5.7), but there was gradual degradation of strength after the peak. The ultimate compression failure occurred after yielding of the steel. It started with inflated flanges like waves at the compression side followed by outward buckling as shown in Figure 5.12(a). Then, a rupture of the GFRP tube in the transverse direction of the tube occurred, as shown in the top views in Figures 5.8 to 5.11 that present the failure pattern of the partially-CFFT beams with circular void. This transverse rupture of fibers indicates confining action on the concrete at the compression zone. This is attributed to the active confining action of the inner GFRP tubes and the passive confining action of the outer GFRP tubes on the concrete at the compression zone. In case of partially-CFFT beams with inner square voids, the transverse fibers rupture was not clear as the axial outward buckling as shown in the top views in Figures 5.12 to 5.15. This confirms the lower flexural performance and strength of the partially-CFFT beams with inner square void compared to that with circular voids as listed in Table 5.1. Further analysis about the effect of the inner void shape will be discussed in the following sections.

Some beams were continued to be loaded to high levels of deformations. It was noticed that the bottom tensile flange remained active and could withstand high axial strains as shown in Figures 5.9, 5.10, 5.11, and 5.15 that present the failure patterns of the partially-CFFT beams OR4₃₀-IC4₃₀, OR4₃₀-IC2₃₀, OR8₃₀-IC4₃₀, and OR8₃₀-IS4₃₀, respectively. While the other beams OR2₃₀-IC4₃₀, OR4₃₀-IS2₃₀, OR4₃₀-IS4₃₀, and OR4₃₀-IS4₆₅ failed at the end by axial rupture of fibers at the tension side as shown in Figures 5.8, 5.12, 5.13, and 5.14, respectively. Note that, this final secondary failure happened at very high levels of deformations and curvature. This observation is attributed to the partially-CFFTs with thicker outer tube and inner circular voids behave better and stronger than that with thin outer tube and inner square voids.

The fourth cycles in Figures 5.12 to 5.15 pronounced an elastic behaviour at low levels of the unloading cycles. Note that, these beams failed in compression and had inner square voids. This elastic behaviour is attributed to the GFRP tubes tension flanges of these beams were still active and had not been failed yet. By continuing loading to high levels of deformations

and curvature, some bottom GFRP tubes flanges failed in tension and accordingly the residual deflection became large as shown in Figure 5.12 to 5.14. The beams OR8₃₀-IS4₃₀, which their tensile flanges attained high levels of strains without failure, pronounced again an elastic return after releasing the load at the end of the test, as shown in Figure 5.15.

5.4.4 Flexural Performance of Rectangular Partially-CFFT Beams

The following sections investigate experimentally the performance of a new design of partially-CFFT beams. Fourteen partially-CFFT beams with different configuration were compared to six control fully-CFFT beams and another two control RC beams. Table 5.1 lists the details of the test matrix and the beams details.

The patterns of failure indicate that the partially-CFFT beams failed in compression with gradual loss of strength unlike the fully-CFFT beams that failed in tension by axial rupture of fibers. In addition, the results indicate non-linear moment-deflection responses of the Partially-CFFT beams with an ascending flexural strength after yielding of the embedded steel. This non-linear behaviour is attributed to the effective confinement of the concrete at the compression side that is considered as a nonlinear material.

Further comparisons and discussion are illustrated in the following sections to study the effect of the outer tube thickness, inner tube thickness, inner tube laminates, and inner tube shape. To facilitate the analysis the reloading cycles are eliminated from the curves and the outer envelopes are used in the comparisons.

5.4.4.1 Effect of the Outer Tube Thickness in Partially-CFFT Beams

Figure 5.16 plots the moment-deflection responses of the Partially-CFFT beams with circular voids OR2₃₀-IC4₃₀, OR4₃₀-IC4₃₀, and OR8₃₀-IC4₃₀ compared to that of the control RC beams. These Partially-CFFT beams were chosen to study the effect of the outer tube thickness since they have three different outer tube thickness and they have the same inner hollow GFRP tube and steel reinforcement.

The results indicate significant gain in strength, stiffness, and ductility of the rectangular partially-CFFT beams compared to the conventional RC beams (see also Table 5.1). For example, the partially-CFFT beam OR2₃₀-IC4₃₀ that has an outer tube of 3.4 mm thickness attained an ultimate flexural strength and ductility 115% and 284% higher than that of the RC beams, respectively. This enhancement increases with increasing the tube thickness. For example, the partially-CFFT beam OR4₃₀-IC4₃₀ that has an outer tube of 5.7 mm thickness attained an ultimate flexural strength and ductility 190% and 380% higher than that of the RC beams, respectively. Moreover, the partially-CFFT beams OR8₃₀-IC4₃₀ that have an outer tube of 8.7 mm thickness attained an ultimate flexural strength and ductility 211% and 332% higher than that of the RC beam, respectively. As seen in OR8₃₀-IC4₃₀, the gain in strength decelerated and the ductility decreased.

The flexural behaviour is illustrated in Figure 5.17, which plots the correlations between the flexural moments at different stages (first crack, yield, ultimate) compared to the normalized strength of the outer FRP tubes represented by their reinforcement ratio $\rho_f (=A_f/A_c)$ multiplied by their modular ratio $n_f (=E_f/E_{co})$. Note that, E_f is taken as the average modulus of elasticity from the compression and tension coupons tests in the axial direction of the outer GFRP tubes.

The results of M_{cr} , shown in Table 5.1, indicate minor difference among the partially-CFFT beams OR2₃₀-IC4₃₀, OR4₃₀-IC4₃₀, and OR8₃₀-IC4₃₀ with changing their tube outer thickness, and the average M_{cr} of them is 35.8 kN.m. The results in Table 5.1 indicate also that M_y of the partially-CFFT beams OR2₃₀-IC4₃₀, OR4₃₀-IC4₃₀, and OR8₃₀-IC4₃₀ was significantly greater than that of the RC beam, and increases with increasing the FRP tube thickness. Figure 5.17(a) indicates a linear increase of M_y with increasing the outer tube thickness. It is attributed to the excess contribution of the elastic GFRP tube material as flexural reinforcement in the cracked section.

Figure 5.17(b) indicates a non-linear increase in the ultimate moment M_u until a certain limit. This limit is also clearly shown in Figure 5.17(c), which mainly represents the post-yielding stage by comparing M_u/M_y to the tube strength where at this stage the reinforcement action of the GFRP tube is effective and significant. This limit is lower than that in case of fully-CFFT

beams (See section 4.4.5.3 in Chapter 4). This is attributed to the early outward buckling of the tube compression flange due to the excessive compression forces developed to balance the section. In other words, the inner tubes increased the internal tensile forces of the section, and accordingly the compression forces increased to balance the section forces. Since the inner tubes restrain the concrete area at the compression side, then the compression forces can be propagated from increasing the compressive contribution of the tube flange and/or increasing the concrete strength due to confinement. The non-linear increase in Figure 5.17(b, c) indicates that increasing the thickness of the tube does not mean increasing the ultimate capacity of the CFFT beam, but there is an optimum FRP reinforcement ratio to achieve the maximum capacity.

Based on the results of the current study and shown in Figure 5.17, the flexural moments at different stages (first crack, yield, and ultimate) of partially-CFFT beam with circular voids could be estimated approximately by regression analysis if one of them is known, for example M_{cr} , as following:

$$M_y = M_{cr} [44.70(\rho_f n_f) + 3.70] \quad (5.4)$$

$$M_u = M_{cr} [-6820.64(\rho_f n_f)^2 + 609.83(\rho_f n_f) - 1.56] \quad (5.5)$$

$$M_u = M_y [-1171.99(\rho_f n_f)^2 + 91.62(\rho_f n_f) + 0.36] \quad (5.6)$$

5.4.4.2 Effect of the Inner Tube Thickness in Partially-CFFT Beams

Figure 5.18(a) plots the moment-deflection response of the partially-CFFT beams OR4₃₀-IC4₃₀ and OR4₃₀-IC2₃₀, which have inner circular tubes with thickness of 3.1 and 2.1 mm, respectively. Figure 5.18(b) plots the moment-deflection response of partially-CFFT beams OR4₃₀-IS4₃₀ and OR4₃₀-IS2₃₀, which have inner square tubes with thickness of 4.7 and 2.9 mm, respectively. The results indicate that the effect of the inner tubes thickness on the ultimate flexural capacity is insignificant. The partially-CFFT beams with circular voids OR4₃₀-IC4₃₀ and OR4₃₀-IC2₃₀ attained average ultimate flexural capacity of 380 and 379.5 kN.m, respectively. While the partially-CFFT beams with square voids OR4₃₀-IS4₃₀ and OR4₃₀-IS2₃₀ attained average ultimate flexural capacity of 289.5 and 291 kN.m, respectively.

These results indicate the minor effect of the inner tube thickness on the flexural capacity of the partially-CFFT beams. This minor effect could be attributed to minor difference between the reinforcement action of the inner FRP tubes in the partially-CFFT beams, because of the irregular distribution of the strains along the inner tube depth and the low modulus of elasticity of the FRP tube. Figure 5.19 shows typical neutral axes locations based on strains distribution along the partially-CFFT beam depth. Almost the total cross section of the inner tubes exists below the neutral axis. The top face of the inner tube is not efficient at all in reinforcing the section due to the almost zero strain values. While the bottom face of the inner tubes has low strains compared to the steel bars and the bottom face of the outer rectangular FRP tube.

Figures 5.18(a, b) show that the primary flexural stiffness of the partially-CFFT beams was the same despite the different thickness of the inner tube thickness. The partially-CFFT beam OR4₃₀-IC4₃₀, which has a thick inner circular tube of 3.1 mm thickness, pronounced an increase in the flexural stiffness at the post-yielding stage. The partially-CFFT beams OR4₃₀-IS4₃₀, which have thick inner square tubes of 4.7 mm thickness, pronounced also an increase in the flexural stiffness at the post-yielding stage, however, it was limited. This increase means an increase in the moment of inertia of the cracked section, I_{cr} . This increase can be attributed to the enhanced properties of the confined concrete between the outer and inner tubes (low cracks, low crushing, and increase of its efficient confined area).

5.4.4.3 Effect of the Inner Tube Laminate Structure in Partially-CFFT Beams

The effect of the inner tube laminate structure is investigated by comparing the flexural results of the partially-CFFT beams OR4₃₀-IS4₃₀ and OR4₃₀-IS4₆₅ shown in Figure 5.20. The beams have inner square GFRP tubes with a similar number of fiber layers but with different fiber stacking sequence. The partially-CFFT beams OR4₃₀-IS4₃₀ have inner GFRP tubes with helical fiber orientation of 30° to the longitudinal axis and thickness of 4.7 mm, while the partially-CFFT beams OR4₃₀-IS4₆₅ have inner GFRP tubes with helical fiber orientation of 65° to the longitudinal axis and thickness of 4.2 mm. The difference in the tube thickness is attributed to the fibers overlap and strokes during the filament-winding process, since the low winding angles (30°) need more strokes to cover the surface area of the mandrels.

The results indicate that the partially-CFFT beams OR4₃₀-IS4₃₀, which have inner GFRP tubes with more fibers in the axial direction, attained average ultimate flexural capacity of 289.5 kN.m. While the partially-CFFT beams OR4₃₀-IS4₆₅, which have inner GFRP tubes with less fibers in the axial direction, attained average ultimate flexural capacity of 273 kN.m that is 6% lower than that of OR4₃₀-IS4₃₀ beams. This difference indicates the reinforcement contribution of the inner FRP tube despite its minor value. The results indicate also similar primary flexural stiffness of OR4₃₀-IS4₃₀ and OR4₃₀-IS4₆₅, but after yielding, the flexural stiffness of OR4₃₀-IS4₃₀ becomes higher than that of OR4₃₀-IS4₆₅.

5.4.4.4 Effect of the Inner Tube Shape in Partially-CFFT Beams

The size of the circular and square voids used in this study was chosen to have almost the same void area ($3.7 \times 10^4 \text{ mm}^2$ for the circular void and $4.0 \times 10^4 \text{ mm}^2$ for the square void). Comparisons were carried out to investigate the effect of the void shape on the performance of the partially-CFFT beams by comparing OR4₃₀-IC2₃₀ versus OR4₃₀-IS2₃₀, OR4₃₀-IC4₃₀ versus OR4₃₀-IS4₃₀, and OR8₃₀-IC4₃₀ versus OR8₃₀-IS4₃₀, as shown in Figure 5.21.

The average M_{cr} of OR4₃₀-IC2₃₀ beams is 35.5 kN.m, which is 15% lower than that of OR4₃₀-IS2₃₀ beams that equals 42 kN.m. Moreover, M_{cr} of OR4₃₀-IC4₃₀ beam is 34 kN.m, which is 15% lower than the average M_y of OR4₃₀-IS4₃₀ beams that equals 40 kN.m. While, the average M_{cr} of OR8₃₀-IC4₃₀ beams is 38.4 kN.m (normalized due to the different compressive strength of concrete), which is 11% lower than that of OR8₃₀-IS4₃₀ beams that equals 43 kN.m. The results indicate that the partially-CFFT beams with square voids have high M_{cr} compared to the partially-CFFT beams with circular voids. This difference is attributed to the cross sectional area of the inner square tubes walls is higher than that of the circular tubes. Therefore, the contribution of the square tube in calculating the gross moment of inertia I_g is higher than the circular tube since they have almost the same tensile axial modulus of elasticity. Note that, the cracks propagation is not critical in this type of FRP-protected beams, but the cracking strength is important in calculation of deflection and cracks width.

The average M_y of OR4₃₀-IC2₃₀ beams is 182 kN.m, which is 3% higher than that of OR4₃₀-IS2₃₀ beams that equals 177 kN.m. Moreover, M_y of OR4₃₀-IC4₃₀ beam is 180 kN.m, which is

3% higher than the average M_y of OR4₃₀-IS4₃₀ beams that equals 175 kN.m. While, the average M_y of OR8₃₀-IC4₃₀ beams is 251 kN.m (normalized due to the different compressive strength of concrete), which is 12% higher than that of OR8₃₀-IS4₃₀ beams that equals 224 kN.m. The results indicate that the partially-CFFT beams with circular voids have high M_y , compared to the partially-CFFT beams with square voids. Note that, the cross sectional area of the inner circular tubes wall is less than that of the inner square tube. Then, the enhancement in M_y can be attributed to the steel bars are not surrounded well with much concrete in the partially-CFFT beams with square voids unlike in the partially-CFFT beams with circular voids, leading to less compatibility with the other structural elements in the section. In other words, the shear flow along the cross section is smoother and more homogeneous around the circular void than the square void.

At ultimate failure, the average M_u of OR4₃₀-IC2₃₀ beams is 379.5 kN.m, which is 30% higher than that of OR4₃₀-IS2₃₀ beams that equals 291 kN.m. Moreover, M_u of OR4₃₀-IC4₃₀ beam is 380 kN.m, which is 31% higher than the average M_u of OR4₃₀-IS4₃₀ beams that equals 289.5 kN.m. While, the average M_u of OR8₃₀-IC4₃₀ beams is 486 kN.m (normalized due to the different compressive strength of concrete), which is 7% higher than that of OR8₃₀-IS4₃₀ beams that equals 455.5 kN.m. The results indicate better performance of the partially-CFFT beams with circular voids more than the partially-CFFT beams with square voids. As seen, the performance increases in the ultimate stage than the yielding stage than the cracking stage. It is attributed to the better compatibility of the circular void shape inside the section, and the confinement action that appear commonly at high levels of load.

5.4.5 Comparison between Fully and Partially-CFFT Beams

Figure 5.22 plots the moment-deflection responses of the partially-CFFT beams OR2₃₀-IC4₃₀, OR4₃₀-IC4₃₀, and OR8₃₀-IC4₃₀ compared to that of the corresponding control fully-CFFT beams. Generally, the results indicate that the fully and partially-CFFT beams have the same primary flexural stiffness since their moments of inertia of their cracked section are almost the same. It is attributed to the contribution of the inner tubes is comparatively low in the overall moment of inertia of the cracked section, since their wall sectional area is small in addition their reinforcement contribution is governed by their modular ratio which is

comparatively small. The overall behaviour of the partially-CFFT beams is nonlinear with multilinear stages compared to that of the fully-CFFT beams, which is considered as bi-linear. After the ultimate capacity, the flexural strength of the partially-CFFT beams was decreasing gradually unlike the fully-CFFT beams that fail suddenly.

The results in Figure 5.22(a) indicate that the partially-CFFT beam OR2₃₀-IC4₃₀ with an outer tube thickness of 3.4 mm attained ultimate flexural strength 9% higher than that of the fully-CFFT beam OR2₃₀. Also, the flexural stiffness of OR2₃₀-IC4₃₀ after yielding was higher than that of OR2₃₀. Note that, OR2₃₀ failed in tension, while OR2₃₀-IC4₃₀ failed in compression. This means, the internal compression forces of the partially-CFFT section increased. This increase can be attributed to:

- 1) The concrete in compression resisted higher compressive forces (confined) within a restrained area (between the outer and inner tubes),
- 2) The compression flange of the tube resisted much compression forces,
- 3) The inner tube act as reinforcement and increased the internal tensile forces of the partially-CFFT section. Then it increased the internal compression forces to balance the section.

Figure 5.22(b) indicates that the flexural stiffness after yielding of OR4₃₀-IC4₃₀ with an outer tube thickness of 5.7 mm was higher than that of OR4₃₀. However, the partially-CFFT beam OR4₃₀-IC4₃₀ attained flexural strength 4% lower than that of the fully-CFFT beams OR4₃₀.

Figure 5.22(c) indicates that the flexural stiffness after yielding of OR8₃₀-IC4₃₀ with an outer tube thickness of 8.7 mm was similar to that of OR8₃₀. However, the partially-CFFT beams OR8₃₀-IC4₃₀ attained flexural strength 27% lower than that of the fully-CFFT beams OR8₃₀.

The same conclusions are obtained in case of partially-CFFT beams with inner square voids as shown in Figure 5.23. Note that, the applied moments in Figure 5.23(b) needed to be normalized due to the different concrete compressive strength as shown in Figure 5.23(c).

Based on the results, increasing the outer tube thickness in partially-CFFT beams does not mean increasing their flexural strength higher than their corresponding fully-CFFT beams.

This is attributed to the flexural performance of the partially-CFFT beams is governed by the compression failure and the strength of the elements in compression as concrete and the tube flange.

5.4.6 Strain Behaviour in CFFT Beams

The correlations between the moment and the longitudinal and transverse strains of the outer and inner GFRP tubes are plotted in Figures 5.25 to 5.34. The strains were measured at different locations as indicated by the alphabets on the cross section on each chart.

Figure 5.24 confirms the tension failure of the fully-CFFT beam (OR2₃₀) since the longitudinal strains at point D (on the outer GFRP tube) reached 0.024 that exceed significantly the ultimate longitudinal tensile strain of the coupon tests that equals 0.0157 as listed in Table 3.1 in Chapter 3. The longitudinal compressive strain at point A was 0.01 exceeding the ultimate coupon compressive strain that equals 0.07. It can be noticed that the coupon test results are smaller than the actual test results. This could be a result of: (1) the hybrid action of the materials in the CFFT section, (2) the good bond between the GFRP tube and the inner concrete core, and (3) additional flexural strains due to high curvatures as illustrated on Figure 5.24. Although the transverse strains on the outer GFRP tube were far from the coupon test results, there was a stretch in the transverse strain values especially at points A and E indicating confinement action. The same observations can be noticed in Figure 5.26 and 5.32 for the fully-CFFT beams OR4₃₀ and OR8₃₀, respectively. Note that, the compressive longitudinal strain at point A in OR8₃₀ reached the maximum coupon compressive strain confirming the first compression failure (buckling) at the top face. At the same time, the tensile longitudinal strain at point D in OR8₃₀ was high enough to cause the axial rupture of fibers at the tension side.

The longitudinal strain at point A at the top face of the partially-CFFT beams indicated a rapid increase of the compressive strains especially in partially-CFFT beams with thick GFRP tubes as shown in Figures 5.28, 5.33, and 5.34. There were signs of buckling at the top face indicated by reverse in the longitudinal strain at point A as shown in Figures 5.25, 5.27, 5.33, and 5.34 where the rate of strain development decreased until failure.

The transverse strains at points A and E in the partially-CFFT beams behaved in the same manner as in the fully-CFFT beams, however, point B gained more transverse tensile strains in the partially-CFFT beams than in the fully-CFFT beams. See Figures 5.25, 5.27, 5.28, 5.33, and 5.34. Note that, at these figures, the longitudinal strains at point B moved toward the compression at high loads. The gained transverse strains and the reversed longitudinal strains at point B indicate confining by a deeper confined area of the concrete at the compression zone, simultaneously a deeper neutral axis.

The longitudinal strains at point G (on the inner GFRP tube) in the partially-CFFT beams show reinforcement action of the inner GFRP tubes especially after yielding of the steel. Because of these high longitudinal tensile strains, compressive transverse strains were propagated due to Poisson's ratio effect as shown in Figures 5.25, 5.27, 5.28, 5.30, 5.33, and 5.34. Generally, the negative transverse strains at points G and H indicate that the inner tube is compressed by surrounding concrete and GFRP tube. The previous notes prove that the inner GFRP tubes work as flexural reinforcement regardless their effective contribution.

The low values of the longitudinal strains (almost zero) at point F on the inner GFRP tubes indicate that the inner tube lay under the neutral axis of the composite section. According to the active confining action of the inner tube on the concrete in the compression zone, an increase in the tensile transverse strain was noticed in some partially-CFFT beams as shown in Figures 5.29, 5.30, and 5.31. At the same time in these figures, the longitudinal strains at point F were reversed toward compression. The reason could be attributed to: (1) the neutral axis was trended downward, or (2) the active confinement action of the inner tube on the concrete in the compression zone increased the tensile transverse strain at point F, and so it increased the compressive strain in the perpendicular direction due to Poisson's ratio effect. The designer should consider the variable strain values along the depth when calculating the reinforcement action of the inner tube.

5.4.7 Strength to Weight Ratio

To study the strength to weight ratio, the weight of the RC beam is considered as a reference and is taken as unit. Note that, the fully-CFFT beams have almost the same weight like the

RC beams. After excluding the void from the weight of the CFFT beams, the partially-CFFT beams with circular voids weigh 70% of the fully-CFFT beams weight, while the partially-CFFT beams with square voids weigh 67% of the fully-CFFT beams weight. Then, the actual flexural moments of every beam at first crack, steel yield, and ultimate failure are divided by its own weight fraction according to the RC beam weight as shown in Eq. 5.7. Accordingly, virtual flexural strength-to-weight ratios can be evaluated as shown in Figures 5.35 and 5.36.

$$M_{virtual} = \frac{M_{actual}}{\zeta} \quad (5.7)$$

$$\zeta = 1 \text{ for RC and Fully-CFFT beams}$$

$$\zeta = 0.7 \text{ for Partially-CFFT beams with circular void}$$

$$\zeta = 0.67 \text{ for Partially-CFFT beams with square void}$$

Generally, Figures 5.35 and 5.36 indicate the superior strength-to-weight ratio of the CFFT beams (Fully or partially filled with concrete) compared to the conventional RC beams. For example, the fully-CFFT beam OR8₃₀ attained ultimate strength-to-weight ratio 427% that of the RC beams. While, the partially-CFFT beam OR8₃₀-IC4₃₀ attained ultimate strength-to-weight ratio 447% that of the RC beams.

The effect of the weight increases obviously at the ultimate stage than yield stage than first crack stage. The virtual cracking moments for the partially-CFFT beams become closer to that of the fully-CFFT beams, which means that the void area is a main factor in reducing M_{cr} of the Partially-CFFT beams compared to the fully-CFFT beams.

The results indicate that the ultimate strength-to-weight ratio of the partially-CFFT beams become greater than that of the corresponding fully-CFFT beam. For example, the partially-CFFT beam OR2₃₀-IC4₃₀ attained ultimate strength-to-weight ratio 157% that of the fully-CFFT beam OR2₃₀. Despite the partially-CFFT beam OR8₃₀-IC4₃₀ attained ultimate strength 73% that of the fully-CFFT beam OR8₃₀, but its virtual ultimate strength-to-weight ratio is 5% higher than that of the fully CFFT beam OR8₃₀.

Based on results, the partially CFFT beams could replace the heavy RC beams and fully-CFFT beams. Accordingly, they could reduce the cost of transportation and installation in addition to reducing the dead weight of structures.

5.4.8 Cracking Moment (M_{cr}) of Rectangular Partially-CFFT Beams

One of the advantages of the CFFT system is that the outer FRP tube acts as a jacket that protects the inner structural elements, such as concrete and steel, against corrosion even if the inner concrete core is cracked. Therefore, there is no worry about the concrete cracks for the durability and appearance requirements. However, it is important for effective design of FRP-concrete composite structures to study the cracking behaviour for serviceability requirements related to deflection and crack width control. Therefore, the cracking moment (M_{cr}) is evaluated for the current study of rectangular fully and partially-CFFT beams. This section is related to section 4.4.6 in Chapter 4 and studies the experimental M_{cr} of the partially-CFFT beams and their gross moment of inertia of the concrete-transformed section to develop an expression for the modulus of rupture of concrete (f_{cr}) as shown in Table 5.3.

Based on the results in the current study, new values for k are proposed to determine well the cracking moment M_{cr} of partially-CFFT beams. Table 5.3 lists an average $k = 0.66$ for partially-CFFT beams with circular voids, while an average $k = 0.77$ for partially-CFFT beams with square voids. These values are assumed in case of calculating the gross moment of inertia for the total section elements (concrete + steel + FRP tubes) transformed to concrete and eliminating the void area. Note that, section 4.4.6 in Chapter 4 proposed $k = 0.69$ for fully-CFFT beams in case of considering reinforcement (see Table 4.3 in Chapter 4). The results indicate enhancement in the cracking strength of the rectangular CFFT beams fully or partially filled with concrete. It is attributed to many factors as mentioned in Chapter 4 (see section 4.4.6). These factors are:

- 5) The FRP tubes contributed positively in the gross section inertia I_g , however, this contribution is comparatively limited due to the low FRP modular ratio,
- 6) The full composite action or the bond due to the roughened tubes surfaces delayed the generation of the cracks,

- 7) The concrete expansion during curing was restrained by the tube inducing chemical pre-stressing on the concrete (Fam and Rizkalla 2002), and
- 8) Confining the concrete with FRP tubes restrained it against crack propagation.

The partially-CFFT beams with square voids experienced the highest cracking strength compared to the other types of the studied CFFT beams (fully-CFFT beams or partially-CFFT beams with circular voids). It can be attributed to the roughened surface area of the inner square tubes was wider than that of the inner circular tubes, and the concrete around the inner square tubes is tightly positioned between the roughened surfaces of the inner square tubes and the roughened surfaces of the outer tubes. Therefore, the roughened surfaces in the partially-CFFT beams with square voids hampered effectively the propagation of the cracks.

5.5 CONCLUSIONS

Twenty-two full-scale rectangular beams, including fourteen partially-CFFT beams, six control fully-CFFT beams, and two control conventional RC beams, were tested under a four-point bending. The partially-CFFT beams had voids provided by inner circular or square GFRP tubes shifted toward the tension zone of the section. All the beams had the same section dimensions and the same flexural steel reinforcement at the tension side. The results indicate superior performance of the rectangular CFFT beams, in terms of strength and ductility, compared to the conventional RC beams.

The main concluded points of these beam tests are:

- 1) The flexural strength of a rectangular fully-CFFT beam with a GFRP tube thickness of 3.4 mm is 97% higher than that of a conventional RC beam and fails in tension. If an inner circular hollow GFRP tube with 3.1 mm thickness is provided at the tension zone, the flexural strength becomes 115% higher than that of a conventional RC beam. Moreover, the ultimate failure changes from sudden tension failure to gradual compression failure.
- 2) The flexural strength of the partially-CFFT beams increases with increasing the outer GFRP tube thickness until certain limit. After this limit, buckling of the compression

flange of the FRP tube governs the ultimate capacity of partially-CFFT beams. Equations are proposed to estimate the flexural moments at different stages (first crack, yield, and ultimate) based on regression analysis.

- 3) The inner hollow GFRP tubes in the rectangular CFFT beams pronounced active confinement action on the concrete in the compression zone. The circular shape of the inner void indicated better performance than the square void shape. Further experimental investigations are required to optimize the inner GFRP tube contribution as flexural reinforcement and confining the concrete at the compression zone.
- 4) The strength-to-weight ratio of the partially-CFFT beams is significantly higher than that of the RC beams and higher than that of the corresponding fully-CFFT beams. Therefore, the partially CFFT beams could replace the heavy RC beams and fully-CFFT beams, consequently could reduce the construction cost and the dead weight of structures.
- 5) The partially-CFFT beams experienced high cracking strength. Based on the results of the current study, new values for k are proposed to determine well the concrete modulus of rupture (f_{cr}) of ACI-318. $k = 0.66$ for partially-CFFT beams with circular voids, while the $k = 0.77$ for partially-CFFT beams with square voids. These values are assumed in case of calculating the gross moment of inertia for the total section elements (concrete + steel + FRP tubes) transformed to concrete and eliminating the void area.

Table 5.1 – Beam specimens and summary of test results

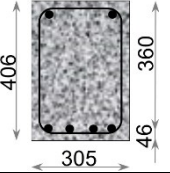
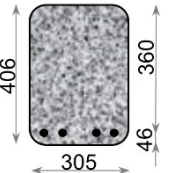
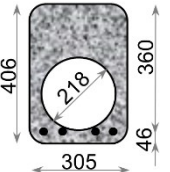
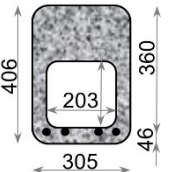
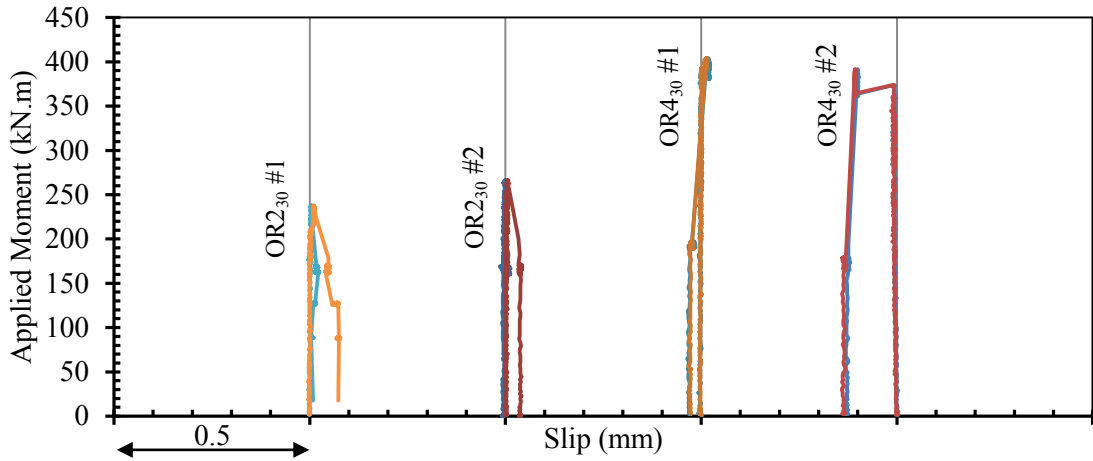
| Group | Beam ID | Section Configuration (mm) | Steel reinforcement | Outer tube | Inner tube | Concrete strength (MPa) | Moment (kN.m) | | | Ultimate Deflection (mm) | Ductility (kN.m ²) | Failure mode |
|--|---|---|---|-------------------|-------------------|-------------------------|---------------|-------|-------|--------------------------|--------------------------------|--------------|
| | | | | | | | M_{cr} | M_y | M_u | | | |
| RC beam | RC #1 |  | Top 2-10M Bot. 4-15M Ties 10M/150 mm | --- | --- | 41.7 | 30 | 113 | 132 | 29 | 3.1 | Tension |
| | RC #2 | | | | | | 31 | 116 | 130 | | | |
| Fully CFFT beams | OR2 ₃₀ #1 |  | Bot. 4-15M | OR2 ₃₀ | --- | 49.7 | 43 | 152 | 249 | 52 | 10.2 | Tension |
| | OR2 ₃₀ #2 | | | OR2 ₃₀ | --- | 49.7 | 43 | 150 | 267 | 69 | 14.3 | Tension |
| | OR4 ₃₀ #1 | | | OR4 ₃₀ | --- | 48.7 | 46 | 161 | 404 | 89 | 27.0 | Tension |
| | OR4 ₃₀ #2 | | | OR4 ₃₀ | --- | 48.7 | 44 | 168 | 392 | 77 | 22.2 | Tension |
| | OR8 ₃₀ #1 | | | OR8 ₃₀ | --- | 41.7 | 48 | 204 | 559 | 82 | 33.0 | Balanced |
| | OR8 ₃₀ #2 | | | OR8 ₃₀ | --- | 41.7 | 45 | 210 | 560 | 92 | 38.4 | Balanced |
| Partially CFFT beams with circular voids | OR2 ₃₀ -IC4 ₃₀ |  | | OR2 ₃₀ | IC4 ₃₀ | 49.7 | 38 | 170 | 282 | 56 | 11.9 | Comp. |
| | OR4 ₃₀ -IC4 ₃₀ | | | OR4 ₃₀ | IC4 ₃₀ | 49.7 | 34 | 180 | 380 | 56 | 14.9 | Comp. |
| | OR4 ₃₀ -IC2 ₃₀ #1 | | | OR4 ₃₀ | IC2 ₃₀ | 49.7 | 36 | 188 | 384 | 63 | 16.8 | Comp. |
| | OR4 ₃₀ -IC2 ₃₀ #2 | | | OR4 ₃₀ | IC2 ₃₀ | 49.7 | 35 | 182 | 375 | 62 | 16.4 | Comp. |
| | OR8 ₃₀ -IC4 ₃₀ #1 | | | OR8 ₃₀ | IC4 ₃₀ | 41.7 | 37 | 216 | 429 | 53 | 15.7 | Comp. |
| | OR8 ₃₀ -IC4 ₃₀ #2 | | | OR8 ₃₀ | IC4 ₃₀ | 41.7 | 34 | 215 | 387 | 42 | 11.1 | Comp. |
| Partially CFFT beams with square voids | OR4 ₃₀ -IS2 ₃₀ #1 |  | OR4 ₃₀ | IS2 ₃₀ | 48.7 | 40 | 175 | 298 | 47 | 10.3 | Comp. | |
| | OR4 ₃₀ -IS2 ₃₀ #2 | | OR4 ₃₀ | IS2 ₃₀ | 48.7 | 44 | 179 | 284 | 44 | 9.0 | Comp. | |
| | OR4 ₃₀ -IS4 ₃₀ #1 | | OR4 ₃₀ | IS4 ₃₀ | 48.7 | 40 | 175 | 290 | 42 | 8.6 | Comp. | |
| | OR4 ₃₀ -IS4 ₃₀ #2 | | OR4 ₃₀ | IS4 ₃₀ | 48.7 | 40 | 175 | 289 | 43 | 9.1 | Comp. | |
| | OR4 ₃₀ -IS4 ₆₅ #1 | | OR4 ₃₀ | IS4 ₆₅ | 48.7 | 40 | 175 | 265 | 40 | 7.4 | Comp. | |
| | OR4 ₃₀ -IS4 ₆₅ #2 | | OR4 ₃₀ | IS4 ₆₅ | 48.7 | 42 | 177 | 281 | 41 | 8.1 | Comp. | |
| | OR8 ₃₀ -IS4 ₃₀ #1 | | OR8 ₃₀ | IS4 ₃₀ | 49.7 | 43 | 224 | 441 | 45 | 13.4 | Comp. | |
| | OR8 ₃₀ -IS4 ₃₀ #2 | | OR8 ₃₀ | IS4 ₃₀ | 49.7 | 43 | 224 | 470 | 48 | 15.5 | Comp. | |

Table 5.2 – Shear forces in fully and partially-CFFT beams

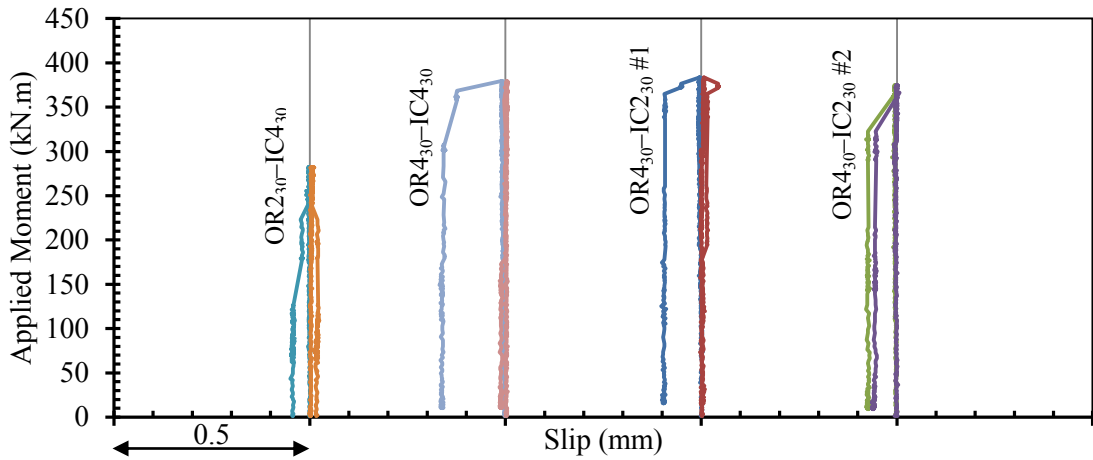
| CFFT Beam | t_f (mm) | f'_c (MPa) | V_n (kN) ($=M_u/a$) | V_c (kN) ($=0.17\sqrt{f'_c}A_c$) | V_f (kN) ($=V_n-V_c$) | F_f (MPa) | $\frac{Exp.}{F_{tr}}$ (MPa) | $\frac{F_f}{F_{tr}} \times 100$ (%) |
|---|---------------|-----------------|----------------------------|---|------------------------------|----------------|--------------------------------|--|
| OR2 ₃₀ #1 | 3.4 | 49.7 | 226.4 | 148.4 | 78.0 | 22.8 | 243 | 9.4 |
| OR2 ₃₀ #2 | 3.4 | 49.7 | 242.7 | 148.4 | 94.3 | 27.6 | 243 | 11.4 |
| OR4 ₃₀ #1 | 5.7 | 48.7 | 367.3 | 146.9 | 220.4 | 38.5 | 214 | 18.0 |
| OR4 ₃₀ #2 | 5.7 | 48.7 | 356.4 | 146.9 | 209.5 | 36.6 | 214 | 17.1 |
| OR8 ₃₀ #1 | 8.7 | 41.7 | 508.2 | 135.9 | 372.2 | 42.6 | 164 | 26.0 |
| OR8 ₃₀ #2 | 8.7 | 41.7 | 509.1 | 135.9 | 373.2 | 42.7 | 164 | 26.0 |
| OR2 ₃₀ -IC4 ₃₀ | 3.4 | 49.7 | 256.4 | 103.7 | 152.7 | 44.7 | 243 | 18.4 |
| OR4 ₃₀ -IC4 ₃₀ | 5.7 | 49.7 | 345.5 | 103.7 | 241.8 | 42.2 | 214 | 19.7 |
| OR4 ₃₀ -IC2 ₃₀ #1 | 5.7 | 49.7 | 349.1 | 103.7 | 245.4 | 42.9 | 214 | 20.0 |
| OR4 ₃₀ -IC2 ₃₀ #2 | 5.7 | 49.7 | 340.9 | 103.7 | 237.2 | 41.4 | 214 | 19.4 |
| OR8 ₃₀ -IC4 ₃₀ #1 | 8.7 | 41.7 | 390.0 | 95.0 | 295.0 | 33.8 | 164 | 20.6 |
| OR8 ₃₀ -IC4 ₃₀ #2 | 8.7 | 41.7 | 351.8 | 95.0 | 256.9 | 29.4 | 164 | 17.9 |
| OR4 ₃₀ -IS2 ₃₀ #1 | 5.7 | 48.7 | 270.9 | 98.0 | 172.9 | 30.2 | 214 | 14.1 |
| OR4 ₃₀ -IS2 ₃₀ #2 | 5.7 | 48.7 | 258.2 | 98.0 | 160.2 | 28.0 | 214 | 13.1 |
| OR4 ₃₀ -IS4 ₃₀ #1 | 5.7 | 48.7 | 263.6 | 98.0 | 165.6 | 28.9 | 214 | 13.5 |
| OR4 ₃₀ -IS4 ₃₀ #2 | 5.7 | 48.7 | 262.7 | 98.0 | 164.7 | 28.8 | 214 | 13.4 |
| OR4 ₃₀ -IS4 ₆₅ #1 | 5.7 | 48.7 | 240.9 | 98.0 | 142.9 | 25.0 | 214 | 11.7 |
| OR4 ₃₀ -IS4 ₆₅ #2 | 5.7 | 48.7 | 255.5 | 98.0 | 157.4 | 27.5 | 214 | 12.8 |
| OR8 ₃₀ -IS4 ₃₀ #1 | 8.7 | 49.7 | 400.9 | 99.0 | 301.9 | 34.5 | 164 | 21.1 |
| OR8 ₃₀ -IS4 ₃₀ #2 | 8.7 | 49.7 | 427.3 | 99.0 | 328.3 | 37.6 | 164 | 22.9 |

Table 5.3 – Details of calculating cracking strength of partially-CFFT beams

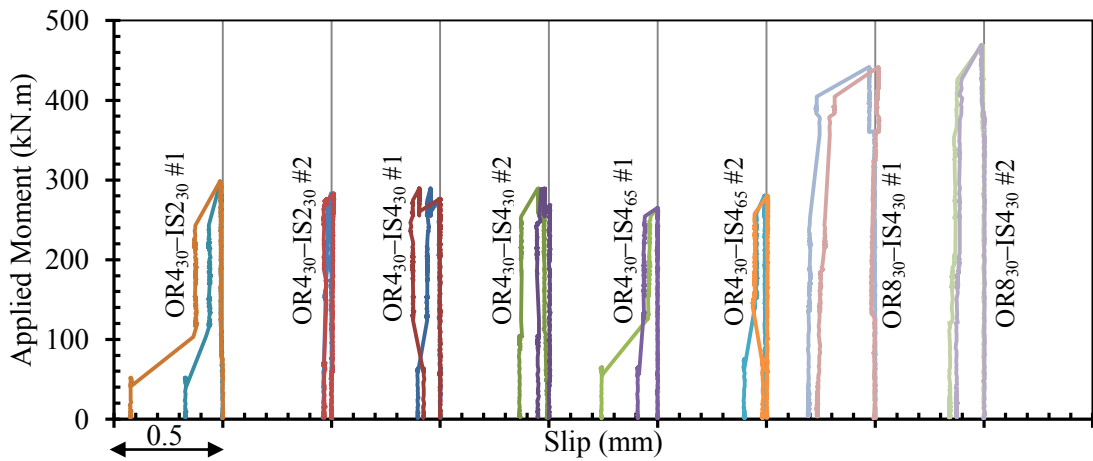
| Group | Beam | f'_c (MPa) | Exp. M_{cr} (kN.m) | Considering reinforcement | | | | Average |
|--|---|-----------------|-------------------------|---------------------------|-----------------------------|-------------------|------|-------------------------|
| | | | | Y_t (mm) | I_g (mm ⁴) | f_{cr} (MPa) | k | |
| Partially -CFFT beams with circular voids | OR2 ₃₀ -IC4 ₃₀ | 49.7 | 38 | 215.6 | 1.64×10 ⁹ | 4.99 | 0.71 | $k = 0.66$ SD = 0.02 |
| | OR4 ₃₀ -IC4 ₃₀ | 49.7 | 34 | 215.4 | 1.69×10 ⁹ | 4.34 | 0.62 | |
| | OR4 ₃₀ -IC2 ₃₀ #1 | 49.7 | 36 | 215.2 | 1.69×10 ⁹ | 4.58 | 0.65 | |
| | OR4 ₃₀ -IC2 ₃₀ #2 | 49.7 | 35 | 215.2 | 1.69×10 ⁹ | 4.45 | 0.63 | |
| | OR8 ₃₀ -IC4 ₃₀ #1 | 41.7 | 37 | 215.1 | 1.76×10 ⁹ | 4.53 | 0.70 | |
| | OR8 ₃₀ -IC4 ₃₀ #2 | 41.7 | 34 | 215.1 | 1.76×10 ⁹ | 4.16 | 0.64 | |
| Partially -CFFT beams with square voids | OR4 ₃₀ -IS2 ₃₀ #1 | 48.7 | 40 | 215.9 | 1.66×10 ⁹ | 5.20 | 0.75 | $k = 0.77$ SD = 0.04 |
| | OR4 ₃₀ -IS2 ₃₀ #2 | 48.7 | 44 | 215.9 | 1.66×10 ⁹ | 5.72 | 0.82 | |
| | OR4 ₃₀ -IS4 ₃₀ #1 | 48.7 | 40 | 216.7 | 1.64×10 ⁹ | 5.29 | 0.76 | |
| | OR4 ₃₀ -IS4 ₃₀ #2 | 48.7 | 40 | 216.7 | 1.64×10 ⁹ | 5.29 | 0.76 | |
| | OR4 ₃₀ -IS4 ₆₅ #1 | 48.7 | 40 | 216.8 | 1.65×10 ⁹ | 5.26 | 0.75 | |
| | OR4 ₃₀ -IS4 ₆₅ #2 | 48.7 | 42 | 216.8 | 1.65×10 ⁹ | 5.53 | 0.79 | |
| | OR8 ₃₀ -IS4 ₃₀ #1 | 49.7 | 43 | 216.3 | 1.71×10 ⁹ | 5.44 | 0.77 | |
| | OR8 ₃₀ -IS4 ₃₀ #2 | 49.7 | 43 | 216.6 | 1.71×10 ⁹ | 5.44 | 0.77 | |



(a) End slip of partially-CFFT beams with circular void

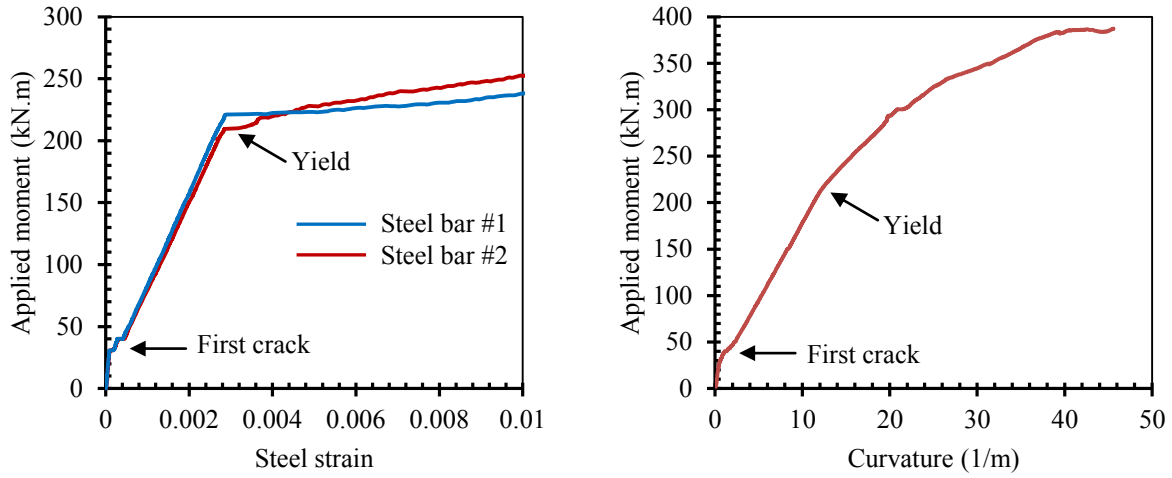


(b) End slip of partially-CFFT beams with circular voids



(c) End slip of partially-CFFT beams with square voids

Figure 5.1 – Moment-slip response in partially-CFFT beams



(a) Steel strains of OR8₃₀-IC4₃₀ #2

(b) Curvature of OR8₃₀-IC4₃₀ #2

Figure 5.2 – Typical steel strains and curvature of partially-CFFT beams

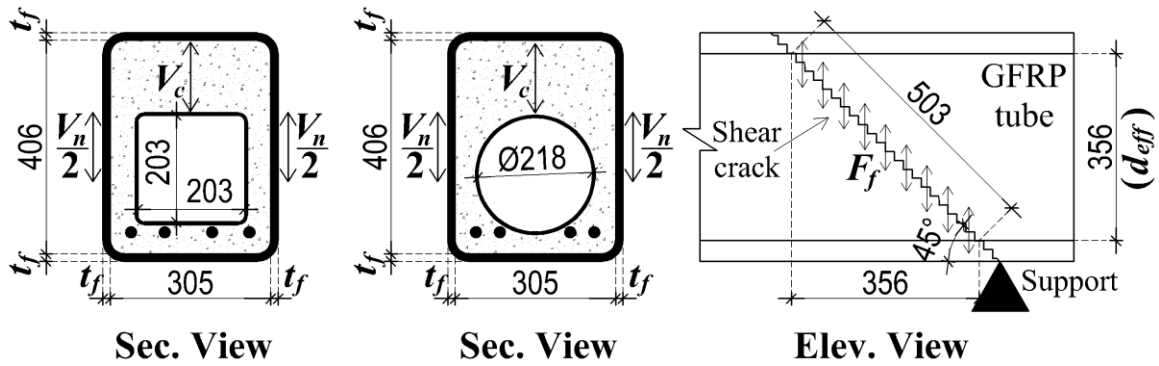
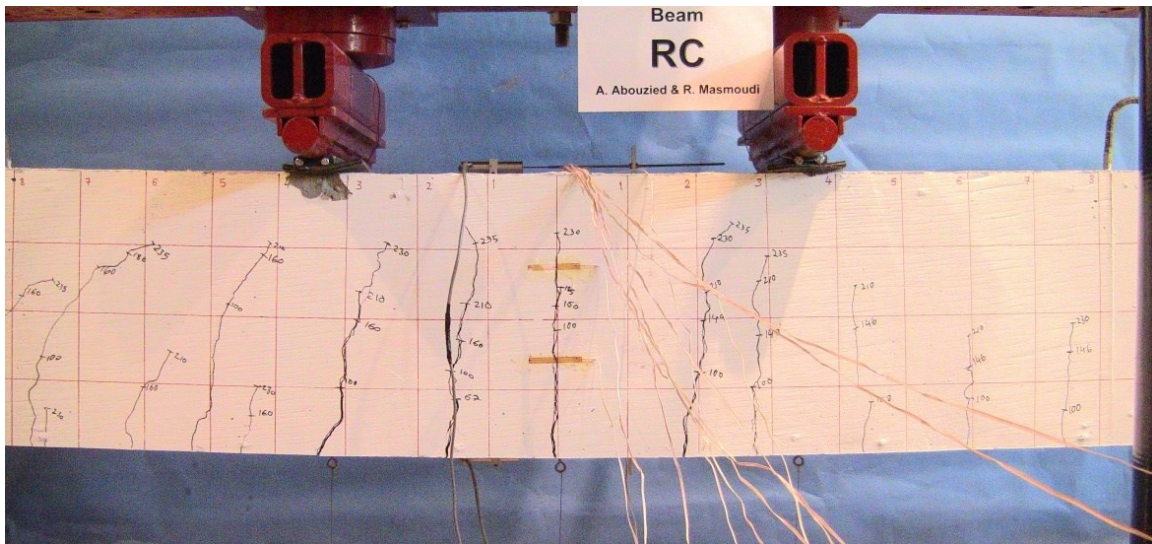
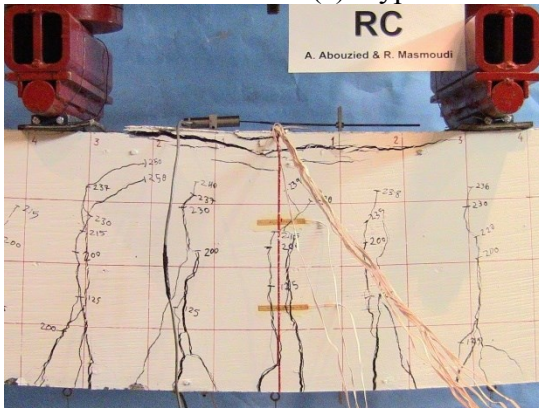


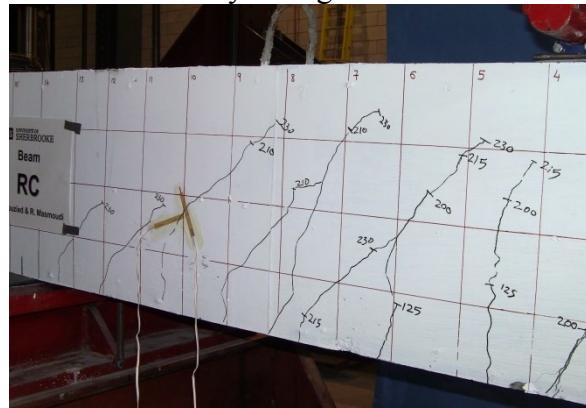
Figure 5.3 – Shear forces in partially-CFFT beams



(a) Typical tension failure due to steel yielding



(b) Final failure



(c) Typical shear cracks near supports

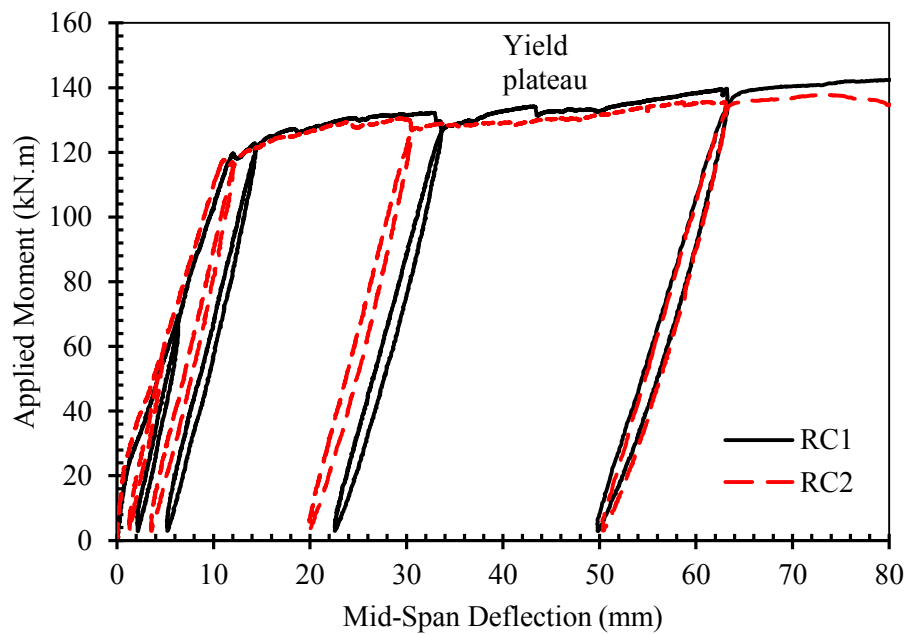
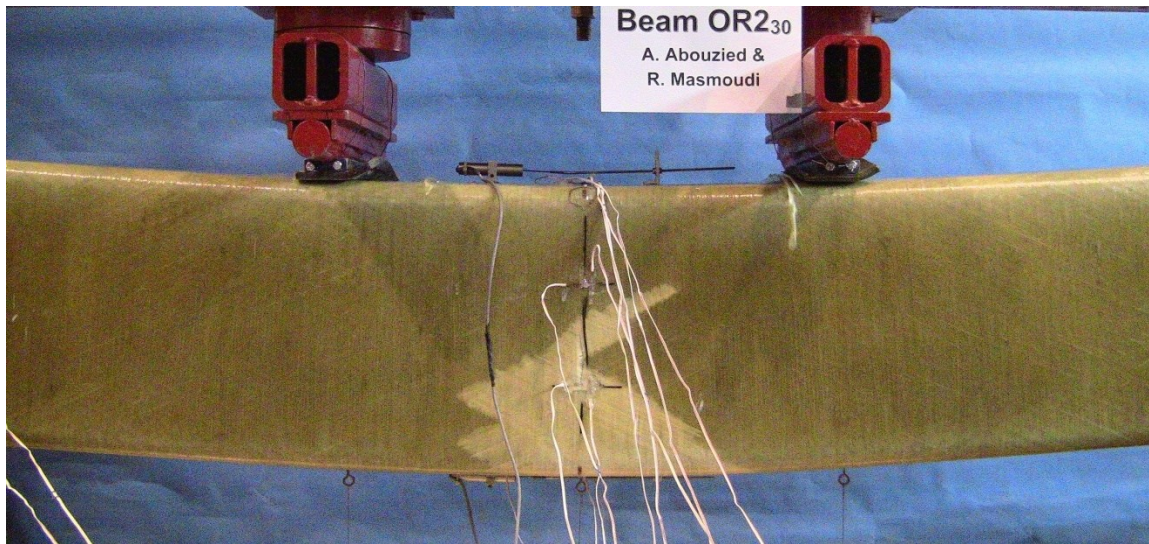


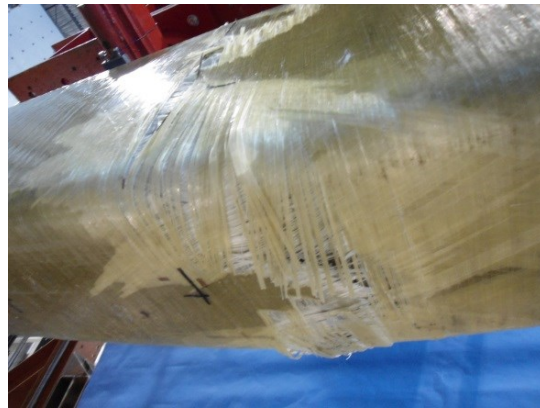
Figure 5.4 – Failure pattern and moment-deflection response of RC beams



(a) Elevation view



(b) Top view



(c) Bottom view

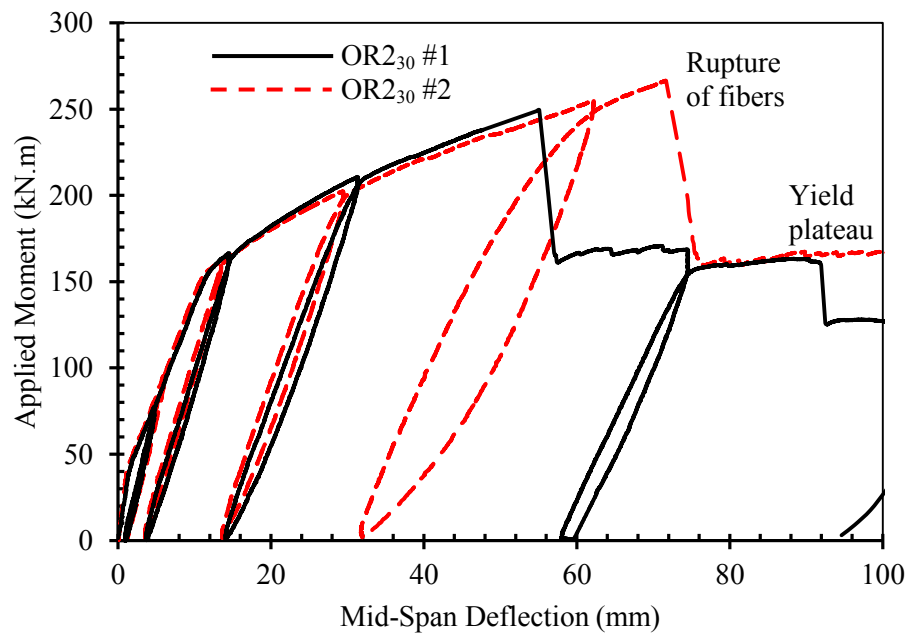
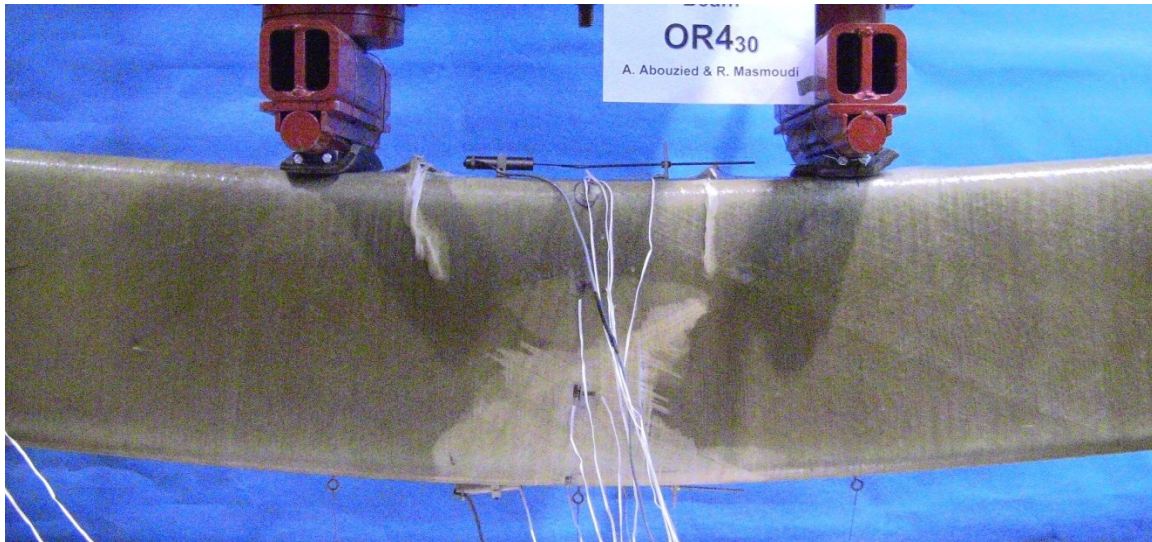


Figure 5.5 – Failure pattern and moment-deflection response of fully-CFFT beams OR₂₃₀



(a) Elevation view



(b) Top view



(c) Bottom view

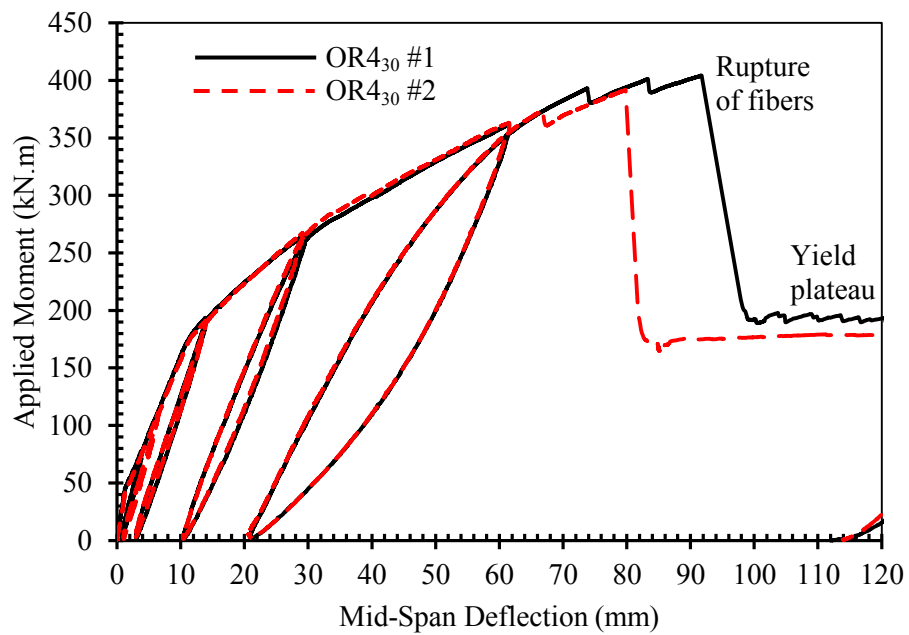
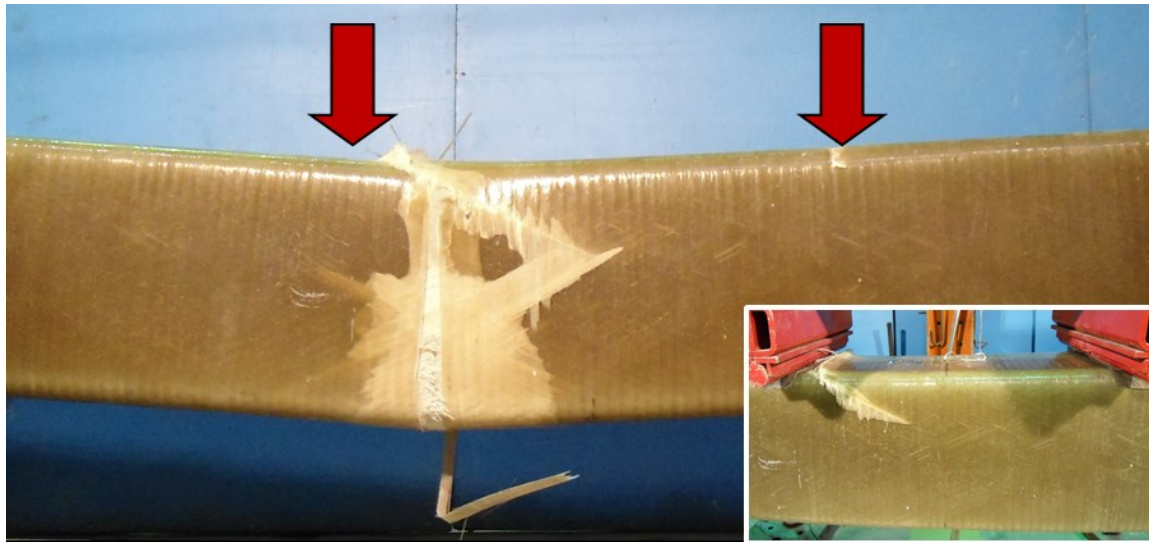


Figure 5.6 – Failure pattern and moment-deflection response of fully-CFFT beams OR4₃₀



(a) Elevation view



(b) Top view



(c) Elevation view

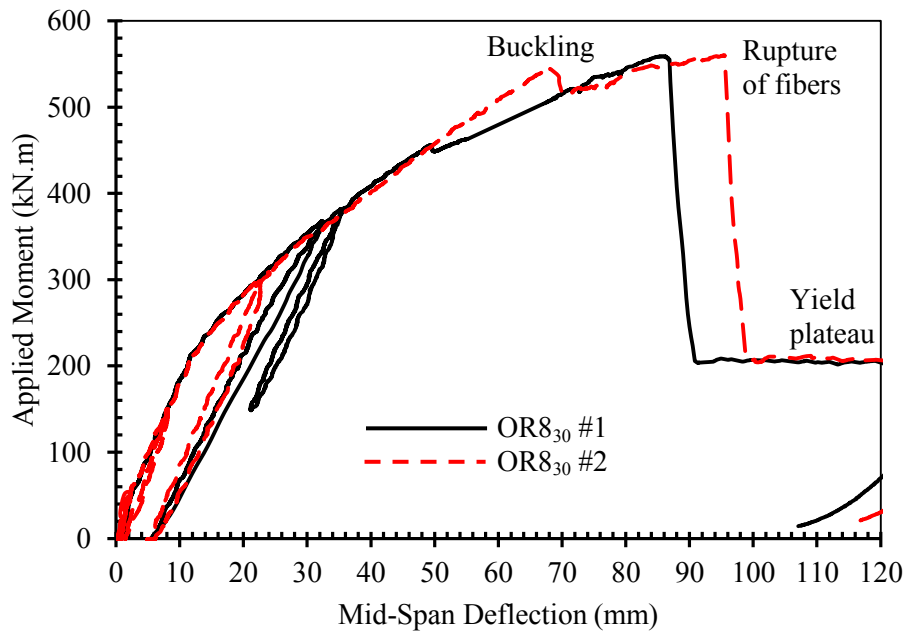


Figure 5.7 – Failure pattern and moment-deflection response of fully-CFFT beams OR8₃₀



(a) Elevation view



(d) Top view



(e) Bottom view

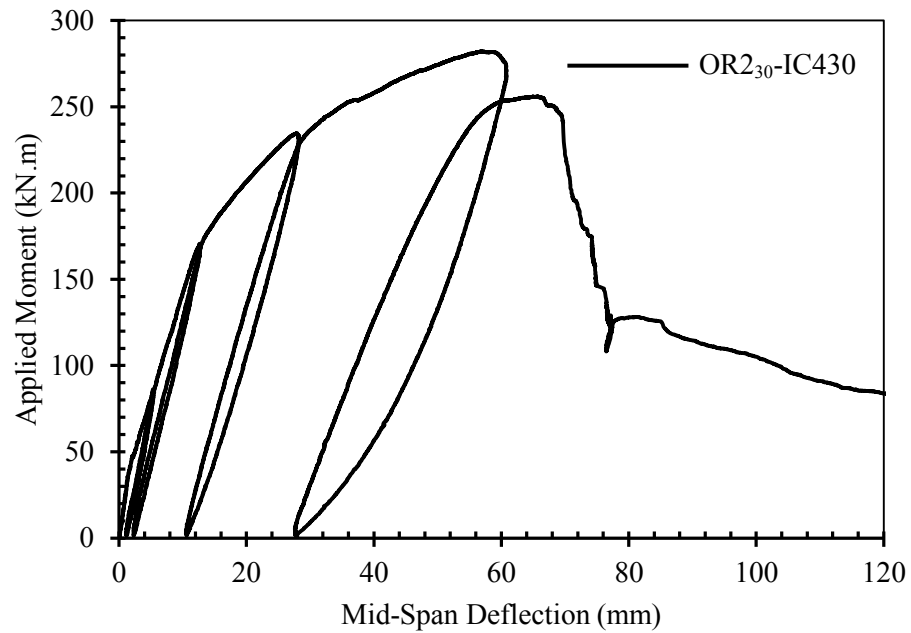


Figure 5.8 – Failure pattern and moment-deflection response of partially-CFFT beam OR230-IC430

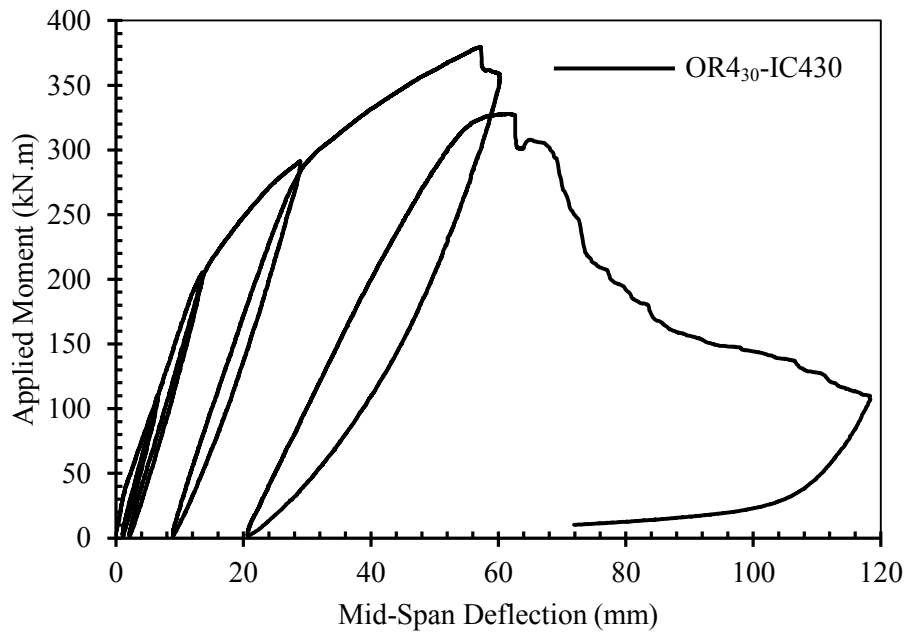
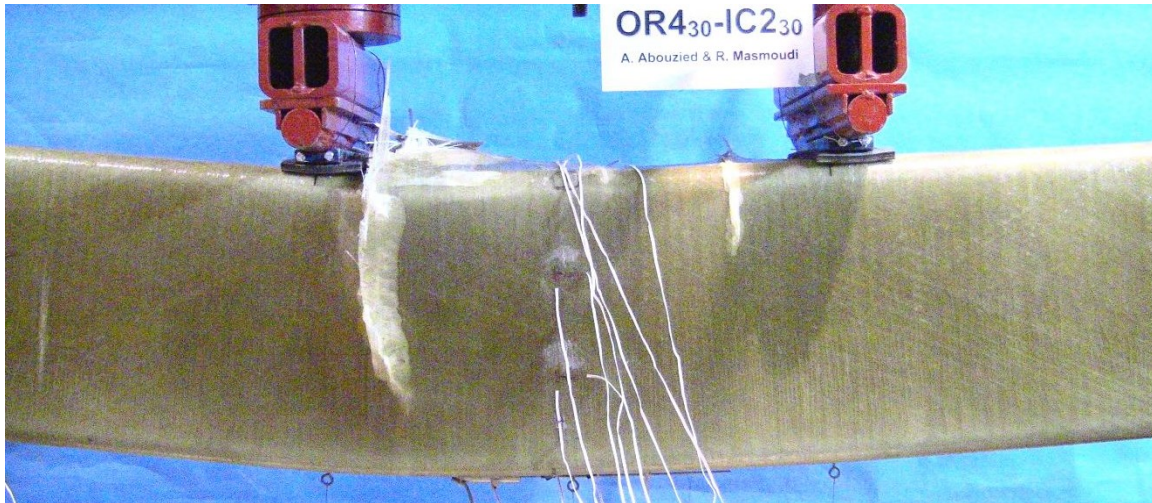


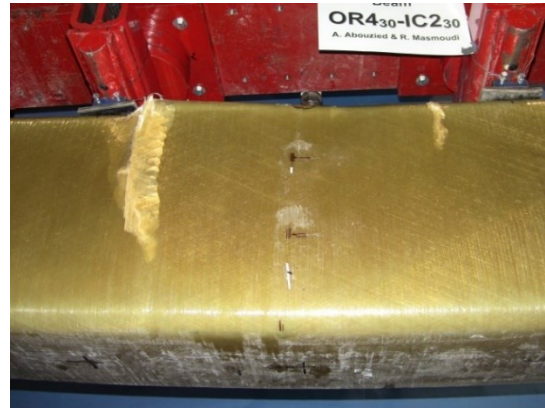
Figure 5.9 – Failure pattern and moment-deflection response of partially-CFFT beam OR430-IC430



(a) Elevation view



(b) Top view



(c) Bottom view

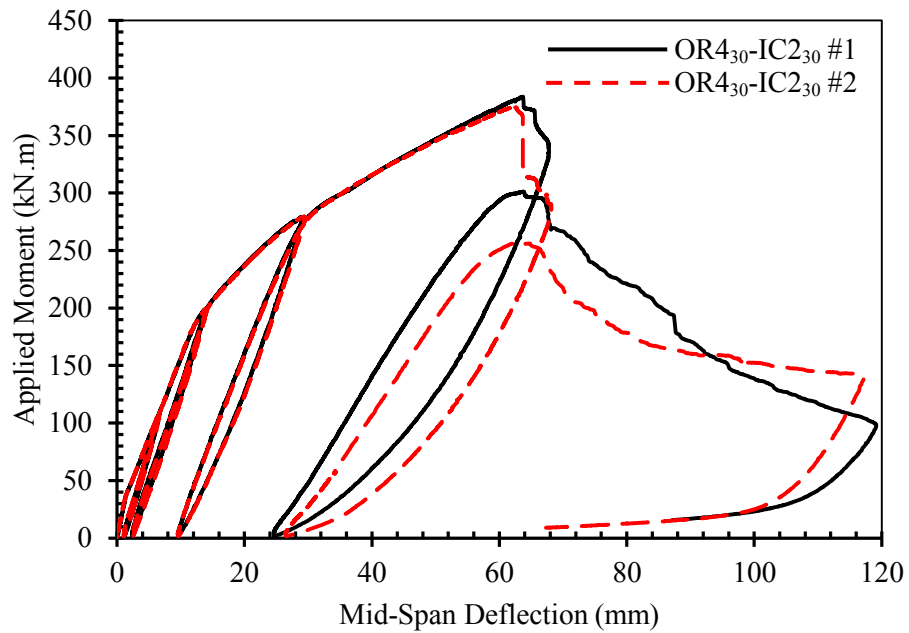
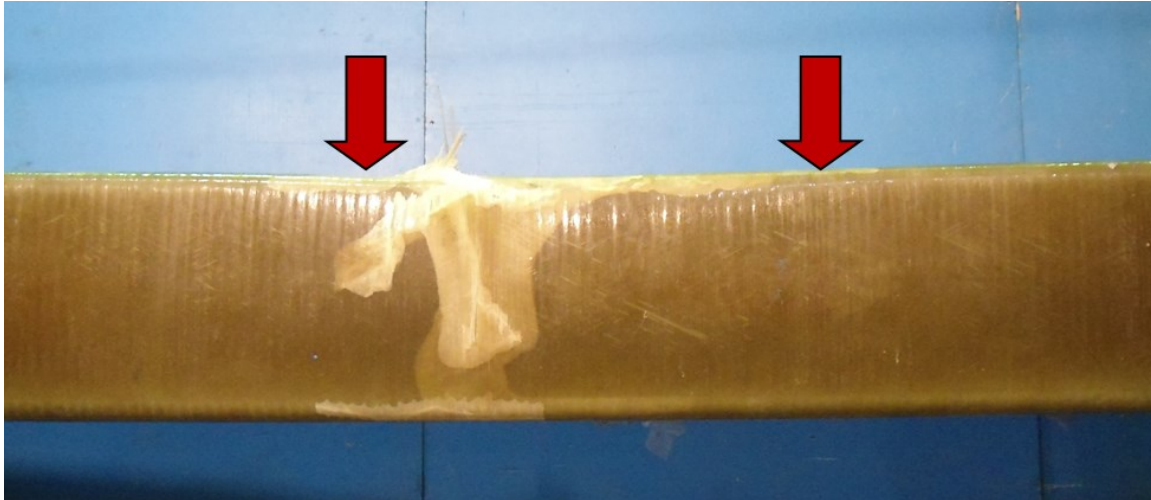


Figure 5.10 – Failure pattern and moment-deflection response of partially-CFFT beams OR430-IC230



(a) Elevation view



(b) Top view



(c) Bottom view

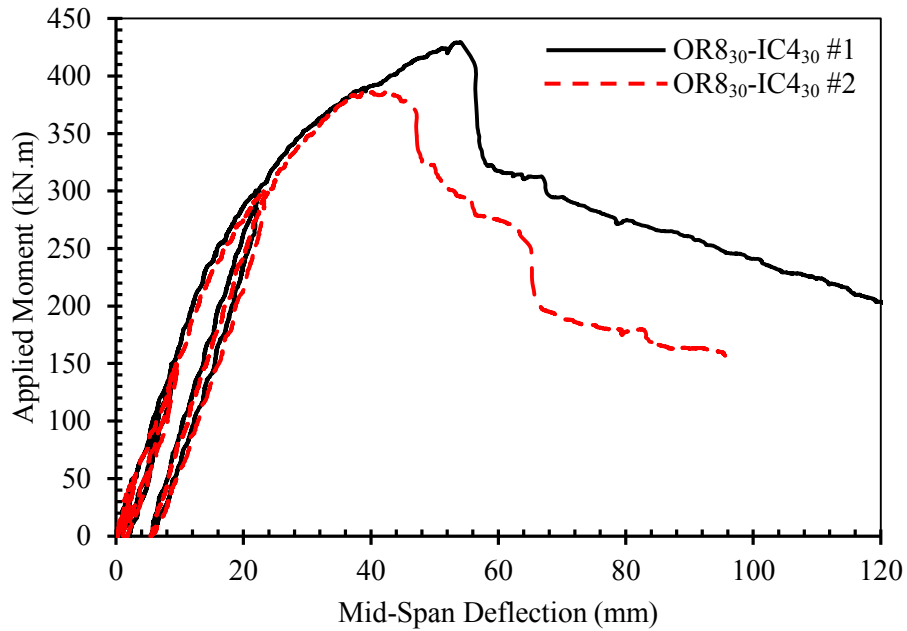
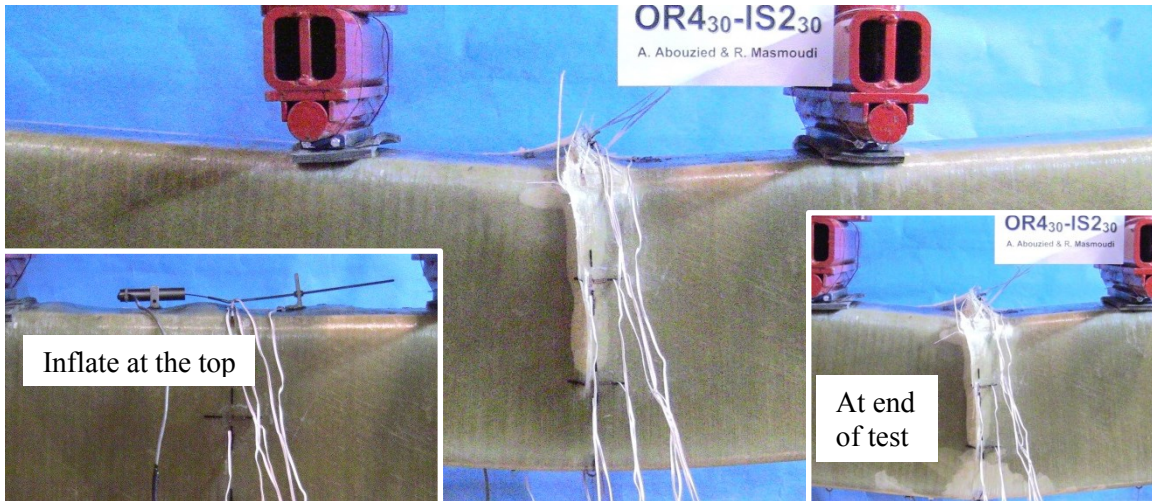
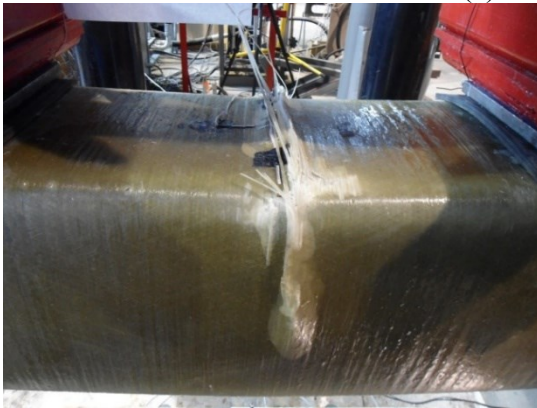


Figure 5.11 – Failure pattern and moment-deflection response of partially-CFFT beams OR8₃₀-IC4₃₀



(a) Elevation view



(b) Top view



(c) Bottom view

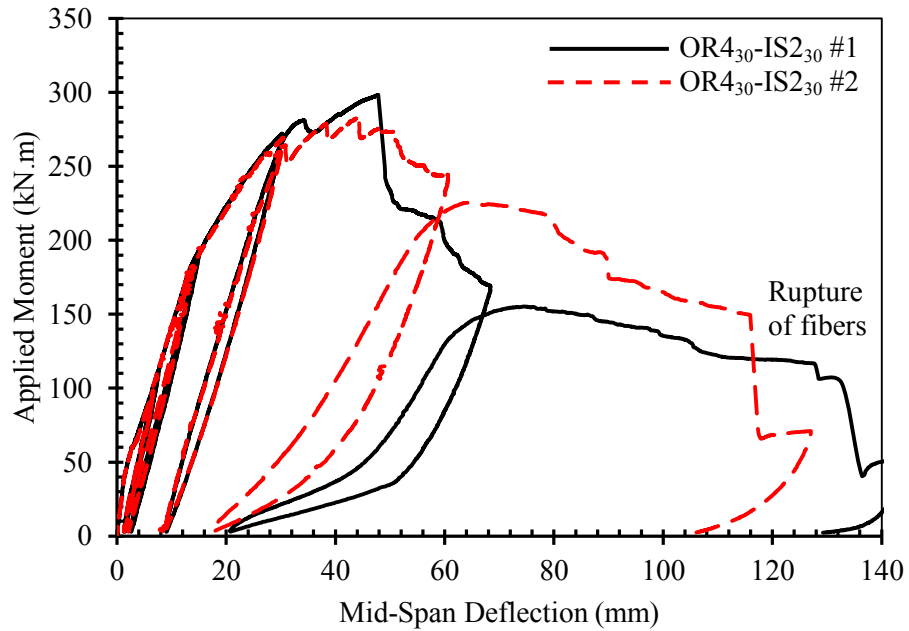
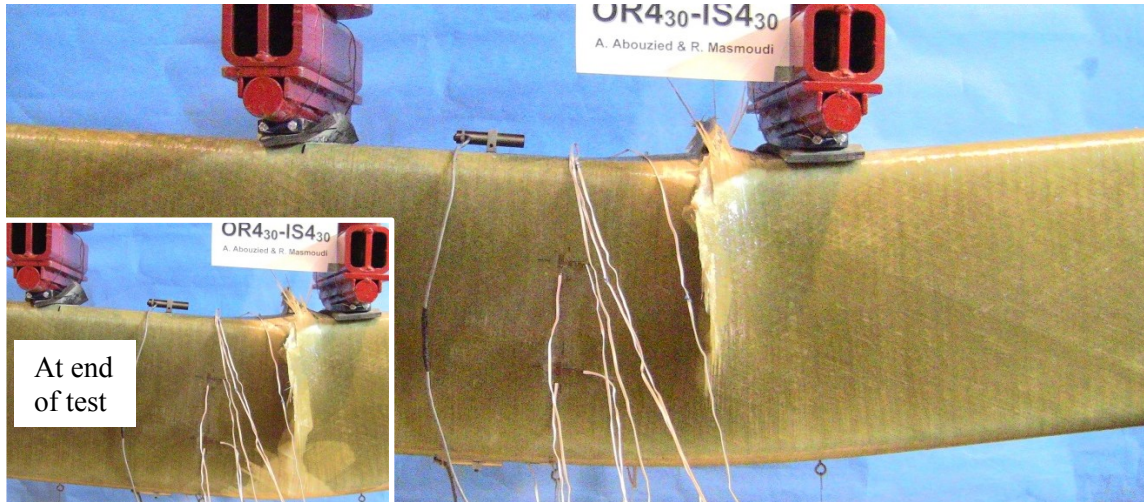


Figure 5.12 – Failure pattern and moment-deflection response of partially-CFFT beams OR430-IS230



(a) Elevation view



(b) Top view



(c) Bottom view

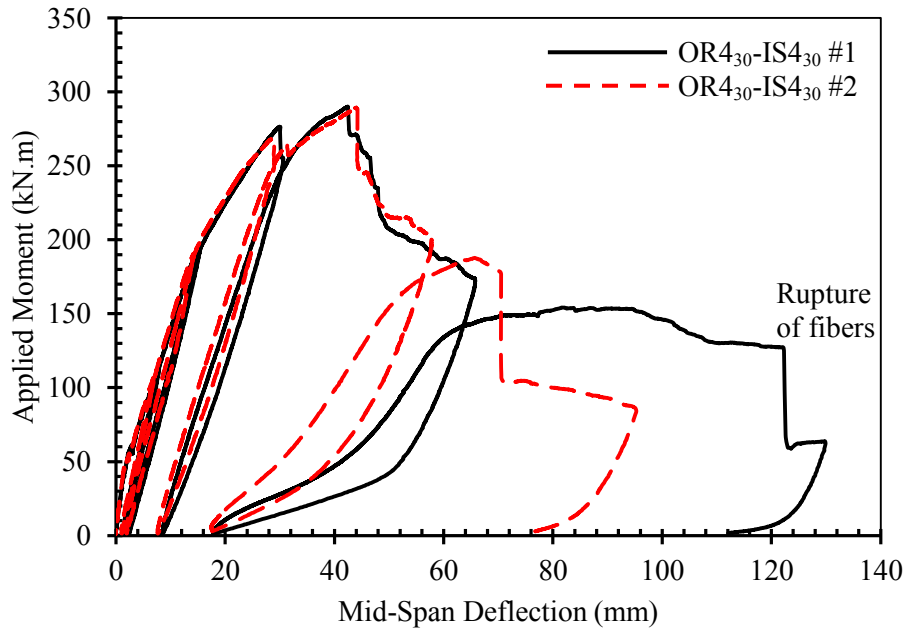
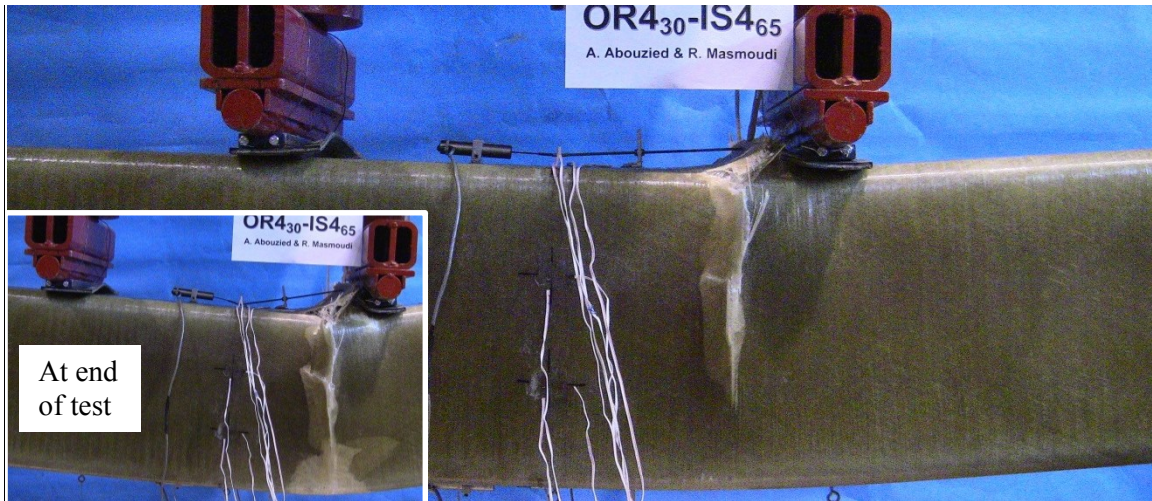


Figure 5.13 – Failure pattern and moment-deflection response of partially-CFFT beams OR430-IS430



(a) Elevation view



(b) Top view



(c) Bottom view

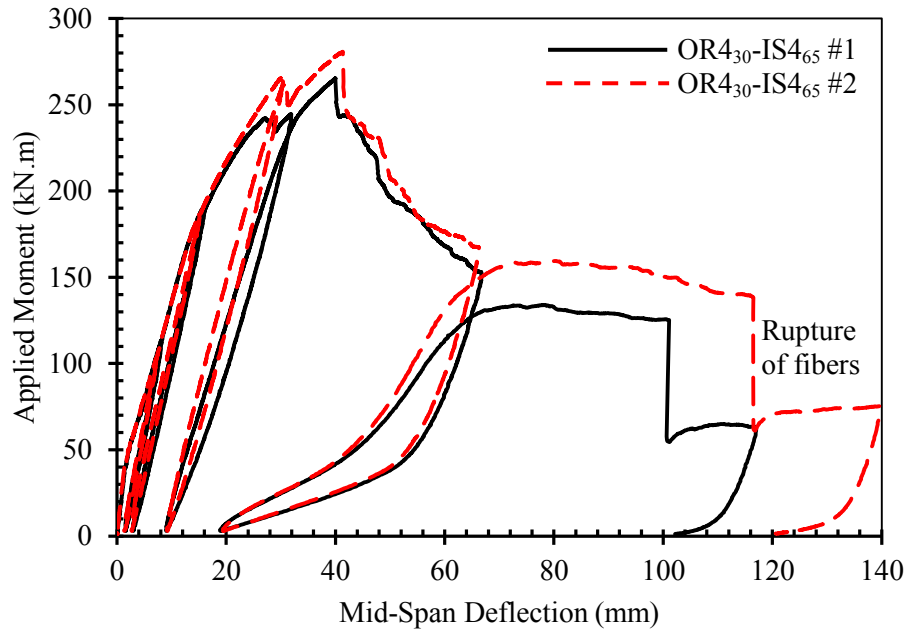
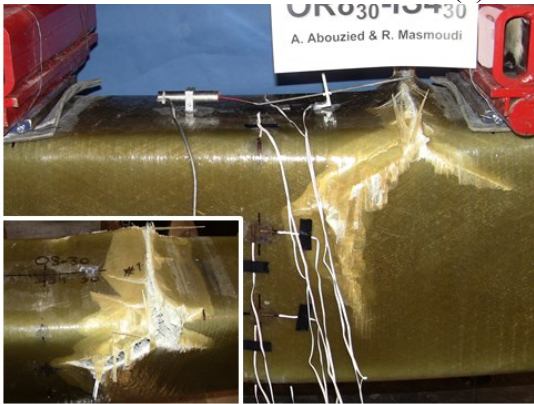


Figure 5.14 – Failure pattern and moment-deflection response of partially-CFFT beams OR430-IS465



(a) Elevation view



(b) Top view



(c) Bottom view

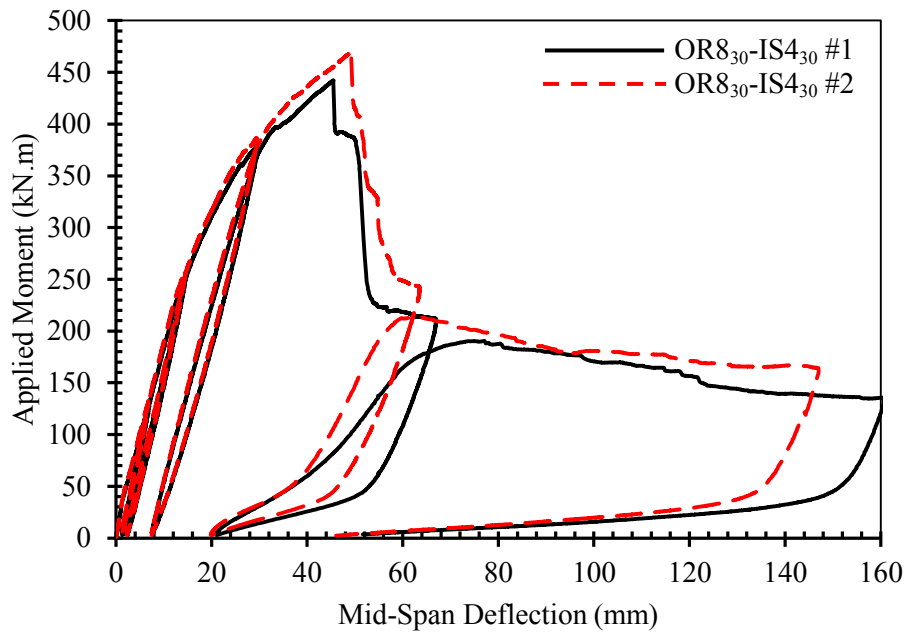


Figure 5.15 – Failure pattern and moment-deflection response of partially-CFFT beams OR830-IS430

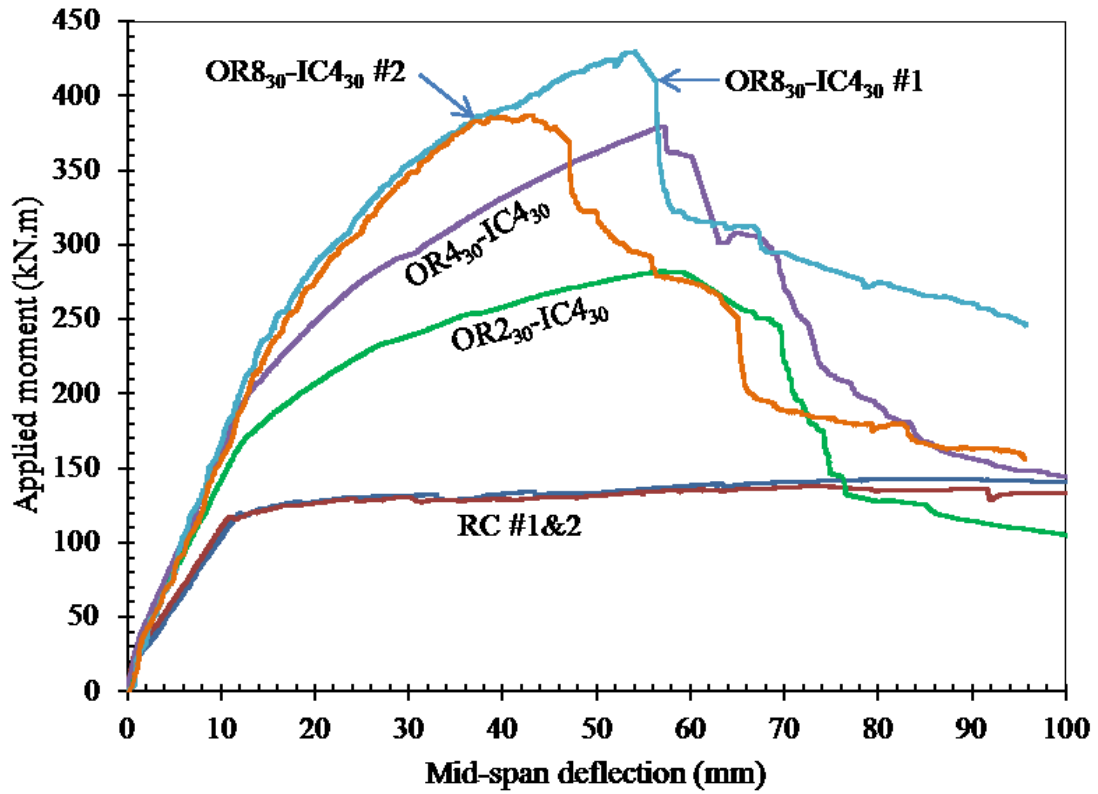


Figure 5.16 – Moment-deflection response of partially-CFFT beams with circular voids

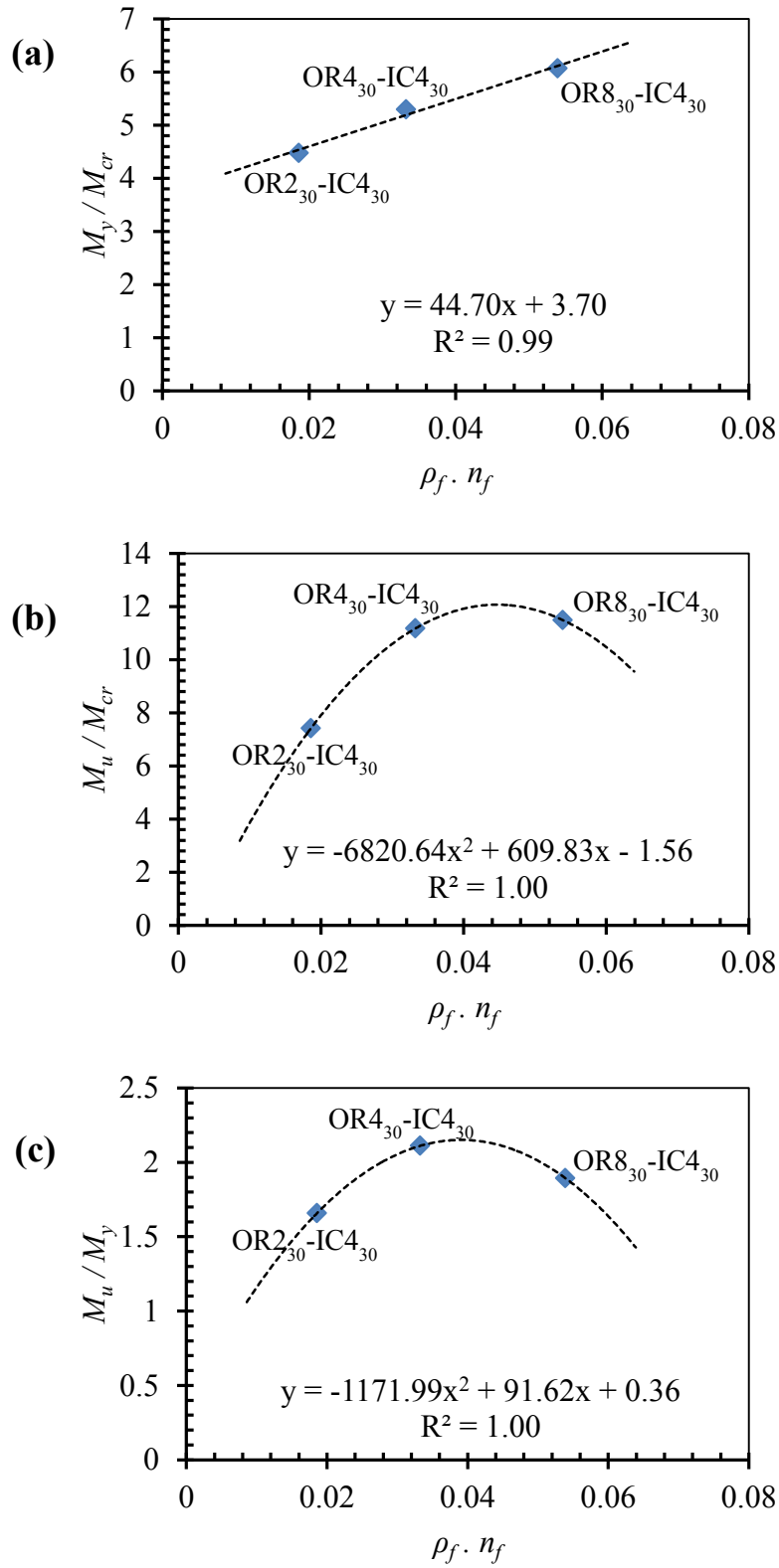


Figure 5.17 – Correlations between M_{cr} , M_y , and M_u of partially-CFFT beams with circular voids

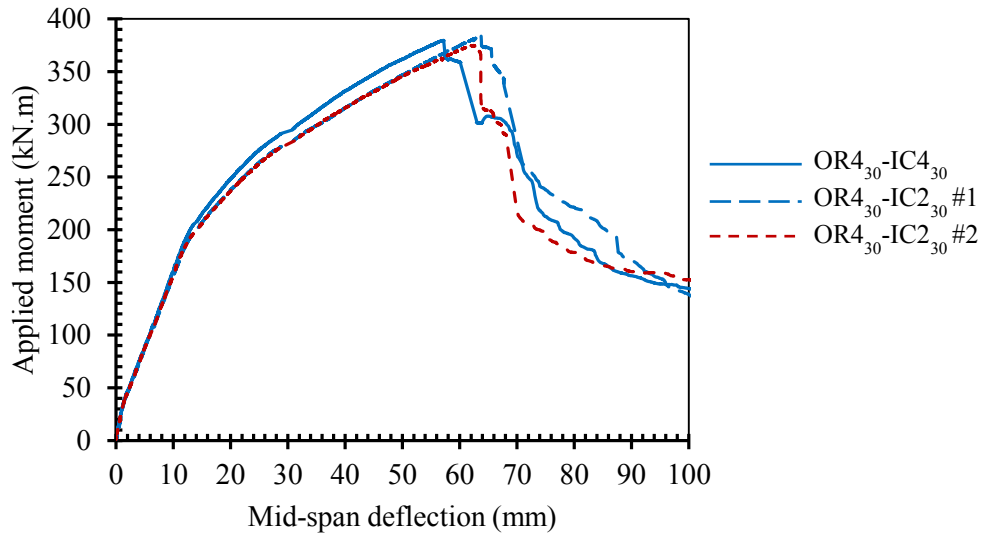
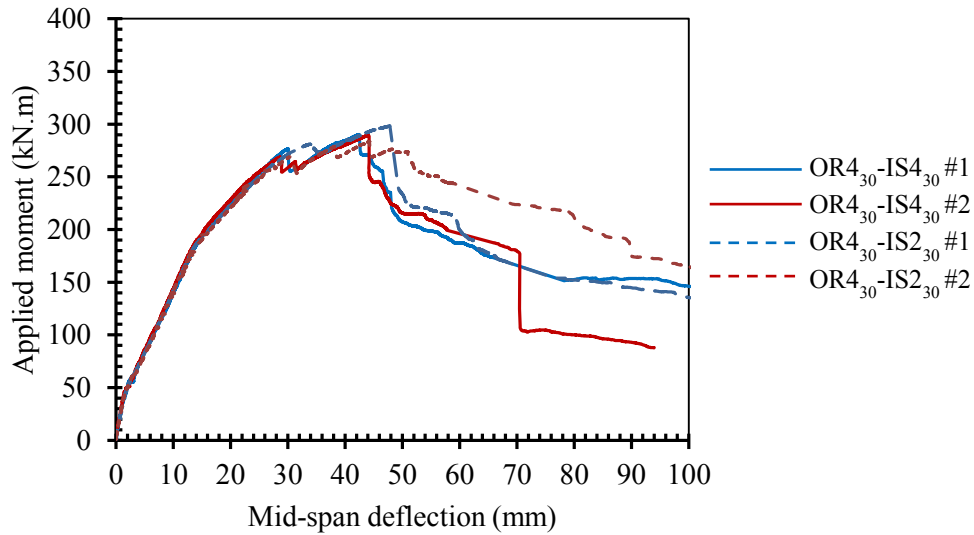
a) Moment-deflection response of OR4₃₀-IC4₃₀ and OR4₃₀-IC2₃₀b) Moment-deflection response of OR4₃₀-IS4₃₀ and OR4₃₀-IS2₃₀

Figure 5.18 – Effect of the inner tube thickness in partially-CFFT beams

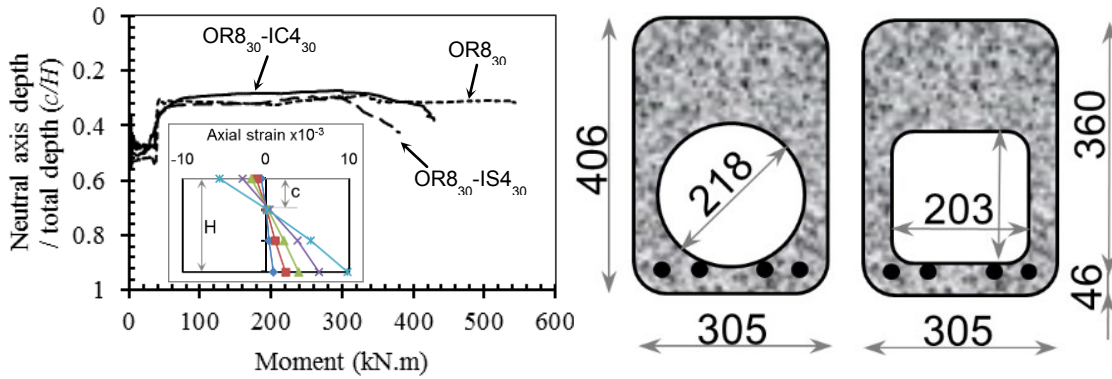


Figure 5.19 – Typical neutral axis location in partially-CFFT beams

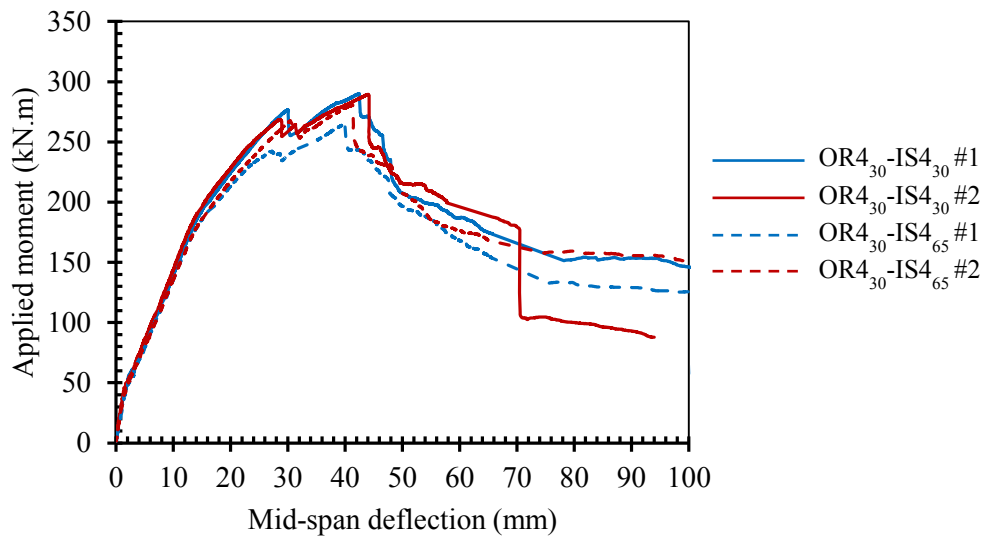


Figure 5.20 – Effect of the inner tube laminates in partially-CFFT beams

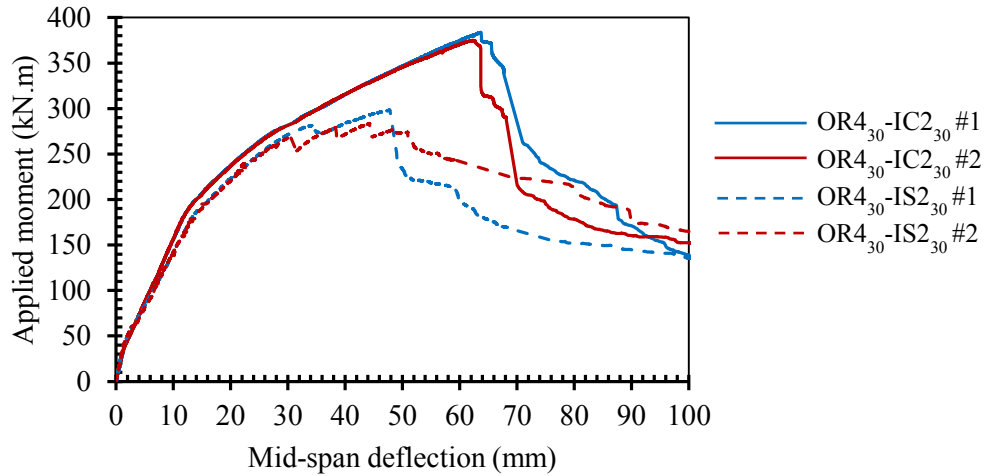
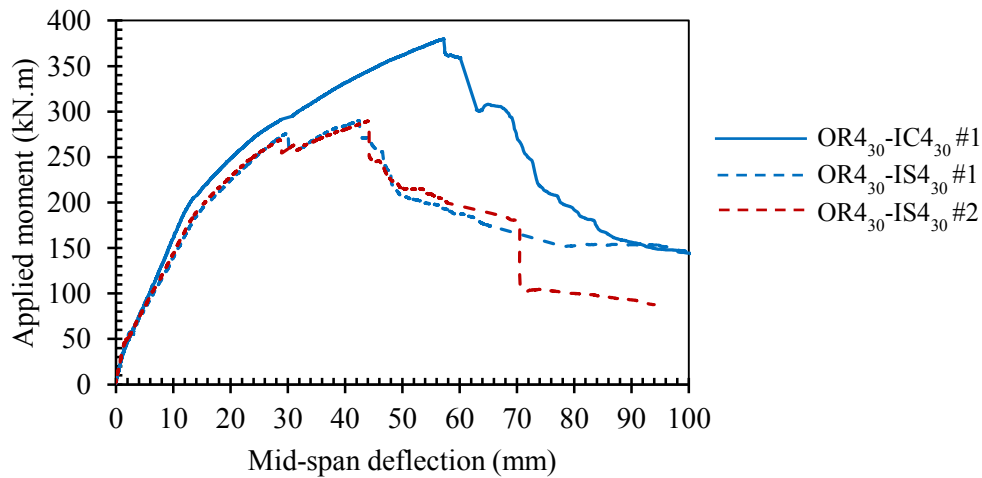
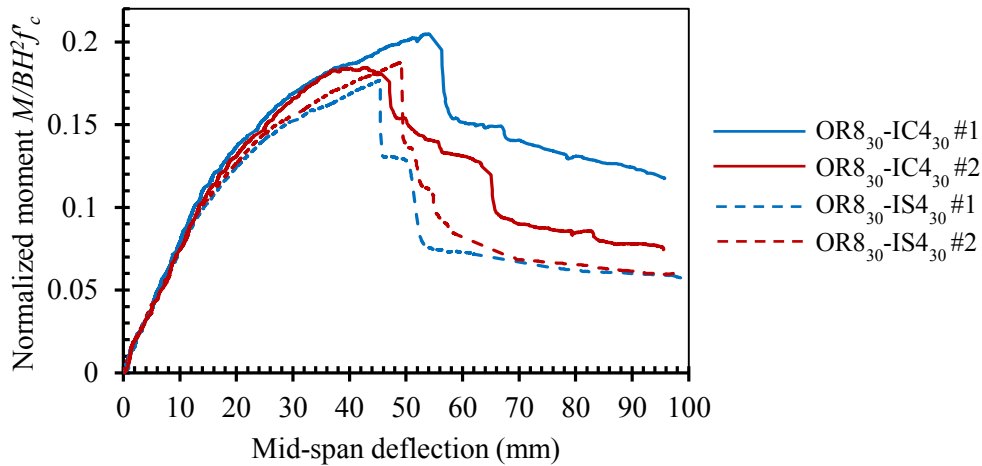
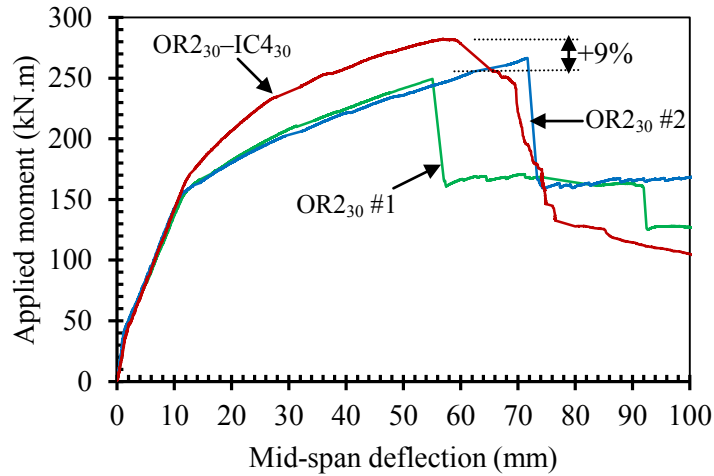
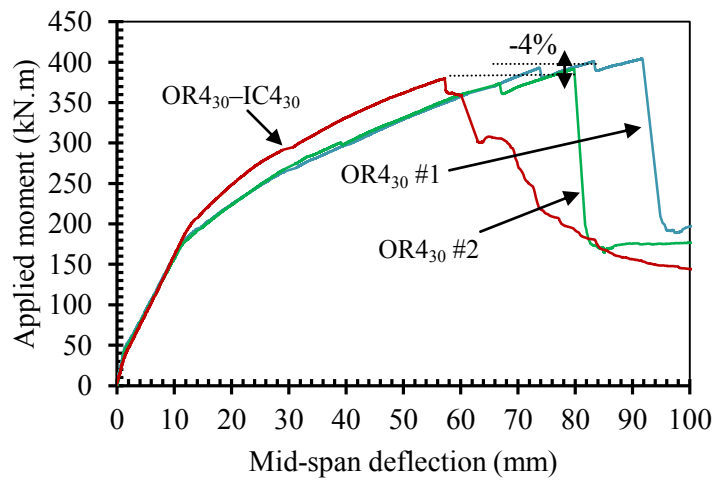
a) Moment-deflection response of OR4₃₀-IC2₃₀ and OR4₃₀-IS2₃₀b) Moment-deflection response of OR4₃₀-IC4₃₀ and OR4₃₀-IS4₃₀c) Normalized moment-deflection response of OR8₃₀-IC4₃₀ and OR8₃₀-IS4₃₀

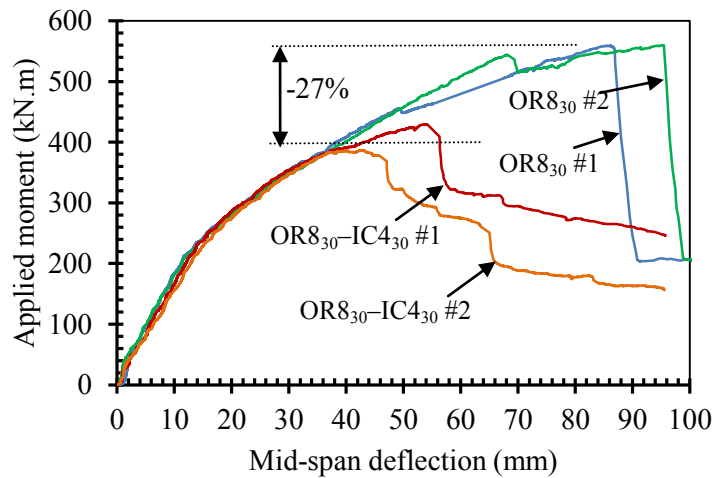
Figure 5.21 – Effect of the inner tube shape in partially-CFFT beams



a) Moment-deflection response of OR2₃₀ and OR2₃₀-IC₄₃₀

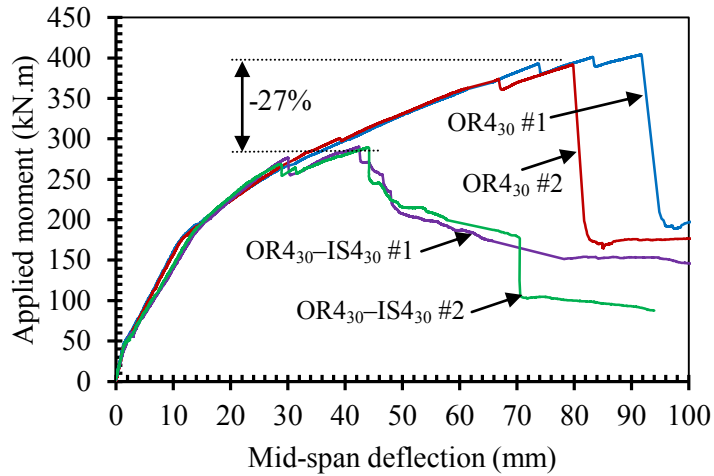


b) Moment-deflection response of OR4₃₀ and OR4₃₀-IC₄₃₀

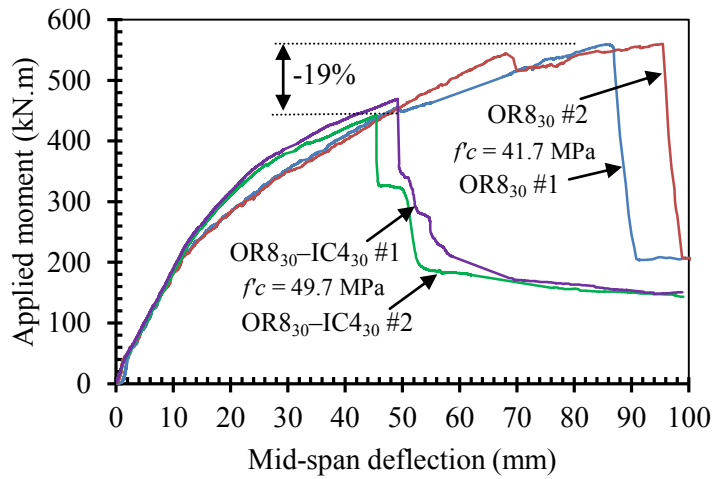


c) Moment-deflection response of OR8₃₀ and OR8₃₀-IC₄₃₀

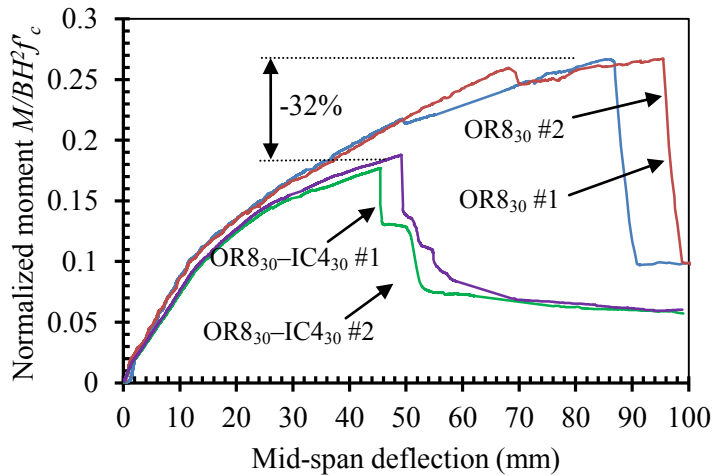
Figure 5.22 –Partially-CFFT beams with circular voids versus fully-CFFT beams



a) Moment-deflection response of OR4₃₀ and OR4₃₀-IS4₃₀



b) Moment-deflection response of OR8₃₀ and OR8₃₀-IS4₃₀



c) Normalized Moment-deflection response of OR8₃₀ and OR8₃₀-IS4₃₀

Figure 5.23 – Partially-CFFT beams with square voids versus fully-CFFT beams

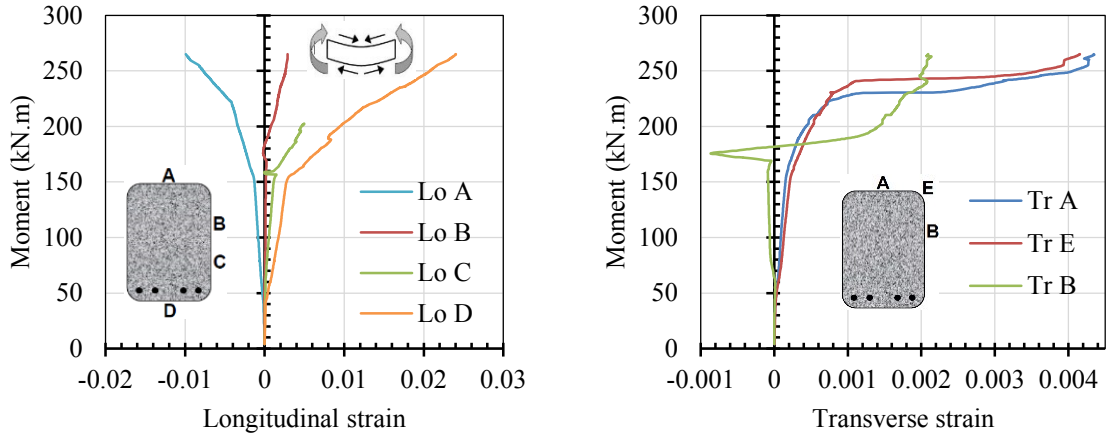


Figure 5.24 – Strains in the FRP tube of OR2₃₀

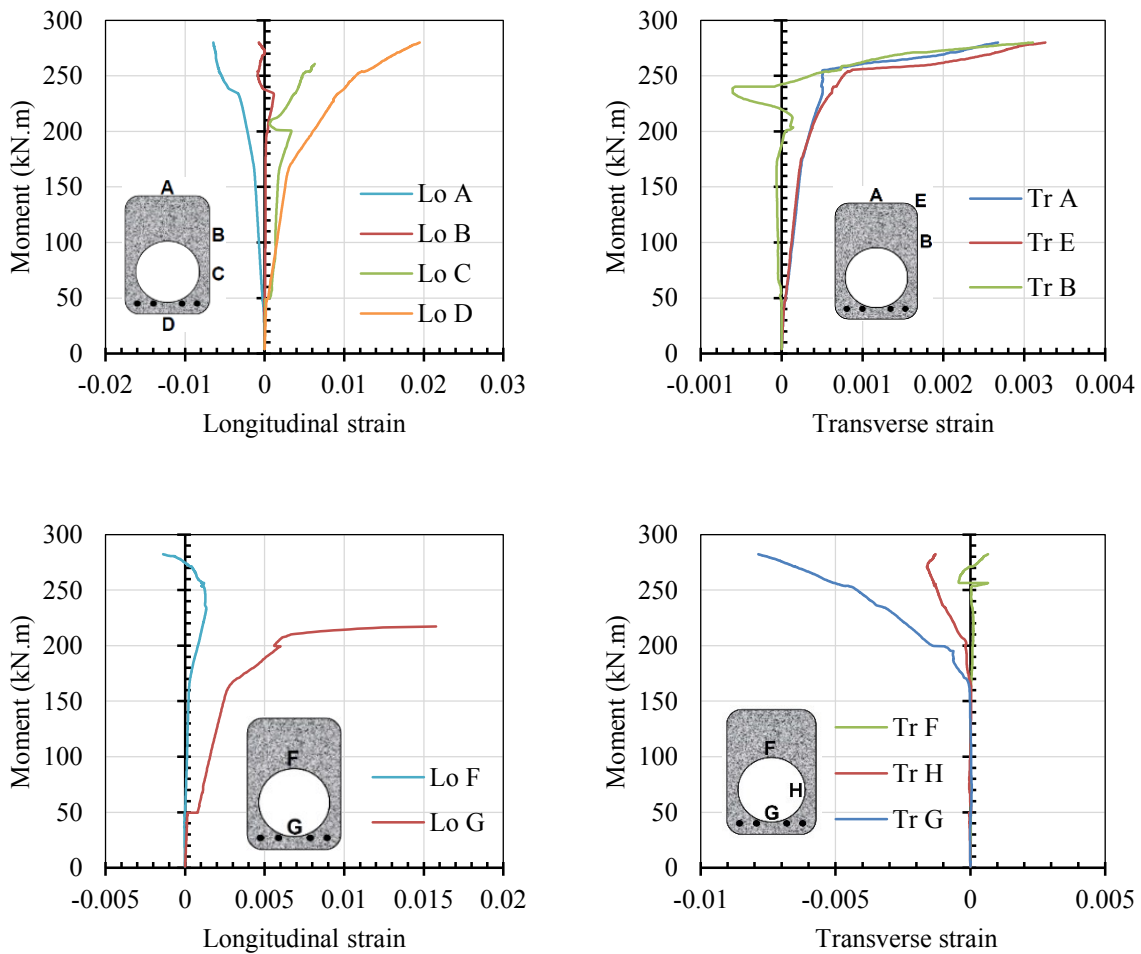


Figure 5.25 – Strains in the FRP tubes of OR2₃₀-IC4₃₀

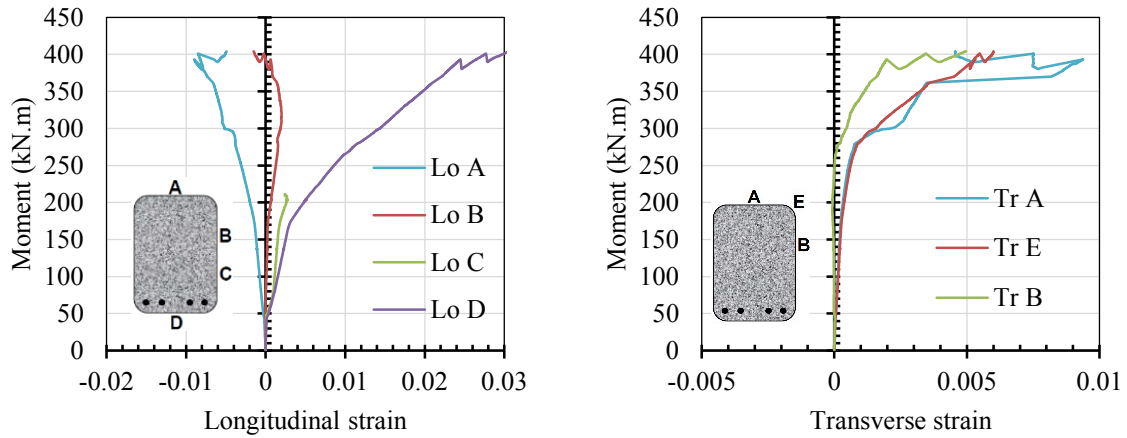


Figure 5.26 – Strains in the FRP tube of OR4₃₀

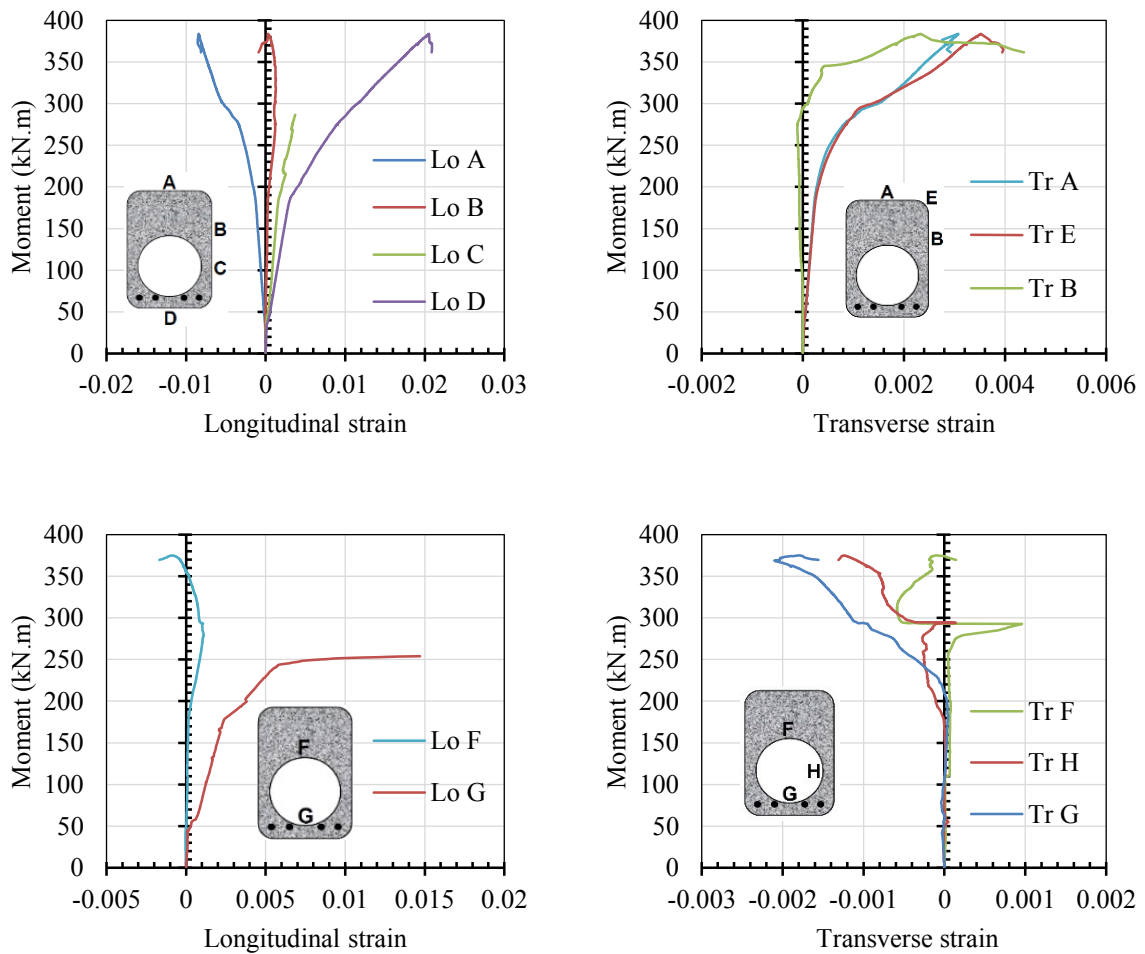


Figure 5.27 – Strains in the FRP tubes of OR4₃₀-IC2₃₀

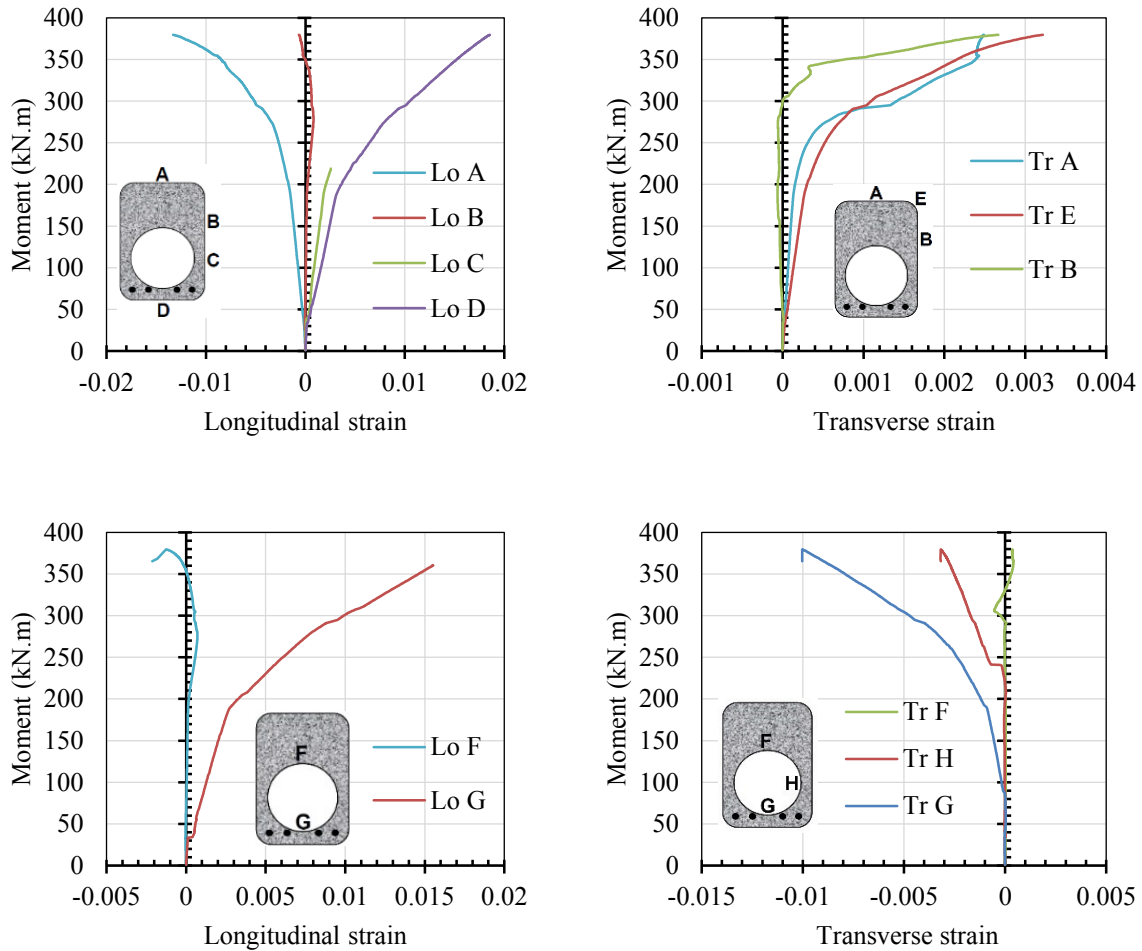


Figure 5.28 – Strains in the FRP tubes of OR4₃₀-IC4₃₀

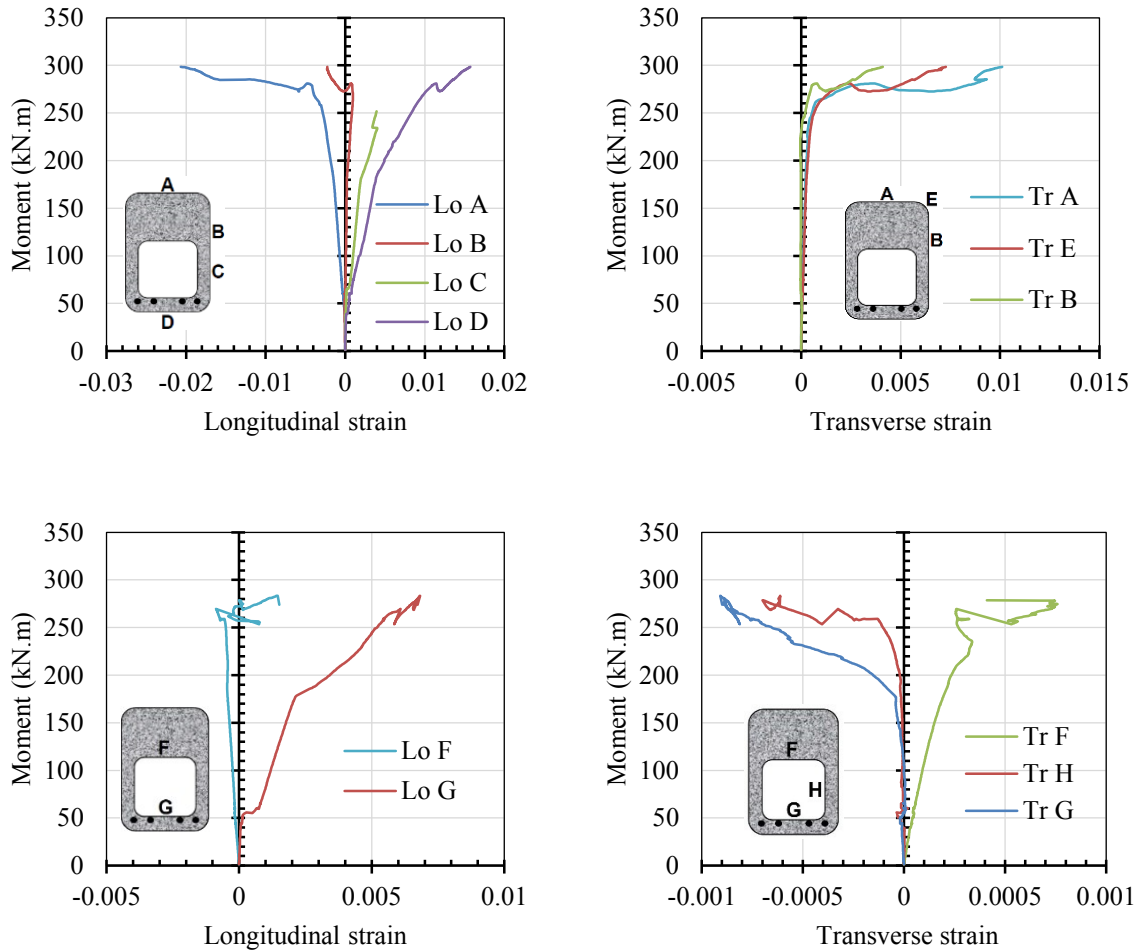


Figure 5.29 – Strains in the FRP tubes of OR4₃₀-IS2₃₀

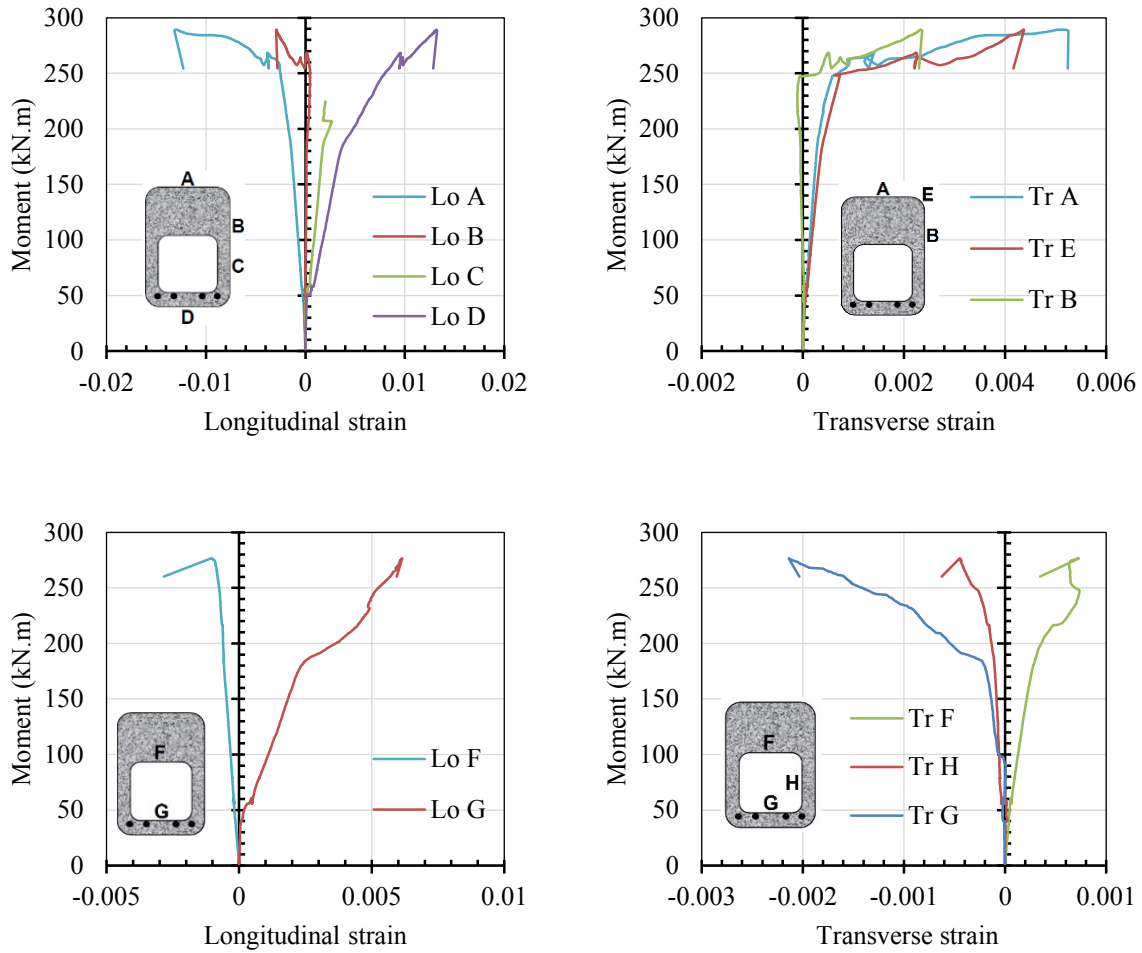


Figure 5.30 – Strains in the FRP tubes of OR4₃₀-IS4₃₀

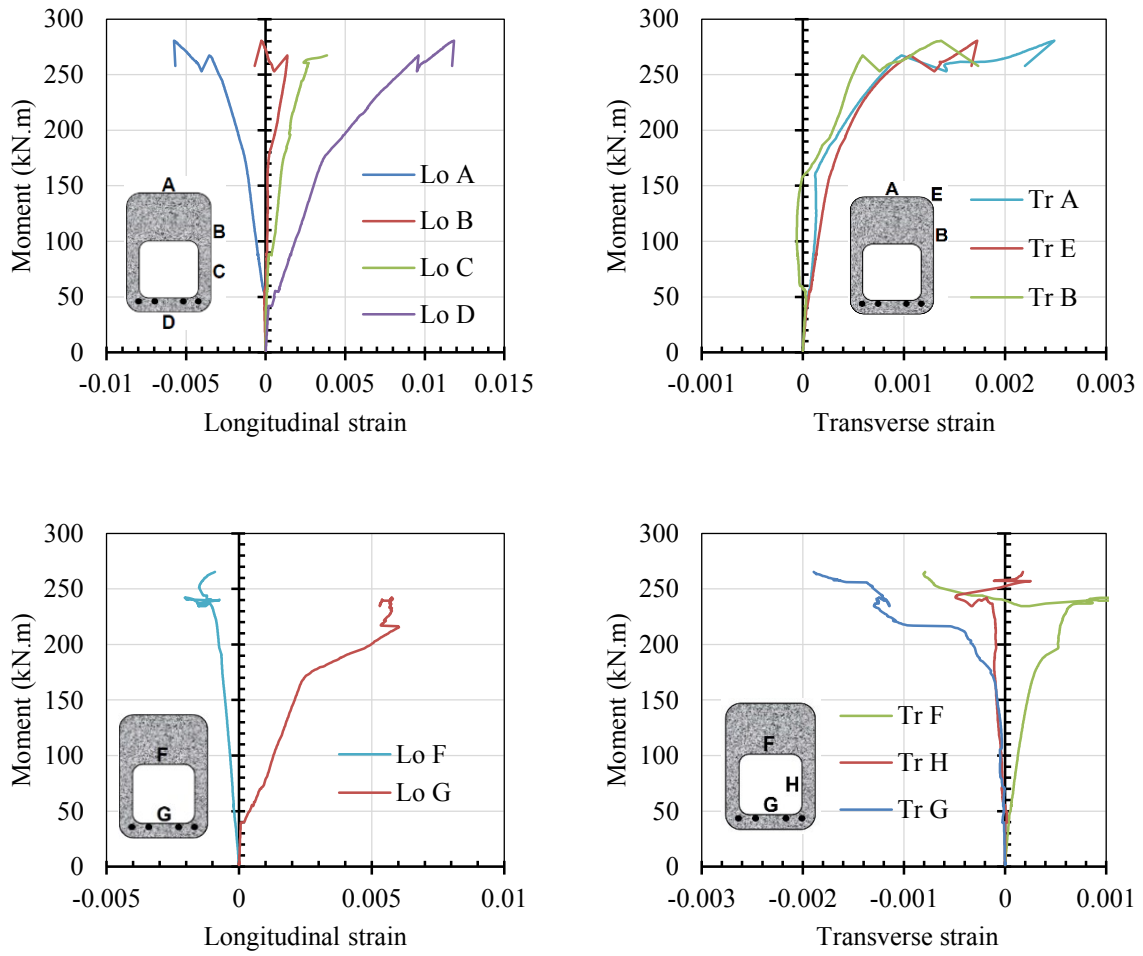


Figure 5.31 – Strains in the FRP tubes of OR4₃₀-IS4₆₅

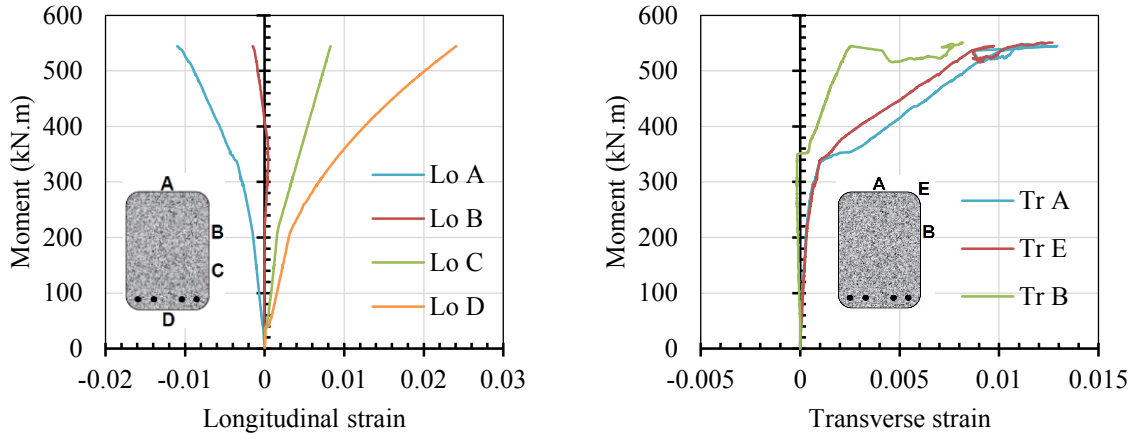


Figure 5.32 – Strains in the FRP tube of OR8₃₀

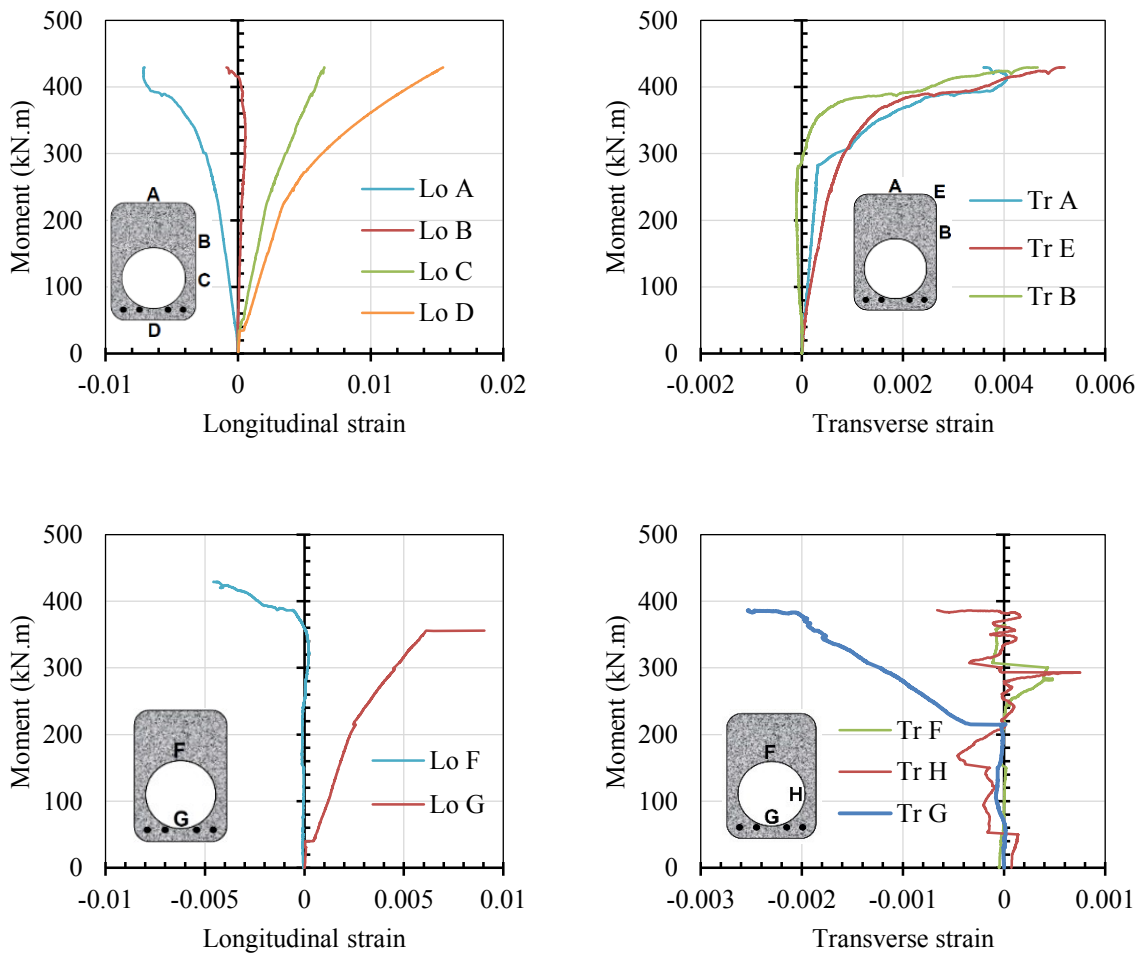


Figure 5.33 – Strains in the FRP tubes of OR8₃₀-IC4₃₀

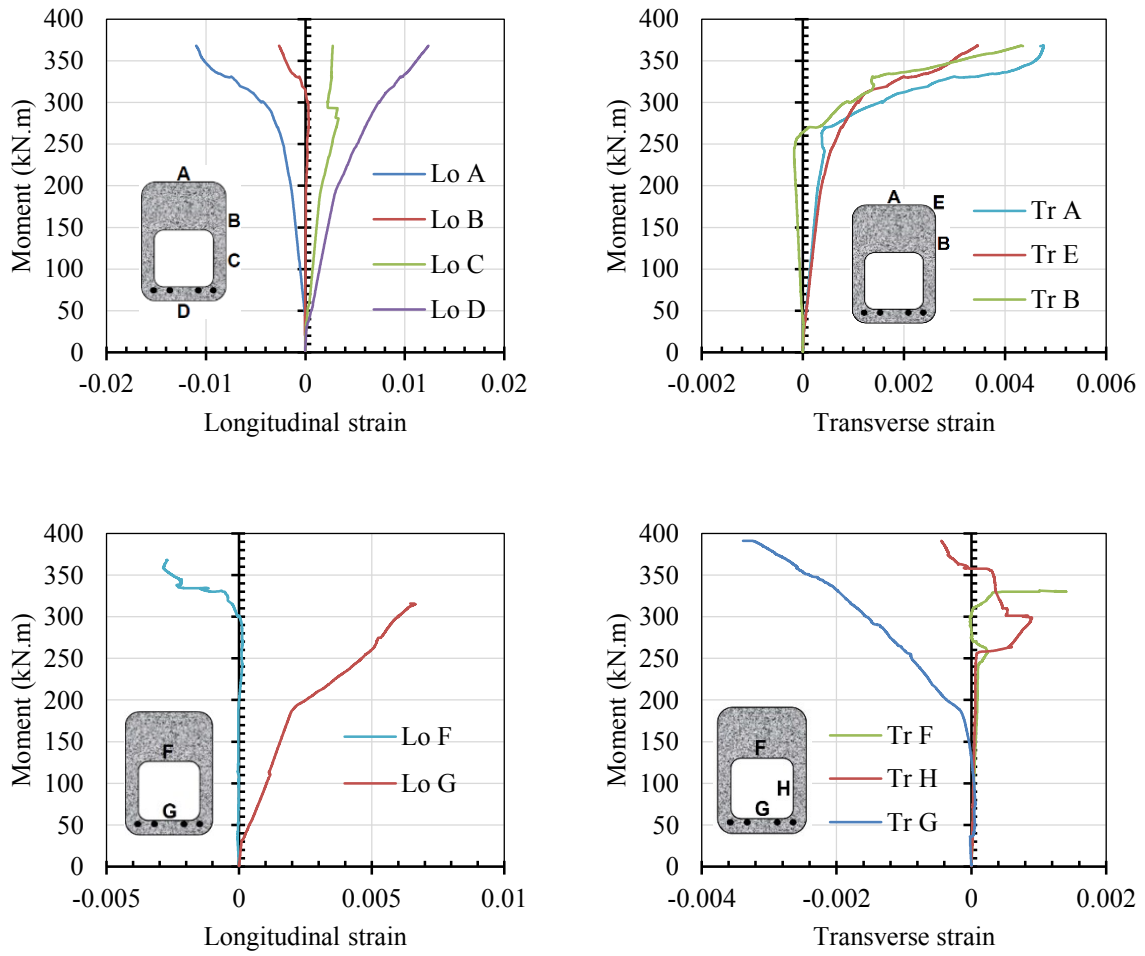


Figure 5.34 – Strains in the FRP tubes of OR8₃₀-IS4₃₀

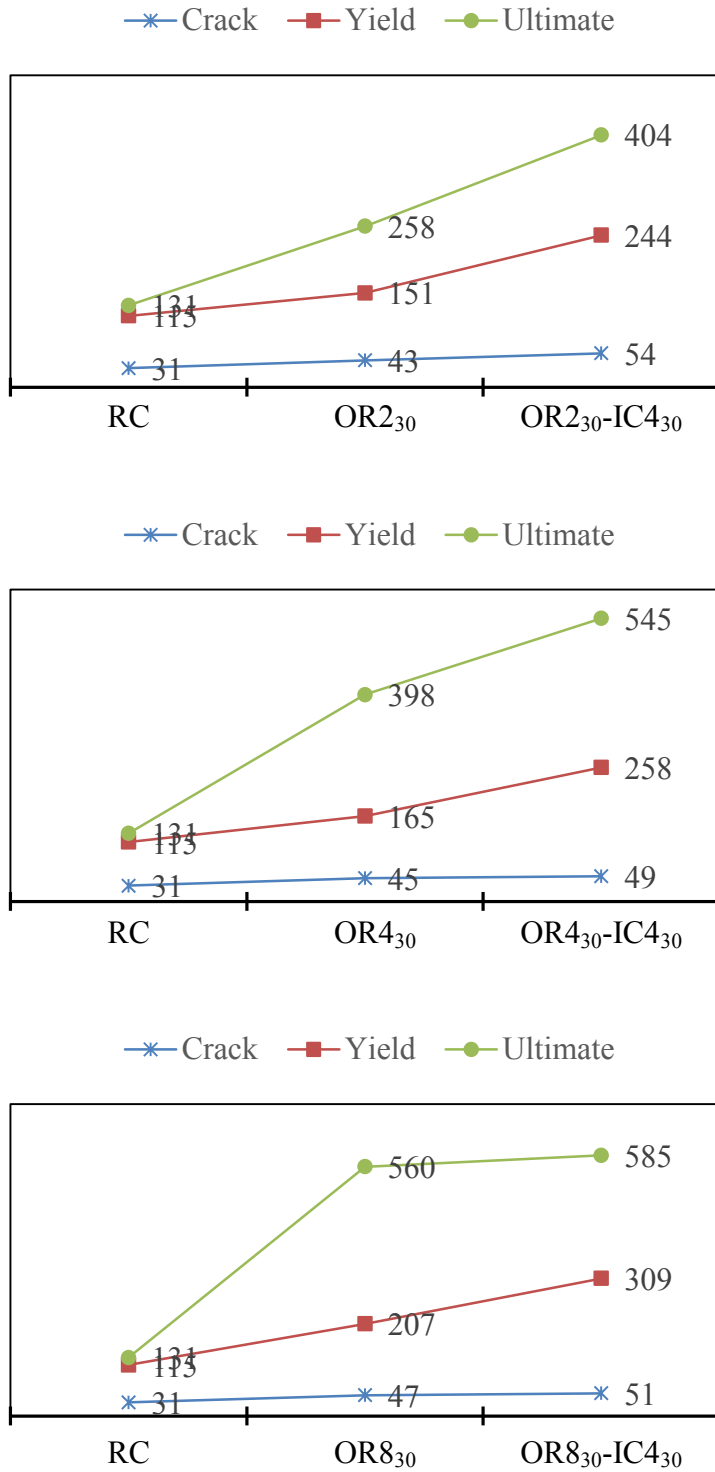
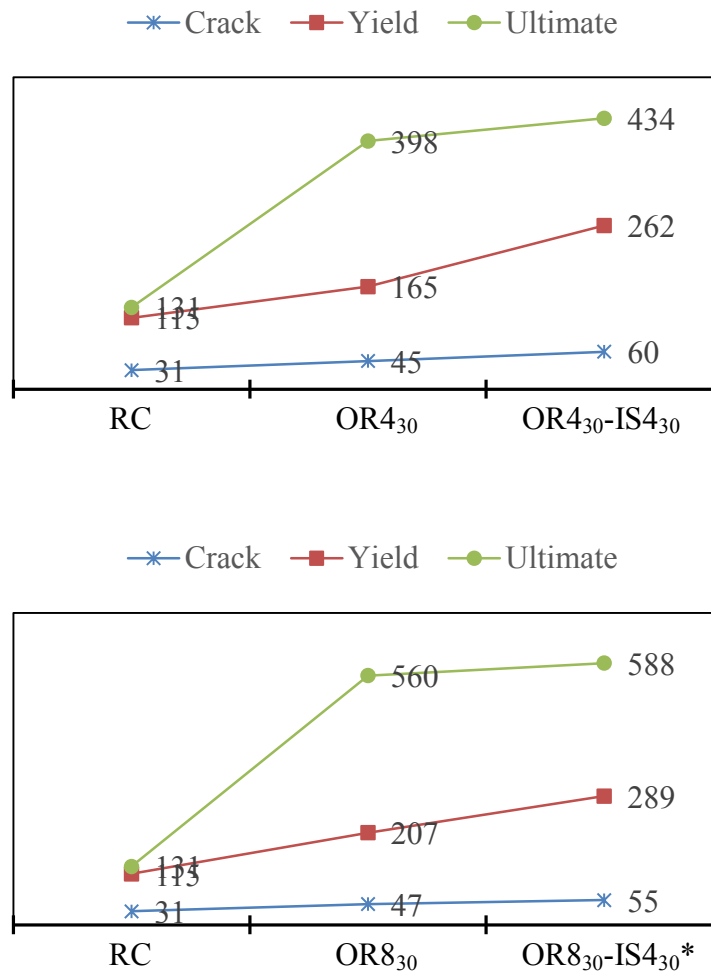


Figure 5.35 – Flexural strength-to-weight ratios of RC beams, fully-CFFT beams, and partially-CFFT beams with circular voids



*: The values are normalized due different concrete compressive strength

Figure 5.36 – Flexural strength-to-weight ratios of RC beams, fully-CFFT beams, and partially-CFFT beams with square voids

CHAPTER 6

DEFLECTION PREDICTION OF RECTANGULAR CFFT BEAMS

Foreword

Authors and Affiliation

- Ahmed Abouzied: PhD candidate, Department of Civil Engineering, Sherbrooke University, Sherbrooke, Quebec, Canada, J1K 2R1.
E-mail: ahmed.abouzied@usherbrooke.ca
- Radhouane Masmoudi: Professor, Department of Civil Engineering, Sherbrooke University, Sherbrooke, Quebec, Canada, J1K 2R1.
E-mail: radhouane.masmoudi@usherbrooke.ca

Journal Title: Journal of Structural Engineering ASCE

Submitted at: January 2016.

Acceptance Status: in review.

Reference: A. Abouzied and R. Masmoudi, (2016). “Effective moment of inertia of rectangular FRP-tube beams fully or partially filled with reinforced concrete”, *Journal of Structural Engineering ASCE*, (Submitted).

6.1 ABSTRACT

Full-scale concrete-filled fibre-reinforced polymer (FRP) tube (CFFT) rectangular beams have been tested under a four-point bending setup. These rectangular CFFT beams were 3200 mm long and 305×406 mm² cross section. They were reinforced with similar flexural steel reinforcement at the tension side. Some CFFT beams were completely filled with concrete. While, other CFFT beams were partially filled with concrete by providing inner hollow GFRP tubes inside the section at the tension zone. The experimental results indicated outstanding performance of the CFFT beams in terms of strength and deformability compared to conventional reinforced concrete (RC) beams. The CFFT beams exhibited additional flexural capacity after yielding of the steel reinforcement. Simultaneously, the deflection was increasing rapidly due to the low elastic modulus of the FRP tubes. This makes the RC models for predicting deflection inapplicable in case of CFFT beams. The experimental results were used to verify the applicability of Branson's equation to predict the effective moment of inertia and consequently the deflection of rectangular CFFT beams. Based on the analysis of the test results, Branson's equation needs to be modified, and new equations are developed to predict accurately the deflection of the rectangular CFFT beams reinforced with steel bars at the pre-yielding stage as well as the post-yielding stage.

Keywords: Beams, Fiber-reinforced polymer, Flexural behaviour, Deflection, Theoretical prediction, Branson's equation.

6.2 INTRODUCTION

In the last two decades, considerable research has been conducted to validate the application of fibre-reinforced polymer (FRP) composites in the construction industry. One of the innovative applications is the concrete-filled FRP tubes (CFFTs). In this dissertation, the author tested rectangular CFFT beams with steel rebar at the tension side. The CFFT beams experienced better performance than the conventional RC beams in terms of flexural strength and ductility. The CFFT beams exhibited superior additional flexural strength after yielding of the embedded steel reinforcement, which is attributed to the confining action of the FRP tube on the concrete core and the tube itself acts as flexural reinforcement in the axial direction. However, the flexural stiffness was small at the post-yielding stage due to the low elastic modulus of the FRP tube. Accordingly, the deflection at the post-yielding stage was increasing rapidly. Based on the results in this study, the deflection may control the design and accordingly equations are needed to predict the deflection with reasonable accuracy.

6.3 REVIEW OF DEFLECTION EQUATIONS

Immediate or short-term deflection can be calculated by using an average effective moment of inertia I_e in conjunction with elastic deflection formulas or by integration of curvature along the length of the beam [Bischoff 2005]. This effective moment of inertia I_e has two limits. First, the gross moment of inertia of a non-cracked section transformed to concrete I_g , which is considered the upper limit for I_e . Second, the moment of inertia of a fully cracked transformed section I_{cr} , which is the lower limit for I_e .

At the pre-cracking stage where the applied moment M_a is less than the cracking moment M_{cr} ($M_a \leq M_{cr}$), no cracks can be initiated. Accordingly I_e can be considered equivalent to I_g ($I_e = I_g$). After cracking ($M_a \geq M_{cr}$), I_e is gradually degraded to a value slightly above I_{cr} . Branson (1965) introduced the concept of using an effective moment of inertia as follows:

$$I_e = \left(\frac{M_{cr}}{M_a} \right)^3 I_g + \left[1 - \left(\frac{M_{cr}}{M_a} \right)^3 \right] I_{cr} \leq I_g \quad (6.1)$$

Where M_{cr} is the cracking moment and M_a is the applied service moment at the critical section. The equation represents a gradual transition from the non-cracked response to the fully cracked response by increasing the load. Note that, Branson calibrated his empirical expression for I_e with results from flexural members having steel reinforcement ratio greater than 0.01.

It was found that, Branson's expression overestimates the member stiffness when the ratio I_g / I_{cr} of the section exceeds 3 [Bischoff 2005]. Hence, deflection is underestimated for steel reinforcement ratios less than 0.01 and for most flexural members reinforced with FRP bars, as these members have a ratio I_g / I_{cr} much greater than 3 [Bischoff 2007]. In fact, many investigators proposed different modifications to Branson's equation for better correlation with the experimental results for both RC beams having low steel reinforcement ratios and FRP-RC beams [Benmokrane et al. 1996; Masmoudi et al. 1998; Toutanji and Deng 2003; Bischoff 2005, 2007; Bischoff and Gross 2011; Al-Sunna et al. 2012]. Nevertheless, Branson's expression is still the common used equation to determine I_e as suggested by North American codes like ACI-318-14, CSA A23.3-14, and CSA S6-14.

Bischoff (2005) developed a new expression for I_e based on fundamental concepts of tension stiffening. His expression is considered a rational replacement for the empirical Branson's equation and is given as follows:

$$I_e = \frac{I_{cr}}{1 - \gamma \left(1 - \frac{I_{cr}}{I_g}\right) \left(\frac{M_{cr}}{M_a}\right)^2} \quad (6.2)$$

Where γ is an integration factor developed by Bischoff and Gross (2011) based on integration of curvature and depends on the loading case and accounts for the change in the stiffness along the beam span. For simply supported beams under a four-point bending load, γ is calculated as:

$$\gamma = \frac{3(a/l) - 4\xi(a/l)^3}{3(a/l) - 4(a/l)^3} \text{ and } \xi = 4(M_{cr}/M_a) - 3 \quad (6.3)$$

Bischoff and Gross (2011) concluded also that the member stiffness is significantly affected by the cracking moment and degrades rapidly after the first crack. They concluded that a reduced cracking moment equals to 80% of that computed by the ACI-318 (2014) code provides a reasonable estimate of deflection for FRP-RC beams using their expression. This decrease accounts for the tensile stresses developed in the concrete from restraint to shrinkage by the embedded reinforcement, and a larger decrease may be necessary when additional tensile stress from restraint by the supports or adjoining parts of the structure is significant. Based on this conclusion, the computed M_{cr} should be decreased in the current study, because the rectangular CFFT beams have steel reinforcement and roughened FRP tubes, in addition, the concrete is tightly positioned between the outer and inner FRP tubes in the partially-CFFT beams.

The American code ACI 440.1R (2015) proposed to compute the effective moment of inertia by Bischoff's expression. The Canadian code CSA-S806 (2012) proposed also using Bischoff's expression in calculating the effective moment of inertia for FRP-reinforced beams but $\gamma = 0.5$. Nevertheless, Bischoff's expression, like most other models, does not address the post-yielding behaviour of strengthened RC beams or CFFT beams with steel rebar as in this study. Few models for predicting the post-yielding deflections of FRP-strengthened concrete beams were developed [Elmihilmy and Tedesco 2000; Charkas et al. 2002; Said 2010], but almost no research was carried out to predict the deflection of CFFT beams whether reinforced with steel or not. Mohamed and Masmoudi (2011) introduced a first attempt to predict the deflection of steel-reinforced CFFT circular beams by modifying Branson's equation at the pre-yielding stage and developing a simple linear equation to predict the deflection at the post-yielding stage. However, their experimental program had limited tests data and did not consider any variation in the FRP tube thickness and reinforcement. In addition, their equations were exclusive for their circular CFFT beams and need to verify its applicability in case of rectangular reinforced CFFT beams.

6.4 DEFLECTION CALCULATIONS

In a four-point bending load system, the flexural component of the deflection (Δ) at the center of a simply supported beam can be calculated as follows:

$$\Delta = \frac{P \cdot a}{48 E_{co} I_e} (3L^2 - 4a^2) \quad (6.4)$$

Where L is the span, P is the total concentrated load which is divided into two loads, $P/2$, each applied at a distance a from the support, E_{co} is the elastic modulus of the concrete, and I_e is the effective moment of inertia of the beam cross section.

The experimental total applied loads P_{exp} and the corresponding measured mid-span deflections Δ_{exp} were retrieved in Eq. (6.4) to evaluate the experimental moment of inertia $I_{e(exp)}$ as follows:

$$I_{e(exp)} = \frac{P_{exp} \cdot a}{48 E_{co} \Delta_{exp}} (3L^2 - 4a^2) \quad (6.5)$$

The applied moment $M_a = \frac{P_{exp} \cdot a}{2}$, then Eq. (6.5) can be written as:

$$I_{e(exp)} = \frac{M_a}{24 E_{co} \Delta_{exp}} (3L^2 - 4a^2) \quad (6.6)$$

The gross moment of inertia of a non-cracked section transformed to concrete (I_g) is calculated as:

$$I_g = I_c + (n_s - 1)I_s + n_f I_f \quad (6.7)$$

Where I_c is the moment of inertia of the concrete section excluding the voids in case of the partially-CFFT beams. I_s and I_f are the local moment of inertia of the steel and FRP tube(s), respectively. n_s is the steel modular ratio ($n_s = E_s/E_{co}$). n_f is the FRP modular ratio ($n_f = E_f/E_{co}$). E_s is the elasticity modulus of steel that equals 200 GPa. E_{co} is the elasticity modulus of concrete calculated as $E_{co} = 4500\sqrt{f'_c}$ based on the cylinders test. E_f is the elasticity modulus of the FRP tube, which is approximated as the average of the axial elasticity modulus in tension and in compression.

In this study, the suggested cracking moment M_{cr}^* in deflection calculations is calculated as:

$$M_{cr}^* = \eta \cdot M_{cr} = \eta \cdot f_{cr} \cdot I_g / Y_t \quad (6.8)$$

$$f_{cr} = 0.62 \sqrt{f'_c} \quad (6.9)$$

η is a proposed reduction factor inspired from Bischoff and Gross (2011) conclusion that the member stiffness is significantly affected by the cracking moment and degrades rapidly after the first crack. This reduction factor, η , accounts for the tensile stresses developed in the concrete from restraint to shrinkage by the embedded reinforcement, the roughened FRP tubes, and the tight position of concrete inside the composite CFFT section. Based on this study, η is proposed as 0.8 and 0.7 for the fully-CFFT beams and the partially-CFFT beams, respectively. Y_t is the distance of the extreme tension fiber of concrete from the centroid, which is calculated as:

$$Y_t = \frac{A_c Y_c + (n_s - 1) A_s Y_s + n_f A_f Y_f}{A_c + (n_s - 1) A_s + n_f A_f} \quad (6.10)$$

Where, Y_c is the distance between the center of gravity (C_g) of the concrete section and a datum (the extreme tension fiber of concrete). Y_s and Y_f are the distance between the C_g of the steel bars and the FRP tube(s) and the datum, respectively.

Many researchers concluded that the reinforcement ratio should be considered in Branson's equation for I_e [Yost et al. 2003; Rafi and Nadjai 2009; Al-Sunna et al. 2012; ACI 440.1R 2015]. The current test program does not contain experimental data for variable steel reinforcement ratio. Therefore, the experimental data was enriched by adding some unreinforced CFFT beam specimens from previous work for Fam et al. (2005) and Belzer et al. (2013) in addition to results from the parametric study carried out on fully-CFFT beams (see Chapter 4) to investigate the steel reinforcement. The results of the parametric study were used to enrich the experimental data as shown in Figure 6.3 and 6.4.

Figures 6.1 and 6.2 plot correlations between I_e / I_g and M_a evaluated from the experimental results of the fully-CFFT beams and some partially-CFFT beams, respectively. Figure 6.3 plots correlations between I_e / I_g and M_a evaluated from the parametric study on two different FRP tubes with variable steel reinforcement ratios. Note that, I_e is evaluated from Eq. (6.6), and I_g is evaluated from Eq. (6.7). As seen, the effective moment of inertia has three stages in reinforced CFFT beams: (1) Pre-cracking stage, (2) Pre-yielding stage, and (3) Post-yielding stage.

Figures 6.5 to 6.10 plot the experimental I_e / I_g and M_a / M_{cr} of the fully-CFFT beams compared to those evaluated from Branson and Bischoff equations. Note that, Figure 6.5 plots the results of the RC beams considering it as a CFFT beam with zero tube thickness. It can be seen that Branson and Bischoff equations do not consider well the change in the tube thickness at the pre-yielding stage and do not consider the post-yielding stage at all.

Figures 6.11 to 6.15 plot the experimental I_e / I_g and M_a / M_{cr} of the partially-CFFT beams compared to those evaluated from Branson and Bischoff equations. Branson and Bischoff equations do not consider well the change in the tube thickness at the pre-yielding stage and do not consider the post-yielding stage at all. In addition, the experimental I_e of the partially-CFFT beams goes down the theoretical I_{cr} . This indicates that the composite action between the concrete and the steel reinforcement may not be as perfect as assumed due to the inner hollow FRP. Accordingly, the equation of I_e should provide a transition between I_g and a certain fraction of I_{cr} . Such an equation was proposed by Benmokrane et al. (1996) as given in Eq. (6.11). Where, they provided a coefficient α , which reflects the reduced composite action between the concrete and the FRP bars in their FRP-RC beams. α and β are specific coefficients for their particular tests and equal 0.84 and 7, respectively.

$$I_e = \alpha I_{cr} + \left(\frac{I_g}{\beta} - \alpha I_{cr} \right) \left(\frac{M_{cr}}{M_a} \right)^3 \quad (6.11)$$

6.4.1 Procedure of Analysis and Assumptions

6.4.1.1 At the Pre-Cracking Stage ($M_a \leq M_{cr}$)

The effective moment of inertia is considered equivalent to the gross moment of inertia of the non-cracked section transformed to concrete ($I_e = I_g$).

6.4.1.2 At the Pre-Yielding Stage ($M_{cr} \leq M_a \leq M_y$)

From every fully-CFFT beam, experimental or parametric, an individual power m is evaluated as follows:

$$I_{e(\text{exp})} = \left(\frac{\eta \cdot M_{cr}}{M_a} \right)^m I_g + \left[1 - \left(\frac{\eta \cdot M_{cr}}{M_a} \right)^m \right] I_{cr} \quad (6.12)$$

$$I_{e(\text{exp})} = I_{cr} + (I_g - I_{cr}) \left(\frac{\eta \cdot M_{cr}}{M_a} \right)^m \quad (6.13)$$

$$\frac{I_{e(\text{exp})} - I_{cr}}{I_g - I_{cr}} = \left(\frac{\eta \cdot M_{cr}}{M_a} \right)^m \quad (6.14)$$

$$m = \log \left(\frac{I_{e(\text{exp})} - I_{cr}}{I_g - I_{cr}} \right) / \log \left(\frac{\eta \cdot M_{cr}}{M_a} \right) \quad (6.15)$$

Then the values of the power m for all the CFFT beams were analyzed by regression analysis considering variable reinforcement ratios of the FRP tubes and the steel reinforcement and the concrete strength as shown in Figure 6.4. Based on the regression analysis factors, the effect of the concrete compressive strength f'_c is negligible and can be eliminated. However, the concrete elasticity modulus is considered in calculating the modular ratio of the FRP tube and steel rebar. A new power m is developed as shown in Eq. (6.16).

$$m = \frac{0.112}{(\rho_f n_f + \rho_s n_s)^{1.165}} \quad (6.16)$$

Where ρ_f is the FRP tube reinforcement ratio ($\rho_f = A_{tube} / bh$), ρ_s is the steel reinforcement ratio ($\rho_s = A_s / bh$), b is the inner width of the section, and h is the inner height of the section.

A new factor α is also proposed to consider the low composite action due to the inner void in the partially-CFFT beams as discussed before. This factor, α , was found equivalent to the ratio between the gross moments of inertia of the CFFT section with a void to a corresponding fully section as shown in Eq. (6.17)

$$\alpha = \frac{I_{g(\text{section with void})}}{I_{g(\text{full section})}} \quad (6.17)$$

Based on the current study, $\alpha = 1$ in case of fully-CFFT beams (no voids), $\alpha = 0.89$ in case of partially-CFFT beams with circular voids, and $\alpha = 0.86$ in case of partially-CFFT beams with square voids.

Then, the effective moment of inertia at the pre-yielding stage of any reinforced or unreinforced fully or partially-CFFT beam can be calculated as:

$$I_e = \left(\frac{\eta \cdot M_{cr}}{M_a} \right)^m I_g + \left[1 - \left(\frac{\eta \cdot M_{cr}}{M_a} \right)^m \right] \alpha \cdot I_{cr} \quad (6.18)$$

Where η is a proposed reduction factor equals 0.8 for the fully-CFFT beams and equals 0.7 for the partially-CFFT beams with circular or square voids as discussed before.

6.4.1.3 At the Post-Yielding Stage ($M_y \leq M_a \leq M_u$)

Figures 6.5 to 6.15 show that at the post-yielding stage, the experimental I_e degraded and became lower than I_{cr} . Note that, I_{cr} was calculated upon a full value of steel elasticity modulus E_s at the pre-yielding stage. While at the post-yielding stage, it is rational to neglect E_s and to re-calculate a new I'_{cr} for the cracked transformed section neglecting the yielded steel. I'_{cr} will be the new lower limit for I_e in Branson's equation, while the upper limit will be taken as the last computed effective moment of inertia from the pre-yielding stage I'_e , which is calculated from Eq. (6.18). Also at the post-yielding stage, M_y should replace M_{cr} since it becomes the beginning moment at this stage. Then, the effective moment of inertia at

the post-yielding stage of any reinforced CFFT beam, fully or partially-CFFT beams, can be calculate as:

$$I_e = \left(\frac{M_y}{M_a} \right)^m I'_e + \left[1 - \left(\frac{M_y}{M_a} \right)^m \right] I'_{cr} \quad (6.19)$$

Where, the power m , calculated from Eq. (6.16), could be used again in the post-yielding stage.

The predicted results give a reasonable estimation for the effective moment of inertia in the pre-yielding stage as well as the post-yielding stage as shown in Figures 6.5 to 6.15

6.5 CONCLUSIONS

Theoretical investigations were carried out to verify the applicability of Branson's equation to predict the effective moment of inertia of rectangular fully and partially-CFFT beams. Based on the results of these investigations, the following findings can be drawn:

- 1) The steel-reinforced CFFT beams exhibit superior additional flexural strength after yielding of the embedded steel reinforcement. However, the flexural stiffness decreases due to the low elastic modulus of the FRP tube. New model for calculating the effective moment of inertia I_e was developed to address the post-yielding behaviour of this type of hybrid composite beams.
- 2) At the pre-yielding stage, a new coefficient η was proposed as a reduction factor for the cracking moment. This coefficient, η , accounts for the tensile stresses developed in the concrete from restraint to shrinkage by the embedded reinforcement, the roughened FRP tube(s), and the tight position of concrete inside the composite section. Based on this study, η is 0.8 and 0.7 for the fully-CFFT beams and the partially-CFFT beams.
- 3) At the pre-yielding stage, a new coefficient α was proposed as a reduction factor for the moment of inertia of the cracked transformed section I_{cr} in the partially-CFFT beams. This coefficient, α , accounts for the imperfect composite action due to the inner void. Based on this study, α is the ratio between the gross moment of inertia for a corresponding fully section to the gross moment of inertia for the voided section.

- 4) A new power m for Branson's equation was developed. This power addresses the reinforcement ratios of the FRP tube and steel, in addition it addresses the concrete strength in terms of its elasticity modulus. This power can be used in the pre-yielding stage and the post-yielding stage.
- 5) New assumptions for Branson's equation were suggested to address the post yielding stage. A new lower limit for I_e should be calculated as the moment of inertia of cracked transformed section neglecting the yielded steel I'_{cr} . While the upper limit should be taken as the last computed effective moment of inertia at the pre-yielding stage I'_e . Also, M_y should replace M_{cr} since it becomes the beginning moment at the post-yielding stage.
- 6) The predicted results give a reasonable estimation of the effective moment of inertia in the pre-yielding stage as well as the post-yielding stage.

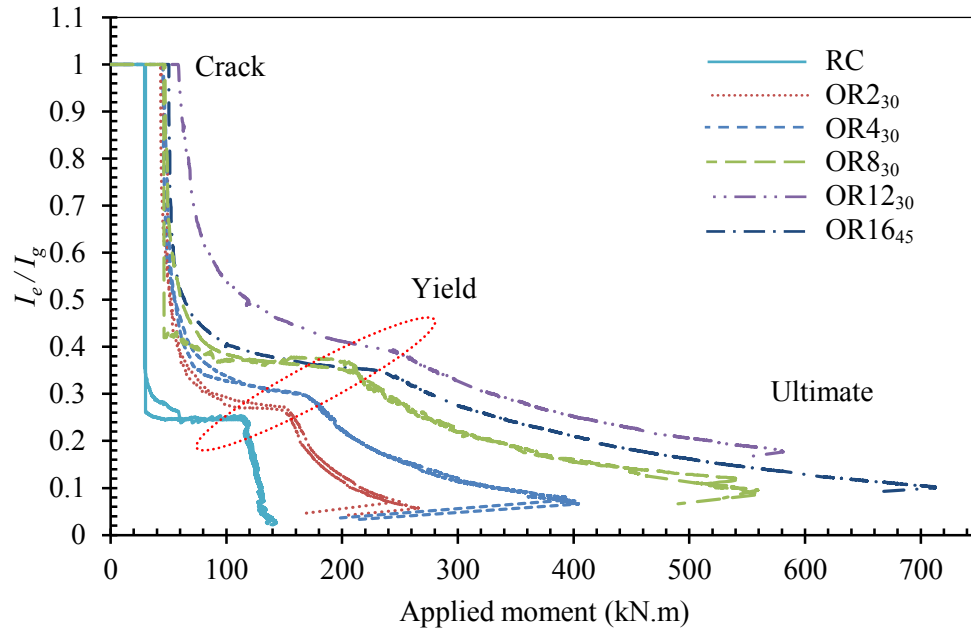


Figure 6.1 – Variation of the effective moment of inertia in fully-CFFT beams

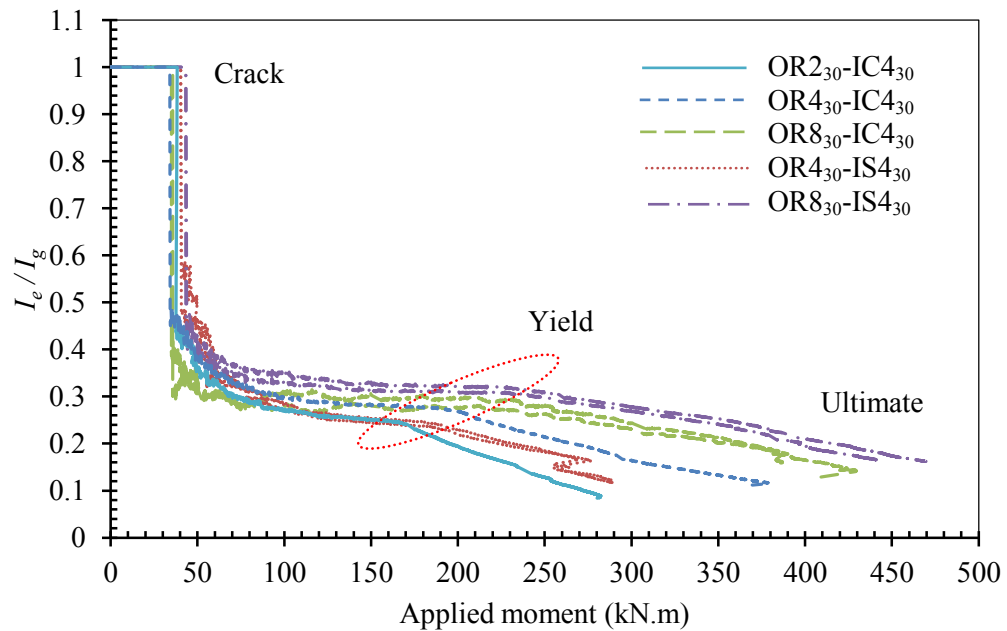
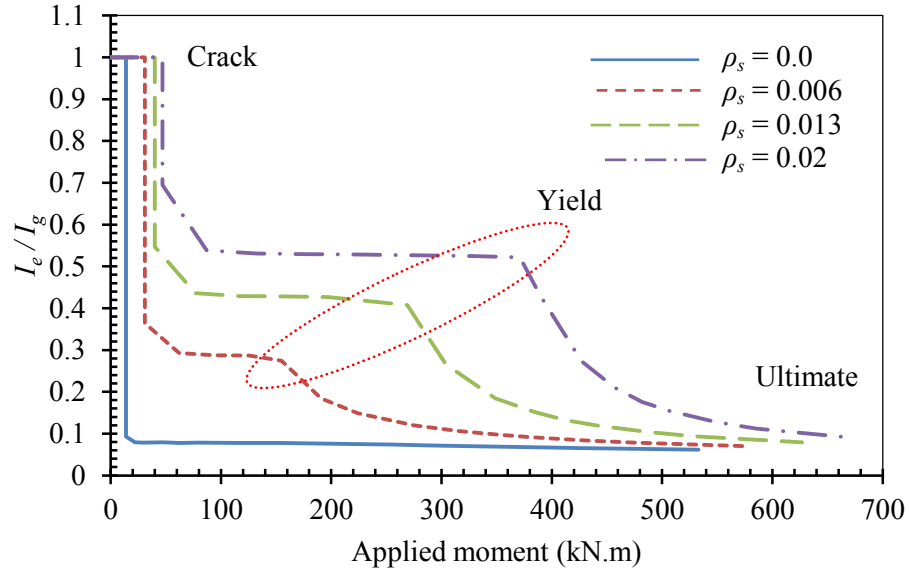
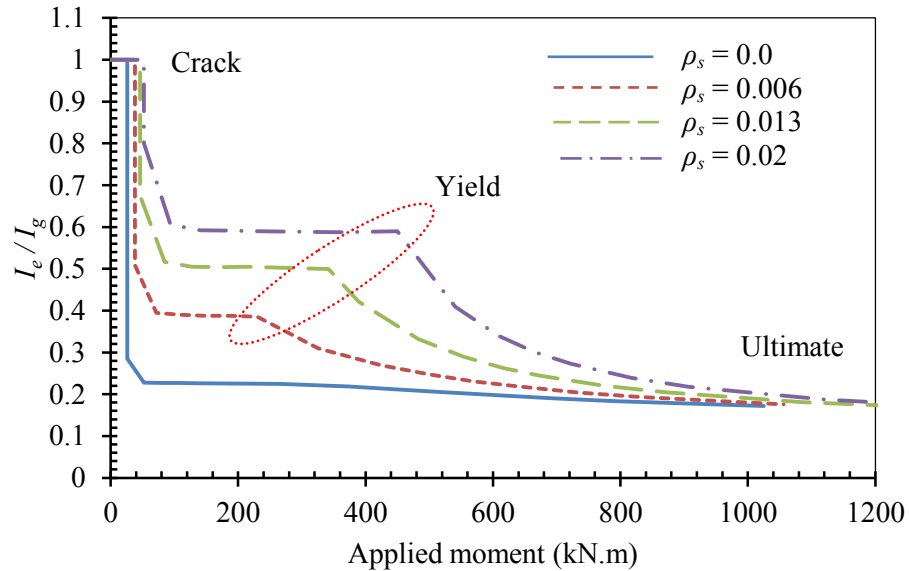


Figure 6.2 – Variation of the effective moment of inertia in partially-CFFT beams



(a) Variation of the effective moment of inertia in a fully-CFFT beam has $t_f = 4$ mm thickness, $E_f = 14$ GPa, and concrete strength 49 MPa



(b) Variation of the effective moment of inertia in a fully-CFFT beam has $t_f = 14$ mm thickness, $E_f = 14$ GPa, and concrete strength 49 MPa

Figure 6.3 – Variation of the effective moment of inertia due to different steel reinforcement ratios in fully-CFFT beams (from parametric study)

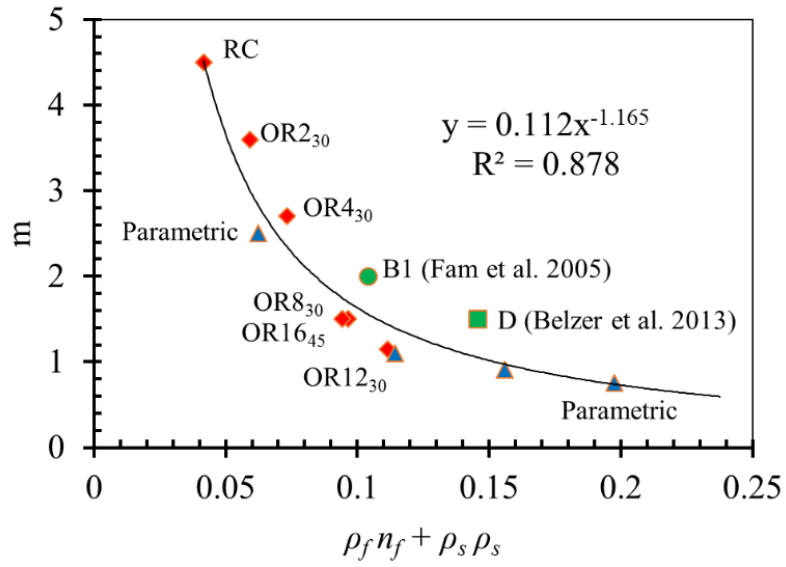


Figure 6.4 – Correlations between m and $\rho_f n_f + \rho_s \rho_s$

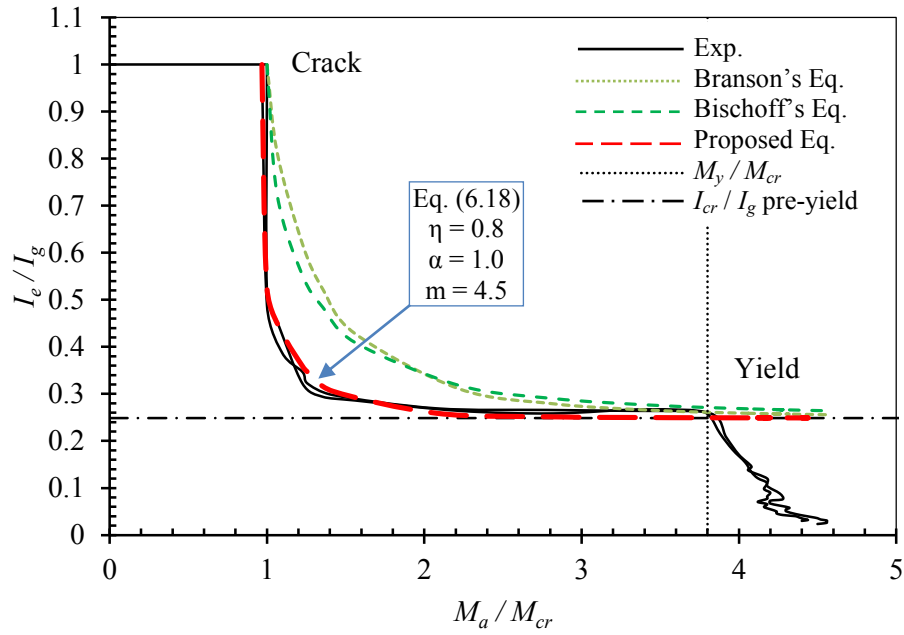


Figure 6.5 – Correlations between $\frac{I_e}{I_g}$ and $\frac{M_a}{M_{cr}}$ in the RC beams

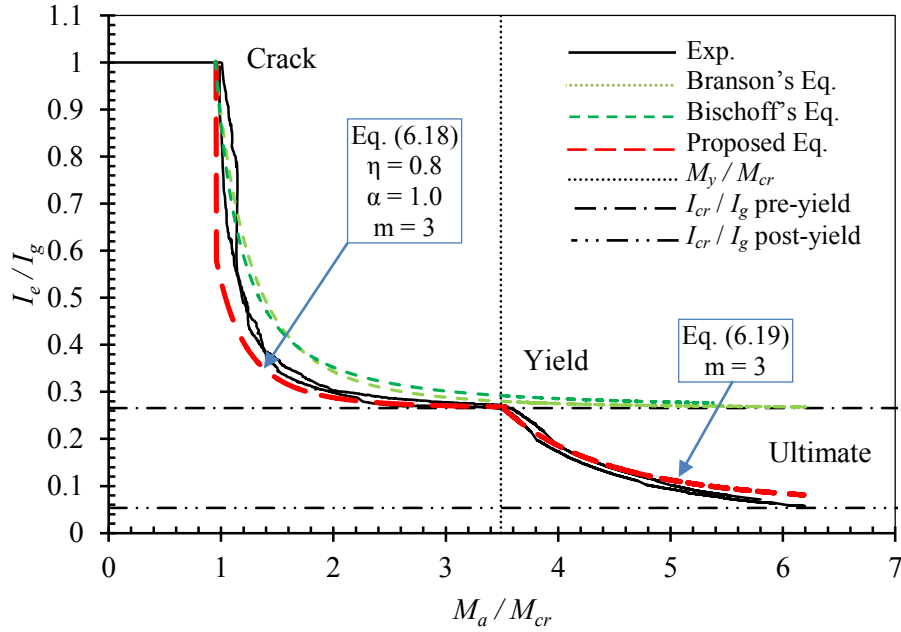


Figure 6.6 – Correlations between $\frac{I_e}{I_g}$ and $\frac{M_a}{M_{cr}}$ in the fully-CFFT beams OR230

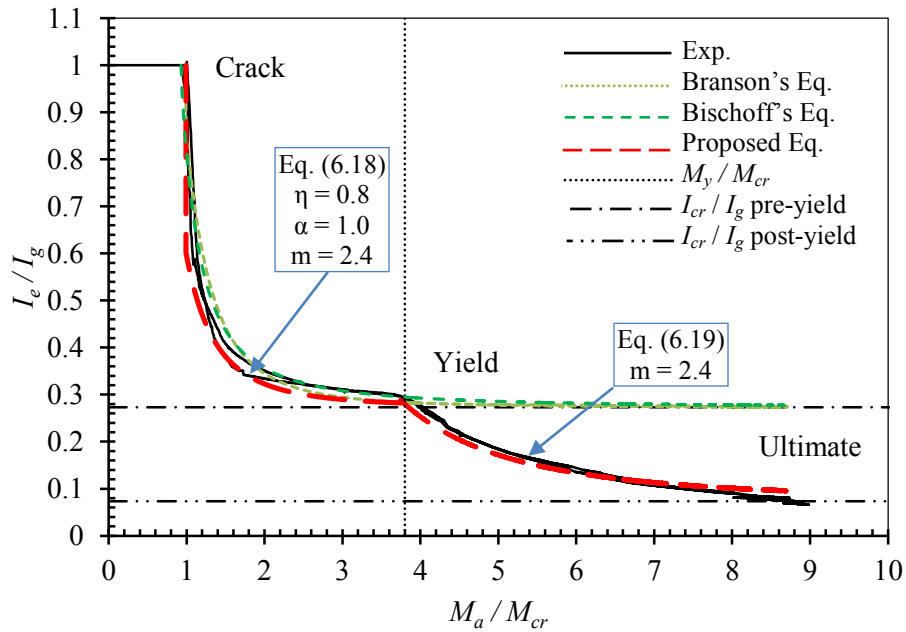


Figure 6.7 – Correlations between $\frac{I_e}{I_g}$ and $\frac{M_a}{M_{cr}}$ in the fully-CFFT beams OR430

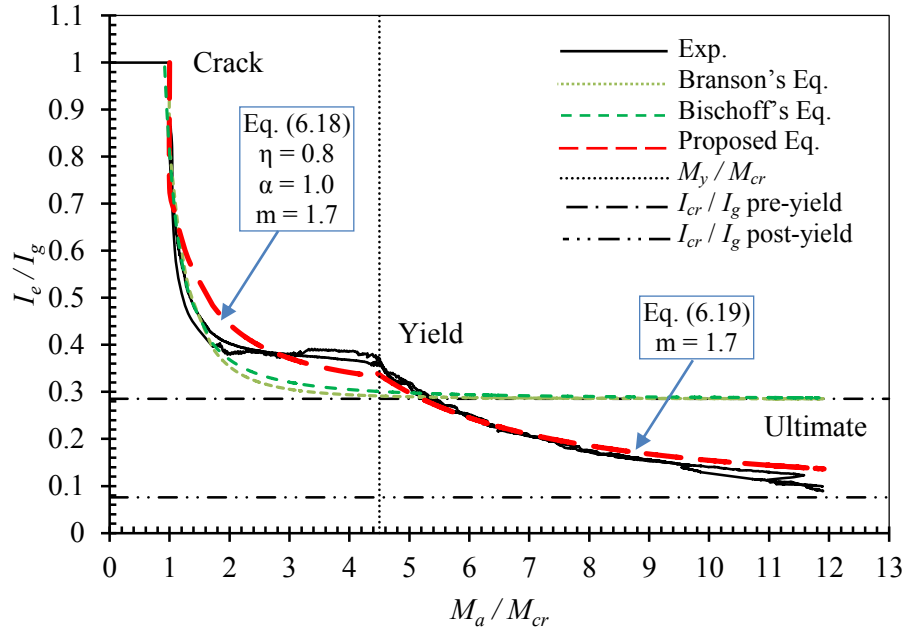


Figure 6.8 – Correlations between $\frac{I_e}{I_g}$ and $\frac{M_a}{M_{cr}}$ in the fully-CFFT beams OR8₃₀

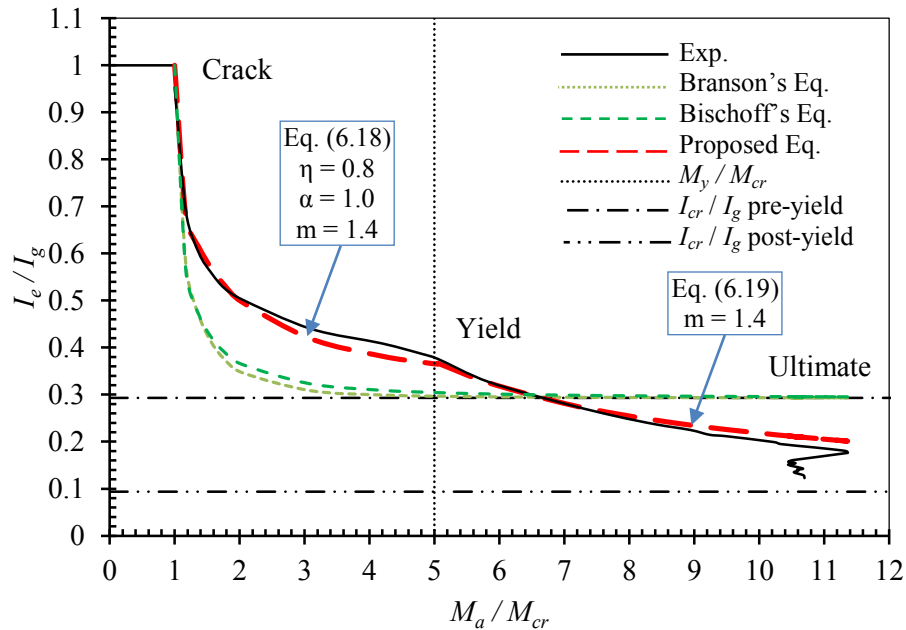


Figure 6.9 – Correlations between $\frac{I_e}{I_g}$ and $\frac{M_a}{M_{cr}}$ in the fully-CFFT beams OR12₃₀

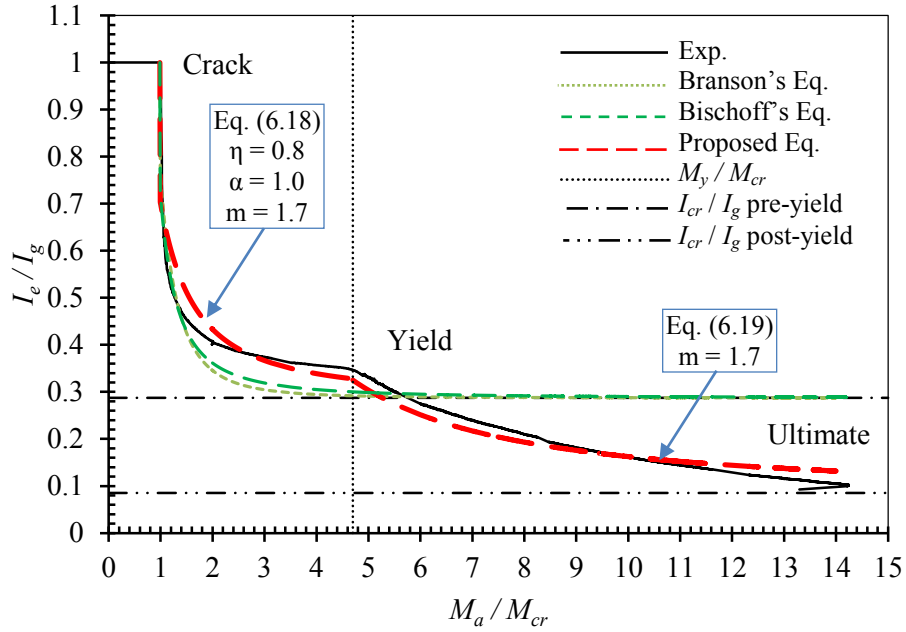


Figure 6.10 – Correlations between $\frac{I_e}{I_g}$ and $\frac{M_a}{M_{cr}}$ in the fully-CFFT beams OR16₄₅

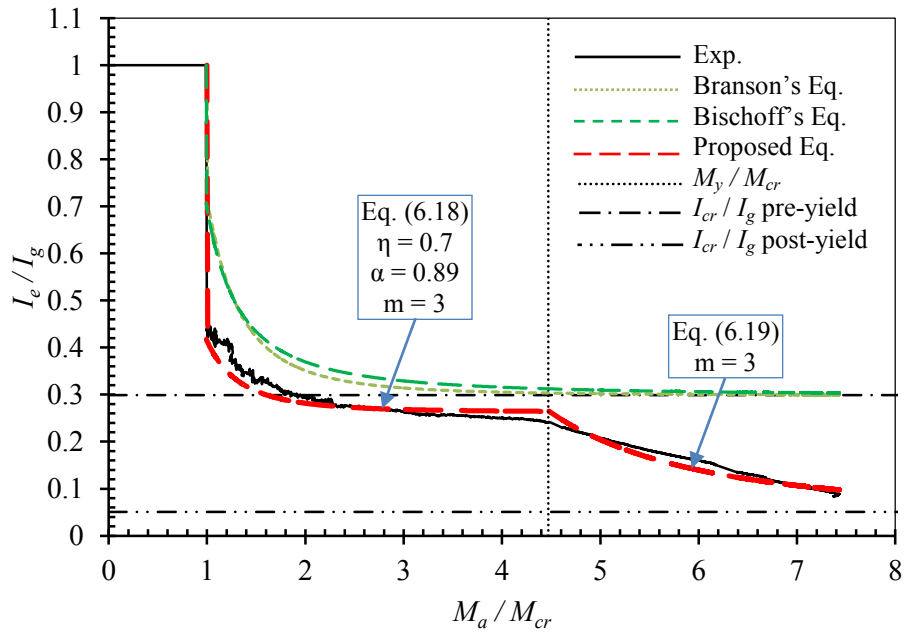


Figure 6.11 – Correlations between $\frac{I_e}{I_g}$ and $\frac{M_a}{M_{cr}}$ in the partially-CFFT beam OR230-IC430

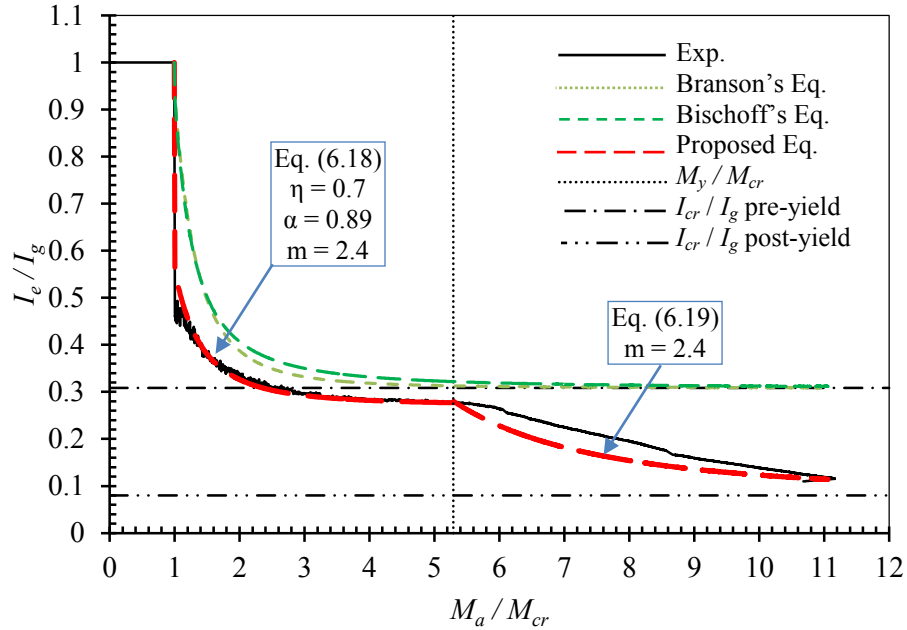


Figure 6.12 – Correlations between $\frac{I_e}{I_g}$ and $\frac{M_a}{M_{cr}}$ in the partially-CFFT beam OR4₃₀-IC4₃₀

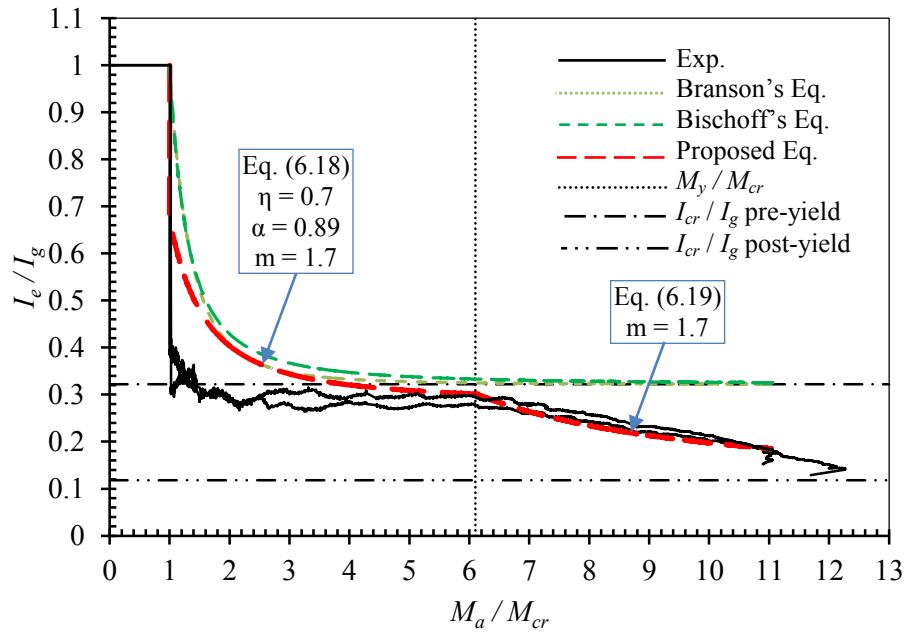


Figure 6.13 – Correlations between $\frac{I_e}{I_g}$ and $\frac{M_a}{M_{cr}}$ in the partially-CFFT beams OR8₃₀-IC4₃₀

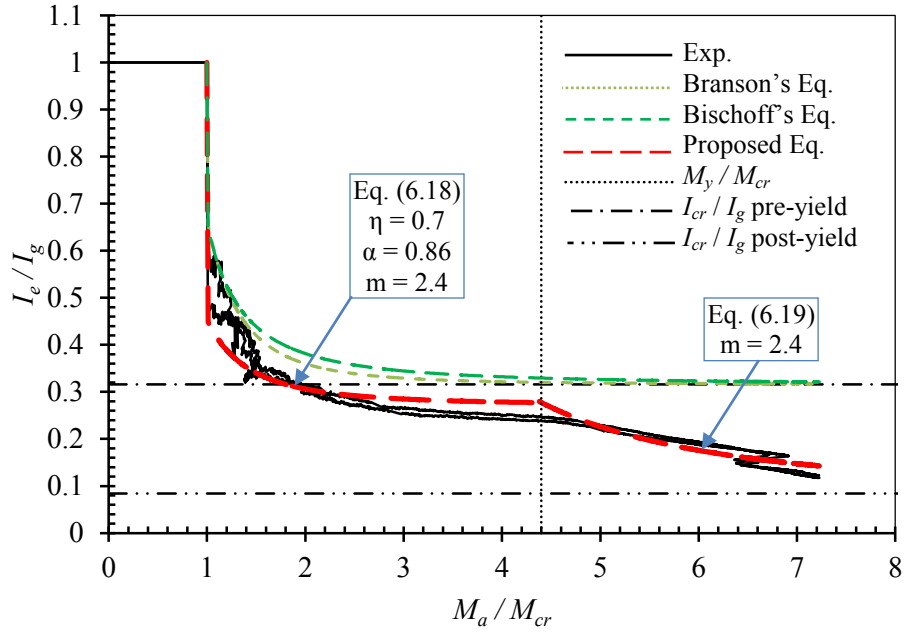


Figure 6.14 – Correlations between $\frac{I_e}{I_g}$ and $\frac{M_a}{M_{cr}}$ in the partially-CFFT beams OR4₃₀-IS4₃₀

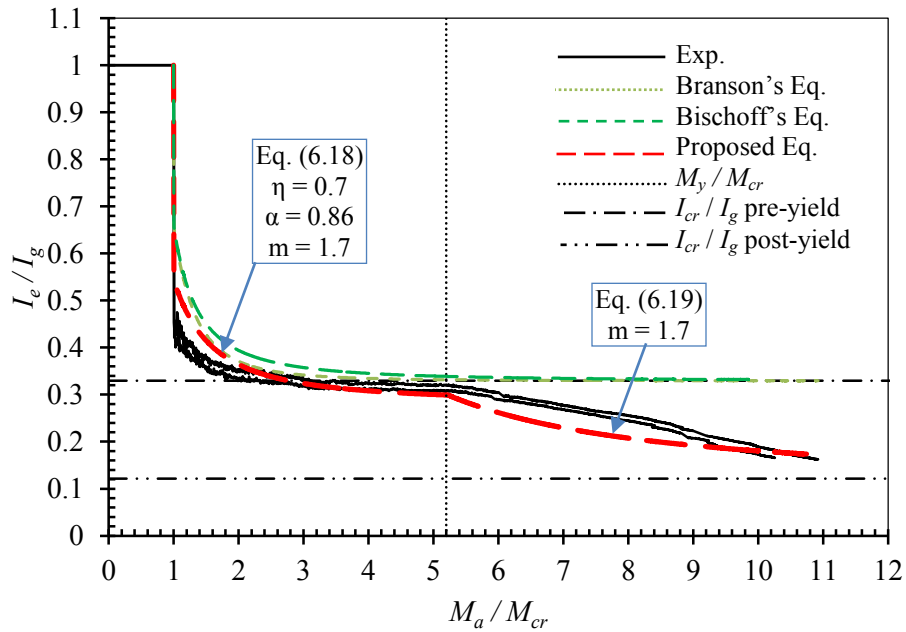


Figure 6.15 – Correlations between $\frac{I_e}{I_g}$ and $\frac{M_a}{M_{cr}}$ in the partially-CFFT beams OR8₃₀-IS4₃₀

CHAPTER 7

CONCLUSIONS AND RECOMMENDATIONS

7.1 CONCLUSIONS

This dissertation presents experimental and theoretical investigations on the flexural behaviour of rectangular concrete-filled fiber-reinforced polymer (FRP) tube (CFFT) beams with steel rebar. The beams contain outer rectangular filament-wound glass-FRP (GFRP) tubes fully-or-partially filled with concrete and were reinforced with steel rebar at the tension side only. Inner hollow circular or square filament-wound GFRP tubes, shifted toward the tension zone, were provided inside the CFFT beam to eliminate the excess weight of the cracked concrete at the tension side. The tube surfaces adjacent to the concrete were roughened by sand coating to achieve a full composite action. Several test variables were chosen to investigate the effect of the outer and inner tubes thickness, fibers laminates, and shape on the flexural behaviour of such hybrid CFFT beams. To fulfil the objectives of the study, twenty-four full-scale beam specimens, 3200 mm long and 305×406 mm² cross section, were tested under a four-point bending. These specimens include eight fully-CFFT beams with wide range of tube thickness of 3.4 mm to 14.2 mm, fourteen partially-CFFT beams with different outer and inner tubes configurations, and two conventional steel-reinforced concrete (RC) beams as control specimens. Analytical study has been developed to predict theoretically the moment-curvature response of rectangular CFFT beams. Then, the curvatures along the span of the beams are integrated to predict the deflection. The analytical model accounts for the confinement and tension stiffening of concrete. Comparison between the experimental results and the theoretical results have been carried out in terms of moment-curvature response, moment-deflection response, strain profile along the beam depth, and the neutral axis position. Moreover, parametric study was carried out to investigate the effect of additional test variables as steel reinforcement ratio and concrete strength. Based on experimental and theoretical results, the applicability of Branson's equation to predict the

effective moment of inertia and deflection for that type of hybrid CFFT system has been verified. Based on these studies, the following concluding remarks can be drawn:

In case of fully-CFFT beams:

- 1) The rectangular CFFT beams experience significantly higher ductility, higher stiffness, and superior strength than the RC beams. For example, the flexural strength and ductility of a rectangular fully-CFFT beam with a GFRP tube thickness of 14.2 mm are 444% and 1432% higher than that of a conventional RC beam.
- 2) The failure pattern of the fully-CFFT beams changes from tension to compression failure with increasing the FRP tube thickness.
- 3) Rectangular CFFT beams with steel rebar fail gradually in a sequential manner (yielding of steel, buckling of compressed tube flange, and finally rupture of the fibers). Even after the peak load, the CFFT beams can keep a residual strength because of the existence of the steel that withstands high strains and elongation.
- 4) The flexural strength of fully-CFFT beams increases with increasing the FRP tube thickness until certain limit at $\rho_f = 10\%$. After this limit, buckling of the compression flange of the FRP tube governs the ultimate capacity of over-reinforced CFFT beams. Based on this study, equations are proposed to estimate approximately the flexural moments at different stages (first crack, yield, and ultimate).
- 5) The compression failure in CFFT beams is governed by the buckling of the compression flange of the tubes, which can be resisted by increasing the transverse fibers percentage in the filament-wound FRP tubes.

In case of partially-CFFT beams:

- 6) The flexural strength of a rectangular fully-CFFT beam with a GFRP tube thickness of 3.4 mm is 97% higher than that of a conventional RC beam and fails in tension. If an inner circular hollow GFRP tube with 3.1 mm thickness is provided at the tension zone, the flexural strength becomes 115% higher than that of a conventional RC beam. Moreover, the ultimate failure changes from sudden tension failure to gradual compression failure.

- 7) The flexural strength of the partially-CFFT beams increases with increasing the outer GFRP tube thickness until certain limit. After this limit, buckling of the compression flange of the FRP tube governs the ultimate capacity of partially-CFFT beams. Equations are proposed to estimate the flexural moments at different stages (first crack, yield, and ultimate) based on regression analysis.
- 8) The inner hollow GFRP tubes in the rectangular CFFT beams pronounced active confinement action on the concrete in the compression zone. The circular shape of the inner void indicated better performance than the square void shape. Further experimental investigations are required to optimize the inner GFRP tube contribution as flexural reinforcement and confining the concrete at the compression zone.
- 9) The strength-to-weight ratio of the partially-CFFT beams is significantly higher than that of the RC beams and higher than that of the corresponding fully-CFFT beams. Therefore, the partially CFFT beams could replace the heavy RC beams and fully-CFFT beams, consequently could reduce the construction cost and the dead weight of structures.

Analytical studies:

- 10) The reinforced CFFT rectangular beams experience high cracking strength and new coefficient k values were proposed to determine well the concrete modulus of rupture ($f_{cr} = k\sqrt{f'_c}$). $k = 0.69$ for fully-CFFT beams, $k = 0.66$ for partially-CFFT beams with circular voids, and $k = 0.77$ for partially-CFFT beams with square voids. These values are assumed in case of calculating the gross moment of inertia for the total section elements (concrete + steel + FRP tubes) transformed to concrete and eliminating the void area.
- 11) The analytical model proposed in this study is capable of predicting well the moment-curvature, moment strains, neutral axis depth, and moment-deflection responses of fully-CFFT rectangular beams. The confinement and tension stiffening issues of concrete are considered in the model.
- 12) Using partially confined model for concrete with plastic strain up to the ultimate compressive strain of the FRP tube indicated better agreement with the experimental

results than using the unconfined concrete model proposed by AASHTO guidelines (2012).

- 13) Concrete tension stiffening can be considered in thick tubes, and should be ignored in thin tubes. However, ignoring the tension stiffening of concrete underestimates the experimental results and achieves safe design.
- 14) Using steel reinforcement in the CFFT beams is very significant. It increases the overall flexural stiffness and strength and decreases the deflection of such type of FRP-concrete composite beams.

Deflection prediction:

- 15) The steel-reinforced CFFT beams exhibit superior additional flexural strength after yielding of the embedded steel reinforcement. However, the flexural stiffness decreased due to the low elastic modulus of the FRP tube. New model for calculating the effective moment of inertia I_e , inspired by Branson's equation, was developed to address the post-yielding behaviour of this type of hybrid composite beams.
 - a) At the pre-yielding stage, a new coefficient η was proposed as a reduction factor for the cracking moment. This coefficient, η , accounts for the tensile stresses developed in the concrete from restraint to shrinkage by the embedded reinforcement, the roughened FRP tube(s), and the tight position of concrete inside the composite section. Based on this study, η is 0.8 and 0.7 for the fully-CFFT beams and the partially-CFFT beams, respectively.
 - b) At the pre-yielding stage, a new coefficient α was proposed as a reduction factor for the moment of inertia of the cracked transformed section I_{cr} in the partially-CFFT beams. This coefficient, α , accounts for the imperfect composite action due to the inner void. Based on this study, α is the ratio between the gross moments of inertia for the voided section to a corresponding fully section.
 - c) A new power m for Branson's equation was developed. This power addresses the reinforcement ratios of the FRP tube and steel, in addition it addresses the concrete strength through its elasticity modulus. This power can be used in the pre-yielding stage and the post-yielding stage.

- d) New assumptions for Branson's equation were suggested to address the post yielding stage. A new lower limit for I_e should be calculated for the moment of inertia of cracked transformed section neglecting the yielded steel I'_{cr} . While the upper limit should be taken as the last computed effective moment of inertia at the pre-yielding stage I'_e . Also, M_y should replace M_{cr} since it becomes the beginning moment at the post-yielding stage.
- e) The predicted results give a reasonable estimation of the effective moment of inertia in the pre-yielding stage as well as the post-yielding stage.

7.2 RECOMMENDATIONS FOR FUTURE WORK

Based on the findings and conclusions of the current study, it is important to continue the research studies in this promising field, knowing that there is still a lot of work to do. Some of the recommendations for future points of research are:

- 1) Additional experimental work is required to optimize the void ratio and position inside the section of the CFFT beams.
- 2) It is recommended to investigate experimentally methods to eliminate the buckling of the tube at the compression side. For example, increasing the transverse fibers percentage, increasing the compression flange thickness, or using resin webs.
- 3) It is recommended to study the effect of reinforcement type (steel bars, GFRP bars, CFRP bars, and CFRP strips).
- 4) The CFFT beams experienced high shear strength. It is recommended to investigate in details the shear and torsion strength of the CFFT beams.
- 5) Experimental and theoretical investigations are required to investigate the performance of the CFFT beam system under different types of loads such as eccentric compression and seismic loads.
- 6) Experimental and theoretical investigations are required to study how to connect the CFFT beam to other structural members as slabs and columns.

These proposed studies will allow better assessment of the demand on such innovative type of hybrid CFFT beams as well as establishing design guidelines for CFFT beams. These

steps will open widely the utilization of the CFFT beams in the construction fields such as bridge girders, marine structures, and in the industry field as ready structural member plants.

7.3 CONCLUSIONS EN FRANÇAIS

Cette thèse présente des investigations théoriques et expérimentales sur le comportement en flexion des poutres rectangulaire des tubes de polymères renforcés de fibres remplis de béton (TPRFB)² avec des barres d'armature en acier. Ces poutres rectangulaires tubulaires hybrides en PRF-béton-acier contiennent des tubes rectangulaires externes de filament en verre bobinés PRF (PRFV). Les tubes extérieurs ont été entièrement ou partiellement remplis de béton et ont été renforcés avec des barres d'armature en acier au côté en tension seulement. Des tubes intérieurs creux (circulaires ou carrés) de PRFV avec des filaments enroulés, déplacés vers la zone en tension, ont été installés à l'intérieur de la poutre en TPRFB pour éliminer l'excès de poids du béton fissuré au côté en tension. Pour s'acquitter de l'intégralité de l'action composite de cette section hybride, les surfaces des tubes adjacents au béton ont été rendues rugueuses par enrobage de sable. Plusieurs variables ont été choisies pour étudier l'effet de l'épaisseur des tubes extérieurs et intérieurs, les laminés de fibres, et la forme sur le comportement en flexion de ces poutres hybrides de TPRFB. Pour atteindre les objectifs de l'étude, vingt-quatre échantillons de poutre pleine grandeur, ayant une longueur de 3200 mm et une section transversale de 305×406 mm², ont été testés sous une flexion à quatre points. Ces échantillons comprennent sept poutres de TPRFB entièrement remplis avec une large gamme d'épaisseur de tube de 3.4 mm à 14.2 mm, quatorze poutres de TPRFB partiellement remplis avec de différentes configurations de tubes extérieurs et intérieurs, et deux poutres en béton conventionnellement armé en acier comme échantillons de référence. Une étude analytique a été développée pour prédire théoriquement la réponse moment-courbure de la section rectangulaire des poutres en TPRFB. Alors, les courbures le long de la portée des poutres sont intégrées pour prévoir la flèche. Le modèle analytique représente la non-linéarité matérielle et la raideur de tension de béton. En outre, le modèle s'occupe du confinement du béton. La comparaison entre les résultats expérimentaux et les résultats théoriques a été effectuée en termes de la réponse moment-courbure, la réponse

² TPRFB est l'acronyme du terme en anglais CFFT : Concrete-Filled FRP-Tubes.

moment-flèche, profils de déformations le long de profondeur des poutres, et la position de l'axe neutre. En outre, l'étude paramétrique a été effectuée pour examiner l'effet de nouvelles variables comme le ratio de l'armature d'acier et la résistance de béton. En se basant sur ces résultats, une étude analytique a été menée afin d'examiner la validité de l'équation de Branson pour prédire le moment d'inertie et la flèche de ce système hybrides en TPRFB. Sur la base de ces études, les conclusions suivantes peuvent être énoncées:

Poutres de TPRFB entièrement remplies:

- 1) Les poutres de TPRFB rectangulaires présentent une ductilité significativement plus élevée, une rigidité plus élevée et une résistance plus élevée que les poutres en béton armé. Par exemple, la résistance à la flexion et la ductilité de la poutre rectangulaire entièrement en TPRFB avec une épaisseur de tube PRFV de 14.2 mm sont 444% et 1432% plus élevées que celles d'une poutre en béton armé conventionnel.
- 2) Le modèle de rupture des poutres rectangulaires entièrement en TPRFB se transforme de la rupture à la tension à la rupture à la compression avec l'augmentation de l'épaisseur de tube PRFV.
- 3) Les poutres rectangulaires en TPRFB avec des barres d'armature en acier s'effondrent progressivement dans une façon séquentielle (déformation plastique de l'acier, flambage de l'aile de tube en compression et finalement la rupture des fibres). Même après la rupture ultime, les poutres en TPRFB peuvent garder une résistance résiduelle à cause de l'existence de l'acier qui résiste les déformations élevées et l'allongement.
- 4) La résistance en flexion des poutres rectangulaires entièrement en TPRFB augmente avec l'augmentation de l'épaisseur de tube PRFV jusqu'à la certaine limite $\rho_f = 10\%$. Après cette limite, le flambage de l'aile en compression de tube PRFV contrôle la capacité ultime de poutres TPRFB sur-renforcées. Basé sur cette étude, on propose des équations pour évaluer les moments aux différentes phases (d'abord la fissuration, les déformations plastiques et l'ultime).
- 5) La rupture en compression dans des poutres rectangulaires de TPRFB est contrôlée par le flambage de l'aile du tube en compression, qui peut être résisté en augmentant le pourcentage de fibres transversales dans les filaments bobinés des tubes PRF.

Poutres de TPRFB partiellement remplis:

- 6) La résistance en flexion des poutres rectangulaires entièrement en TPRFB avec une épaisseur de tube PRFV de 3.4 mm est 97% plus élevée que celle d'une poutre conventionnelle en béton armé et elles se sont agressivement effondrées en tension. Si on fournit un tube circulaire et évidé en PRFV à l'intérieur de la zone en tension, la résistance devient 115% plus élevée que celle d'une poutre conventionnelle en béton armé. De plus, le comportement de la rupture ultime a été changé d'une soudaine rupture en tension (à cause de la rupture axiale de fibres au côté de tension) pour une rupture graduelle en compression (flambage de l'aile du tube en compression).
- 7) La résistance en flexion des poutres rectangulaires partiellement en TPRFB augmente avec l'augmentation de l'épaisseur de tube PRFV extérieure jusqu'à une certaine limite. Après cette limite, le flambage de l'aile en compression du tube en PRF contrôle la capacité ultime des poutres partiellement en TPRFB. On propose des équations pour évaluer les moments aux différentes phases (d'abord la fissuration, les déformations plastiques et l'ultime) basé sur l'analyse de régression.
- 8) La cavité intérieure des tubes PRFV dans les poutres rectangulaires en TPRFB a engendré une action de confinement active sur le béton dans la zone de compression. La forme circulaire des vides internes a indiqué une meilleure performance que le vide carré.
- 9) Les ratios résistance-poids des poutres rectangulaires partiellement en TPRFB sont significativement plus hauts que ceux des poutres en béton armé et plus haut que ceux de poutres correspondantes entièrement en TPRFB. Donc, des poutres partiellement en TPRFB pourraient remplacer les lourdes poutres en béton armé et les poutres entièrement en TPRFB, et par conséquent, elles pourraient réduire le coût de transport et d'installation ainsi que la charge permanente des structures.

Étude analytique:

- 10) Les poutres en TPRFB partielles et entières éprouvent une résistance à la fissuration élevée et le module de rupture du béton (f_{cr}) peut être augmenté. Basé sur les résultats de l'étude actuelle, on propose de nouvelles valeurs pour k pour bien déterminer le

module de rupture du béton (f_{cr}) d'ACI 318. $k = 0.69$ pour de poutres entièrement en TPRFB, $k = 0.66$ pour de poutres partiellement en TPRFB avec des vides circulaires, $k = 0.77$ pour de poutres partiellement en TPRFB avec des vides carrés. Ces valeurs sont présumées en cas du calcul du moment d'inertie brut pour la section totale des éléments (le béton + acier + des tubes PRFV) transformés en béton et l'élimination de la zone des vides.

- 11) Le modèle analytique proposé dans cette étude est capable de prévoir bien la réponse moment-courbure, la réponse moment-déformations, la position de l'axe neutre et la réponse moment-flèche des poutres rectangulaires entièrement en TPRFB.
- 12) L'utilisation du modèle partiellement confiné pour le béton ayant des déformations plastiques jusqu'à la déformation ultime en compression des tubes PRF conforme mieux aux résultats expérimentaux que l'utilisation du modèle du béton non-confiné proposé par AASHTO (2012).
- 13) La contribution du raidissement en tension du béton peut considérer cette contribution dans des tubes épais et on peut l'ignorer dans des tubes minces. Cependant, ignorant le raidissement en tension du béton sous-estime les résultats expérimentaux et réalise une conception sécuritaire.
- 14) L'utilisation du renforcement d'acier dans Les poutres en TPRFB est très significative. Il augmente la rigidité et la force et diminue la flèche.

La flèche:

- 15) les poutres en TPRFB avec des barres d'armature en acier manifestent une résistance additionnelle en flexion après que l'armature dépasse la limite élastique. Cependant, la résistance en flexion a été diminuée en raison du module élastique bas du tube PRF. Le nouveau modèle pour calculer le moment d'inertie effectif I_e , inspiré par l'équation de Branson, a été développé pour adresser le comportement après la limite élastique de ce type des poutres composées hybrides.
 - a) Avant la limite élastique, un nouveau coefficient (η) a été proposé comme un facteur de réduction pour le moment de fissuration. Ce coefficient (η) représente la tension développée dans le béton de la contrainte au rétrécissement par le renforcement incorporé, le tube(s) PRF devenu rude et la position serrée de béton à

l'intérieur de la section composée. Basé sur cette étude, η est 0.8 et 0.7 pour les poutres entièrement et partiellement en TPRFB, respectivement.

- b) Avant la limite élastique, on a proposé un nouveau coefficient (α) comme un facteur de réduction pour le moment d'inertie de la section (I_{cr}) dans de poutres partiellement en TPRFB. Ce coefficient (α) représente l'imperfection de l'action composite à cause des vides internes. Basé sur cette étude, α est le ratio entre le moment d'inertie brut (I_g) pour une section entière équivalente au moment d'inertie brut pour la section évidée.
- c) Un nouvel exposant m pour l'équation de Branson a été développé. Cet exposant s'occupe des ratios d'armature du tube PRF et de l'acier, de plus il s'occupe de la de la résistance du béton en utilisant le module d'élasticité. Cet exposant (m) peut être également utilisé dans les phases de déformation élastique et plastique.
- d) De nouvelles suppositions pour l'équation de Branson ont été suggérées pour s'occuper de la phase après la limite élastique. Une nouvelle limite inférieure, I_e devrait être calculée pour le moment d'inertie de section transformée fissurée en négligeant l'acier dépassé la limite élastique (I'_{cr}). Tandis que la limite supérieure devrait être prise comme le dernier moment d'inertie effectif calculé à la phase avant la limite élastique (I'_e). En outre, M_y devrait remplacer M_{cr} puisque cela devient le moment commençant à la phase après la limite élastique.
- e) Les résultats prévus donnent une évaluation raisonnable du moment d'inertie effectif dans l'étape avant la limite élastique autant qu'après la limite élastique.

7.4 RECOMMANDATIONS POUR DES TRAVAUX FUTURS

Basé sur les découvertes et les conclusions de l'étude actuelle, il est important de continuer les études de recherche dans ce domaine prometteur, connaissant il y a toujours beaucoup de travail à faire. Certaines des recommandations pour de recherche sont :

- 1) On recommande aux travaux expérimentaux supplémentaires d'optimiser le ratio des vides et la position à l'intérieur de la section des poutres TPRFB.
- 2) On recommande d'examiner expérimentalement des méthodes pour éliminer le flambage des tubes en compression. Par exemple, en augmentant le pourcentage de

fibres transversales, en augmentant l'épaisseur de l'aile en compression, ou en utilisant des réseaux résineux

- 3) Il est recommandé d'étudier l'effet du type d'armature (des barres d'acier, des bars de PRFV, des bars de CPRF et des bandes de CPRF).
- 4) Le système de poutre TPRFB a éprouvé une résistance au cisaillement élevée. On recommande d'examiner en détail la résistance au cisaillement, la résistance à la torsion et le comportement de système de poutre TPRFB.
- 5) Des investigations expérimentales et théoriques sont exigées pour examiner la performance du système de poutre TPRFB sous les différents types de charges comme la compression excentrique et les charges sismiques.
- 6) Des investigations expérimentales et théoriques sont exigées pour étudier comment connecter la poutre TPRFB à d'autres membres structurels comme les dalles et les poteaux.

Ces études proposées permettront une meilleure évaluation de la demande sur un tel type novateur de poutres TPRFB hybrides aussi bien que l'établissement des directives de conception exigées pour des poutres TPRFB. Ces pas ouvriront largement l'utilisation des poutres TPRFB dans les champs de construction comme les poutrelles de pont, les travaux maritimes et dans le domaine d'industrie comme des usines de membres structurels prêts.

REFERENCES

- Abouzied, A., Ammar, M., and Masmoudi, R. (2011). “Nanoparticles effect on the physical and mechanical properties of FRP filament-winded composites”, *Proceedings of 26th ASC Annual Technical Conference (the Second Joint US-Canada Conference on Composites)*, Montreal, Canada, September 2011, pp 1131-1140.
- Abouzied, A., Ammar, M., and Masmoudi, R. (2012b). “Nanoparticles effect on FRP filament-winded composites performance”, *Proceedings of CICE 6th International Conference on FRP Composites in Civil Engineering (CICE)*, Rome, Italy, June 2012.
- Abouzied, A., and Masmoudi, R. (2012). “Square columns confined by GFRP tube or steel ties”. *Proceedings of 11th International Symposium on fiber reinforced Polymer for reinforced Concrete structures FRPRCS-11*, Portugal, December 2012.
- Abouzied, A., and Masmoudi, R. (2013). “Performance of square concrete-filled FRP tubes versus steel reinforced concrete columns”. *Proceedings of 2nd conference on Smart Monitoring, Assessment and Rehabilitation of Civil Structures SMAR2013*, Istanbul, Turkey, September 2013.
- Abouzied, A., and Masmoudi, R. (2014). “Flexural behaviour of new partially concrete-filled filament-wound rectangular FRP tube beams”. *Proceedings of 4th International Structural Specialty Conference CSCE2014*, Halifax, NS, May 2014, CST-171:1-10.
- Abouzied, A., and Masmoudi, R. (2015). “New high-performance rectangular FRP-tube beams partially filled with concrete”. *ACI-Special Publication*, SP-15.
- Abouzied, A., and Masmoudi, R. (2015). “New design of rectangular partially concrete-filled filament-wound FRP tube beam”. *Proceedings of 3rd conference on Smart Monitoring, Assessment and Rehabilitation of Civil Structures SMAR 2015*, Antalya, Turkey, September 2015.

- Abouzied, A., and Masmoudi, R. (2015). “Structural performance of new fully and partially concrete-filled rectangular FRP-tube beams”. *Elsevier–Construction and Building Materials Journal*, 101: 652–660.
- Abouzied, A., Masmoudi, R., Gagne, R., and Tagnit-Hamou, A. (2012a). “Effect of nanoparticles added to vinyl ester resin on the compressive behaviour of square concrete-filled GFRP tubes”, *Proceedings of 6th International Conference on Advanced Composite Materials in Bridges and Structures ACMPS-VI*, Kingston, Canada, May 2012, pp 496-503.
- Al-Sunna, R., Pilakoutas, K., Hajirasouliha, I., and Guadagnini, M. (2012). “Deflection behaviour of FRP reinforced concrete beams and slabs: An experimental investigation”. *Elsevier Journal of Composites: Part B*, 43: 2125-2134.
- American Association of State Highway and Transportation Officials (AASHTO). (2012). “Guide specifications for design of concrete-filled FRP tubes for flexural and axial members”. 1st edition, Washington, DC.
- American Composites Manufacturers Association. (2004). “Composites basics: composites manufacturing”. <http://www.mdacomposites.org> (online).
- American Concrete Institute Committee. (2015). “Guide for the design and construction of concrete reinforced with FRP bars”. ACI 440.1R-15, Farmington Hills, MI, USA.
- American Concrete Institute. (2014). “Building code requirements for structural concrete”. ACI 318-14, Detroit, USA.
- American Society for Testing of Materials. (2008). “Standard test method for transition temperatures and enthalpies of fusion and crystallization of polymers by differential scanning calorimeter”. ASTM D 3418-08, West Conshohocken, PA, USA.
- American Society for Testing of Materials. (2009). “Standard specification for deformed and plain carbon steel bars for concrete reinforcement”. ASTM A615/A615M-09, West Conshohocken, PA, USA.

- American Society for Testing of Materials. (2009). “Standard test methods for constituent content of composite materials”. ASTM D 3171-09, West Conshohocken, PA, USA.
- American Society for Testing of Materials. (2010). “Standard test method for compressive properties of rigid plastics”. ASTM D695-10, West Conshohocken, PA, USA.
- American Society for Testing of Materials. (2010). “Standard test method for tensile properties of plastics”. ASTM D 638-10, West Conshohocken, PA, USA.
- American Society for Testing of Materials. (2012). “Standard test method for compressive strength of cylindrical concrete specimens”. ASTM C39-12, West Conshohocken, PA, USA.
- American Society for Testing of Materials. (2014). “Standard test method for tensile properties of polymer matrix composite materials”. ASTM D3039/D3039M, West Conshohocken, PA, USA.
- American Society for Testing of Materials. (2014). “Standard test method for apparent hoop tensile strength of plastic or reinforced plastic pipe by split disk method”. ASTM D2290-14, West Conshohocken, PA, USA.
- Balya, B. (2004). “Design and analysis of filament wound composite tubes”. M.Sc. thesis, Middle East technical University, Ankara, Turkey, p.14-20.
- Beckwith, S. (2006). “Composites innovations and advanced technology synonymous with pacific rim in 06”. Arlington, Composite Manufacturing.
- Belzer, B., Robinson, M., and Fick, D. (2013). “Composite action of concrete-filled rectangular GFRP tubes”. *ASCE Composites for Construction Journal*, 17(5): 722-731.
- Benmokrane, B., Chaallal, O., and Masmoudi, R. (1996). “Flexural response of concrete beams reinforced with FRP reinforcing bars”. *ACI Structural Journal*, 93(1): 46-55.

- Bischoff, P. H. (2005). "Re-evaluation of deflection prediction for concrete beams reinforced with steel and fiber reinforced polymer bars". *Structural Engineering Journal*, 131(5): 752-767.
- Bischoff, P. H. (2007). "Deflection calculation of FRP reinforced concrete beams based on modification to the existing Branson equation". *ASCE Composites for Construction Journal*, 11(1): 4-14.
- Bischoff, P. H., and Gross, P. (2011). "Equivalent moment of inertia based on integration of curvature". *ASCE Composites for Construction Journal*, 15(3): 263-273.
- Branson, D. E. (1965). "Instantaneous and time-dependent deflections of simple and continuous reinforced concrete beams". *HPR Report No.7: Part 1*, Alabama Highway Department, Bureau of Public Roads, Montgomery, AL, USA, p. 78.
- Canadian Standard Association. (2014). "Design of concrete structures". *CSA Standard CAN/CSA-A23.3-14*, Rexdale, ON, Canada.
- Canadian Standard Association. (2014). "Canadian Highway Bridge design code". *CSA Standard CAN/CSA-S6-14*, Toronto, ON, Canada.
- Canadian Standard Association. (2012). "Design and construction of building components with fiber reinforced polymers". *CSA Standard CAN/CSA-S806*, Toronto, ON, Canada.
- Canning, L., Hollaway, L., and Thorne, A. (1999). "Manufacture, testing and numerical analysis of an innovative polymer compo-site/concrete structural unit". *Proceedings of the Institution of Civil Engineers-Structures and Buildings*, 134(3): 231-241.
- Chakrapan, T. (2005). "Use of fiber-reinforced polymer composite in bridge structures". M.Sc. thesis, Department of Civil and Environmental Engineering, Massachusetts Institute of Technology, Cambridge, MA, USA.

- Charkas, H., Rasheed, H., and Melhem, G. (2002). "Simplified load-deflection calculations of FRP strengthened RC beams based on a rigorous approach". *Proceedings of 15th Engineering Mechanics Conference (ASCE)*, New York, USA, June 2002.
- Cole, B. (2005). "Flexural and shear performance of reinforced concrete-filled fibre reinforced polymer tubes". MSc thesis, Queen's University, Kingston, ON, Canada.
- Cole, B., and Fam, A. (2006). "Flexural load testing of concrete-filled FRP tubes with longitudinal steel and FRP rebar". *ASCE Composites for Construction Journal*, 10: 161-171.
- Collins, M. P., and Mitchell, D. (1997). "Prestressed concrete structures", Response Publications, Canada.
- Davol, A., Burgueno, R., and Seible F. (2001). "Flexural behavior of circular concrete filled FRP shells". *ASCE Structural Engineering Journal*, 127(7): 810-817.
- Deskovic, N., and Trinatafillou, T. (1995). "Innovative design of FRP combined with concrete: short term behaviour". *ASCE Structural Engineering Journal*, 121(7): 1069-1078.
- Elmahdy, A., El-Hacha, R., and Shrive, N. (2008). "Flexural behaviour of hybrid composite girders in bridge construction". *Fourth International Conference on FRP Composites in Civil Engineering (CICE2008)*, Zurich, Switzerland, July 2008.
- Elmihilmy, M., and Tedesco, W. (2000). "Deflection of reinforced concrete beams strengthened with fiber-reinforced polymer (FRP) plates". *ACI Structural Journal*, 97(5): 679-688.
- Fam, A. (2000). "Concrete-filled fibre-reinforced polymer tubes for axial and flexural structural members". Ph.D thesis, Department of Civil and Geological Engineering, The University of Manitoba, Winnipeg, Manitoba, Canada, p. 183-191.

- Fam, A., and Rizkalla, S. (2001). "Behaviour of axially loaded concrete-filled circular fiber reinforced polymer tubes". *ACI Structural Journal*, 98: 280-290.
- Fam, A., and Rizkalla, S. (2002). "Flexural Behaviour of Concrete-Filled Fiber-Reinforced Polymer Circular Tubes". *ASCE Composites for Construction Journal*, 6(2): 123-132.
- Fam, A., and Rizkalla, S. (2003). "Large scale testing and analysis of hybrid concrete /composite tubes for circular beam-column applications". *Elsevier Journal of Construction and Building Materials*, 17: 507-516.
- Fam, A., and Son, J. K. (2008). "Finite element modeling of hollow and concrete-filled fiber composite tubes in flexure: Optimization of partial filling and a design method for poles". *Engineering Structures Journal*, 30: 2667-2676.
- Fam, A., Schnerch, D., Rizkalla, S. (2005). "Rectangular filament-wound glass fiber-reinforced polymer tubes filled with concrete under flexural and axial loading: experimental investigation". *ASCE Composites for Construction Journal*. 9(1): 25-33.
- Frank, C. S. (1995). "A filament-wound structure technology overview", *Materials Chemistry and Physics Journal*, 42: 96-100.
- Hazra, T. (2011). "A low cost 2-axis plc controlled filament winding machine with simplified fiber winding angle and tension control system". M.Sc. Thesis, Department of Civil Engineering, Dalhousie University, Halifax, NS, Canada, p. 6-12.
- Hong, W. K., and Kim, H. C. (2004). "Behavior of concrete columns confined by carbon composite tubes". *Canadian Journal of Civil Engineering*, 31(2): 178-188.
- Idris, Y., and Ozbakkaloglu, T. (2013). "Seismic behavior of high-strength concrete-filled FRP tube columns". *ASCE Composites for Construction Journal*, 17(6): 04013013.
- Idris, Y., and Ozbakkaloglu, T. (2014). "Flexural behaviour of FRP-HSC-steel composite beams". *Elsevier Journal of Thin-Walled Structures*, 80: 207-216.

- Iftekhar, A. (2004). "Shear response and bending fatigue behaviour of concrete-filled fiber-reinforced polymer tubes". Ph.D. thesis, Civil and Environmental Engineering Department, North Carolina State University, Raleigh, NC, USA, p. 6-8.
- ISIS Canada. (2008). "FRP rehabilitation of reinforced concrete structures". *Design Manual No.4*, Winnipeg, Manitoba, Canada.
- Kaynak, C., Erdiller, E. S., Parans, L., and Senel, F. (2005). "Use of split-disk tests for the process parameters of filament wound epoxy composite tubes". *Polymer Testing Journal*, 24: 648-655.
- Khennane, A. (2008). "A new design concept for a hybrid FRP-high strength concrete beam for infrastructure applications". *Fourth International Conference on FRP Composites in Civil Engineering (CICE2008)*, Zurich, Switzerland, July 2008.
- Khennane, A. (2010). "Manufacture and testing of a hybrid beam using a pultruded profile and high strength concrete". *Australian Journal of Structural Engineering*, 10(2): 145-156.
- Lam, L., and Teng J. G. (2003). "Design-oriented stress-strain model for FRP-confined concrete". *Elsevier Journal of Construction and Building Materials*, 17: 471-489.
- Lam, L., and Teng, J. G. (2004). "Ultimate condition of FRP-confined concrete". *ASCE Composites for Construction Journal*, 8(6): 539-548.
- Li, J., and Hadi, M. (2003). "Behaviour of externally confined high strength concrete columns under eccentric loading". *ASCE Composites for Construction Journal*, 62(2): 145-153.
- Mallick, P. K. (2007). "Fiber-reinforced composites: materials, manufacturing, and design". Third edition, Taylor & Francis Group, FL, USA, sec. 5.5.

- Mandal, S., Hoskin, A., and Fam, A. (2005). "Influence of concrete strength on confinement effectiveness of fiber-reinforced polymer circular jackets". *ACI Structural Journal*, 102(3): 383-392.
- Masmoudi, R., Abouzied, A., and Mohamed, H. (2015). "New hybrid concrete filled FRP stay-in-place forms as high-performance structural members". *13th Arab Structural Engineering Conference ASEC*, University of Blida, Algeria, December 2015.
- Masmoudi, R., Theriault, M., and Benmokrane, B. (1998). "Flexural behaviour of concrete beams reinforced with deformed fiber reinforced plastic reinforcing rods". *ACI Structural Journal*, 95(6): 665-676.
- Mirmiran, A., Samaan, M., Cabrera, S., and Shahawy, M. (1998). "Design, Manufacture and Testing of a New Hybrid Column", *Elsevier Journal of Construction and Building Materials*, 12(1): 39-49.
- Mirmiran, A., Shahawy, M., and Beitleman, T. (2001). "Slenderness limit for hybrid FRP concrete columns". *ASCE Composites for Construction Journal*, 5(1): 26-34.
- Mirmiran, A., Shahawy, M., El Khoury, C., and Naguib, W. (2000). "Large beam-column tests on FRP-filled composite tubes". *ACI Structural Journal*, 97(2): 268-276.
- Mohamed, H., Abdel-Baky, H., and Masmoudi, R. (2010). "Nonlinear stability analysis of concrete-filled fiber-reinforced polymer-tube columns: experimental and theoretical investigation". *ACI Structural Journal*, 107: 699-708.
- Mohamed, H., and Masmoudi, R. (2008a). "Compressive behaviour of filament wound GFRP tube-encased concrete columns". *Proceedings of Fourth International Conference on FRP Composites in Civil Engineering (CICE2008)*, Zurich, Switzerland, July 2008.
- Mohamed, H., and Masmoudi, R. (2008b). "Compressive behaviour of reinforced concrete filled FRP tubes". *ACI Special Publications*, SP-257, 6: 91-108.

- Mohamed, H., and Masmoudi, R. (2010a). "Axial load capacity of reinforced concrete- filled FRP tubes columns: experimental versus theoretical predictions". *ASCE Composites for Construction Journal*, 14(2): 1-13.
- Mohamed, H., and Masmoudi, R. (2010b). "Flexural strength and behaviour of steel and FRP-reinforced concrete-filled FRP tube beams". *Elsevier Journal of Engineering Structures*, 32: 3789-3800.
- Mohamed, H., and Masmoudi, R. (2011). "Deflection prediction of steel and FRP-reinforced concrete-filled FRP tube beams". *ASCE Composites for Construction Journal*, 15(3): 462-472.
- Ozbakkaloglu, T. (2013a). "Compressive behavior of concrete-filled FRP tube columns: assessment of critical column parameters". *Engineering Structures Journal*, 51: 188-99.
- Ozbakkaloglu, T. (2013b). "Concrete-filled FRP tubes: manufacture and testing of new forms designed for improved performance". *ASCE Composites for Construction Journal*, 17(2): 80-91.
- Ozbakkaloglu, T., and Oehlers, D. J. (2008a). "Concrete-filled square and rectangular FRP tubes under axial compression". *ASCE Composites for Construction Journal*, 12(4): 69-77.
- Ozbakkaloglu, T., and Oehlers, D. J. (2008b). "Manufacture and testing of a novel FRP tube confinement". *Engineering Structures Journal*, 30(9): 48-59.
- Park, J. H., Jo, B. W., Yoon, S. J., and Park, S. K. (2011). "Experimental investigation on the structural behavior of concrete filled FRP tubes with/without steel rebar". *KSCE Civil Engineering Journal*, 15(2): 37-45.
- Popovics, S. (1973). "A numerical approach to the complete stress-strain curve of concrete". *Cement and Concrete Research Journal*, 3(5): 583-599.

- Qasrawi, Y. (2007). "Flexural behaviour of spun-cast concrete-filled fiber-reinforced polymer tubes for pole applications". M.Sc. thesis, Department of Civil Engineering, Queen's University, Kingston, Ontario, Canada.
- Rafi, M. M., and Nadjai, A. (2009). "Evaluation of ACI 440 deflection model for fiber-reinforced polymer reinforced concrete beams and suggested modification". *ACI Structural Journal*, 106(6): 762-771.
- Said, H. (2010). "Deflection prediction for FRP-strengthened concrete beams". *ASCE Composites for Construction Journal*, 14(2): 244-248.
- Samaan, M. (1997). "An analytical and experimental investigation of concrete-filled fiber-reinforced plastics (FRP) tubes". Ph.D thesis, Department of Civil and Environmental Engineering, University of Central Florida, Orlando, FL, USA, p. 107-108.
- Taheri, F. (1996). "Lecture notes on civil fiber-reinforced plastics". Dalhousie University, Halifax, NS, Canada.
- Teng, J. G., Yu, T., Wong, Y. L., and Dong, S. L. (2007). "Hybrid FRP concrete-steel tubular columns: concept and behavior". *Elsevier Journal of Construction and Building Materials*, 21(4): 846-854.
- Toutanji, H. A., and Deng, Y. (2003). "Deflection and crack-width prediction of concrete beams reinforced with glass FRP rods". *Elsevier Journal of Construction and Building Materials*, 17: 69-74.
- Vincent, T., and Ozbakkaloglu, T. (2013). "Influence of fiber orientation and specimen end condition on axial compressive behavior of FRP-confined concrete". *Elsevier Journal of Construction and Building Materials*, 47(8): 14-26.
- Yost, J. R., Gross, S. P., and Dinehart, D. W. (2003). "Effective moment of inertia for glass fiber-reinforced polymer bars". *ACI Structural Journal*, 97(5): 712-719.

- Yu, T., Wong, Y. L., Dong, S. L., and Lam, E. (2006). “Flexural behavior of hybrid FRP-concrete steel double skin tubular members”. *ASCE Composites for Construction Journal*, 10(5): 443-452.
- Zakaib, S., and Fam, A. (2012). “Flexural performance and moment connection of concrete-filled GFRP tube-encased steel I-sections”. *ASCE Composites for Construction Journal*, 16(5): 604-613.
- Zhu, Z., Ahmad, I., Mirmiran, A. (2006). “Seismic performance of concrete-filled FRP tube columns for bridge substructure”. *Bridge Engineering Journal*, 11(3): 359–370.

APPENDIX A

Coupon Test Results of the Filament-Wound GFRP Tubes

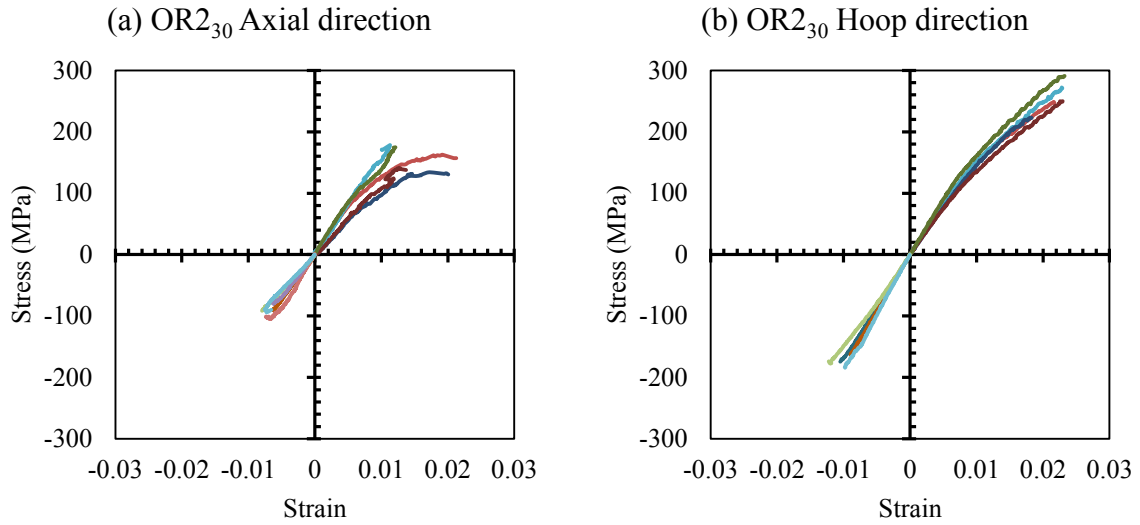


Figure A.1 – Coupons tests results of OR2₃₀

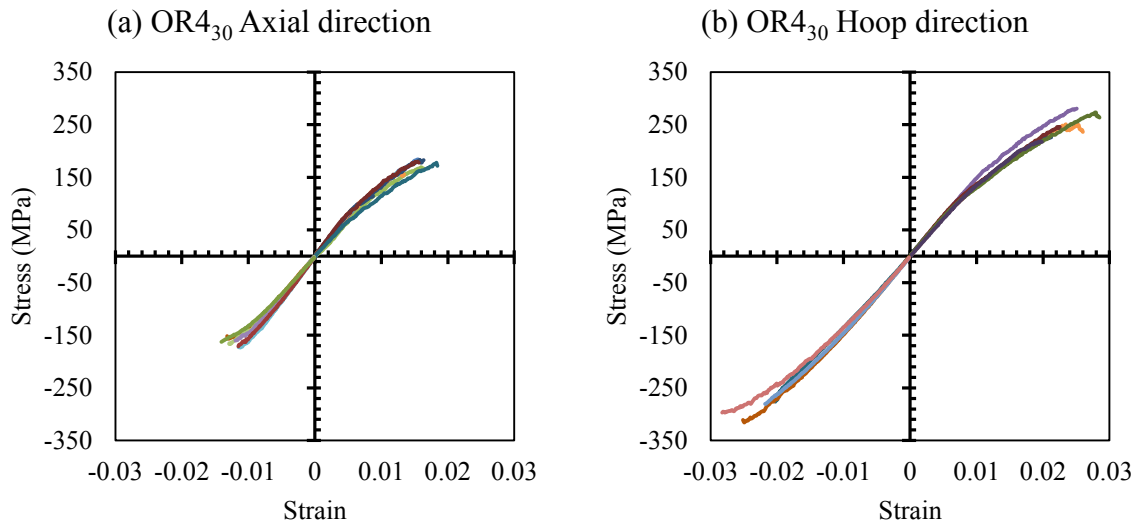
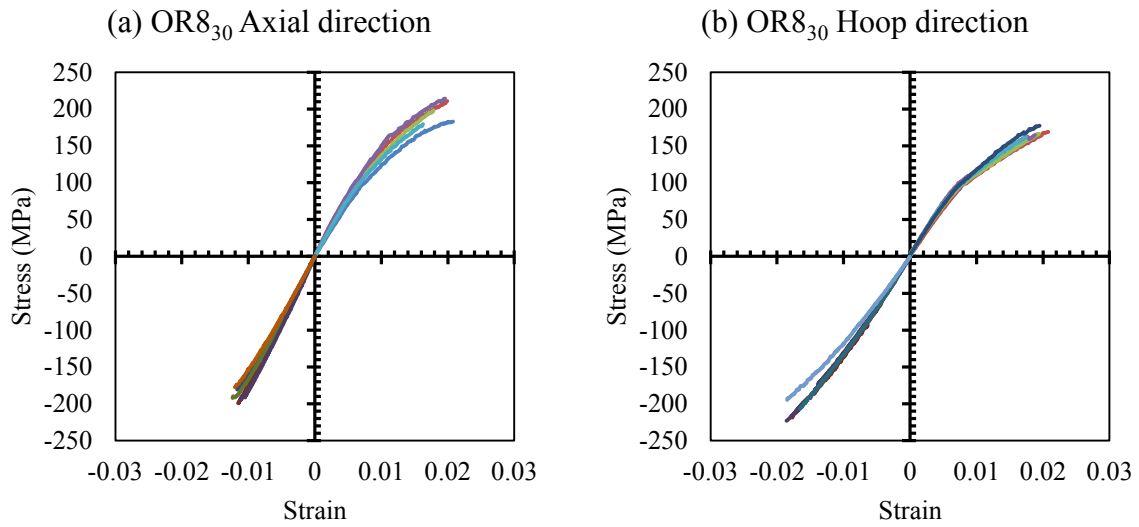
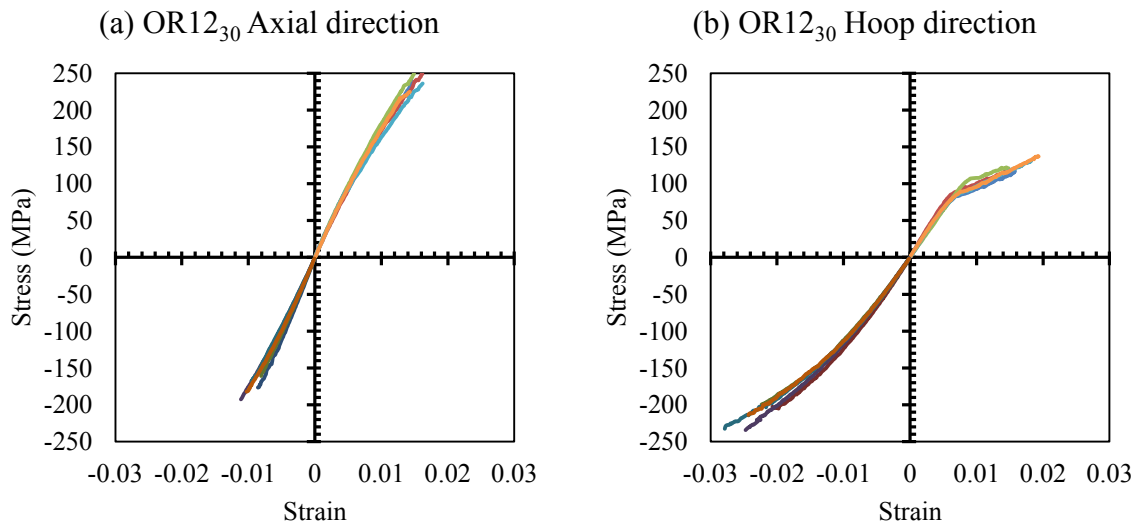
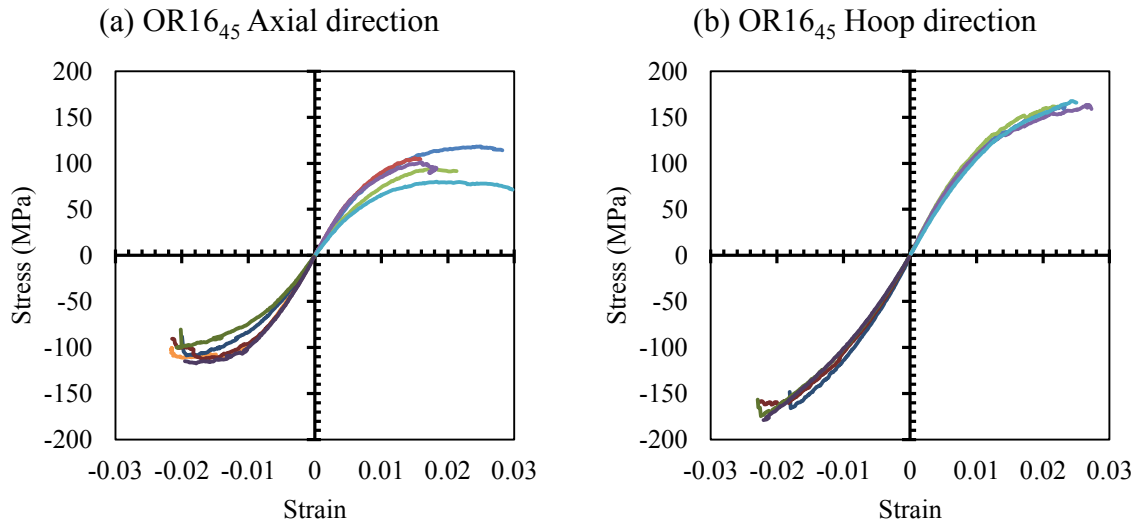
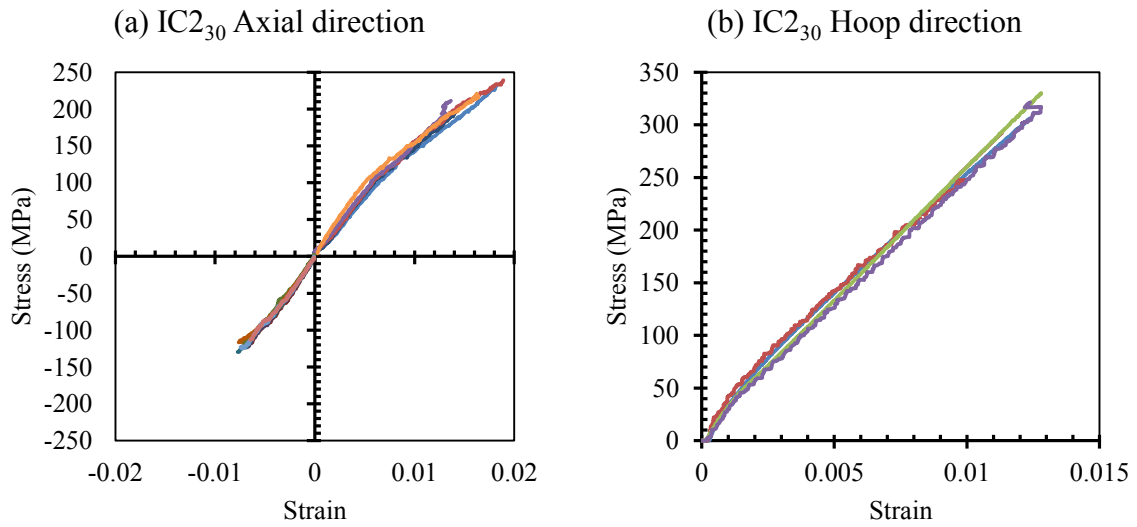
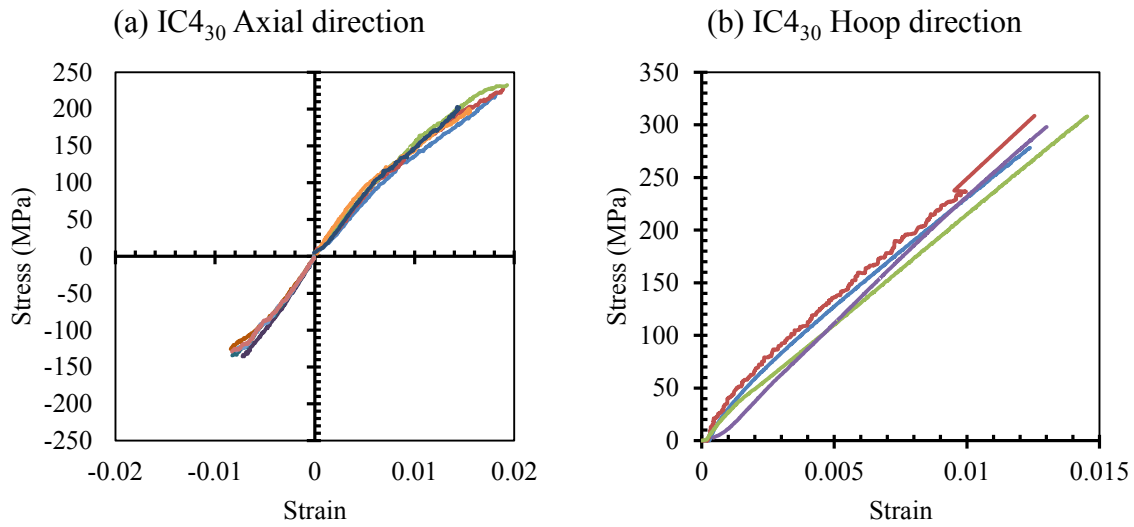
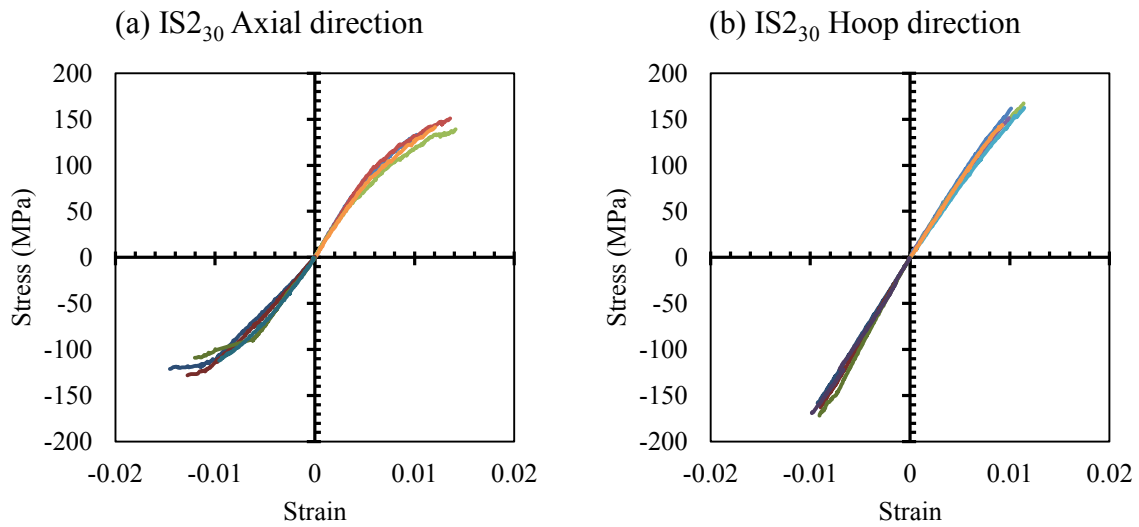
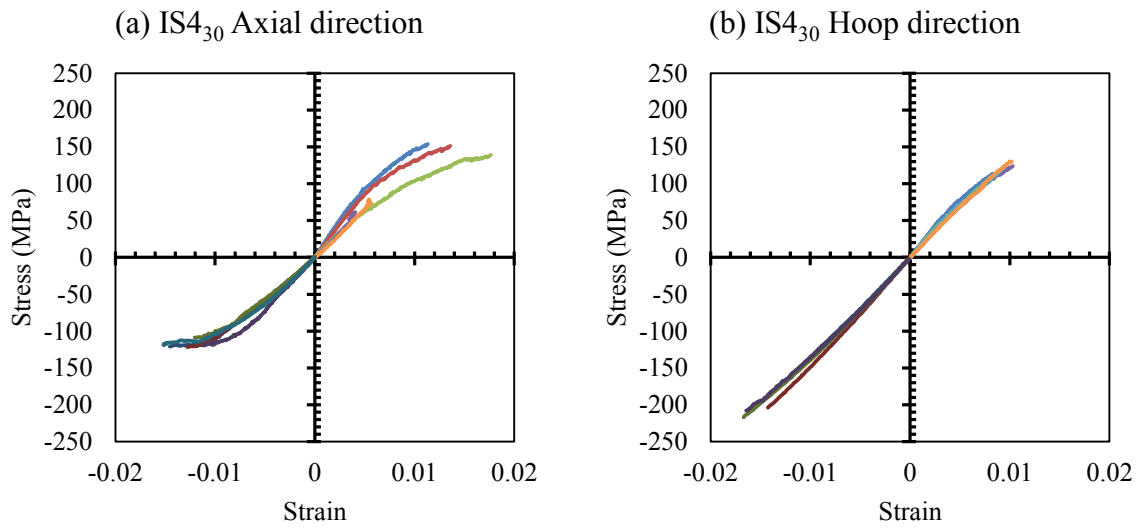
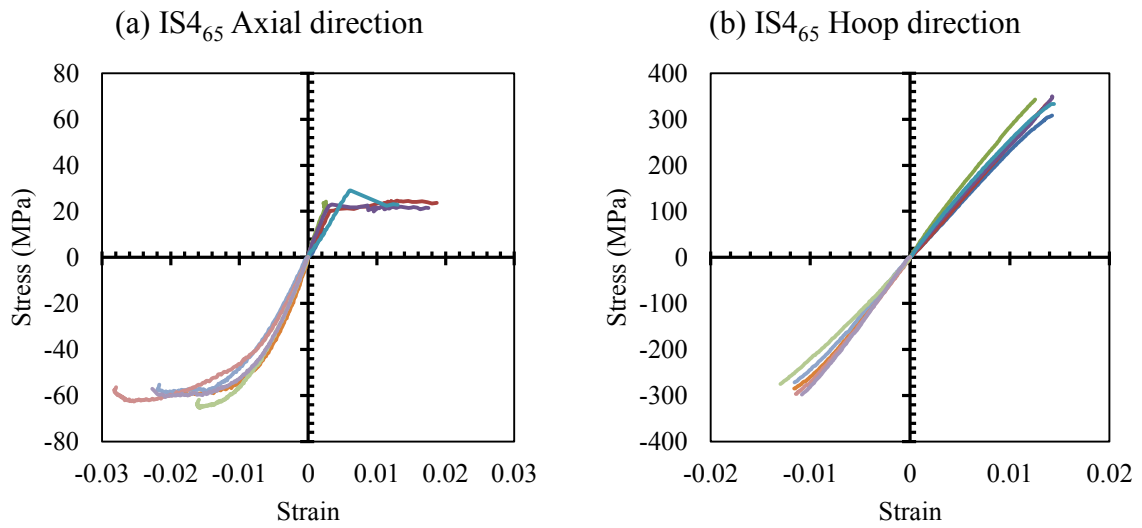


Figure A.2 – Coupons tests results of OR4₃₀

Figure A.3 – Coupons tests results of OR8₃₀Figure A.4 – Coupons tests results of OR12₃₀

Figure A.5 – Coupons tests results of OR16₄₅Figure A.6 – Coupons tests results of IC2₃₀

Figure A.7 – Coupons tests results of IC₄₃₀Figure A.8 – Coupons tests results of IS₂₃₀

Figure A.9 – Coupons tests results of IS4₃₀Figure A.10 – Coupons tests results of IS4₆₅

APPENDIX B

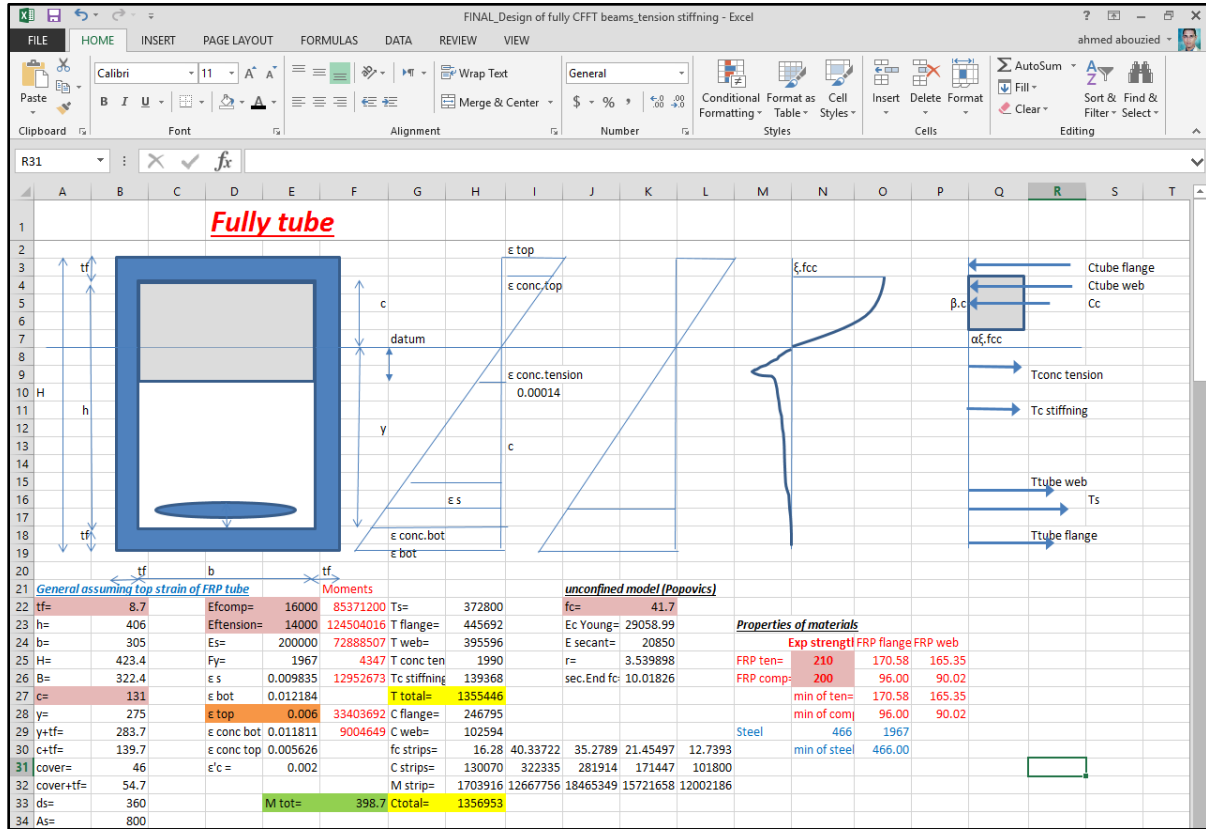


Figure B.1 – A spreadsheet for analytical study